DESIGN AND PERFORMANCE

EVALUATION OF HYBRID

PARALLEL LINK MACHINE TOOLS

2003

Tsann-Huei CHANG

Acknowledgements

I would like to express my sincere appreciation to my thesis advisor, Dr. Ichiro INASAKI, for his continual encouragement, and patient guidance throughout my research work and preparation of this dissertation. I would also like to thank the members of the thesis committee: Prof. Kimiyuki MITSUI, Prof. Masatsugu YOSHIZAWA, and Prof. Toshiyuki MURAKAMI of KEIO University, who invest the time and effort in providing the creditable critiques and feedback the thesis up to the academic standard.

Special thanks to Prof. Shang-Liang CHEN of National Cheng-Kung University and to Prof. Chun-Pau KUO and Prof. Meng-Shiun TSAI of National Chung Cheng University. The collaboration with Mr. Kuan-Wen CHEN, Mr. Chao-An KANG and Mr. Yu-Binn GU in my laboratory has proven to be valuable to our research. Besides, I would put special mention to Dr. Cheng CHEN, Ms. Li-Chen YANG who is my secretary, Ms. Weiting HSIN and Ms. Ema SHIEH. Without their help, this research work could have never been accomplished.

This research was conducted under the support of the Mechanical Industry Research Laboratories- Industrial Technology Research Institute (ITRI) in Taiwan. Here, I would specially devote my thanks to Dr. Bill TSAI, director of MIRL, who strongly recommended me for the advanced study on this dissertation subject. Without his encouragement, this research work could have never been started.

Finally, I will take this opportunity to thank my families for their unwavering supports all the time. My love and appreciation to them are well beyond the word of gratefulness.

KEIO UNIVERSITY

ABSTRACT

Design and performance evaluation of hybrid parallel link machine tools

by Tsann-Huei CHANG

Machine tools with high speed and high acceleration have been sought and expected for a long time. Technology development in this area realizes that the high acceleration maybe achieved by substituting serial link mechanisms by parallel link mechanism. Parallel link mechanisms have been used in many types of machine tools. However, many related problems are still required to be solved for the practical applications of this type machine tool. The main related problems are seriously restricting the application of the machine tools. This dissertation presents a novel machine tool, called the TRR-XY hybrid parallel link machine tool which provides the advantages of both serial link mechanism and parallel link mechanism. Here, the hybrid parallel link machine tool means that the α, β and Z motion degree of freedoms of this machine tool are achieved by a parallel link mechanism and the x and y translation motion degree of freedoms are achieved by a serial link mechanism. Its theoretical models of inverse kinematics and dynamics are established; angular workspace and singularities are analyzed; inverse dynamic analysis with driving force is also discussed. A new theory for optimizing its dimensions is proposed. Two error models are developed in this research: manufacturing error model and controller parameters error model. A prototype machine tool is designed and developed to perform the experiments for verifying the correctness of the theory. This study demonstrates some results about hybrid machine tool that have not been reported before. All the aforementioned models will contribute to develop a new type hybrid

parallel machine tool by providing helpful advice on such aspects as the optimization of the workspace, the minimum of the driving force, the improvement of machining accuracy, and the development of a parallel machine tool with high speed, high acceleration and high accuracy.

Table of Contents

Nomenclatures

$\underline{\underline{A}}_{Kp}^{p-1}$: D-H transformation matrix between coordinate systems $(XYZ)_{Kp}$ and $(XYZ)_{K(p-1)}$ on the K chain. (K = A, B, C ; p = 1~7)

$\underline{\underline{A}}_{P}^{P-1}$: D-H transformation matrix between coordinate systems $(XYZ)_p$ and $(XYZ)_{p-1}$ (p = 1~7). Similarly, $\underline{\underline{A}}_t^0$, $\underline{\underline{A}}_W^0$, $\underline{\underline{A}}_L^W$, $\underline{\underline{A}}_t^L$

a_c : motion acceleration if a prismatic joint is discussed

a_i : D-H transformation translates the offset along x-axis from coordinated systems $(XYZ)_{i-1}$ and $(XYZ)_i$

$\underline{b}_{j-1}$: 3×1 unit vector along joint axis j-1

$C\underline{F}_{ext}$: force on the C chain

CP : cutting point

$C\underline{\tau}$: represents the $\underline{\tau}$ on the C chain

c_i : constraint of joint I

d_i : D-H transformation translates the offset along z-axis from coordinated systems $(XYZ)_{i-1}$ and $(XYZ)_i$

E : horizontal distance

F : vertical distance

$\underline{F}_{CP}$: force exerted on the cutter at the cutting point

$\underline{F}_{ext}$: external force

$\underline{f}_{ext}$: equal to $\underline{F}_{CP}$

$\underline{g}$: gravitational acceleration

$\underline{G}(\underline{q})$: gravity torques

$\underline{h}(q,\dot{q})$: Coriolis forces and centrifugal forces

$h_{ijk}(\dot{q}_j\dot{q}_k)$: Coriolis forces and centrifugal forces

hs : thickness of the slider

H_{ij} : i-th row and j-th column component of $\underline{\underline{H}}(\underline{q})$

$\underline{\underline{H}}(\underline{q})$: a 6×6 configuration-dependent positive-definite symmetric matrix for inertia torques and interaction torques

I_{xxi} : mass of moment inertia referred to x-axis, Kg-mm^2

I_{yyi} : mass of moment inertia referred to y-axis, Kg-mm^2

I_{zzi} : mass of moment inertia referred to z-axis, Kg-mm^2

$\underline{i}_0\ \underline{j}_0\ \underline{k}_0$: the orientation of the three unit vectors of the fixed coordinate system $(XYZ)_0$

j : number of joints

$\hat{\underline{j}}_7\quad \hat{\underline{k}}_7$: unit vector of frame $(XYZ)_7$

$\underline{j}_L$: unit vector of the feed direction at the cutting point

$\underline{\underline{J}}$: Jacobian matrix

$\dot{\underline{\underline{J}}}$: differential of Jacobian matrix

$(\underline{\underline{J}}^T)^{-1}(:,1)\quad (\underline{\underline{J}}^T)^{-1}(:,2)$: the 1st and 2nd column vectors of $\left(\underline{\underline{J}}^T\right)^{-1}$

$k\underline{F}_{ball}$: force applied on tool platform from ball joints (k = A, B, C)

$\underline{k}_{C6}$: direction of the cutter axis

$\underline{k}_L$: unit vector of the normal direction of the part surface

L : length of the links

m_i : mass of link i, Kg

$\underline{m}_{ext}$: external momentum (cross product of $\underline{r}_{6,L}$ and $\underline{F}_{CP}$)

n : number of links. In this research, n = 6.

n_C : number of the constraints

n_L : total numbers of mechanisms

O_0 : center of the upper base frame

O_{C1} : intersection point of the linear sliding axis and the upper base frame

O_{C2} : intersection point of sliding axis and link

$O_{C3...C5}$: centers of ball joints

O_{C6} : center of the circle that formed by the three ball joints

O_L : coordinate system after the yaw angle (ω) and tilt angle (λ) transformation

O_7 : cutter tip point

$\underline{P}$: position of origin of coordinate $(XYZ)_{C6}$ in the C chain

$\underline{P}_{07}$: distance between the origin of $(XYZ)_7$ and the origin of $(XYZ)_0$

$\underline{P}_{O_0O_W}$: distance between the origin of $(XYZ)_W$ and the origin of $(XYZ)_0$ described by vector

Pi : position vector of the cutting surface relative to the work-piece local coordinate system (i = X, Y, Z)

$\underline{P}_{WL}$: distance between the origin of $(XYZ)_L$ to the origin of $(XYZ)_W$

Px_6 Py_6 Pz_6 : position that the frame $(XYZ)_6$ respect to the frame $(XYZ)_0$

Px_7 Py_7 Pz_7 : position that the frame $(XYZ)_7$ respect to the frame $(XYZ)_0$

$\dot{\underline{P}}$: velocity of origin of coordinate $(XYZ)_{C6}$ in the C chain

$\ddot{\underline{P}}$: acceleration of origin of coordinate $(XYZ)_{C6}$ in the C chain

PowC : required actuator driving force for C chain

Q_i : all non-conservative generalized forces (i = 1, 2…, n)

$\underline{q}_i$: joint space (i = A, B, C)

$\dot{\underline{q}}$: (angular) velocity of the components

$\ddot{\underline{q}}$: (angular) acceleration of the components

R : circle radius on upper base frame that three driving axes are evenly located

r : circle radius of tool platform that three ball joints are evenly located

r_C : radius of cutting edge

$\underline{r}_{6,L}$: distance between $(XYZ)_L$ and $(XYZ)_6$ referred to $(XYZ)_0$

$\underline{r}_{j-1,ci}$: position vector of the centroid of link i referred to the origin of coordinate $(XYZ)_{j-1}$

S_i : displacement of the slider, subscript i = A, B, C separately represents the different A, B, C kinematic chains.

t : tool length between O_{C6} and O_7

$\underline{t}$: tool axis

$\underline{\underline{T}}_7^0$: D-H transformation matrix between coordinate systems $(XYZ)_0$ and $(XYZ)_t$

V_c : motion velocity if a prismatic joint is discussed

$\underline{V}_e$: velocity of end-effector

$\underline{\dot{V}}_e$: acceleration of end-effector

$(XYZ)_0$: upper base coordinate

$(XYZ)'_0$: coincident with $(XYZ)_0$

$(XYZ)_7$: cutter tip coordinate

$(\dot{X}\dot{Y}\dot{Z})_7$: axis of the moving coordinate

$(XYZ)_{fp}$: coordinate systems for D-H notation $(XYZ)_{fp}$, f = A, B, C, p = 1~6

$(XYZ)_L$: part surface local coordinate

$(XYZ)''_L$: coordinate system after the yaw angle and tilt angle transformation

$(XYZ)_t$: cutting location coordinate

$(XYZ)_W$: working coordinate

Y_L : feed direction

Z_t : cutter axis

α : an angle rotate about $\underline{\hat{X}}_7$

α_i : angular errors along x-axis based on coordinate 1

α_{ki} : angular acceleration (k = A, B, C ; i = 3, 4, 5, 6)

β : an angle rotate about $\underline{\hat{Y}}_7$

β_i : orientation errors along y-axis of frame in i-chain

δ_{Fxi} : position errors along x-axis of frame in i-chain

δ_{Fyi} : position errors along y-axis of frame in i-chain

δ_{Jxi} : position errors along x-axis of ball joint in i-chain

δ_{Jzi} : position errors along z-axis of ball joint in i-chain

δ_{Sxi} : position errors along x-axis of spindle location

δ_{Syi} : position errors along y-axis based on coordinate 7

ϕ : angle between cutter and Z'-axis

ϕ_i : angular errors along y-axis based on coordinate 2

γ : an angle rotate about $\underline{\hat{Z}}_7$

γ : freedom expected

γ_i : angular errors along z-axis based on coordinate 1

φ : angle between the tool axis X'-Y' projection and X'-axis

λ : tilt angle

λ_f : freedom expected

λ_i : angular errors along x-axis based on coordinate 2

Ψ : angle of cutting point

θ_a : the angle between the link and sliding axis. (a = A3, B3, C3)

θi : D-H transformation joint angle from coordinate systems $(XYZ)_{i-1}$ and $(XYZ)_i$

θ_{ik} : rotation angle (i = A, B, C ; k = 1 ~ 6)

ω : yaw angle

$\underline{\omega}_e$: angular velocity of end-effector

$\dot{\underline{\omega}}_e$: angular acceleration of end-effector

ω_{ki} : angular velocity (k = A, B, C ; i = 3, 4, 5, 6)

$\underline{\tau}$: torque derived by Lagrange equations

$\underline{\tau}_{c1}$: moment applied to the upper base by C chain

Foot notes

i	i = A, B, C chains
F	the errors defined inside [Frame] matrix
J	the errors defined inside [Ball] matrix
S	the errors defined inside [Spindle] matrix
x, y, z	based on the x, y, or z-axis direction

Chapter 1 Introduction

1.1 Background and motivation

Stewart platform based machine tools have recently been exhibited to be very impressive at international machine tool shows. Designers of machine tools have been astonished at the emergence of this parallel link mechanism machine tool. V.E. Gough created this mechanism in 1948, which was adapted by D. Stewart in 1965 for the applications of flight simulator [1]. The so-called Stewart platform or Gough Stewart platform includes a 6 Degree of Freedom (DOF) parallel mechanism with six identical kinematic chains, consisting of universal joints, prismatic actuators, and spherical joints. In 1994, a Stewart platform based six-axis machine tool (typically called a hexapod), Variax [2], produced by Giddings & Lewis Company, was introduced at the International Manufacturing Technology Show (IMTS)'94, in Chicago.

In the international machine tool exhibition, Exposition Mondiale de la Machine Outil (EMO)'2001, over 15 machine tool builders had produced parallel link machine tools (also called parallel machine tools, parallel mechanism machine tools, and parallel link machine tools (PLM)). Until now, parallel link machine tools are still in research stage and no great developments in their engineering applications.

Traditional machine tools have been used for more than two centuries. In this construction, axes are stacked in series and a closed-loop chain is formed between the tool and the workpiece (or part) through linear axes X, Y and Z and rotary axes, α and β. A traditional machine has a serial link mechanisms (SLMs), and so the axis motion is constrained by accelerating the mass of the other axes that linked with the motion axis. Furthermore, each axis on the SLM bears the full load of the end effector, namely the cutting tool, the weights of joints and actuators. Therefore, every axis must be made very rigid. This will increase the size of the machine tool and increase the weight of the

serial link machine tool. This increased weight worsens the tool's dynamic behavior and worsens the tracking errors.

In the parallel link machine tool of Variax, the spindle is mounted on a platform. There are six links (or legs) with length adjustable directly connected to the platform. The position of the spindle depends on the length of the links. The spindle has six independent DOF, including three translational DOF and three rotational DOF. Cartesian coordinates are invisible in this machine tool, only existing in the control system. So the corresponding axes are called, "virtual axes". In a traditional serial link machine tool, the axes are defined by Cartesian coordinates which makes understanding easy and facilitating the operation of the machine. Moreover, each axis is independent controlled and error compensation can be performed separately. The main differences between a parallel link and a serial link machine tool are that each link is separately driven by an actuator and that the links are in parallel and are coupled. Each link transmits only tension or compression and the load is distributed onto the links to increase the theoretical structural stiffness. Therefore, the machine tool can achieve higher rigidity with lower mass. High speed is easily realized using a parallel link chains mechanism since it benefits from the combination of a smaller moving mass and a higher stiffness. Although the parallel link machine tool provides these advantages, disadvantages remain. For example, the workspace is always rotationally symmetrical. The mechanical efficiency may be very low in some regions, and singularities exist in the workspace. For example, the workspace of the machine tool produced by Ingersoll is around $1m^3$, but the side length of the machine is as large as 6m. Compared with a traditional machine tool, this machine tool suffers from being too large. With respect to engineering, an extensible link is not a standard part and a high stiffness extensible link is difficult to be obtained. Heat generation by the actuators may cause structure errors, which are difficult to be compensated. The ball joint is the

key component of the system but a high stiffness and accurate ball joint is very difficult to be made, which mitigates the advantages mentioned above. Weak ball joints causing the entire structure errors may not be able to meet the demands of cutting process of a machine tool.

To control and adjust the parallel link mechanism is more complicated. As the axes of the machine do not follow the concept of Cartesian coordinates. Thus, the controller must perform complicate computations. In some special conditions, the direction of acceleration of one axis may be opposite to that of another axis and this mistake may cause the mechanism to be collapsed. Therefore, the Multi-input Multi-output (MIMO) system, rather than the Single-input Single-output (SISO) system, is always used in compensatory feedback. Thus, a high speed MIMO control system with a rapid dynamic response is always required. This critical obstacle has already been overcome nowadays. Developing a new machine tool with parallel link mechanism as basic structure that can operate at high speed is of great interest if its shortcomings can be overcome to make it more competitive than the serial link machine tools.

The main purpose of a machine tool is to cut in a high speed. High accuracy and high speed cutting depends on high rigidity and stability of the machine tool. A new hybrid parallel link machine tool was presented by the author, Mr. Yeou-Bin Gou and Dr. Shang-Liang Chen in 1999. We have obtained American patent for this new type machine tool, which is also patented in Taiwan and China [3]. To apply a parallel mechanism into a machine tool motivates this research.

1.2 Problem statements

To apply a hybrid parallel link mechanism (PLM) into a machine tool is an interesting but challenging research topic. Very few literatures on this topic are found.

Most of the literatures have focused on the characteristics of manipulators based on a multi-kinematic chain structure.

This study starts from a kinematic analysis of the parallel link mechanism. For practical machining applications, only inverse kinematic solution is required. The workspace of the parallel link mechanisms has two main problems. First, the workspace includes singularities. The singularity cannot be solved using Jacobian analytical theory because a forward kinematic solution is unavailable. Second, the ratio of the workspace to the machine volume cannot be very small, so the ratio of the machining volume to the machine volume must be optimized.

The unavailability of forward kinematic solution causes the difficulty in analyzing velocity, acceleration and energy consumption. The error analysis has also been rarely discussed in the applications of hybrid PLM into machine tool.

Models and methods of analyzing machining errors are studied by many previous researchers for traditional serial link machine tools. However, for the hybrid PLM structure, the verification and measurement of the manufacturing error are difficult. This research concentrates on the improving of the machining accuracy of the parallel machine tool. The main aim is focused on the machine space ratio, driving force variation, and effects of the manufacturing errors of the hybrid PLM machine tool.

1.3 Thesis outline

The main purpose of this research is to investigate the feasibility of using a novel hybrid parallel link mechanism for the design and development of a new machine tool. There are three main topics are focused in this research. The first one is the ratio of workspace/machine volume of the developed machine tool. The second one is the driving force variation for different mechanism configurations. The third one is the effects of the manufacturing errors on the machining accuracy. From the analysis

results, it is found that applying the new developed hybrid machine tool for five-axis machining within a limited angle range may have several advantages compared with the conventional serial type machine tool. For example, the high accuracy, the low power consumption, and cost down. The theory and results obtained in this research will be very helpful for the designer to understand the essential and important performances of this machine tool in the first stage of the development.

The thesis is organized as follows.

Chapter 1 introduction

Chapter 2 provides more detailed background information on hybrid PLM machine tools. This chapter discusses technical developments in the industry and related scientific literatures.

Chapter 3 defines the basic structure of the hybrid PLM machine tool, derives an inverse kinematic model, examines singularities of the workspace, also includes the optimization of the workspace.

Chapter 4 analyzes the inverse dynamics model. The parametric tool concept and Lagrange-equation theory are also included in the derivation, and the driving force of every axis is calculated.

Chapter 5 develops two error models. One analyzes for machining and the other based on the compensation parameters of the commercial controller. An error verification is also proposed and a simulation is performed.

Chapter 6 analyzes accuracy using real cutting tests and the DBB (Double Ball Bar) method. Theoretical models are verified.

Chapter 7 concludes the work, summarizes findings and suggests for future research. The appendices present supplementary information.

References

1. D. Stewart, “A platform with six degrees of freedom” proceedings of the Institution of Mechanical Engineering (London); 180, Part 1 (15), PP. 371-386, 1965
2. Giddings & Lewis Variax (http://www.giddings.com)
3. Patent title : Composite mechanism multi-axis machine tool, R. O. C,

   (Utility) Patent No. : 149487, Patent term: 19990701 ~ 20100730

   Application No. : 87212408 Filing Date: 19980803

   Patent title: Composite mechanism multi-axis machine tool

   (Patent) Patent No. : 6,048,143, Patent term: 20000411 ~ 20190129

   Application No. : 09/240,792, Filing Date: 19980806

Chapter 2 Overview of parallel link machine tools

2.1. Introduction

The CNC machine tool is an important facility of today's manufacturing industry. As global competition intensifies, manufacturers are being asked to produce machine tool with greater accuracy while keeping costs down. One key to do so is to increase the accuracy of the CNC machine tool. There is a promising development of the machine tool in the recent years: the introduction of hexapod design. A hexapod machine tool radically is different from the conventional multi axis configuration that has been used for decades. The hexapod relies on a parallel series of actuators to create the tool motion. Several manufacturers including Ingersoll, Giddings and Lewis, Hexel, Geodetics, Hitachi Seiki and others have introduced many machines based on the hexapod (or the Stewart Platform as it is commonly called). It is hoped that the parallel design will offer better rigidity, stability and accuracy.

There are some challenges such as complicated control, restricted workspace, position-dependent features, etc. in bringing hexapod machine tool into real machining applications at present. The comparing and analyzing between the traditional hexapod machine tool and the newly exhibited twelve types of parallel link machine tool on Exposition mondiale de la Machine Outil (EMO)'2001 and Japan International Machine Tool Fair (JIMTOF)'2002, are shown in this chapter. We not only investigated hybrid type structure of parallel link machine tool but also presented a new structure to overcome the drawbacks of Stewart-base structure. Whether a new parallel link structure can be used to be a machine tool is decided by the characteristics of workspace, singularity restraints, dynamic and static rigidity, self-adjustable ability, and error compensation. Confirming the application fields of this new developed parallel link machine tool and discussing the advantages or drawbacks are also the major topics studied here.

2.2 History of the development of parallel link machine tools

A new machine tool was introduced at IMTS 94. The new machine tool was based on the Stewart platform architecture and was designed for machining. The Giddings & Lewis Co. of USA developed this parallel mechanism machine tool and was called "Variax" [1](Figure 2-1). This 6 DOF machining tool has several shortcomings such as very limited workspace and 15 degree spindle tilting angles only. The Ingersoll Co. and NIST of USA also jointly develop a parallel link machine tool named "Hexapod"[2] (Figure 2-2). An upside down structure of Stewart Platform was used in this machine tool. This machine tool has total of 45 degree tilting angle including 30 degree from the spindle unit and 15 degree from the base plate.

The "G500" [3] (Figure 2-3) of Geodetics Technology International Holdings N.V. Co. also has 45degree spindle tilting angles. By adding a 2-DOF structure on the spindle unit, this "G500" machine tool can perform 90 degree spindle tilting angle. A "Sinumeric 840D" controller of Commercial Co was used in this machine tool.

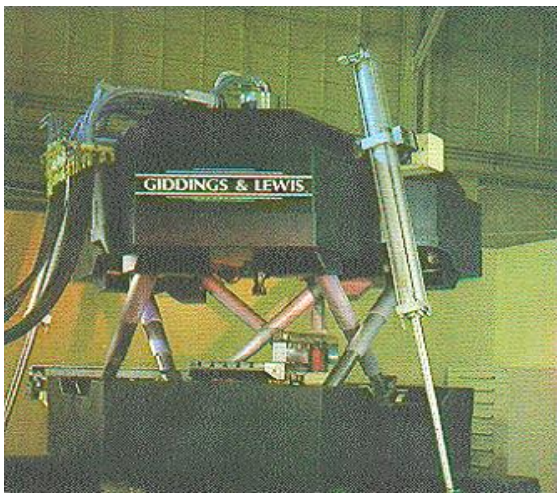

Figure 2-1 VARIAX (Giddings & Lewis, USA)

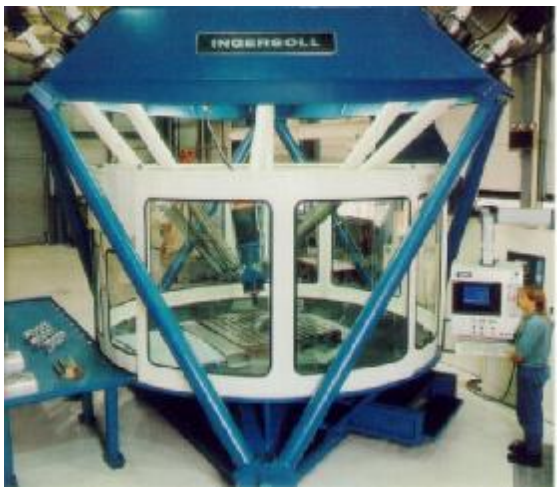

Figure 2-2 Hexapod (Ingersoll, USA)

Two new types of parallel link machine tools were introduced at JIMTOF' 96 in Japan. The HexaM [4] (Figure 2-4) was developed by Toyoda Co. Instead of changing the length of the links the fixed links of HexaM moves along the tilted slideway in order to improve the stiffness of the system. The spindle unit can tilt up to 30 degrees. Hitachi Seiki Co. developed a drilling machine named "PXA" [5] based on the 3 DOF "Delta" parallel link machine, of France (Figure 2-5). To decrease the inertia mass, "Delta" uses DD (Direct Drive) motors at base, and

increase the speed of the system. Instead of DD motors, additional links are used in "PXA" to control the spindle unit and this increases the stiffness of the system.

Hexaglide (Figure 2-6) of ETHZ [6] in Switzerland is a 6 DOF machining workstation. The lengths of links are fixed and the links are moved on horizontal slides by linear motors. This machine is particularly effective for long-shaped workpieces along the horizontal slide. The 3 DOF parallel link milling machine, Dynamill [7] (Figure 2-7) of T.H Aachen of Germany was also developed. The Hexact [8] (Figure 2-8) is jointly developed by Stutgart University, Commercial INA and introduced at EMO' 97

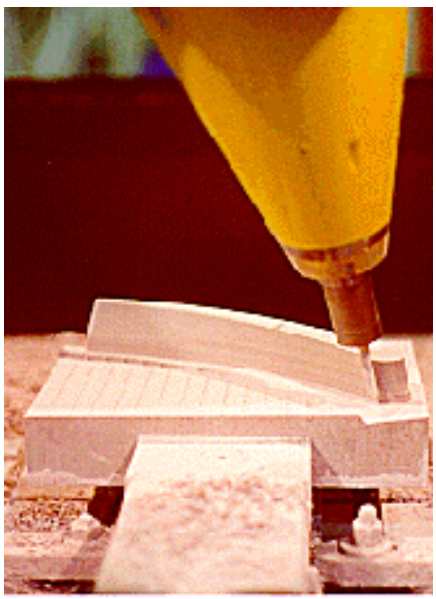

Figure 2-3 G500 (Geodetics, UK)

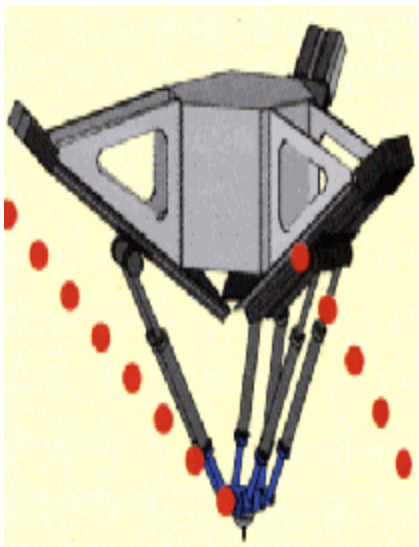

Figure 2-4 HexaM (Toyoda, Japan)

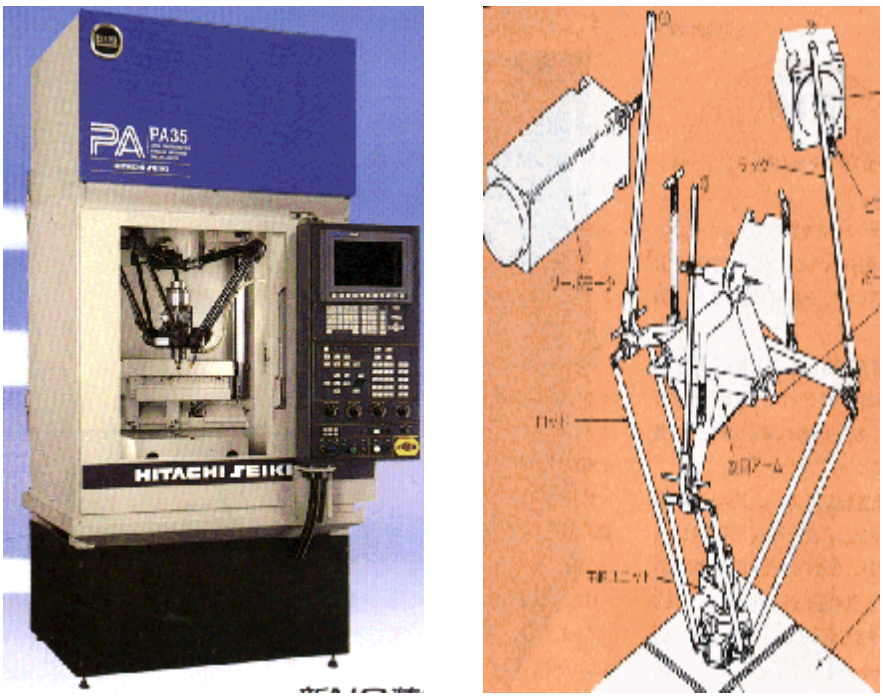

Figure 2-5 PXA (Hitachi Seiki, Japan)

Figure 2-6 Hexaglide (ETHZ, Swiss)

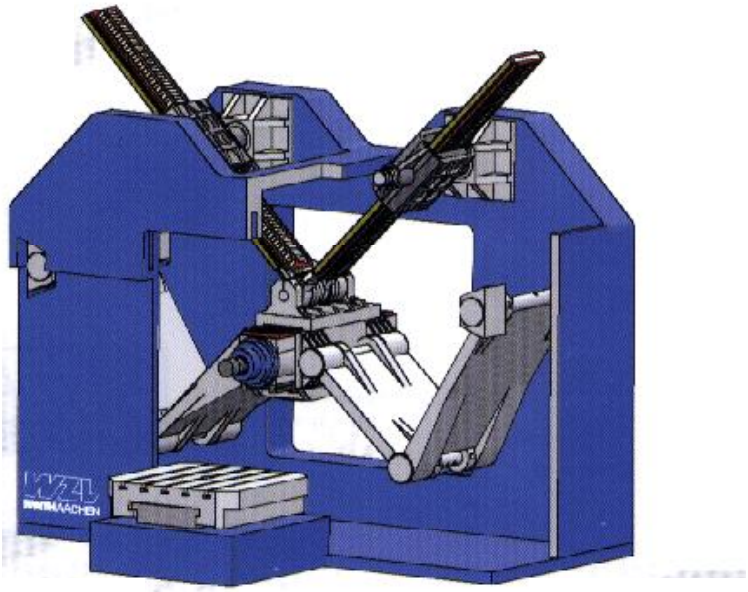

Figure 2-7 Dynamill (T. H. Aachen Univ. Germany)

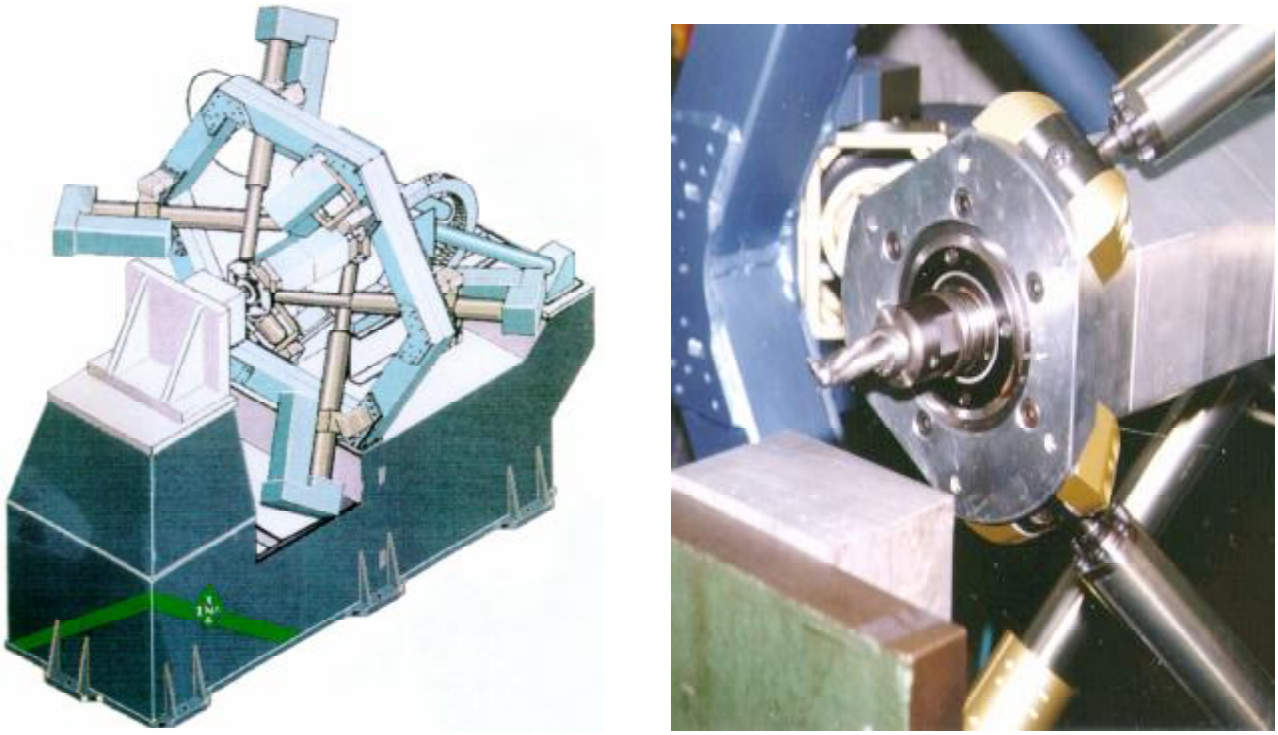

Figure 2-8 Hexact (INA/Commercial, Germany)

Cincinnati Machine and DS Technology GmbH (DST) [9] cooperatively introduced a Hypermach horizontal machining center （See Figure 2-9）. This machine tool adopted a tripod with struts not variable in length, and a X-Y table of serial link mechanism with maximum speed 50m/min and 1g acceleration. This machine tool was announced to be used in milling for aeroplane industry and machine tool market.

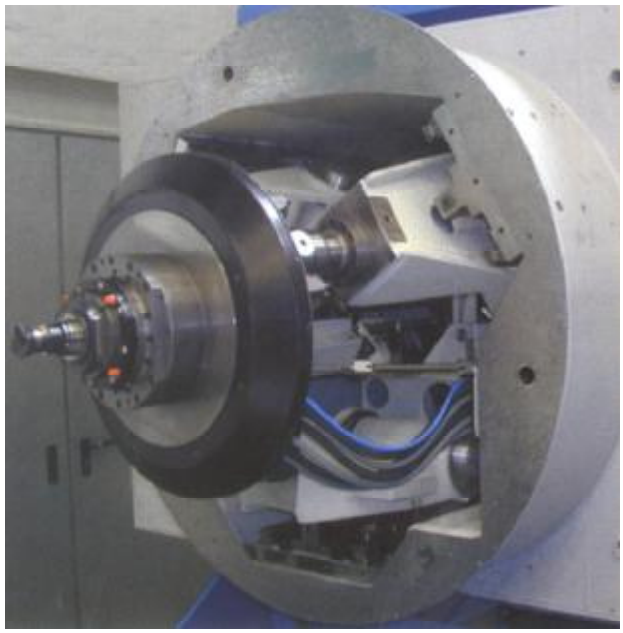

Figure2-9 Cincinnati Machine and DS Technologie Gmbh (DST)

The following six types of machine tools were exhibited in the EMO'2001:

The "Kinematic SKM 400" in Fig 2-10 [10] was exhibited by Heckert (Germany). It is a tripod structure with fixed struts length and passive crank mechanism. This is a three DOF horizontal machining center with maximum speed of 100m/min and acceleration of 1g.

Figure 2-10 SKM 400, Heckert, Germany

Renault Automation Comau developed a parallel link machine tool named "Urane Sx"[11] (see Fig 2-11). Urane Sx is made based on Delta parallel structure with one fixed arm, which provides only two translational degrees of freedom along x and y axes. Z axis is quill type and each axis is driven by linear motor. Built-in motor (12kw,40000rpm) is used in spindle[10]. The maximum speed is 100m/min and acceleration of 3.5g. This machine tool is found mainly to be used in drilling applications.

Figure 2-11 Renault Automation Comau: URANE SX

NEOS Robotics (see Fig 2-12) [12] is a kind of parallel link machine driven by three extensible limbs. Its most distinguishing feature is that a set of DMS (Direct Measuring System) with feedback components optical ruler and encoder mounted on a canister of center of limbs. The precise position of the end-effector is able to be defined by using the DMS, thus, distortion error of joints or limbs generated by external forces or its weight during machining process is directly measured and input to the controller so as to achieve precise control of machine tool. The maximum speed is 90m/min and the maximum acceleration is 2g.

Figure 2-12 NEOS Robotics Tricept Machining Centre TR845

DMG introduced NEOS licensed tricenter DMT 100 (see Fig 2-13). At present, Tricept [13] parallel link machine tool of NEOS takes the lead in both application and sale.

Figure 2-13 DMT 100, DECKEL MAHO, Pfronten, Germany

Table 2-1 shows the characters of Dumbo(Fig 2-14) [14] machine tool. Two sets of extensible parallel limbs one used to drive the motion offend-effector along x and y direction and the linear motion of cutting tool along z-axis is realized by a linear feed mechanism fixed on the vertical column of the machine tool. The working space and the flexibility of cutting tool are relatively bettor compared with the other type of parallel link machine tool.

Figure 2-14 Dumbo, IFW, University Hannover Germany

Table 2-1 The character analysis of Dumbo

Structure	2-strut with additional z-axis and 2 wrist axes
Application	repair of die and mould, milling
Drive system	Siemens driver and INA ballscrew and spindles
Control system	Siemens 840 D
Working volume	500, 500, 500 mm (x,y,z)
Degrees of freedom	5

A new, hanging-spindle, vertical turning lathe (VTL) (Fig 2-15) has been introduced by Index. The spindle head can move freely in three dimensional space[15]. Three groups of parallel four-linkage mechanism are constituted by six rods, and accelerates the construction at 1g to reach 60 m/min high speed moving in all three orthogonal directions simultaneously.

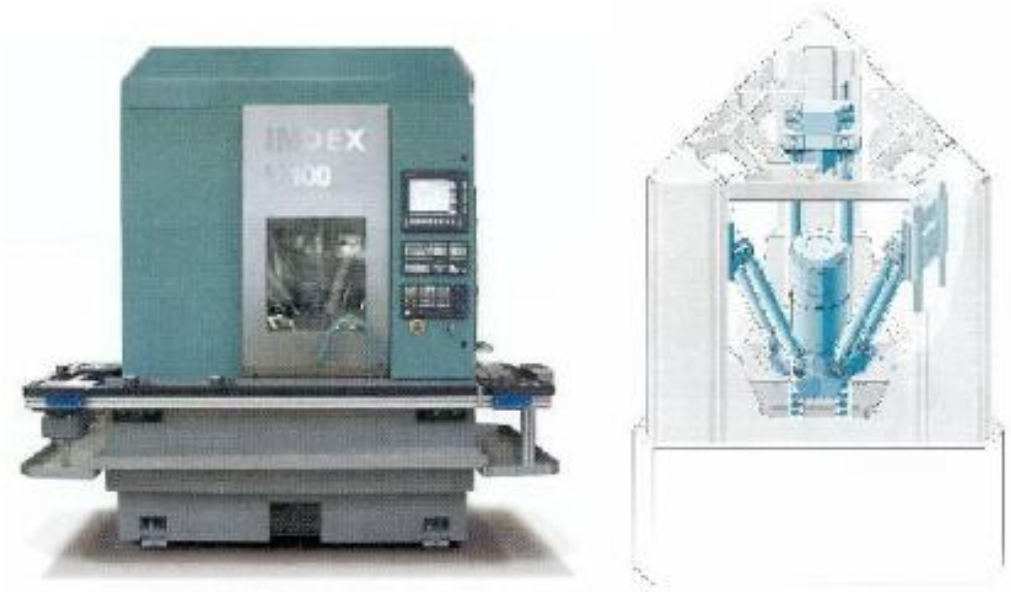

Figure 2-15 Index V100, Index, Germany

The structures of parallel link machine tool are found to be greatly changed in the exhibitions of IMTS'94 and JIMTOF'2002. From analysis of the exhibited machine tool structure tool (table 2-2), it is found that the major developing tendency of parallel link machine tool is as follows:(1) reduce the required axis number of parallel link mechanism, and (2) overcome the drawbacks of parallel link mechanism by using serial link mechanism.

Table 2-2 Configurations of the PLM in the international machine tool Exhibition

No	Company	Machine	year	Stewart-Base structure				others	
				redundant axes		5-axes		Hybrid	
				Linear Motion	Rotation motion	Length variable	Joint slide	PLM & SLM	PLM
1	NEOS	Tricept	1993	*					
2	Giddings & Lewis	Variax Herelenter	1994/IMTS			*			
3	Geodetics	GDM	1994/IMTS			*			
4	Ingersoll	Hexapod	1996/IMTS			*			
5	TOYODA	Hexam	1996/JIMTOF				*		
6	T.H Aachen	Dynamill	1997/EMO						*
7	Hitachi Seiki	PXA	1998/JIMTOF	*					
8	OKUMA	PM-600	1998/JIMTOF			*			
9	Cincinnati	Hyper Mach	2000/IMTS	*	*			*	
10	Heckert	SKM 400	2001/EMO						*
11	Renault AutomationComau	Urane Sx	2001/EMO	*					
12	IFW	DUMBO	2001/EMO					*	*

2.3 The characteristics of typical parallel link machine tools

Investigations of parallel structures by many previous researchers have showed that there are great advantages by using parallel machine tool compared to conventional machines.

These mechanisms have following advantages [16-21].

(1) Decrease the inertia mass and increase the velocity and acceleration of a machine.

(2) The parallel link mechanism is a closed kinematic chain. Therefore the stiffness of a parallel link machine tool can be substantially increased. The links between the base and the spindle unit are under only tension and compression force, no bending.

(3) The accuracy can be improved. The link errors are not accumulated.

(4) The parallel mechanisms may have 6-DOF. They have the abilities of 5-face or 6-axis machining.

(5) The manufacturing cost can be decreased since the machine parts can be modularized.

There are some disadvantages with the parallel link machine tool. They are summarized as follows [22-25]:

(1) The ratio of occupied space to working volume is too large to be used in a proper factory. The ratio of occupied space of a traditional machine tool to its working volume is approximate three to six, whereas that of a parallel link machine tool is approximate five to ten.

(2) The non-linear characteristics are existed in the mechanical design of parallel link machine tool. The working space can only be analyzed numerically using a special searching algorithm.

(3) Static stiffness is not high enough. The tools thus fail to satisfy the general expectance that parallel link machine tools must be highly rigid. The main reason is that the six-DOF parallel link machine tool uses several universal and ball joints, of which the stiffness and manufacturing accuracy are not similar to those of the sliding pairs. For example, INA - Schaefler KG (INA) ball joint with the best stiffness has a rigidity of

450N/μm whereas the rigidity of the NSK Ltd., linear slider can reach 6000 N/μm. Today, the stiffness of parallel link machine tools is under 70 N/μm and is worse than that of traditional machine tools.

(4) Dynamic and static properties of the machines are position dependent. The stress is increased very quickly as rods and joints approaching singular points.

(5) Machining accuracy of the machine tool is poor (see Figure 2-16). This problem mainly results from the lack of a position-detecting device in a parallel link machine tool. Such a device is used to directly detect the position of a cutting tool tip. Generally, the moving path of a cutting tool tip is estimated from the measurements of the change in every rod. The accuracy of a parallel link machine tool, which involves indirect measurement and control, cannot be compared to that of a traditional machine tool.

(6) The costs of servo control systems are very high and the control is very complex.

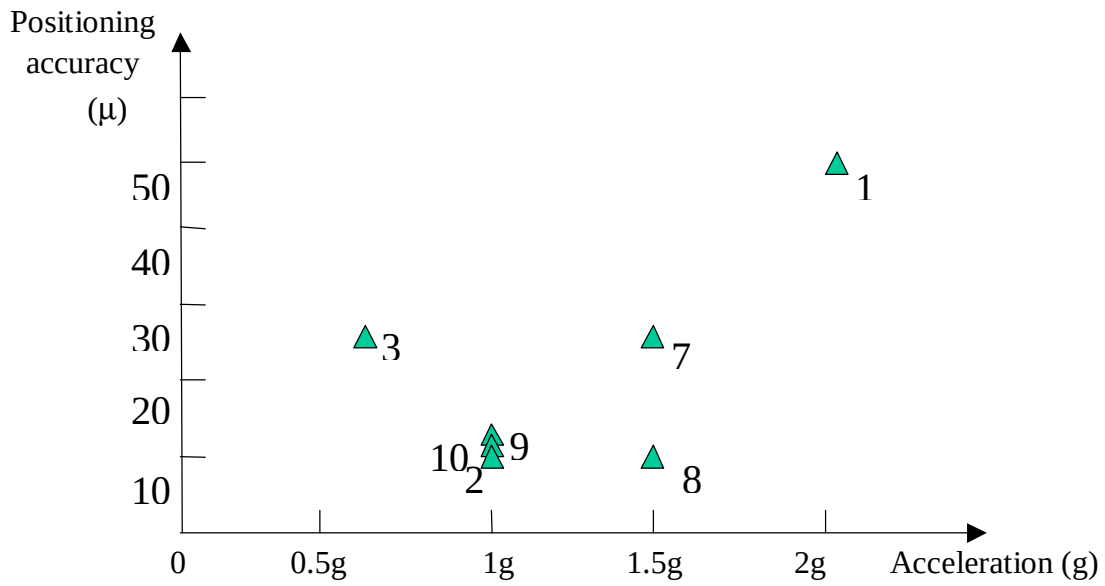

Fig 2-16 Positioning accuracy and acceleration of the PLM in the international machine tool exhibition. The company names of No.1-No.12 are shown in table 2-2

2.4 TRR-XY hybrid parallel link machine tool

The traditional five-axis machine tool is usually composed of rotational working table driven by worm and gear and linear driving axis driven by slide and ball screw. Generally, the traditional five-axis machine tool has two rotary axes A and B, and three linear axes XYZ. The main drawback is that the volume of rotary axes is too large and it cannot make high-speed motion because it is driven by worm and gear. The drawbacks of PLM are already discussed and analyzed in section 2.3. The main solutions for overcoming the drawbacks of PLM can be classified into two kinds as follows:

1. Employing redundant axes theory[22].

   By decreasing the number of axis in parallel link machine tool, the number of ball-joints can be decreased and kinematics complexity can be reduced. Decreasing the number of ball-joints can increase the rigidity of whole structure and reduce non-linear phenomena. So, the control system design of entire machine tool is become simple.

2. Adopting hybrid structure of serial-parallel link mechanism

   Substituting traditional rotary axes and by parallel link mechanism can make the machine structure simple, easy to reach the high speed machining and overcome the drawbacks of interfering. Serial link mechanism (SLM) is used to improve the poor ratio of working space and total machine volume of parallel link machine tool.

This thesis presents a new hybrid type parallel link machine tool called TRR-XY. It is a five-axis machine tool, shown in Figure 2-17. It is consisted of a 3 DOF fully parallel link mechanism and a 2 DOF X-Y table. From the design viewpoint, this hybrid machine tool possess the advantages of both closed-loop chains and open-loop

chains. The parallel link mechanism provides three DOF - a translational DOF and two rotary DOF of the spindle. They are separately corresponding to the A/B rotary axes and the Z axis of five-axis machine tool.

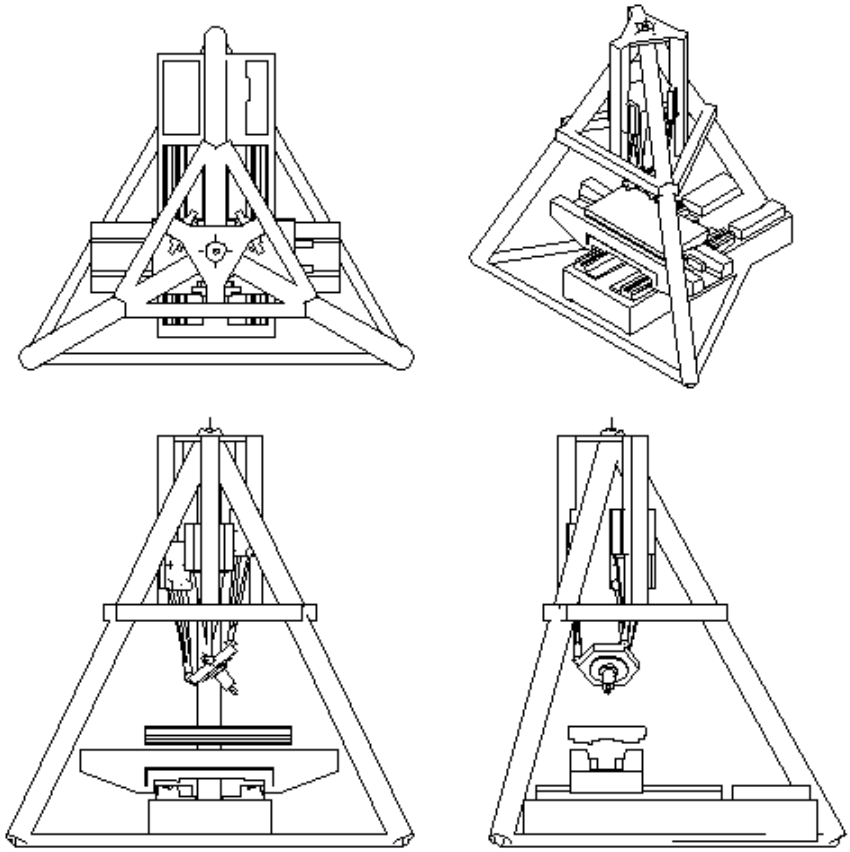

Figure 2-17 TRR-XY Hybrid Parallel Link Machine

Here, “TRR” is the tool frame independent motion DOF of the upper parallel link mechanism. “T” stands for translation DOF and “R” stands for rotation DOF. From mechanism viewpoint, this system may also be named as PRS-XY. “P” stands for prismatic motion pair. “R” stands for rotation motion pair and “S” stands for spherical joint.

This TRR-XY hybrid machine tool has the following advantages over the typical parallel link machine tool and five-axis serial machine tool:

1. Decrease the complexity of the mathematical model. The designer can easily analyze and design the machine tool.

2. The ratio of the total machine space to the working volume can be decreased to 3-6, which is close to that of a traditional serial type machine tool.
3. The reduction in the numbers of parallel axes simplifies the coupling effects between the driving axes, so that the control algorithm can be easily executed in the control system.
4. The rigidity of the machine tool is improved because half of the number of ball and universal joints are used.
5. The small inertial mass of the simple structure makes the high acceleration of the machine tool can be realized.
6. The modular components can be applied for the three symmetric link structure. This makes the manufacturing cost down.

2.5 Conclusions

Traditional five-axis SLM machine tool has drawbacks such as slow response, too large rotary axes' volume, too large interfered space and accuracy difficult to be improved. The typically stewart-based parallel link machine tool has shortcomings such as too small ratio of the working space and machine volume and low rigidity of ball joints. The low rigidity of ball joints leads the rigidity of whole machine tool lower than the ideal situation. The dynamic characters are worse and stress greatly increased when approaching the vicinity of singularity. Improvement in structure is not enough to break through these drawbacks. So the advantages of serial and parallel link mechanism are combined, the number of axes of parallel link mechanism is decreased to three (Tripod), traditional rotary axes driven by worm-gear is substituted, and working space is enlarged by using X-Y linear feed axis of SLM.

A new type TRR-XY hybrid machine tool with advantages such as high speed, high accuracy and low cost is presented in this research. This dissertation is aiming

to develop this hybrid structure into prototype machine and perform further investigation into the workspace, singularities, kinematics and dynamic characteristics and error compensation, etc.

References

1. The catalog of GIDDINGS & LEWIS "CP 10M/8/94 VARIAX-1"
2. Ingersoll Milling Machine Company (http://www.ingersoll.com)
3. Geodetic Technology (http://www.hexapod.co.uk/g500.htm)
4. Toyoda (http://www.toyoda-kouki.co.jp/_pub_html/sub_html/tmw/prodlines/paralink/hexam.htm)
5. The catalog of Hitachi Seiki "PA35-J.2.9809.05"
6. ETH Zurich-IFR & IWF(http://www.iwf.bepr.ethz.ch/projekte/hexaglide/home.html)
7. Dyna-M (http://www.ifw.uni-hannover.de/robotool/pages/maschinen_pages/wzl_AachenM_konzept.html)
8. INA(www-ifw.uni-stuttgart.de/forschung/ konstruktion/hexapod_emo.html)
9. DST Hypermach (http://www.mmsonline.com/articles/1000rt1.html)
10. SKM 400 (http://www.groatmachinery.com/Heckert/CWKDynamic.htm)
11. Raenault-Automation (http://www.pkm-news.de/deu/uranesx.html)
12. The catalog of SMT Tricept (Tricept 845/2002.07/ & Tricept 805/2002.07/)
13. DMT100 (http://www.ifw.uni-hannover.de/robotool/pages/maschinen_pages/DMG.html)
14. IFW (http://www.ifw.uni-stuttgart.de/for/hexapod-emo.html)
15. Index (www.index-werke.de/en/index/produkte/verticalline/V100/)
16. Khol, R., "A machine tool built from mathematics," American Machinist, pp. 53-55, Oct. 1994.
17. Eastman, M., "With hexapods go from show floor to shop floor,", Cutting Tool Engineering, pp. 102-110, June. 1995.
18. "Putting the hexapod on machining," Tooling and Production, pp. 37-42, Sept.

1996.

19. Aronson, R. B., “Hexapod: Hot or Ho Hum?,” Manufacturing Engineering, pp. 60-67, Oct. 1997.
20. “Visions of hexapods danced in their heads,”, Tooling and Production, pp. 23-26, Nov. 1997.
21. Koepfer, C., “Hexapod-It’s Working”, Modern Machine Shop, pp. 82-88, Oct. 1997.
22. G. Prisschow and R. Neugebauer, st. Inlengeldt. C. Eppler T. Garber, “New Approaches to Machine structures to overcome the limits of classical parallel structures”. Annals of the CIRP.
23. 彭明輝, “從學理論並聯式與串並聯工具機之優劣”, pp. 452-456, 機械月刊第 296 期, 2000.
24. 張燦輝, 陳響亮, “串並聯混合式工具機特性研究”, pp. 441-446, 機械月刊第 296 期, 2000.
25. Tlusty, J. Eiegert, J. Ridgeway, S. “Fundamental Comparison of the use of serial and parallel kinematics for machine tools”, pp. 351-356, Annals of the CIRP Vol. 48, 1999.

Chapter 3 General concept and structure

3.1 Introduction

A five DOF machine tool composed of a 3 DOF fully parallel link mechanism and a two DOF XY table (Fig.3-1 (a)(b)) was created in this research. The major consideration of this machine tool is to combine the merits of both an open-chain system and a closed chain system into one machine. The parallel link mechanism with three DOF (one translation and two rotations), has higher load capacity, higher structure stiffness, and less accumulated errors. The XY table is used to improve the limited workspace in a parallel link design. Moreover, the mechanism analysis for the hybrid structure is generally simpler than the closed-chain parallel mechanism with six DOF.

This machine tool includes an upper base frame, guide, slide, links, and tool frame. The cutter is fixed at the center of the tool frame (see Fig. 3-1). The tool frame contains three ball joints located at the trisection of the circumference of radius r. One end of the link is connected to the ball joint and the other end is connected to the slide that is moving up and down along the guide. The guides are vertically fixed on the trisection of the circumference of radius R and centered at the upper base frame.

The relevant freedom between the guide is 1; the relevant freedom of pin joints connecting block with link is also 1 and that of ball joints is 3, which is used to connect link with spindle frame. According to the definition of freedom employed in Grübler (1917)、Kutzbach (1929) [1]:

$$DOF = \lambda_f (n_L - 1) - \sum_{i=1}^{j} c_i \qquad (3\text{-}1)$$

l_f : Freedom expected

n_L : Total number of links

c_i : Constraint of joint i

j : Number of joints

In this hybrid machine tool, there are 3 blocks, 3 links, upper and lower platforms, so the total number of links is 8 and DOF of spindle is:

$$\mathrm{DOF} = (8-1)\times 6 - 3\times 5 - 3\times 5 - 3\times 3 = 3 \qquad (3\text{-}2)$$

Three DOF of the spindle and two translational DOF of the X-Y table make the hybrid machine tool having five DOF. From the design viewpoint, the machine tool can be divided into two parts to be analyzed respectively. This means that the parallel link mechanism and XY table can be dealt with separately.

A three DOF parallel link mechanism is located on the upper side of the machine tool that is investigated in this research. The kinematics relationship of the three DOF parallel link mechanism and the XY table was analyzed separately in this research. From design viewpoint, these two mechanisms generate different DOF independently. The adoption of XY table is very popular in the industry. Therefore, the characteristic investigation of the XY table is not the focal point of this research. Only the characteristic of the three DOF parallel link mechanisms will be focussed and investigated.

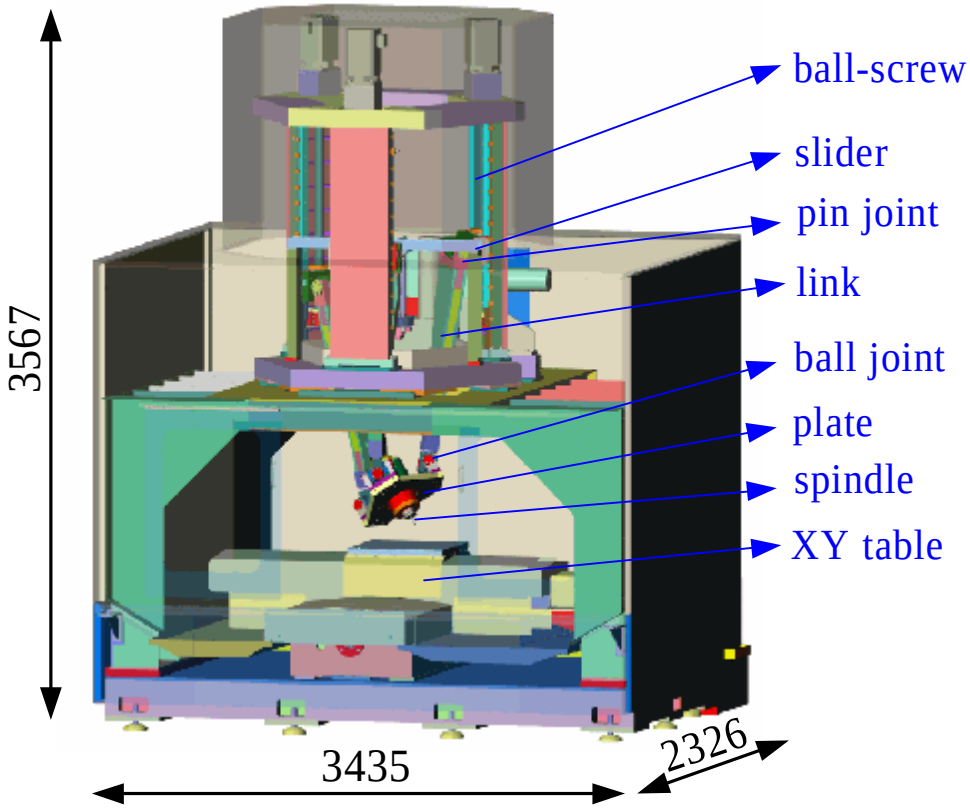

Figure 3-1a TRR-XY hybrid parallel link machine tool

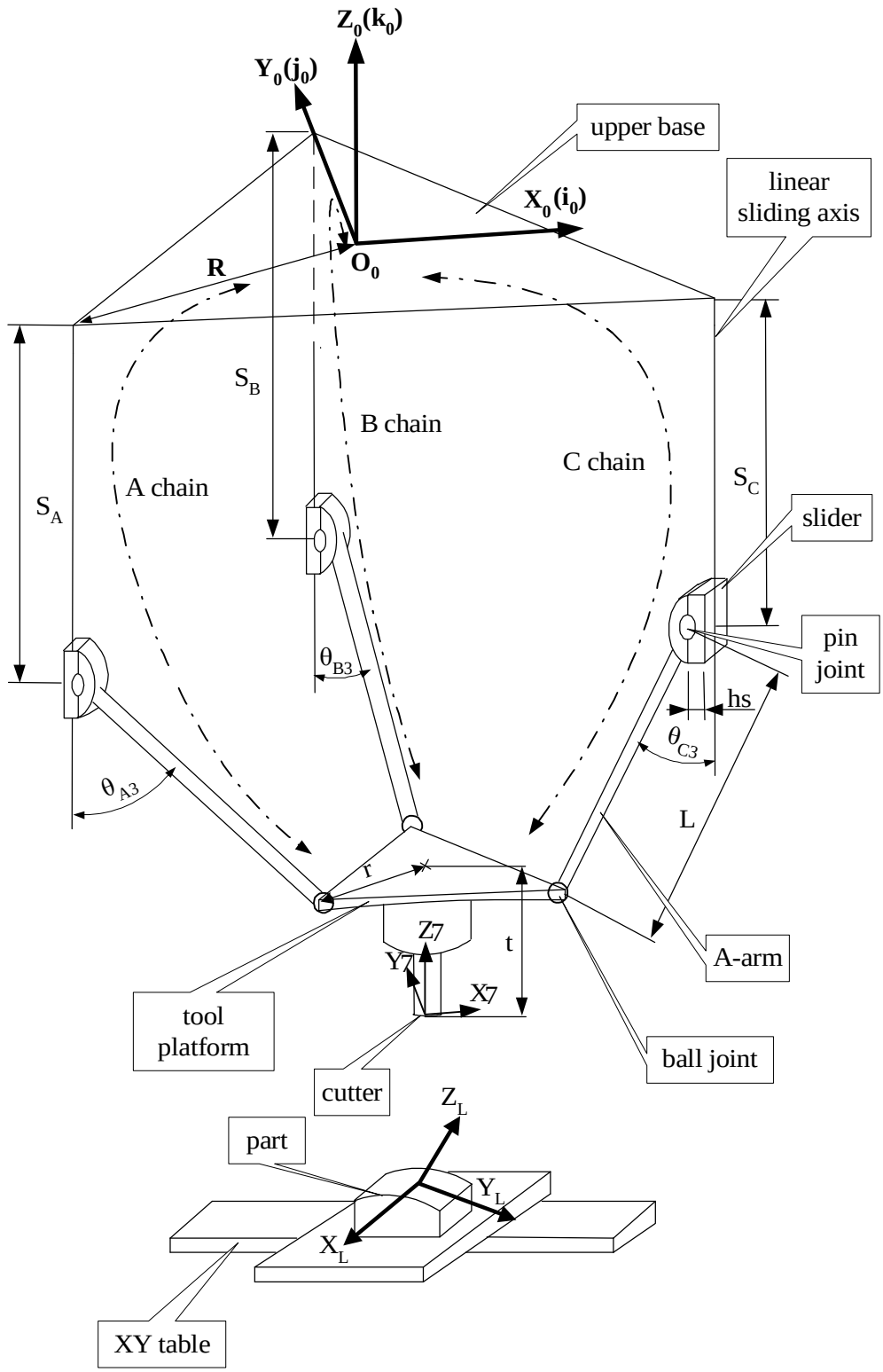

Fig. 3.1b Schematic diagram of the TRR-XY hybrid five DOF parallel link machine tool developed in this research

3.2 Denavit-Hartenberg notation for inverse kinematics analysis

Two problems can be distinguished for the kinematics aspects: inverse kinematics and direct kinematics. The inverse kinematics problem involves mapping a known position of the moving end effector output to a set of input joints variables that will achieve that position. The direct kinematics problem involves the mapping from a known set of input joint variables to a position of the moving platform that results from those given inputs.

The Stewart Platform is a closed kinematics system with parallel links which is considered to be far more rigid than the serial counterparts of the same size and weight. Its force output to manipulator weight ratio is generally an order of magnitude bigger than most industrial robots [2]. This same closed kinematics structure that gives its rigidity also complicates the solution of the forward kinematics in such a way that no closed (form) solution for this problem has been found.

Liu et al. [3] presented a method to analyze the forward kinematics of the general Stewart-Gough platform using three nonlinear algebraic equations. Dasgupta and Mruthyunjaya [4] presented a canonical formulation for the direct kinematics of the general Stewart-Gough platform and proved that the maximum number of the solutions is 64. Raghavan [5] showed that 40 solutions to the direct kinematics problem were obtained by utilizing continuation method. Wampler [6] used the Soma coordinates to prove the existing of 40 direct kinematics solutions.

Various configurations, which modified the general 6-DOF Stewart-Gough platforms, have been proposed to overcome the difficulties of solving the direct kinematics problem. Griffis and Duffy [7] proposed an octahedral Stewart platform. The kinematics problems for this design were analyzed by several researchers (Nanua

et al. [8], Inncocenti and Parenti-Castelli [9] and Ku [10]). Hunt and Primrose [11] studied several assembly configurations for Stewart platform based manipulators. Other types of the Stewart platform based manipulator such as the "3-2-1" Stewart platform configuration (Geng and Haynes [12]), "3-1-1-1" Stewart platform (Husian and Waldron [13]), and "3/2" Hunt-Primrose parallel manipulator (Bryuninckx [14]) were proposed in the past.

In addition to the modified Stewart-Gough platforms described above, other types of parallel mechanisms, which only have 3 DOF, have also been widely studied. Lee and Shah [15] proposed a three-limbed fully parallel structure and Waldron et al. [16] presented the direct kinematics solution for the parallel mechanism. The kinematics characteristics of another three-limbed mechanism were analyzed by Husain and Waldron [17] and Huang et al. [18]. Carretero et al. [19] presented the solutions for the inverse kinematics of a similar 3-PRS mechanism; however, the direct kinematics problem for the 3-PRS mechanism still remains unsolved.

In this research, the method of Denavit-Hartenberg notation [20], which has been used maturely in robotics, is adopted to define the geometric relationship among the mechanisms in the virtual axes machine tool and then to derive the inverse kinematics solution. The following research on five DOF virtual axes machine tool is emphasized on the analysis of the kinematics mechanism of spindle, namely the three DOF parallel link mechanism. Kinematics analysis of XY table is not necessary for it has long been used in mechanisms of open-chain structure and technologies involved in all aspects are very mature. In the end, the inverse kinematics solution of XY table can be defined by harmonizing the compensation value according to offset along X, Y-axes produced by kinematics mechanism of spindle and the practical position to be machined in X, Y directions, which is to be

discussed in the following section.

3.2.1 Definition of coordinate system of parallel link machine tool

This research employed the method of Denavit-Hartenberg notation to analyze both inverse and direct (or forward) kinematics problem through defining homogenous transformation matrix between two coordinate systems and then deriving the kinematics relationship of the entire mechanism. The method of Denavit-Hartenberg notation is the algorithm that is used to define homogenous transformation matrix between two coordinate systems. The kinematics relationship can be derived by setting of four parameters: linkage length a, offset d, twist angle α, joint angle θ and also the constraint of linkage. First, The method of Denavit-Hartenberg notation is introduced as follows:

To describe the relationship between two parts of which one is next to the other in a spatial mechanism having n linkages, each linkage should be numbered above all, from No. 0 to No. n according to the connecting order. Linkage of No. i-1 is connected to that of No. i through joint i. Then, proper coordinates $(XYZ)_i$ are set up on each linkage i (i = 1, 2, 3, 4…) so as to describe the spatial relationship of linkage i relative to linkage i-1. Under ideal condition, the spatial relationship between these two coordinates such as $(XYZ)_i$ and $(XYZ)_{i-1}$ can be transformed through the following procedures, as shown in Figure 3-2:

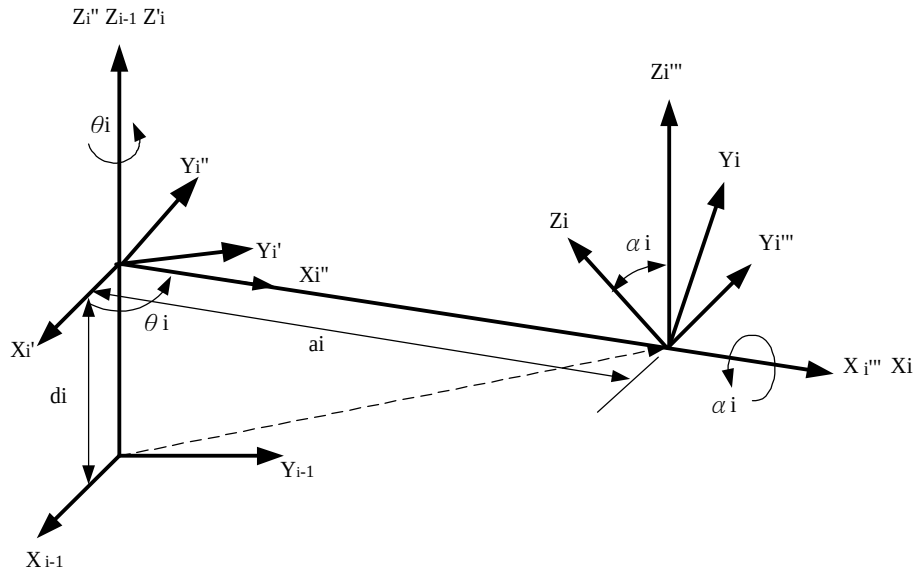

Figure 3.2 Denavit-Hartenberg transformation from $(X\ Y\ Z)_{i-1}$ to $(X\ Y\ Z)_i$

1. coordinates system $(XYZ)_{i-1}$ becomes new coordinates system $(XYZ)_i'$ when it translates the first offset d_i along z-axis.
2. coordinates system $(XYZ)_i''$ is obtained through $(XYZ)_i'$ rotating θ_i about Z_i'-axis.
3. $(XYZ)_i''$ translates offset a_i along X_i''-axis, then we get coordinates system $(x\ y\ z)_i'''$.
4. Rotating coordinates system $(XYZ)_i'''$ by angle α_i, coordinates system $(x\ y\ z)_i$ is attained.

The homogenous transformation matrix between two coordinate systems $(x\ y\ z)_i$ and $(x\ y\ z)_{i-1}$ can be written as follows:

$$^{i-1}\underline{A}_i = \underline{T}rans(0,0,d_i)\underline{R}ot(Z_i, \theta_i)\underline{T}rans(a_i,0,0)\underline{R}ot(x_i, \alpha_i)$$

$$= \begin{pmatrix} \cos(\theta_i) & -\sin(\theta_i)\cdot\cos(\alpha_i) & \sin(\theta_i)\cdot\sin(\alpha_i) & a_i\cdot\cos(\theta_i) \\ \sin(\theta_i) & \cos(\theta_i)\cdot\cos(\alpha_i) & -\cos(\theta_i)\cdot\sin(\alpha_i) & a_i\cdot\sin(\theta_i) \\ 0 & \sin(\alpha_i) & \cos(\alpha_i) & d_i \\ 0 & 0 & 0 & 1 \end{pmatrix} \qquad (3\text{-}3)$$

This method is called Denavit-Hartenberg notation, which is used to describe the transformation matrix between two coordinate systems of two links. As shown in Figure 3-1 R is defined as the distance from the center of upper base to the pin joint; S_C is the feed of slide on guide (such are the other two S_A and S_B). The length of the link is L; the distance between the center of ball joint and the center of spindle base is r; t is defined as the distance from the center of spindle base to the center of cutting tool. Figure 3-3 is the set-up of coordinate system in C-chain. Coordinate system {0} is set up at the center of upper base platform and coordinate system {7} is set up at the center of the cutting tool. The defined parameters of each coordinate system are shown is Table 3-1. To be mentioned particularly, coordinate systems {3}～{5} are all set up at the center of ball joint because of it having three different rotary degrees of freedom. So we can define the kinematics relation by using three coordinate systems.

Table 3-1 Definition of parameters of D-H notation

Link No.	A-chain				B-chain				C-chain			
	d	θ	a	α	d	θ	a	α	d	θ	a	α
1	0	-150^0	R	180^0	0	90^0	R	180^0	0	-30^0	R	180^0
2	S_A	0^0	-hs	90^0	S_B	0^0	-hs	90^0	S_C	0^0	-hs	90^0
3	0	θ_{A3}	L	90^0	0	θ_{B3}	L	90^0	0	θ_{C3}	L	90^0
4	0	θ_{A4}	0	90^0	0	θ_{B4}	0	90^0	0	θ_{C4}	0	90^0
5	0	θ_{A5}	0	90^0	0	θ_{B5}	0	90^0	0	θ_{C5}	0	90^0
6	0	θ_{A6}	r	90^0	0	θ_{B6}	r	90^0	0	θ_{C6}	r	90^0
7	- t	-30^0	0	0^0	-t	90^0	0	0^0	- t	$-150°$	0	0^0

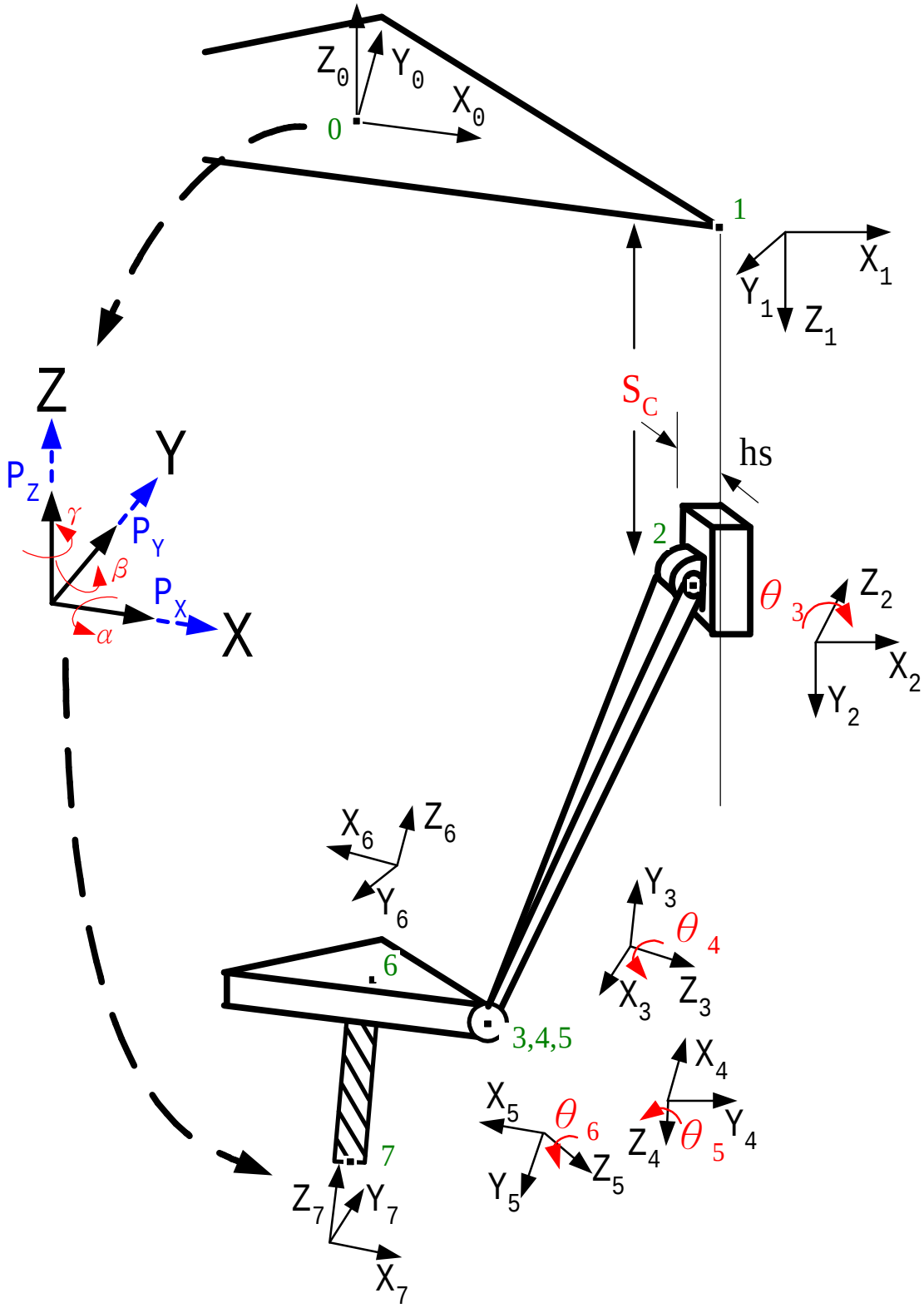

Fig 3-3 The define coordinate system in C-chain of D-H notation

3.2.2 Analysis of inverse kinematics

To analyze the ideal kinematics model of hybrid TRR-XY machine tool, three hypotheses should be assumed first:

1. Rotary movement of joints is ideal.
2. The position of rotary center of joints must be defined precisely.
3. Origins of two coordinate systems, which are set up on upper base and tool frame are all at the geometric center of platforms.

To establish the homogenous transformation matrix between coordinate system $(XYZ)_7$ of tool tip and coordinate system $(XYZ)_0$ of upper base, the parameters of D&H notation are listed in Table 3-1. For example, as for B-chain, the transformation relation can be written as follows:

$$({}^0A_7)_B={}^0A_1\,{}^1A_2\,{}^2A_3\,{}^3A_4\,{}^4A_5\,{}^5A_6\,{}^6A_7 \tag{3-4}$$

in the above equation,

$${}^0A_1 = \begin{pmatrix} 0 & 1 & 0 & 0 \\ 1 & 0 & 0 & R_B \\ 0 & 0 & -1 & 0 \\ 0 & 0 & 0 & 1 \end{pmatrix} \tag{3-5}$$

$${}^1A_2 = \begin{pmatrix} 1 & 0 & 0 & -hs \\ 0 & 0 & -1 & 0 \\ 0 & 1 & 0 & S_B \\ 0 & 0 & 0 & 1 \end{pmatrix} \tag{3-6}$$

$$ {}^{2}A_{3} = \begin{pmatrix} \cos(\theta_{B3}) & -\sin(\theta_{B3}) & 0 & L\cdot\cos(\theta_{B3}) \\ \sin(\theta_{B3}) & \cos(\theta_{B3}) & 0 & L\cdot\sin(\theta_{B3}) \\ 0 & 0 & 1 & 0 \\ 0 & 0 & 0 & 1 \end{pmatrix} \tag{3-7} $$

$$ {}^{3}A_{4} = \begin{pmatrix} \cos(\theta_{B4}) & 0 & \sin(\theta_{B4}) & 0 \\ \sin(\theta_{B4}) & 0 & -\cos(\theta_{B4}) & 0 \\ 0 & 1 & 0 & 0 \\ 0 & 0 & 0 & 1 \end{pmatrix} \tag{3-8} $$

$$ {}^{4}A_{5} = \begin{bmatrix} \cos(q_{B5}) & 0 & \sin(q_{B5}) & 0 \\ \sin(q_{B5}) & 0 & -\cos(q_{B5}) & 0 \\ 0 & 1 & 0 & 0 \\ 0 & 0 & 0 & 1 \end{bmatrix} \tag{3-9} $$

$$ {}^{5}A_{6} = \begin{bmatrix} \cos(q_{B6}) & 0 & \sin(q_{B6}) & r\cdot\cos(q_{B6}) \\ \sin(q_{B6}) & 0 & -\cos(q_{B6}) & r\cdot\sin(q_{B6}) \\ 0 & 1 & 0 & 0 \\ 0 & 0 & 0 & 1 \end{bmatrix} \tag{3-10} $$

$$ {}^{6}A_{7} = \begin{pmatrix} 0 & -1 & 0 & 0 \\ 1 & 0 & 0 & 0 \\ 0 & 0 & 1 & -t \\ 0 & 0 & 0 & 1 \end{pmatrix} \tag{3-11} $$

Where θ_{B3} is twist angle of pin joint, and θ_{B4}, θ_{B5}, θ_{B6} are twist angles of ball joints. The geometric meaning is referenced as the relationship of coordinate system as shown in Figure 3-3. Apart from S_B being defined by the inverse kinematics solution, parameters θ_{B3}, θ_{B4}, θ_{B5}, θ_{B6} are also more or less relevant to interference angle of ball joint.

Due to matrixes ${}^{0}A_{1}$ and ${}^{6}A_{7}$ containing no variables, rearrange these matrixes into the matrixes that contain some variables for the convenience of computing, so the entire

transformation matrix can be written as:

$$({}^{0}A_{7})_{B}={}^{0}A_{2}{}^{2}A_{3}{}^{3}A_{4}{}^{4}A_{5}{}^{5}A_{7} \tag{3-12}$$

Let the homogeneous transformation matrix between coordinate system {0} of upper base and coordinate system {7} of cutting tool be

$$({}^{0}A_{7})_{B}=\begin{pmatrix} Nx & Tx & Bx & Px \\ Ny & Ty & By & Py \\ Nz & Tz & Bz & Pz \\ 0 & 0 & 0 & 1 \end{pmatrix} \tag{3-13}$$

The parameters of $({}^{0}A_{7})_{B}$ can be defined by using the geometric relation between tool position and the direction of tool axis, which is to be discussed and defined in next section. Let equation (3-12) be equal to equation (3-13), rearrange the matrix and we have

$$({}^{0}A_{2})^{-1}({}^{0}A_{7})_{B}\ ({}^{5}A_{7})^{-1}={}^{2}A_{3}{}^{3}A_{4}{}^{4}A_{5} \tag{3-14}$$

Transformation matrix of both sides of Equation (3-14) is equal. Comparing the last column of the two transformation matrixes and we have left hand side:

$$[I3\quad 0]({}^{0}A_{2})^{-1}({}^{0}A_{7})_{B}\ ({}^{5}A_{8})^{-1}\begin{bmatrix}0\\0\\0\\1\end{bmatrix}$$

$$= \begin{pmatrix} Ty \cdot r + By \cdot t + Py + hs - R \\ -Tz \cdot r - Bz \cdot t - Pz - S_B \\ -Tx \cdot r - Bx \cdot t - Px \end{pmatrix} \tag{3-15}$$

Right hand side:

$$[I3 \quad 0]^2A_3{}^3A_4{}^4A_5 \begin{bmatrix} 0 \\ 0 \\ 0 \\ 1 \end{bmatrix} = \begin{bmatrix} L \cdot \cos(q_{B3}) \\ L \cdot \sin(q_{B3}) \\ 0 \end{bmatrix} \tag{3-16}$$

Let equation (3-15) be equal to equation (3-16), the inverse kinematics relation can be attained as follows:

$$\begin{pmatrix} Ty \cdot r + By \cdot t + Py + hs - R \\ -Tz \cdot r - Bz \cdot t - Pz - S_B \\ -Tx \cdot r - Bx \cdot t - Px \end{pmatrix} = \begin{pmatrix} L \cdot \cos(\theta_{B3}) \\ L \cdot \sin(\theta_{B3}) \\ 0 \end{pmatrix} \tag{3-17}$$

Rearranging equation (3-17), the inverse kinematics solution of B-chain and twist angle of joint can be written as the following equations:

$$s_B = (\ Tz \quad r \quad Bz \quad t \quad Pz) \quad \sqrt{[L^2 \quad (Ty \quad r + By \quad t + Py + hs \quad R)^2]} \tag{3-18}$$

$$\cos(\theta_{B3}) = \frac{Ty \cdot r + By \cdot t + Py + hs - R}{L} \tag{3-19}$$

$$\sin(\theta_{B3}) = \frac{-Tz \cdot r - Bz \cdot t - Pz - S_B}{L} \tag{3-20}$$

$$\theta_{B3} = \tan^{-1}\left(\frac{\sin(\theta_{B3})}{\cos(\theta_{B3})}\right) \tag{3-21}$$

Thus, the inverse kinematics result of B-chain is obtained and the inverse solutions of the other two chains (A chain and C chain) are also solved using the same algorithm, so do the twist angles. The results of the other two kinematics chains are summarized as follows:

$$S_A := \left(\frac{1}{2}\cdot Nz\cdot r\cdot\sqrt{3}+\frac{1}{2}\cdot Tz\cdot r - Bz\cdot t - Pz\right) - \sqrt{\left[L^2-\left(\frac{3}{4}\cdot r\cdot Nx+\frac{1}{4}\cdot r\cdot\sqrt{3}\cdot Ny+\frac{1}{4}\cdot r\cdot\sqrt{3}\cdot Tx+\frac{1}{4}\cdot r\cdot Ty-\frac{1}{2}\cdot t\cdot\sqrt{3}\cdot Bx-\frac{1}{2}\cdot t\cdot By-\frac{1}{2}\cdot\sqrt{3}\cdot Px-\frac{1}{2}\cdot Py+hs-R\right)^2\right]} \tag{3-22}$$

$$\cos(\theta_{A3}) = \frac{\frac{3}{4}\cdot r\cdot Nx+\frac{1}{4}\cdot r\cdot\sqrt{3}\cdot Ny+\frac{1}{4}\cdot r\cdot\sqrt{3}\cdot Tx+\frac{1}{4}\cdot r\cdot Ty-\frac{1}{2}\cdot t\cdot\sqrt{3}\cdot Bx-\frac{1}{2}\cdot t\cdot By-\frac{1}{2}\cdot\sqrt{3}\cdot Px-\frac{1}{2}\cdot Py+hs-R}{L} \tag{3-23}$$

$$\sin(\theta_{A3}) = \frac{\frac{1}{2}\cdot Nz\cdot r\cdot\sqrt{3}+\frac{1}{2}\cdot Tz\cdot r - Bz\cdot t - Pz - S_A}{L} \tag{3-24}$$

$$\theta_{A3} = \tan^{-1}(\sin(\theta_{A3}),\cos(\theta_{A3})) \tag{3-25}$$

$$S_C := \left(\frac{-1}{2}\cdot Nz\cdot r\cdot\sqrt{3}+\frac{1}{2}\cdot Tz\cdot r - Bz\cdot t - Pz\right) - \sqrt{\left[L^2-\left(\frac{3}{4}\cdot r\cdot Nx-\frac{1}{4}\cdot r\cdot\sqrt{3}\cdot Ny-\frac{1}{4}\cdot r\cdot\sqrt{3}\cdot Tx+\frac{1}{4}\cdot r\cdot Ty+\frac{1}{2}\cdot t\cdot\sqrt{3}\cdot Bx-\frac{1}{2}\cdot t\cdot By+\frac{1}{2}\cdot\sqrt{3}\cdot Px-\frac{1}{2}\cdot Py+hs-R\right)^2\right]} \tag{3-26}$$

$$\cos(\theta_{c3}) = \frac{\frac{3}{4}\cdot r\cdot Nx - \frac{1}{4}\cdot r\cdot\sqrt{3}\cdot Ny - \frac{1}{4}\cdot r\cdot\sqrt{3}\cdot Tx + \frac{1}{4}\cdot r\cdot Ty + \frac{1}{2}\cdot t\cdot\sqrt{3}\cdot Bx - \frac{1}{2}\cdot t\cdot By + \frac{1}{2}\cdot\sqrt{3}\cdot Px - \frac{1}{2}\cdot Py + hs - R}{L}$$

(3-27)

$$\sin(\theta_{c3}) = \frac{\frac{-1}{2}\cdot Nz\cdot r\cdot\sqrt{3} + \frac{1}{2}\cdot Tz\cdot r - Bz\cdot t - Pz - Sc}{L}$$

(3-28)

$$\theta_{C3} = \tan^{-1}\left(\frac{\sin(\theta_{C3})}{\cos(\theta_{C3})}\right)$$

(3-29)

3.2.3 Derivation for the relationship among angle α, β, γ

The transformation matrix contains six variables between every two coordinates in space. ${}^{0}\mathbf{A}_{7}$ is defined as the transformation matrix from the center of upper base to the center to the cutting tool and it contains 3×3 rotating matrix and 3×1 translation vector. The 3×1 translation vector is the offset among origins of coordinates, and 3×3 rotating matrix is the rotating value about X, Y, Z-axis. According to the definition of rotating matrix by Craig [24], the matrix have 12 groups of Euler angle.

Let $\mathbf{R}_{zyx}$ of the fixed-angle rotating matrix represent the rotating matrix in ${}^{0}\mathbf{A}_{7}$. Rotating matrix is obtained through rotating angle γ about Z-axis first, then rotating the rotated axis about Y-axis by angle β, and lastly rotating the changeable axis angle α about X-axis as shown in Figure 3-3. By rotating axis three times by angle α, β and γ, then we get the designed coordinate system direction. So the homogenous transformation matrix ${}^{0}A_{7}$ can be represented as:

$$
{}^{0}A_{7}=\begin{pmatrix}
\cos(\beta)\cdot\cos(\gamma) & -\cos(\beta)\cdot\sin(\gamma) & \sin(\beta) & Px \\
\sin(\alpha)\cdot\sin(\beta)\cdot\cos(\gamma)+\cos(\alpha)\cdot\sin(\gamma) & -\sin(\alpha)\cdot\sin(\beta)\cdot\sin(\gamma)+\cos(\alpha)\cdot\cos(\gamma) & -\sin(\alpha)\cdot\cos(\beta) & Py \\
-\cos(\alpha)\cdot\sin(\beta)\cdot\cos(\gamma)+\sin(\alpha)\cdot\sin(\gamma) & \cos(\alpha)\cdot\sin(\beta)\cdot\sin(\gamma)+\sin(\alpha)\cdot\cos(\gamma) & \cos(\alpha)\cdot\cos(\beta) & Pz \\
0 & 0 & 0 & 1
\end{pmatrix}
\tag{3-30}
$$

During practical applications cutter location file (CL-file) of the workpiece surface is usually generated by using general CAM software. The base form of CL-file is written as (x y z $\vec{i}$ $\vec{j}$ $\vec{k}$); (x y z) is the position of cutting point and ($\vec{i}$ $\vec{j}$ $\vec{k}$) represent the axis vector of cutting tool. To reduce the derivation process, think about making the direction of tool be the same as that of normal vector of curved surface of workpiece. Let

$$
\begin{bmatrix} \vec{i} \\ \vec{j} \\ \vec{k} \\ 0 \end{bmatrix} = {}^{0}A_{7}\begin{bmatrix} 0 \\ 0 \\ 1 \\ 0 \end{bmatrix} \tag{3-31}
$$

Computing equation (3-31), we get the result equal to the following equation

$$
\begin{bmatrix} \vec{i} \\ \vec{j} \\ \vec{k} \\ 0 \end{bmatrix} = \begin{bmatrix} \sin(b) \\ -\sin(a)\cos(b) \\ \cos(a)\cos(b) \\ 0 \end{bmatrix} \tag{3-32}
$$

From equation (3-32), we obtain the relationship between twist angles α and β

$$
b = \sin^{-1}(\vec{i}) \tag{3-33}
$$

$$
a = a\tan 2(\sin(a),\cos(a)) \tag{3-34}
$$

where

$$\sin(a) = (-\vec{j}) / \cos(b) \tag{3-35}$$

$$\cos(a) = \vec{k} / \cos(b) \tag{3-36}$$

To solve the derivation of twist angle γ, three groups of linkage movements are mainly used, which are restricted to three planes by pin joints as shown in Figure 3-4. Relationship is as follows:

X = 0 ---------- for B-chain

X = $\sqrt{3}Y$ ---------- for A-chain

X = $-\sqrt{3}Y$ ---------- for C-chain (3-37)

Define positions of three sets of ball joints as O_{bA}, O_{bB}, O_{bc}. During spindle movement the position of ball joint must be restricted to three planes. According the definition of transformation relationship between coordinate systems, firstly, define the position under coordinate system {0}

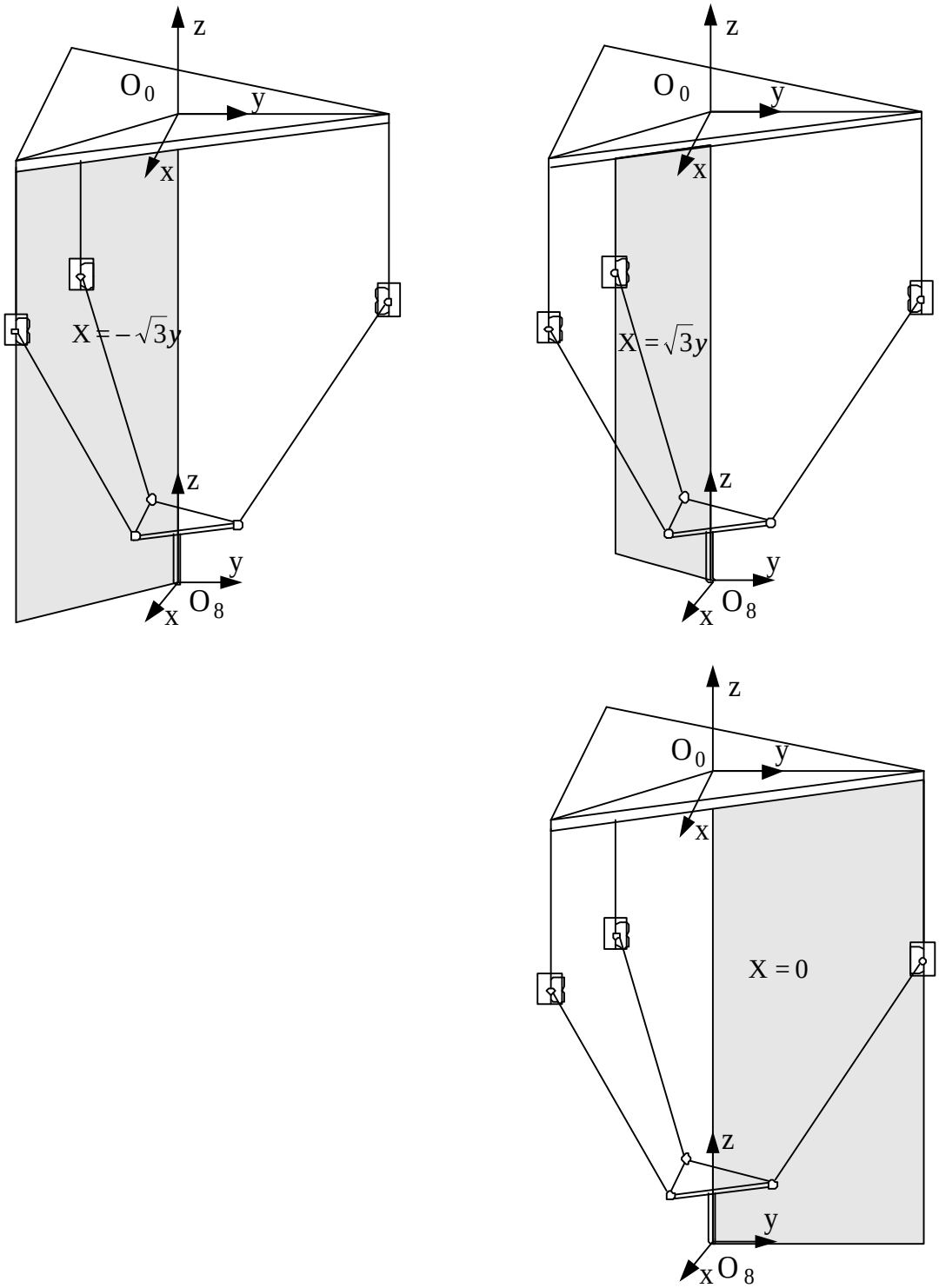

Fig 3-4 Three restricted planes by pin joints

$$O_{bA} = {}^{0}A_{7}\begin{bmatrix} -\frac{\sqrt{3}}{2}\cdot r \\ -\frac{r}{2} \\ t \\ 1 \end{bmatrix}$$

$$= \begin{pmatrix} \frac{-1}{2}\cdot\cos(\beta)\cdot\cos(\gamma)\cdot\sqrt{3}\cdot r + \frac{1}{2}\cdot\cos(\beta)\cdot\sin(\gamma)\cdot r + \sin(\beta)\cdot Lr + Px \\ \frac{-1}{2}\cdot\sqrt{3}\cdot r\cdot\sin(\alpha)\cdot\sin(\beta)\cdot\cos(\gamma) - \frac{1}{2}\cdot\sqrt{3}\cdot r\cdot\cos(\alpha)\cdot\sin(\gamma) + \frac{1}{2}\cdot r\cdot\sin(\alpha)\cdot\sin(\beta)\cdot\sin(\gamma) - \frac{1}{2}\cdot r\cdot\cos(\alpha)\cdot\cos(\gamma) - \sin(\alpha)\cdot\cos(\beta)\cdot t + Py \\ \frac{1}{2}\cdot\sqrt{3}\cdot r\cdot\cos(\alpha)\cdot\sin(\beta)\cdot\cos(\gamma) - \frac{1}{2}\cdot\sqrt{3}\cdot r\cdot\sin(\alpha)\cdot\sin(\gamma) - \frac{1}{2}\cdot r\cdot\cos(\alpha)\cdot\sin(\beta)\cdot\sin(\gamma) - \frac{1}{2}\cdot r\cdot\sin(\alpha)\cdot\cos(\gamma) + \cos(\alpha)\cdot\cos(\beta)\cdot t + Pz \\ 1 \end{pmatrix}$$

$$O_{bB} = {}^{0}A_{7}\begin{bmatrix} 0 \\ r \\ t \\ 1 \end{bmatrix}$$

$$= \begin{pmatrix} -\cos(\beta)\cdot\sin(\gamma)\cdot r + \sin(\beta)\cdot t + Px \\ r\cdot\sin(\alpha)\cdot\sin(\beta)\cdot\sin(\gamma) + r\cdot\cos(\alpha)\cdot\cos(\gamma) - \sin(\alpha)\cdot\cos(\beta)\cdot t + Py \\ r\cdot\cos(\alpha)\cdot\sin(\beta)\cdot\sin(\gamma) + r\cdot\sin(\alpha)\cdot\cos(\gamma) + \cos(\alpha)\cdot\cos(\beta)\cdot t + Pz \\ 1 \end{pmatrix}$$

$$O_{bC} = {}^{0}A_{7}\begin{bmatrix} \frac{\sqrt{3}}{2}\cdot r \\ -\frac{r}{2} \\ t \\ 1 \end{bmatrix}$$

$$= \begin{pmatrix} \frac{1}{2}\cdot\cos(\beta)\cdot\cos(\gamma)\cdot\sqrt{3}\cdot r + \frac{1}{2}\cdot\cos(\beta)\cdot\sin(\gamma)\cdot r + \sin(\beta)\cdot t + Px \\ \frac{1}{2}\cdot\sqrt{3}\cdot r\cdot\sin(\alpha)\cdot\sin(\beta)\cdot\cos(\gamma) + \frac{1}{2}\cdot\sqrt{3}\cdot r\cdot\cos(\alpha)\cdot\sin(\gamma) + \frac{1}{2}\cdot r\cdot\sin(\alpha)\cdot\sin(\beta)\cdot\sin(\gamma) - \frac{1}{2}\cdot r\cdot\cos(\alpha)\cdot\cos(\gamma) - \sin(\alpha)\cdot\cos(\beta)\cdot t + Py \\ \frac{-1}{2}\cdot\sqrt{3}\cdot r\cdot\cos(\alpha)\cdot\sin(\beta)\cdot\cos(\gamma) + \frac{1}{2}\cdot\sqrt{3}\cdot r\cdot\sin(\alpha)\cdot\sin(\gamma) - \frac{1}{2}\cdot r\cdot\cos(\alpha)\cdot\sin(\beta)\cdot\sin(\gamma) - \frac{1}{2}\cdot r\cdot\sin(\alpha)\cdot\cos(\gamma) + \cos(\alpha)\cdot\cos(\beta)\cdot t + Pz \\ 1 \end{pmatrix}$$

(3-38)

Coordinates of ball joint defined by equation (3-38) are surely satisfying the plane relation given by equation (3-37). Rearranging point coordinates of three ball joints

(O_{bA}, O_{bB}, O_{bc}) into three plane relations restricted by equation (3-27) and we get solutions of twist angle γ and Px, Py

$$\gamma = \tan^{-1}\left(\frac{-\sin(\alpha)\cdot\sin(\beta)}{\cos(\alpha)+\cos(\beta)}\right) \tag{3-39}$$

$$Px = r\cdot\cos(b)\cdot\sin(g) - t\cdot\sin(b) \tag{3-40}$$

$$Py = t\cdot\sin(a)\cdot\cos(b) - \frac{r}{2}\cdot(\sin(a)\cdot\sin(b)\cdot\sin(g) - \cos(a)\cdot\cos(g) + \cos(b)\cdot\cos(g)) \tag{3-41}$$

From equations (3-39) through (3-41), we know g, Px, Py are functions of a, b and other fixed parameters of mechanisms, and we also know that the independent variables of spindle mechanisms are a, b, Pz. Thus the three degrees of freedom calculated previously are two rotary degrees of freedom along X, Y direction and one translation degree of freedom along Z-axis.

3.2.4 Inverse kinematics relationship of XY table

Furthermore, according to equations (3-40) and (3-41), we can define the XY displacements of spindle mechanisms and then the inverse kinematics relation of XY table can be given out as follows:

$$S_X = -X_0 + Px \tag{3-42}$$

$$S_Y = -Y_0 + Py \tag{3-43}$$

where S_X, S_Y are feeds along X, Y-axis; X_0, Y_0 is the position being machined by cutting tool (in coordinate system {0}).

3.3 Singularity analysis of workspace

3.3.1 Introduction

The parallel link mechanism machine tool is more complicate and more difficult to do the kinematics and dynamic analysis compared with the open-chain orthogonal type traditional machine tool. Specially, the singular position of the parallel link mechanism is very easy to be encountered during the machining processes. Therefore, the analysis and understanding of the singular position of the parallel link machine tool is very essential for the applications of the machine tool in the real machining processes. In general, there are six motion DOF in a parallel link machine tool. To control the cutter location (3 DOF) and cutter orientation (3 DOF), six actuators (driving axes) to generate six driving forces are required. The unit vectors of these six driving forces are required to keep linear independent to fully control the cutter location and orientation. If the six driving forces are not linear independent, the tool frame will lose control and cause some control problems. The tool location and orientation that six driving forces are not linear independent is usually defined as the singular position. A singular region (volume) may be formed by all the singular positions of the parallel link machine tool. A hybrid TRR-XY parallel link machine tool is selected to show the calculation of the singularity in this section (see Figure 3-5). A three DOF (one translation and two rotations) parallel link mechanism and a two DOF XY table (two translations) are included in this hybrid machine tool. The two DOF XY-table is an open and orthogonal mechanism and no any singular position will be encountered. Therefore, the two DOF XY-table will not be discussed in the later sections. The singularity of the three DOF parallel link mechanism used in the machine tool is focused in this research. The singular position of the hybrid TRR-XY machine tool will be only caused by this three DOF parallel link mechanism.

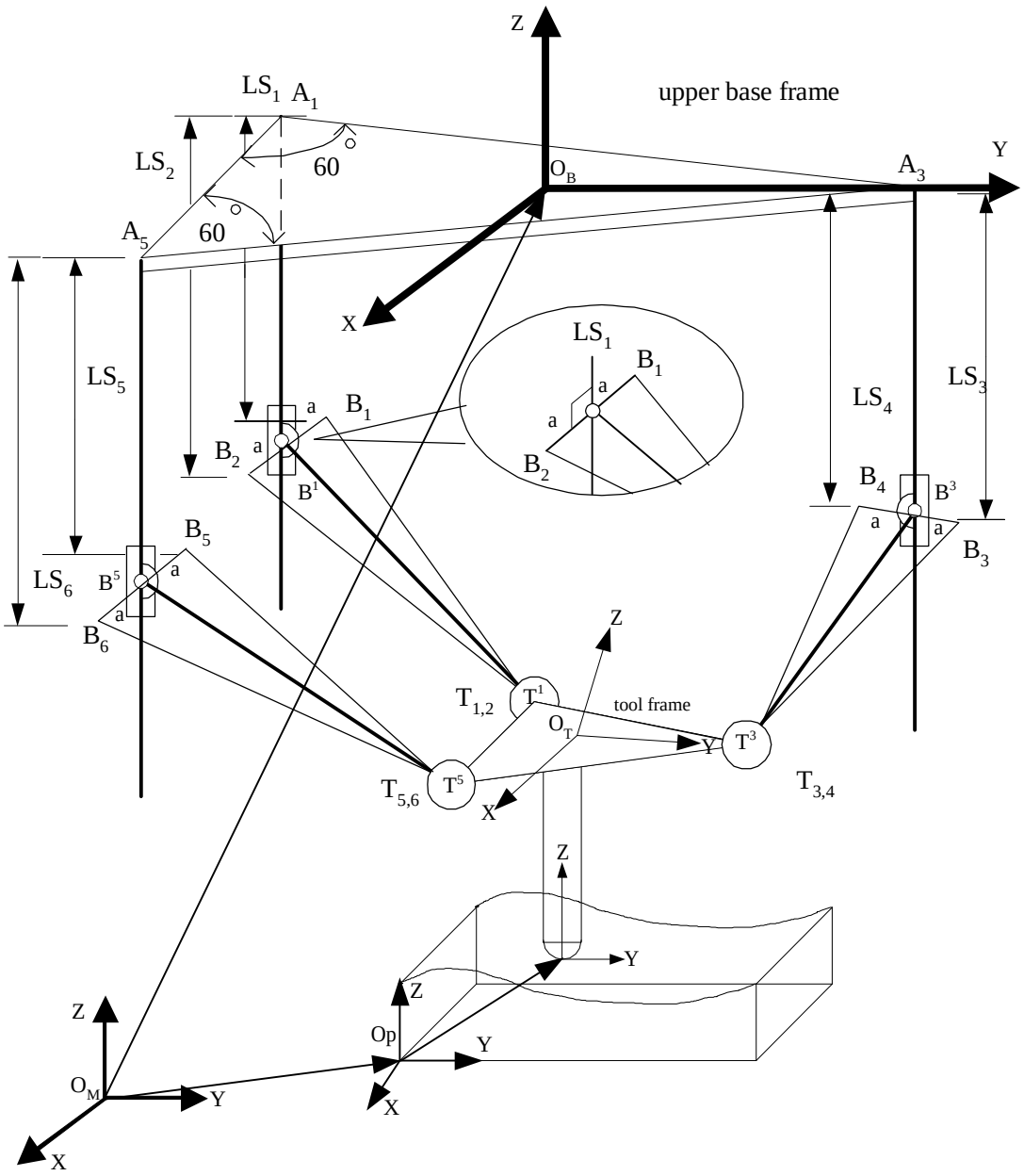

Figure 3-5 The schematic diagram shows the coordinate system and the equivalent component concept of the hybrid machine tool.

The screw theory was first addressed in 1990 and adopted by many previous researchers [21-23]. The screw theory can be also applied for the singular position analysis of a parallel link machine tool. According to the screw theory, the six-DOF

mechanism must be constraint by six linear independent forces. The unit vectors of the six forces is usually coincided with the axes of the six parallel links. Based on the Plücker coordinate system, there is a U matrix defined used in the screw theory for analyzing the independence of the six forces. The Plücker coordinate system is constructed based on the unit vector of the parallel links. For a six DOF parallel link machine tool, the U matrix of the Plücker coordinates can be defined as:

$$U=\begin{bmatrix} s1_x & s1_y & s1_z & M1_x & M1_y & M1_z \\ s2_x & s2_y & s2_z & M2_x & M2_y & M2_z \\ s3_x & s3_y & s3_z & M3_x & M3_y & M3_z \\ s4_x & s4_y & s4_z & M4_x & M4_y & M4_z \\ s5_x & s5_y & s5_z & M5_x & M5_y & M5_z \\ s6_x & s6_y & s6_z & M6_x & M6_y & M6_z \end{bmatrix} \quad (3\text{-}44)$$

The Jacobian matrix method is the similar theory with the U matrix method. Both of them use the concept of the six linear independent forces (equations) to analyze the singular condition of the parallel link mechanism. It is at least six linear independent equations required for the analysis of the singular position. In the six DOF parallel link machine tool, the six linear independent equations can be clearly identified very easily. However, only three linear independent equation can be obtained in a three DOF parallel link mechanism. To increase the number of the linear independent equations, some other functions must be considered. The acceleration and velocity relationships are adopted to obtain three more linear independent equations here. The U matrix or Jacobian matrix method can then be used for the analysis of the singular position.

3.3.2 Theory

In this section, an equivalent component concept is addressed. The equivalent components of the pin joints that used in the hybrid machine tool are created (see Figure 3-5). The links of the machine tool has a one DOF pin joint on one end and a three DOF of ball joint on the other end. These links B^1T^1, B^3T^3 and B^5T^5 are

separately equivalent to three virtual links (B_1T_1, B_2T_2), (B_3T_3, B_4T_4), (B_5T_5, B_6T_6). Each virtual link has two virtual ball joints on the both ends. For example, the two virtual ball joints B_1, B_2 are symmetrically located on the rotation axis of the pin joint B^1. The two virtual ball joints at the other end of the virtual links T_1, T_2 are arranged at the same position. The position is the same as the position of the ball joint T^1. Therefore, six virtual links can be obtained to give six linear virtual independent equations that can be used to analyze the singular position of the machine tool. Although the machine tool using virtual links concept can give six linear virtual independent equations, the DOF of the virtual system is still three. The reason is that the equivalent components of this research do not change (increase or decrease) the DOF of the origin components (pin joints or ball joints).

In Figure 3-5, the displacement of the six virtual driving axes related to the $(XYZ)_B$ coordinate system can be obtained as follows:

$$[X_{B1} \quad Y_{B1} \quad Z_{B1} \quad 1]^T = [-0.866R - 0.5a \quad 0.866a - 0.5R \quad LS_1 \quad 1]^T \tag{3-45a}$$

$$[X_{B2} \quad Y_{B2} \quad Z_{B2} \quad 1]^T = [-0.866R + 0.5a \quad -0.5R - 0.866a \quad LS_2 \quad 1]^T \tag{3-45b}$$

$$[X_{B3} \quad Y_{B3} \quad Z_{B3} \quad 1]^T = [a \quad R \quad LS_3 \quad 1]^T \tag{3-45c}$$

$$[X_{B4} \quad Y_{B4} \quad Z_{B4} \quad 1]^T = [-a \quad R \quad LS_4 \quad 1]^T \tag{3-45d}$$

$$[X_{B5} \quad Y_{B5} \quad Z_{B5} \quad 1]^T = [0.866R - 0.5a \quad -0.5R - 0.866a \quad LS_5 \quad 1]^T \tag{3-45e}$$

$$[X_{B6} \quad Y_{B6} \quad Z_{B6} \quad 1]^T = [0.866R + 0.5a \quad -0.5R + 0.866a \quad LS_6 \quad 1]^T \tag{3-45f}$$

In the above equation, R is the diameter of the circle on the upper base frame that the three driving axes evenly located. LS_i，i=1，2…6 are the vertical

displacement of the six virtual ball joints related to the upper based frame. On the tool frame, the coordinate T_i , i=1 , 2…6 related to the fixed tool frame coordinate $(XYZ)_T$ can be obtained as follows:

$$[x_{T1} \quad y_{T1} \quad z_{T1} \quad 1]^T = [-0.866r \quad -0.5r \quad t \quad 1]^T \tag{3-46a}$$

$$[x_{T2} \quad y_{T2} \quad z_{T2} \quad 1]^T = [X_{T1} \quad Y_{T1} \quad Z_{T1} \quad 1]^T \tag{3-46b}$$

$$[x_{T3} \quad y_{T3} \quad z_{T3} \quad 1]^T = [0 \quad r \quad t \quad 1]^T \tag{3-46c}$$

$$[x_{T4} \quad y_{T4} \quad z_{T4} \quad 1]^T = [X_{T3} \quad Y_{T3} \quad Z_{T3} \quad 1]^T \tag{3-46d}$$

$$[x_{T5} \quad y_{T5} \quad z_{T5} \quad 1]^T = [0.866r \quad -0.5r \quad t \quad 1]^T \tag{3-46e}$$

$$[x_{T6} \quad y_{T6} \quad z_{T6} \quad 1]^T = [X_{T5} \quad Y_{T5} \quad Z_{T5} \quad 1]^T \tag{3-46f}$$

In the above equation, r is the diameter of the tool frame and t is the tool length. They are considered as constant in this research. The calculation of the vertical displacement LS_i, i=1,2…6 of the each driving axis from the given tool path is very essential from the control viewpoint of the machine tool. Representing the B_i and T_i i=1,2…6 coordinates related to the upper base frame coordinate system $(XYZ)_B$ is beneficial for the above calculation. In Figure 3-5, O_p is the origin of the designed CAD model related to the origin of the mechanical coordinate system $(XYZ)_M$ of the machine tool. The coordinate system of the designed CAD model is defined as $(XYZ)_P$. In Figure 3-5, $A_{O_{MXYZ}}^{O_{Bxyz}}$ represents the homogeneous transformation matrix between the coordinate system of the upper base frame O_{Bxyz} and the mechanical origin O_{MXYZ}. Then, the $[x_{Bi} \quad y_{Bi} \quad z_{Bi} \quad 1]^T$ displacement of the driving axis related to the O_{MXYZ} coordinate system can then be represented as $[X_{Bi} \quad Y_{Bi} \quad Z_{Bi} \quad 1]^T$ and can be obtained as:

$$\begin{bmatrix} X_{Bi} \\ Y_{Bi} \\ Z_{Bi} \\ 1 \end{bmatrix} = A^{O_{Bxyz}}_{O_{MXYZ}} \begin{bmatrix} x_{Bi} \\ y_{Bi} \\ z_{Bi} \\ 1 \end{bmatrix} = \begin{bmatrix} 1 & 0 & 0 & X_{P_{OB}} \\ 0 & 1 & 0 & Y_{P_{OB}} \\ 0 & 0 & 1 & Z_{P_{OB}} \\ 0 & 0 & 0 & 1 \end{bmatrix} \begin{bmatrix} x_{Bi} \\ y_{Bi} \\ z_{Bi} \\ 1 \end{bmatrix} \quad i=1,2\cdots6 \qquad (3\text{-}47)$$

In the above equation, the $[x_{Bi} \quad y_{Bi} \quad z_{Bi} \quad 1]^T$ i=1，2…6 is already given in the Eq.(3-45). Similarly, $A^{O_{Pxyz}}_{O_{MXYZ}}$ is used to represent the homogeneous transformation matrix between the coordinate systems of O_{Pxyz} and O_{MXYZ}. Therefore, the point vector $[p_x \quad p_y \quad p_z \quad 1]^T$ on the designed CAD model related the O_{MXYZ} coordinate system is represented as $[X_p \quad Y_p \quad Z_p \quad 1]^T$ and can be obtained as follows:

$$\begin{bmatrix} X_p \\ Y_p \\ Z_p \\ 1 \end{bmatrix} = A^{O_{Pxyz}}_{O_{MXYZ}} \begin{bmatrix} p_x \\ p_y \\ p_z \\ 1 \end{bmatrix} = \begin{bmatrix} 1 & 0 & 0 & X_{P_{OP}} \\ 0 & 1 & 0 & Y_{P_{OP}} \\ 0 & 0 & 1 & Z_{P_{OP}} \\ 0 & 0 & 0 & 1 \end{bmatrix} \begin{bmatrix} p_x \\ p_y \\ p_z \\ 1 \end{bmatrix} \quad i=1,2\cdots6 \qquad (3\text{-}48)$$

To simplify the analysis of the derivation, the cuter is assumed to be located along the normal direction of the designed surface. The tilt angle and yaw angle are not included in the derivation here. To complete a five DOF machining processes, the cutter orientation and location must be coincided with the local coordinate of the designed surface (see Figure 3-5). The coordinate of Ti, i=1,..6 related to the O_{MXYZ} coordinate system is represented as $[X_{Ti} \quad Y_{Ti} \quad Z_{Ti} \quad 1]^T$ and can be obtained as follows:

$$\begin{bmatrix} X_{Ti} \\ Y_{Ti} \\ Z_{Ti} \\ 1 \end{bmatrix} = A^{O_{Pxyz}}_{O_{MXYZ}} A^{O_{Txyz}}_{O_{Pxyz}} \begin{bmatrix} x_{Ti} \\ y_{Ti} \\ z_{Ti} \\ 1 \end{bmatrix} \quad i=1,2\cdots 6 \tag{3-49}$$

In the above equation, $A^{O_{Txyz}}_{O_{Pxyz}}$ is the homogeneous transformation matrix between tool frame coordinate system O_{Txyz} and the CAD model coordinate system O_{Pxyz}. Replace Eq.(3-48) into Eq.(3-49), we have

$$\begin{bmatrix} X_{Ti} \\ Y_{Ti} \\ Z_{Ti} \\ 1 \end{bmatrix} = A^{O_{Pxyz}}_{O_{MXYZ}} A^{O_{Txyz}}_{O_{Pxyz}} \begin{bmatrix} x_{Ti} \\ y_{Ti} \\ z_{Ti} \\ 1 \end{bmatrix} = \begin{bmatrix} 1 & 0 & 0 & X_{Pop} \\ 0 & 1 & 0 & Y_{Pop} \\ 0 & 0 & 1 & Z_{Pop} \\ 0 & 0 & 0 & 1 \end{bmatrix} A^{O_{Txyz}}_{O_{Pxyz}} \begin{bmatrix} x_{Ti} \\ y_{Ti} \\ z_{Ti} \\ 1 \end{bmatrix}$$

$$= \begin{bmatrix} 1 & 0 & 0 & X_{P_{OP}} \\ 0 & 1 & 0 & Y_{P_{OP}} \\ 0 & 0 & 1 & Z_{P_{OP}} \\ 0 & 0 & 0 & 1 \end{bmatrix} \begin{bmatrix} 1 & 0 & 0 & p_x \\ 0 & 1 & 0 & p_y \\ 0 & 0 & 1 & p_z \\ 0 & 0 & 0 & 1 \end{bmatrix} \begin{bmatrix} \cos\beta & 0 & \sin\beta & 0 \\ 0 & 1 & 0 & 0 \\ -\sin\beta & 0 & \cos\beta & 0 \\ 0 & 0 & 0 & 1 \end{bmatrix}$$

$$\begin{bmatrix} 1 & 0 & 0 & 0 \\ 0 & \cos\alpha & -\sin\alpha & 0 \\ 0 & \sin\alpha & \cos\alpha & 0 \\ 0 & 0 & 0 & 1 \end{bmatrix} \begin{bmatrix} \cos\gamma & -\sin\gamma & 0 & 0 \\ \sin\gamma & \cos\gamma & 0 & 0 \\ 0 & 0 & 1 & 0 \\ 0 & 0 & 0 & 1 \end{bmatrix} \begin{bmatrix} x_{Ti} \\ y_{Ti} \\ z_{Ti} \\ 1 \end{bmatrix} \tag{3-50}$$

3.3.3 Singularity analysis

The Plücker coordinate system must be defined before using the screw theory for analyzing the machine tool singular position. In this research, each axis of the six virtual links is considered as one of the coordinate axis of the Plücker coordinate system. The six axes of the Plücker coordinate system are represented as $\mathbf{S_i}$, i = 1,..6 and can be obtained as:

$$S_i = T_i - B_i \tag{3-51}$$

The Plücker coordinate system and the screw theory can be found from the literatures [22]. In the above equation, $\mathbf{B_i}$ is the coordinate that already given in the Eq.(3-47). T_i is the coordinate that already given in the Eq.(3-49). Here, the ball characters of $\mathbf{S_i}$, $\mathbf{B_i}$ and $\mathbf{T_i}$ mean that they are vectors. Define the moment matrix $M_i^{'}$ as the cross product of the $\mathbf{B_i}$ and $\mathbf{S_i}$,

$$M_i^{'} = B_i \times S_i \tag{3-52}$$

Applying the vector components of the calculated S_i and M_i results, the i-th component of the $U_i^{'}$ matrix of the screw theory can be obtained as,

$$U_i^{'} = \begin{bmatrix} S_{ix} & S_{iy} & S_{iz} & M_{ix}^{'} & M_{iy}^{'} & M_{iz}^{'} \end{bmatrix} \tag{3-53}$$

The unit vector of the S_i is defined as s_i :

$$s_i = \frac{S_i}{|S_i|} \tag{3-54}$$

The unit vector of the M'_i is defined as M_i :

$$M_i = \frac{M_i^{'}}{|S_i|} \tag{3-55}$$

In the above equation, $|S_i|$ is defined as:

$$|S_i| = \sqrt{S_i \bullet S_i} \tag{3-56}$$

Normalize the U_i' matrix by replacing the Eq.(3-54) and Eq.(3-55) into Eq.(3-56), we have the U matrix as follows:

$$U = \begin{bmatrix} S_{1x} & S_{1y} & S_{1z} & M_{1x} & M_{1y} & M_{1z} \\ S_{2x} & S_{2y} & S_{2z} & M_{2x} & M_{2y} & M_{2z} \\ S_{3x} & S_{3y} & S_{3z} & M_{3x} & M_{3y} & M_{3z} \\ S_{4x} & S_{4y} & S_{4z} & M_{4x} & M_{4y} & M_{4z} \\ S_{5x} & S_{5y} & S_{5z} & M_{5x} & M_{5y} & M_{5z} \\ S_{6x} & S_{6y} & S_{6z} & M_{6x} & M_{6y} & M_{6z} \end{bmatrix} \quad (3\text{-}57)$$

The determinant of the U matrix is used as the singularity judgement of the machine tool. The non-zero of the U matrix determinant means the six force vectors generated from the six virtual links are linear independent and can completely constrain the structure of the machine tool. The zero result of the U matrix determinant means that the six virtual links can not completely constrain the machine tool. Therefore, location with zero U matrix determinant is the singular location of the machine tool [24-25].

3.3.4 Results and discussions

The effects of the L/R ratio on the singularity of the hybrid machine tool are very significant and the results are shown in the Figure 3-6 and Figure 3-7. For L/R >1, the results are shown in Figure 3-6. For L/R < 1, the results are shown in Figure 3-7. Both of the results have the tendency that smaller L/R ratio has smaller safe workspace (volume). The safe workspace (volume) here means that the workspace expanded from the center position of the machine tool but without crossing any singular area or path. There are some workspaces that may be reached from geometry viewpoint. If a singular area must be passed before reaching this workspace, this workspace will not be considered as a safe workspace here. In the real machining applications by using the hybrid parallel link machine tool, the cutter with the large orientation variation can be completely avoided and no necessity for passing the singular region. This is the reason that a XY table is adopted. It is worth mentioning that the workspace is approaching to zero (no workspace is found) with L/R = 0.5 in Figure 3-7. This is caused by the too short link length that can not

create any workspace using the given design dimensions. The α and β are separately defined as the cutter rotation angle along the x-axis and y-axis related to the workpiece coordinate.

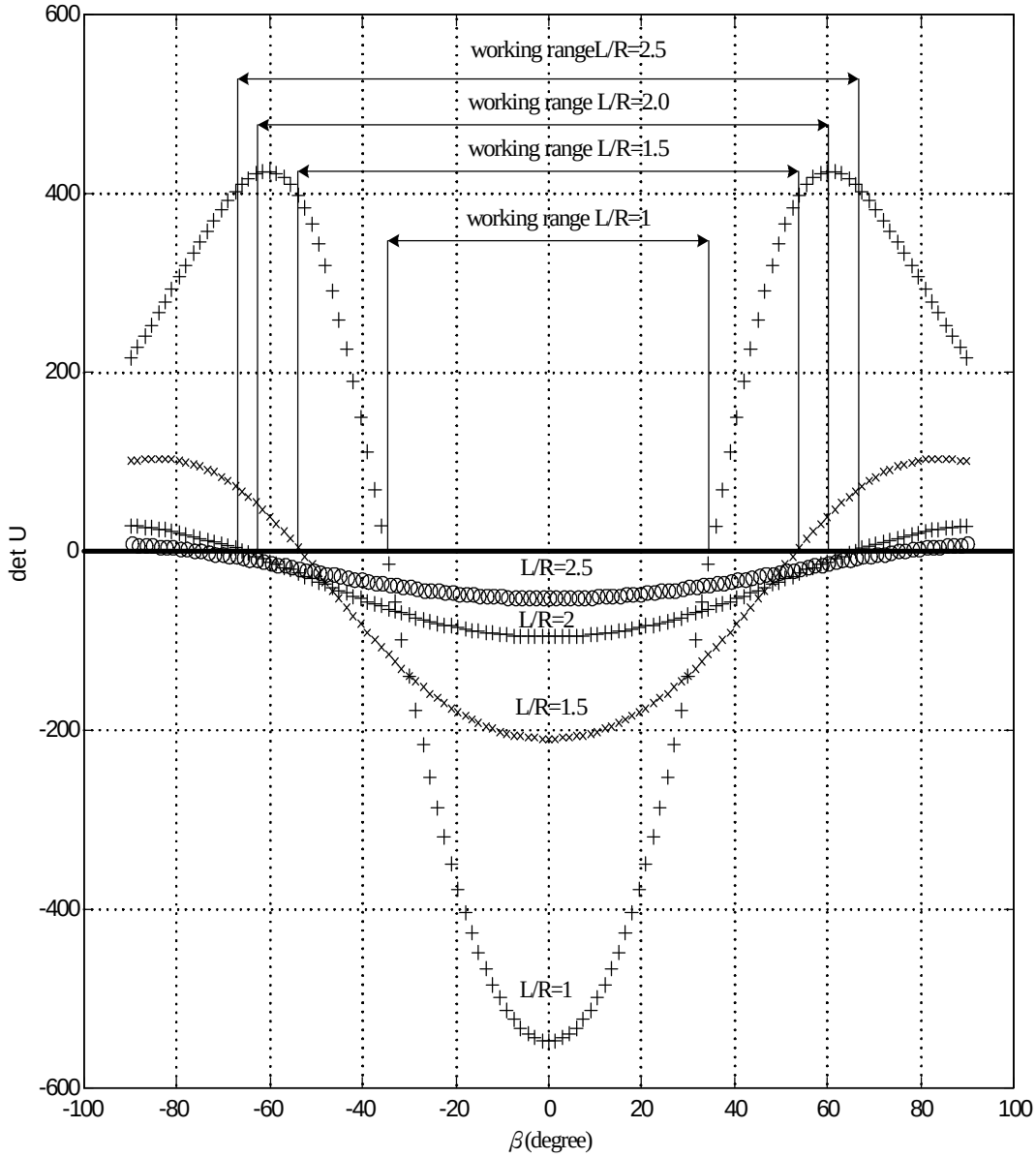

Figure 3-6 The Umatrix determinant (singular) analysis of the machine tool with L/R larger than 1 (R=750mm; r=0.5R; a=5mm).

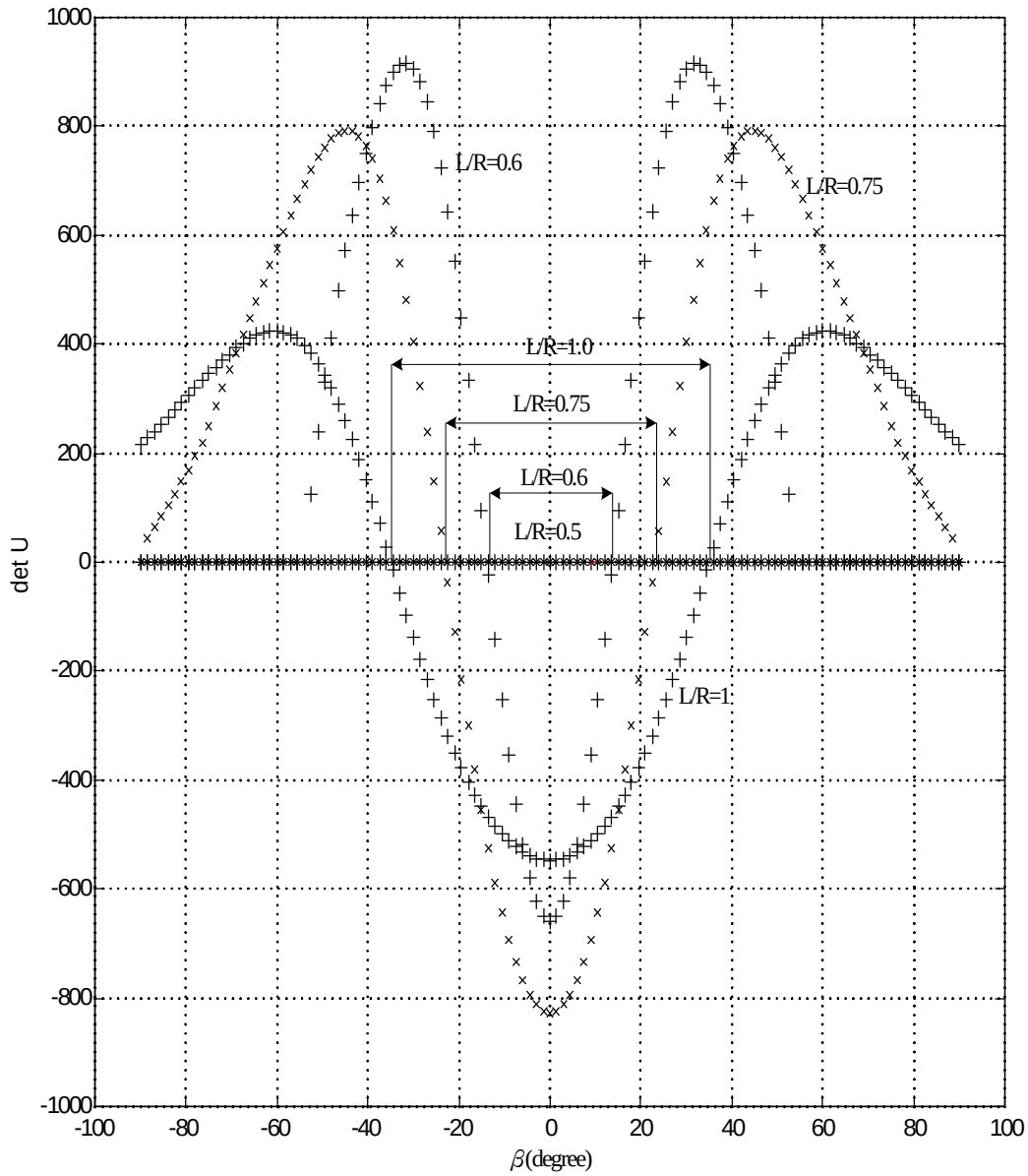

Figure 3-7 The singular analysis of the machine tool with L/R smaller than 1 (R=750mm; r=0.5R; a=5mm).

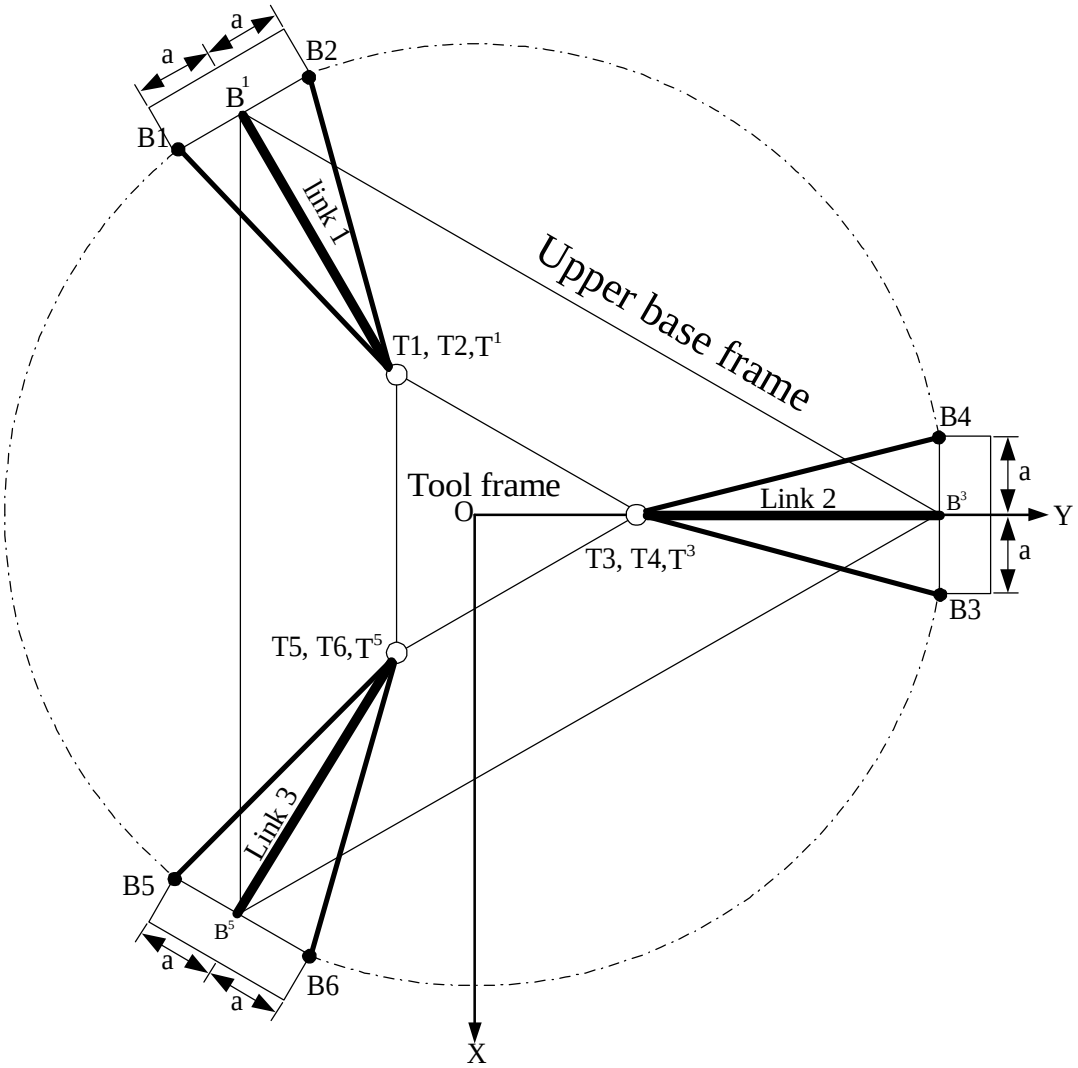

Figure 3-8 Top view of equivalent length “a”.

Figure 3-8 shows the top view of the equivalent length “a”. The effects of the length “a” on the singularity are shown in the Figure 3-9. This is the length between two virtual ball joints. It is found that the larger a length the larger U matrix determinant can be obtained and has better structure rigidity. With a=0mm, the two three DOF ball joints are located at the same position and the equivalent component has three DOF (not one DOF). In this case, the constraint of the links on the machine tool is lost. This is reasonable from the geometric relationship.

The effects of the r/R on the singular position of the machine tool are shown in the Figure 3-10. Although the determinant values of the U matrix are significantly varied with different r/R ratio, the workspace is not significantly varied with different r/R ratio. This means that nearly the same β angle (-45^0, $+45^0$) is obtained at the determinant U=0 with various r/R ratio. The larger absolute value of the U matrix implies the better independence of the constraints from the six virtual links. Therefore, the larger U matrix determinant can be obtained with the larger r/R ratio and this implies that the better structure rigidity can be obtained.

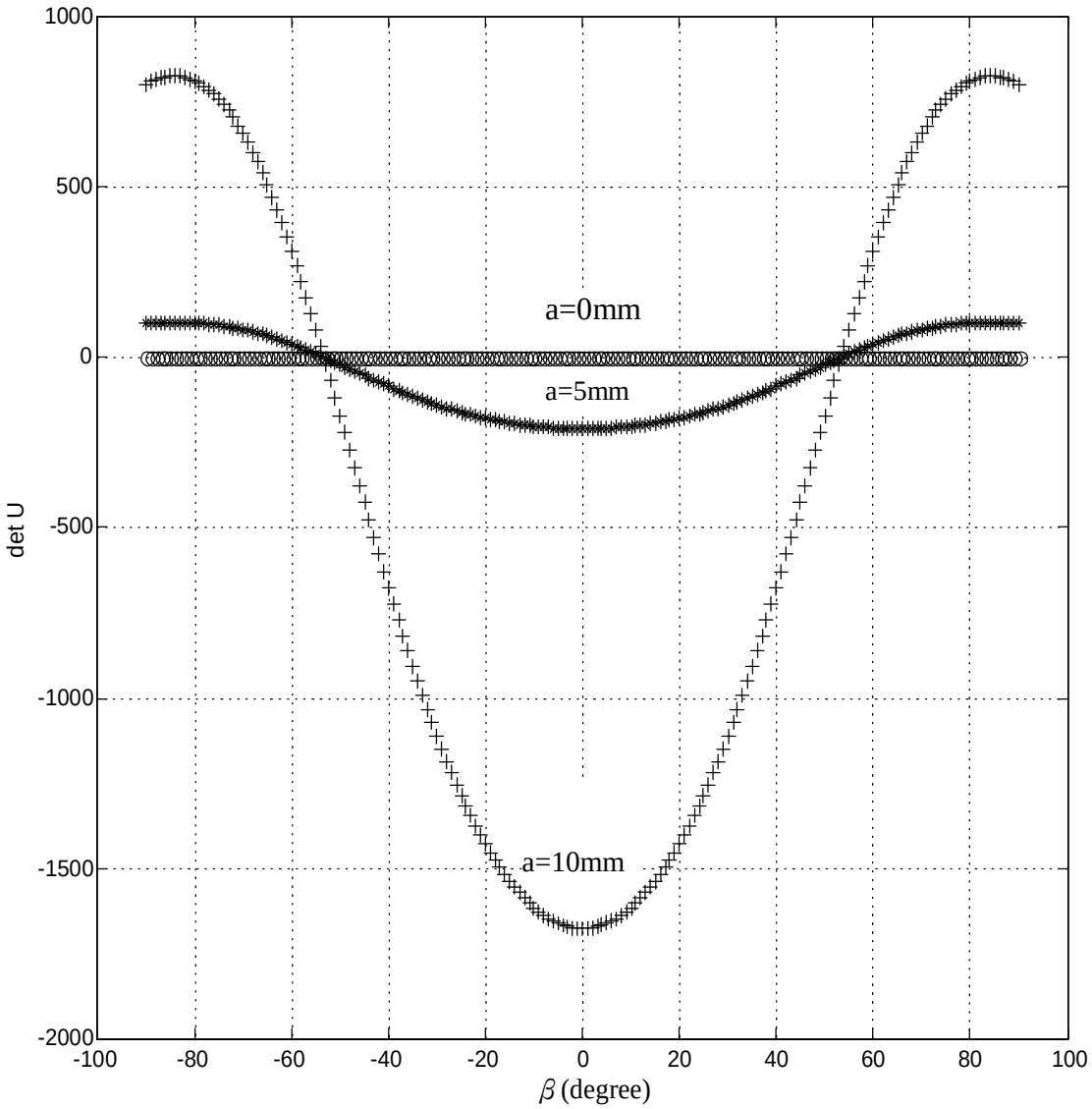

Figure 3-9 The effects of the length a on the singularity of the machine tool (R=750mm; r=0.5r; L=1.5R).

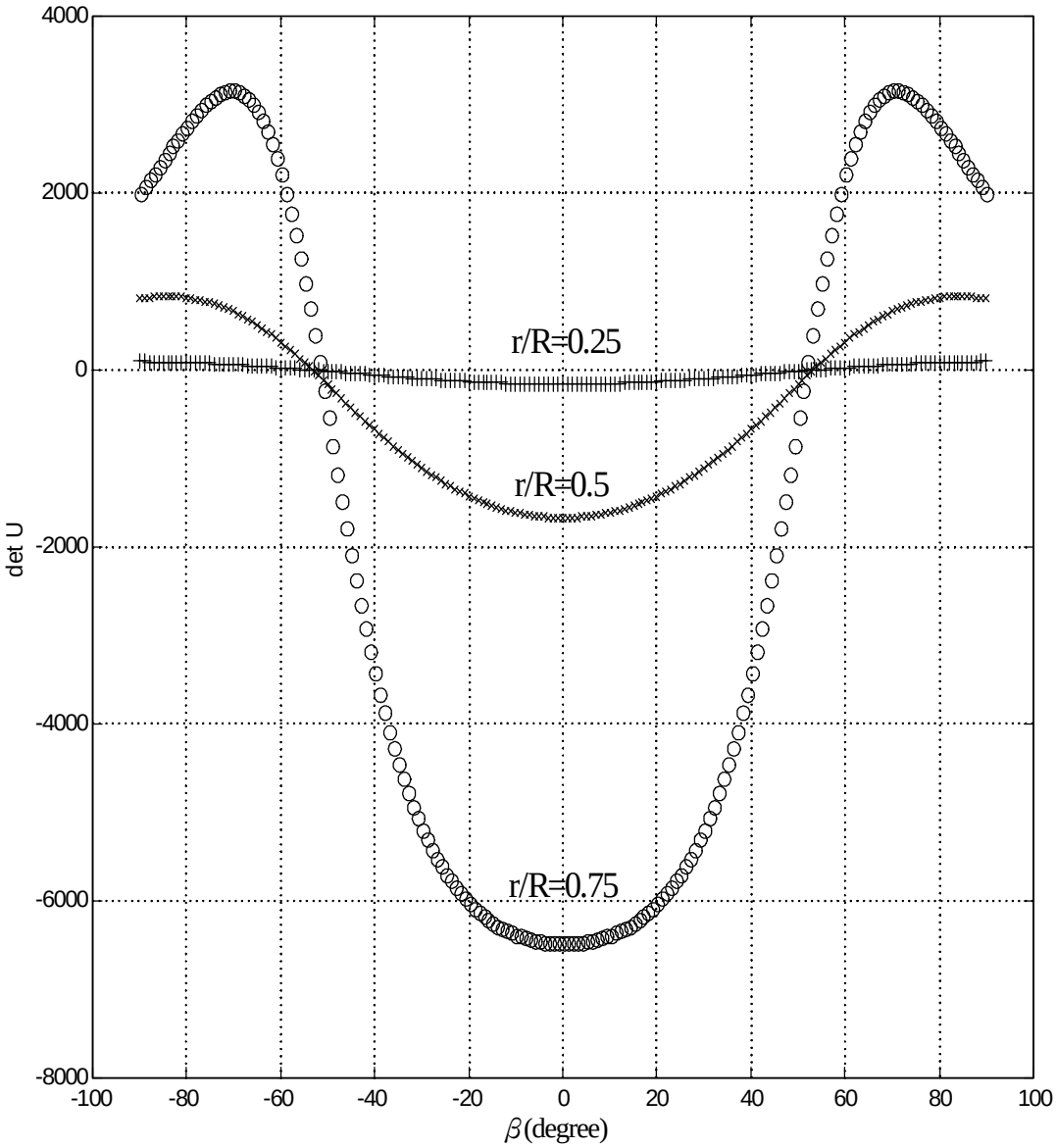

Figure 3-10 The effects of the r/R ratio on the determinant results of U matrix (R=750mm; a=10mm; L=1.5R)

The effects of L/R, r/R on the workspace are shown in Figure 3-11. Here, the workspace is defined as the (α, β) region that enclosed by a boundary with determinant of U matrix to be zero. In Figure 3-11, there are three parameter groups – (L/R=2, r/R=0.75), (L/R=3, r/R=0.5), (L/Rb=4, r/R=0.25). The (L/R=2, r/R=0.75) parameter implies that the system has a very short link length and with very large tool frame diameter. Contradictory, the (L/R=4, r/R=0.25) parameter implies that the system has a very long link length and very small tool frame diameter. The (L/R=3，r/R=0.5) parameter is the mediate case. The searching domain for the workspace investigated in Figure 3-11 are ($-110^\circ \leqq \alpha, \beta \leqq 110^\circ$). For each parameter group, the searching calculation is started from $\alpha=-100^\circ$ to $\alpha= +100^\circ$ with β fixed at a specific value. The calculation result will show the left and right limitation of the workspace. Then, the similar searching calculation is repeated again with next β value. The angle interval of α and β in each searching calculation is set to be 5° in Figure 3-11. The β is calculated from -110° to $+100^\circ$ step by step. A semi-closed workspace is found with the parameter (L/R=2, r/R=0.75). The other two workspaces are open regions. The semi-closed workspace is obviously smaller than the two open workspaces. Therefore, it is deduced that machine tool system designed with the shorter link length and a larger tool frame diameter is a worse design from the workspace viewpoint. The results in the Figure 3-11 are further investigated in Figure 3-12 and only focused on a specific angle $\alpha = 40^\circ$ tool path. The shorter link length with larger tool frame (L/R=2，r/R =0.75) has a relative smaller workspace but has a relative better independent degree of constraint compared with the longer link length with smaller tool frame diameter (L/R=4，r/R =0.25).

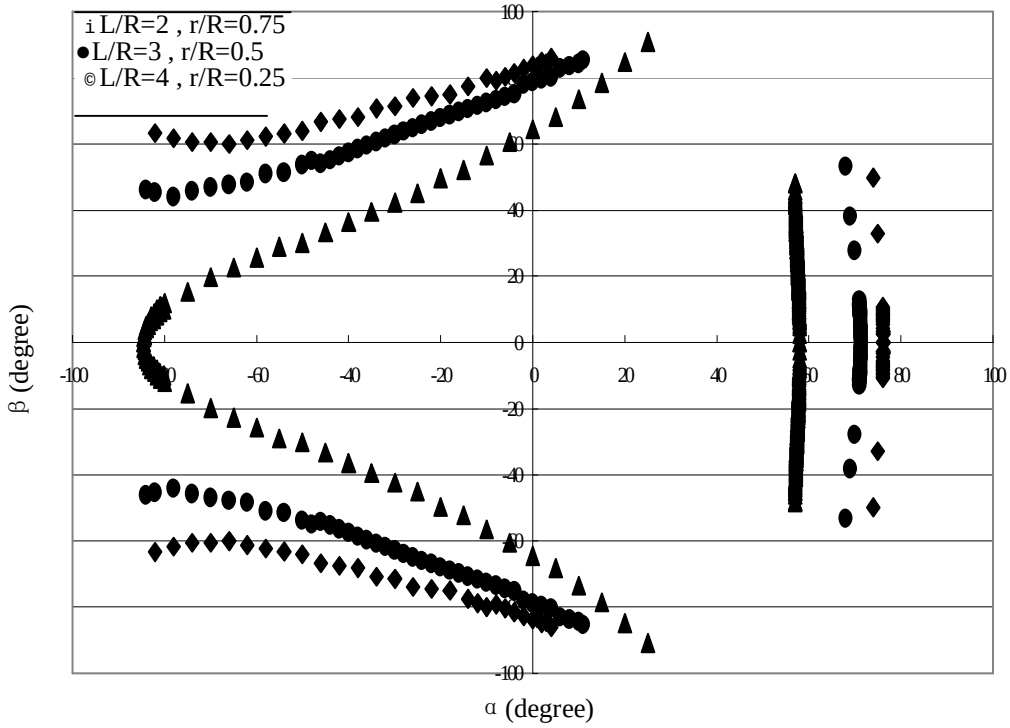

Figure 3-11 Comparison of the workspace (region enclosed by determinant U=0) of the cases: (L/R=2, r/R=0.75), (L/R=3, r/R=0.5), (r/R=4, r/R=0.25)

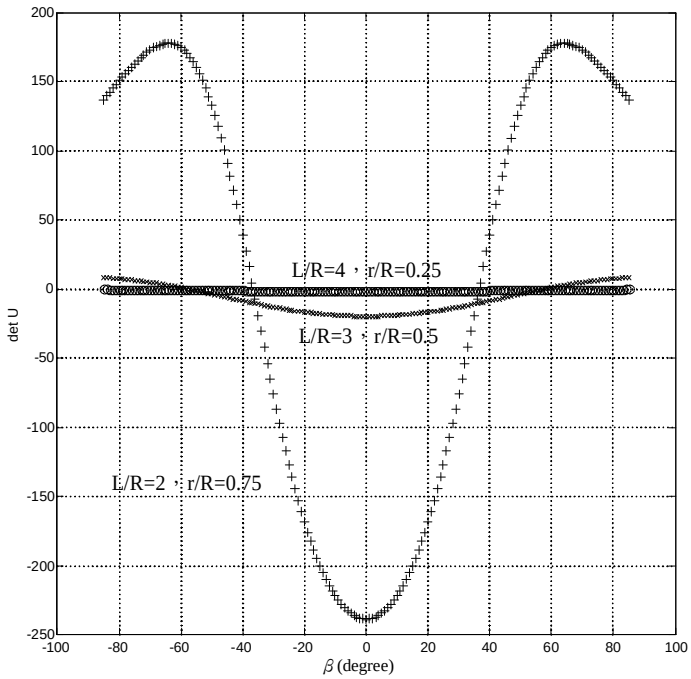

Figure 3-12 Singularity comparison of (L/R=2, r/R=0.75), (L/R=3, r/R=0.5), (L/R=4, r/R=0.25) with $\alpha = -40^{\circ}$.

3.4 Design optimization of link dimension

3.4.1 Introduction

Using the geometric vectors definition and Euler angle transformation method, Lee solved the kinematics and geometric relationship of a parallel mechanism with 3 DOF [26-27]. For workspace, there were also several researches published. For example, a two-dimensional domain only considering the constraints of maximum and minimum link length was discussed by Tosatt et al [28]. Using the same method as described in [28], Wang further considered the machine element constraints and interference into workspace analysis [29]. A method separating the workspace into discrete points is also proposed by Wang et al [30]. A 3D workspace is then defined by a collection of all points that satisfy the machine constraints.

There are many researches related to the workspace of parallel link machine tool, but very few literatures contributed on the optimum design of the workspace. However, fully understanding of the workspace for parallel link machine tool is very important for the practical applications of the systems. The workspace of a parallel link machine tool is mainly determined by the designed dimensions and the mechanical component (joints) constraints. In this research, one optimization method for investigating the effects of the designed dimensions on the workspace results of the three DOF parallel link machine tool is proposed. The optimal strategy is also introduced for obtaining the optimal workspace.

3.4.2 Definition of workspace

The workspace (for 5 DOF machine tool) is generally classified into three types.

1. Constant orientation workspace, Ω_C: all points that are reachable by a point on the end-effector with the orientation fixed during the motion.
2. Maximal workspace, Ω_M: all points that are reachable by a point on the end-effector with the orientation located at the most beneficial posture.
3. Total orientation workspace, Ω_T: all points that are reachable by a point on the

end-effector with the orientation within a prescribed range.

The investigated parameters of the machine tool include stroke in the Z direction, the rotating angle α, the rotating angle β. The above three parameters are controlled by the upper 3 DOF parallel link mechanism. In the analysis process, the rotation movement of the 3 DOF parallel link mechanism will generate a relative X, Y displacements. The X, Y displacements are not independent variables for this mechanism. Therefore, the X, Y displacements can be treated as two compensation-values (of XY table) with respect to the controlled position. The lower XY table controls two translation DOFs, its analysis algorithm is very simple. Therefore, it was already mentioned in the previous section that only the workspace generated by the upper mechanism (translation in the Z direction, the rotating angle α , and the rotating angle β) will be considered.

As two rotating DOF and one translating DOF investigated, the solution of 3 DOF space can be analyzed by using a 3D domain. The three axes of the 3D workspace domain separately represent the variation of two rotating and one translating DOF respectively. For solving the workspace, the inverse solution combines with the concept described in reference [12] is adopted. The 3D workspace domain construct by the Z, α, β was divided into many infinitesimal points. The infinitesimal points are calculated using the algorithm of inverse solution and judged whether it is satisfied the constraint of the mechanism or not. A (0 or 1) boolean function is used to represent the satisfaction condition. The points are set to be 1 if satisfy the constraints. Otherwise the points are set to be 0 (i.e., the position where the mechanism can't reach). One of a 3D diagram of the workspace analysis results was built up that was shown in Figure 3-13 by using CAD/CAM software (UG solution). The boundary points of the workspace are determined by the points with the boolean function value varied from 0 to 1.

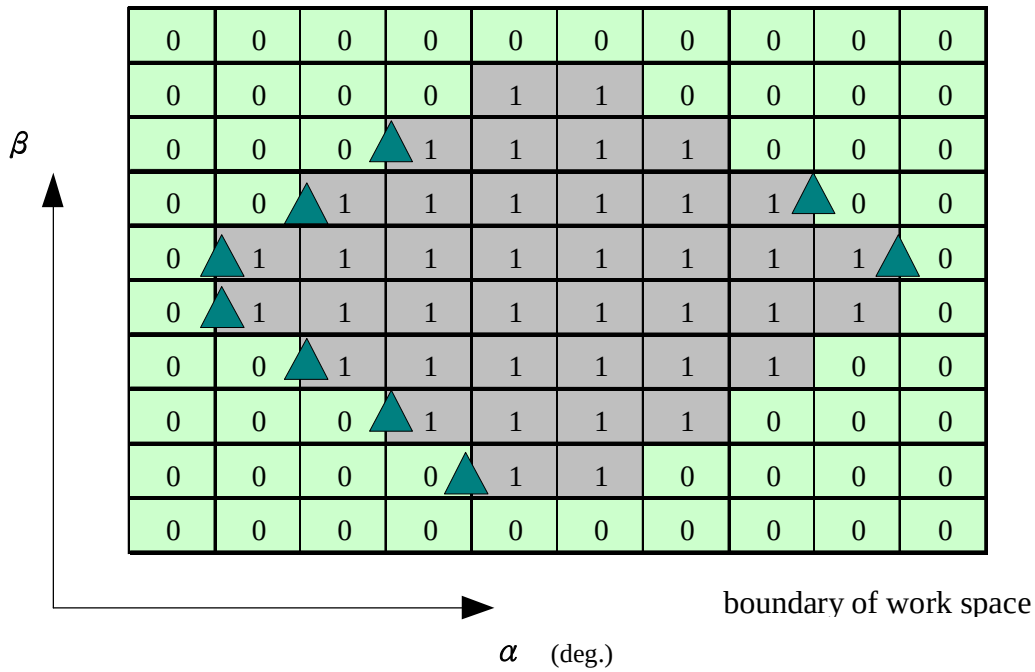

Figure 3-13 The schematic diagram for the workspace analysis

Two kinds of joints are used in the machine tool. Pin joint connects the linkage and sliding block that slides on the guide way and is driven ball screw. Ball joint connects the linkage and tool frame. Therefore, two kinds of joint constraints must be defined. The constraint of pin joint is the angle between the centerline of linkage and the moving axis of ball screw. The constraint of ball joint is the angle between normal direction of tool frame and the axial direction of linkage. Figure 3-14 is a schematic diagram shows the geometric relationship of the constraints of pin and ball joints.

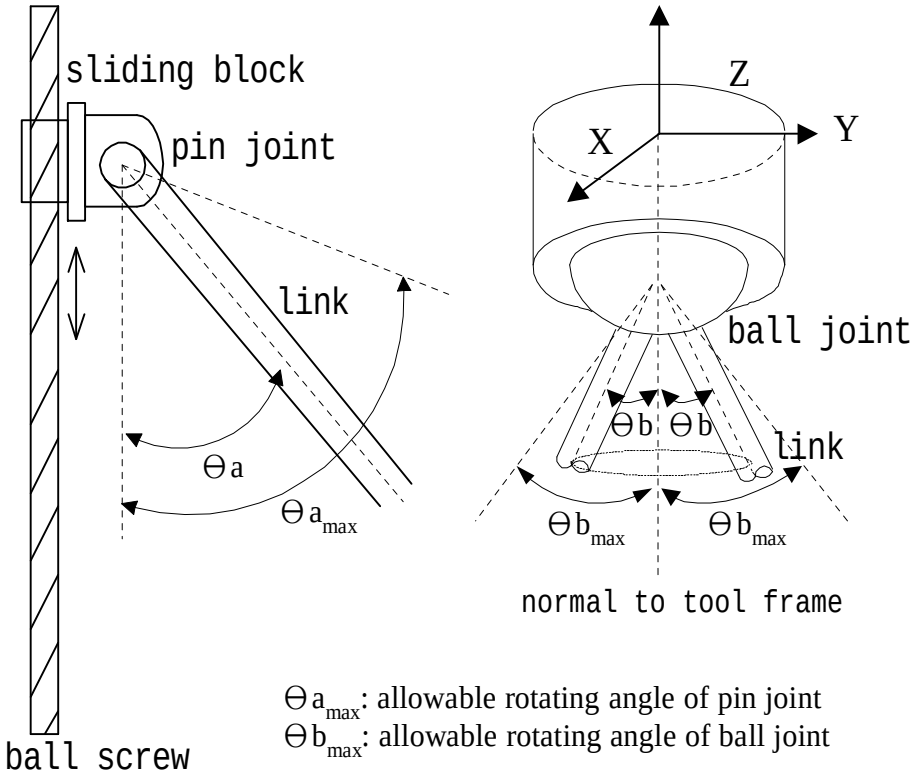

Figure 3-14 The constraint on the rotating angle of the joint.

3.4.3 Design optimization of angular workspace

To obtain a maximum workspace of the machine tool by adjusting dimensional parameters is the main purpose of this section. The maximum workspace means that the moving range of the five DOF mechanism approaching to maximum. As mentioned in previous section, the upper and lower parts of the machine tool were analyzed independently. The analysis for XY table is simple and will not be discussed (the bigger size XY table, the larger workspace). In the 3 DOF parallel mechanism, the workspace was varied with the changes of dimension parameters. Therefore, it is meaningful to investigate the maximum 3D workspace that created by the optimized dimension parameters.

The parameters related to the machine tool include the radius R of upper base frame, the radius r of tool frame and the length L of linkage. The kinematics

parameters include translation in z direction, rotating angle α and rotating angle β. The dimensional parameters of the machine tool are the dominating factors in the workspace optimization procedure. The radius R of the upper base frame is the parameter for deciding the whole size of the machine system. Therefore, the radius R of upper base frame was used as a dimensionless denominator. Then the dimensionless parameters of machine tool can be defined as L/R, and r/R.

The optimization algorithm is that the variable Z was firstly set to be fixed and the other two DOF (α, β) are varied for finding out the optimal values of L/R and r/R. From the geometrical relationship, it was found that the factors affecting the workspace in the Z direction is the total length of ball screw. The longer ball screw length, the larger workspace in Z direction. Therefore, the analysis of the Z direction workspace is not necessary in the optimized procedure. The Z coordinate was set to be a constant to find out the effects of the design parameters on the workspace (α, β) of the machine tool. The physical meaning of the above description is that the maximal (α, β) workspace can be expected to be obtained by adjusting the ratio of L/R and r/R.

In this research, the workspace optimization condition for parallel link machine tool was defined as: the difference of the maximum and minimum results of (S_A, S_B, S_C) approaches to minimum with the same cutter pose. The (S_A, S_B, S_C) results are referred to the base frame coordinate system(O-X-Y-Z). The S_1, S_2 and S_3 have their own possible maximum and minimum values with a designed parallel link machine tool. However, the difference of the maximum and minimum results of (S_A, S_B, S_C) means that the situation may be occurred with S_A maximum and S_C minimum. Here, a symbol "DS" is used to represent the difference of maximum and minimum results of (S_A, S_B, S_C) and will be used in the following sections. For example, two machine tools have the same cutter pose and the same ball screw length 1000 mm. However, the difference of maximum and minimum (S_A, S_B, S_C) of the first machine is 800mm, and the difference of the maximum and minimum (S_A, S_B, S_C) of the second machine

is 500mm. It means that the second machine has 300mm Z-direction moving distance more than the first machine with the same cutter pose. Therefore, the maximum workspace can be obtained at the condition of the difference value of controlled feed stroke (S_A, S_B, S_C) approaching to minimum. Based on the above discussion, the basic procedures of the design parameter optimization of the machine tool can be obtained. They are: 1. Varying the design parameters and calculating the difference of the maximum and minimum values of controlled feed stroke (S_A, S_B, S_C). 2. Then, select the minimum difference as the optimized design parameter at the kinematics parameters.

A. Design dimension optimization

One set of limits of the representative design parameters for analyzing and searching the whole workspace are given as followings:

1. Parameters α and β rotate between $\pm 45^0$.
2. The radius R of the upper base frame is 300 mm.
3. The height of the cutter Z is fixed at 2000 mm.
4. The ratio of (r/R) is limited to $0.31 \le (r/R) \le 0.8$. Therefore, the radius of the tool frame, r, is defined from 93 mm to 240 mm.
5. The ratio of (L/R) is limited to $2.02 \le (L/R) \le 3.0$. Therefore, the linkage length is defined from 606 mm to 900 mm.

The calculation and analysis flow chart are shown in Figure 3-15. In the calculation, the Z coordinate was fixed. There are two loops for effectively calculating all the possible conditions of design parameters r/R , L/R. Each design parameters has another two calculating loop for searching the whole work space of α , β. The calculation results are compared and the optimized design parameters are obtained. The decision algorithm (minimum DS) of the optimization was already

mentioned in the previous section. Here, a symbol MinDS was used to represent the results of the calculated minimum DS. It is worth mentioning that the constraint of the pin joint is 90 ^{o} and the constraint of the ball joint is 85^{o}. All the calculation results of the α , β in the above analysis must be satisfied with both of the constraints of pin joints and ball joints.

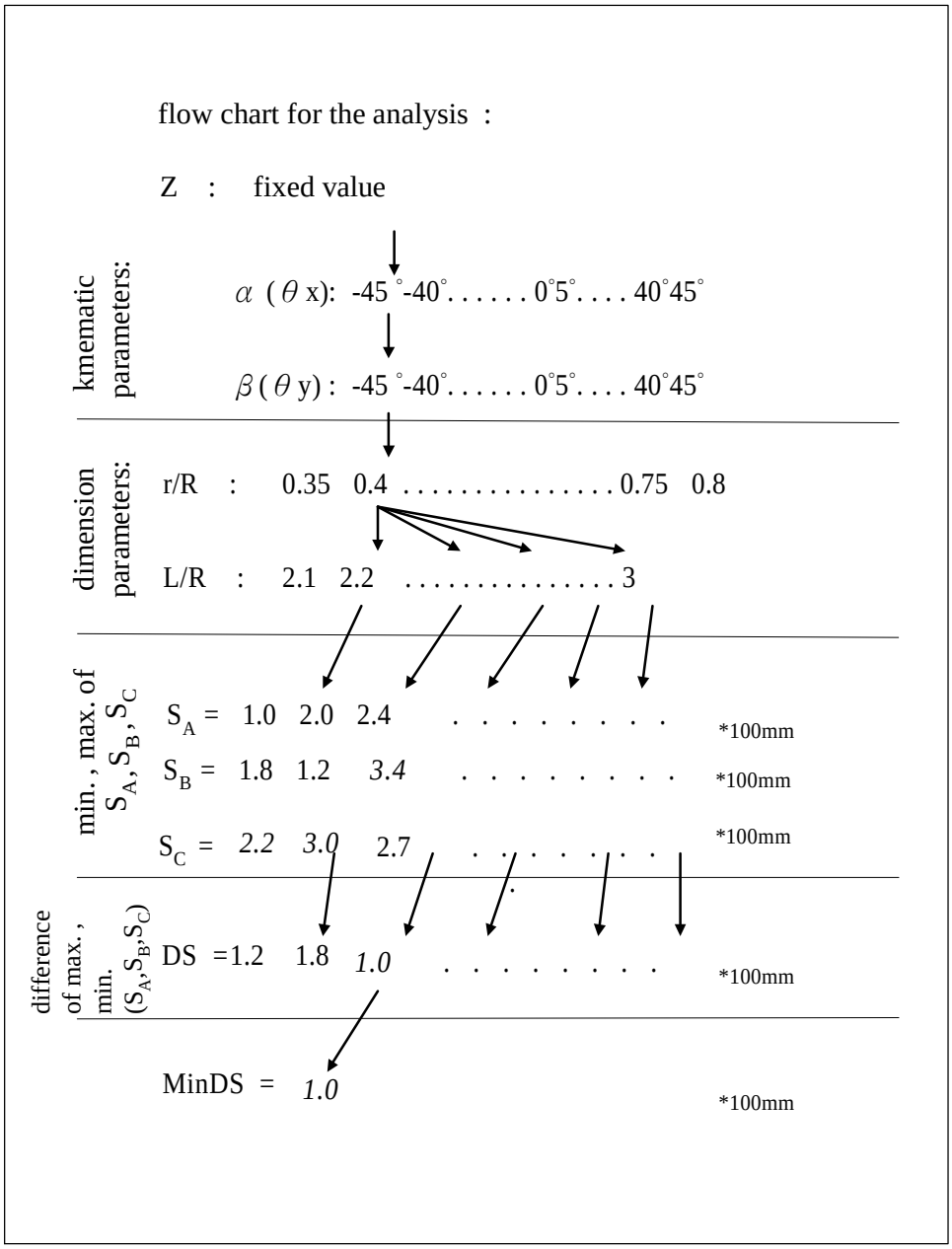

Figure 3-15 Flow chart for the analysis and the iteration in the optimization.

The minimum difference MinDS of the maximum and minimum (S_A, S_B, S_C) is calculated in the optimization procedure. Figure 3-16a shows the three-dimensional distribution of the MinDS values. There are six regions in Figure 3-16b and the center is located at (α , β) = (0^0,0^0). It is reasonable that the MinDS value equals to zero at (α , β) = (0^0,0^0) and rapidly increased with the increased of the α and β. There is an edge line clearly seen between each two regions. The six regions built by the surfaces with different curvatures are also found to be asymmetric.

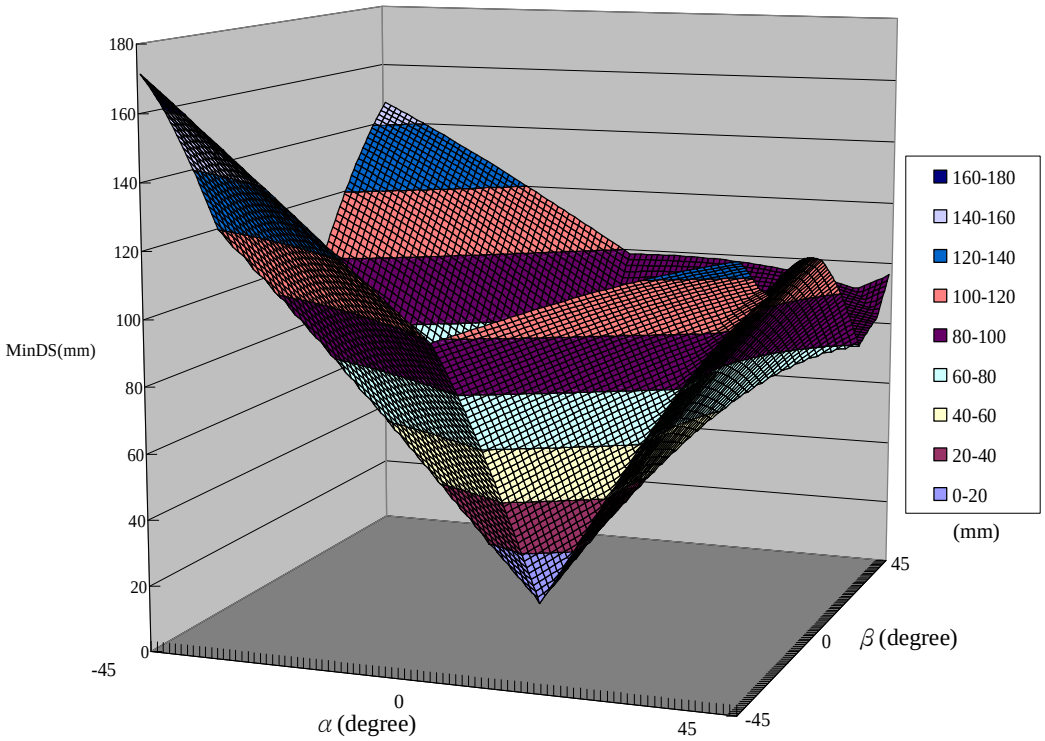

Figure 3-16a The optimum results for the parameter MinDS. (R = 300mm; r = 93~240mm; L = 606~900mm; pin joint constraint = 0~90˚; ball joint constraint = 0~85˚)

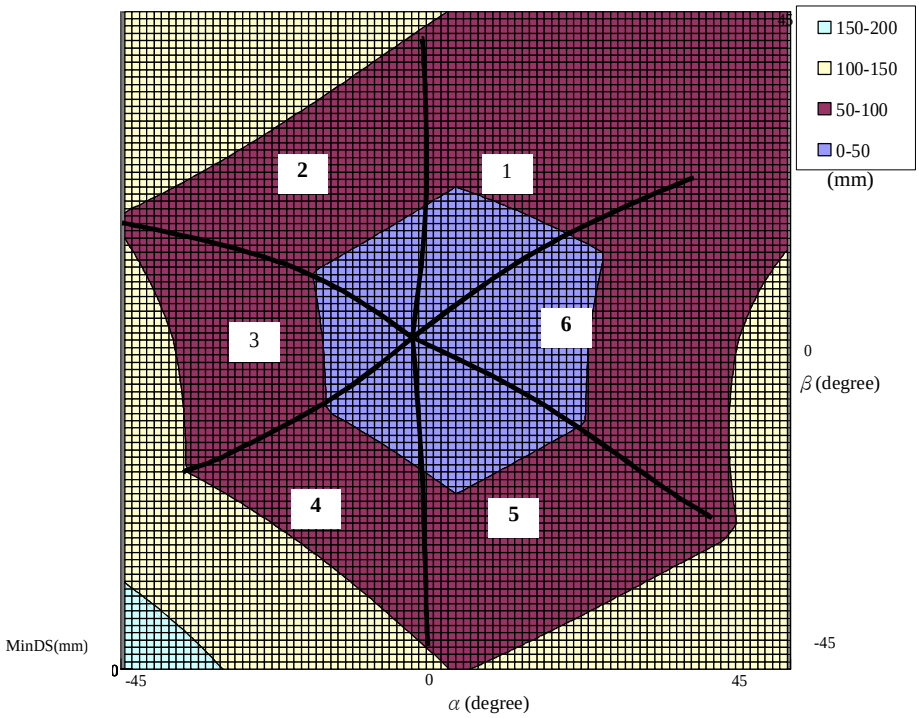

Figure 3-16b The top view of Figure 3-16a

The results of the optimized linkage length are displayed in Figure 3-17a. The workspace in Figure 3-17b is also divided into six regions. The six regions are labeled with characters from A to F. Each optimal value of the L/R ratio was found approaching to its upper bound value or lower bound value in each region. Region A: L/R = 2.02; Region B: L/R = 3.00; Region C: L/R = 2.02; Region D: L/R = 3.00; Region E: L/R = 2.02; Region F: L/R = 3.00. It is very interesting that the optimal values of the ratio L/R go toward the upper bound in regions B, D, F and the optimal values go toward the lower bound in regions A, C, E. These results imply that the optimal rotating positions of different regions need to be considered separately. Because the motion of the tool point will move across some regions for completing a mechanical part machining, the optimized workspace evaluation of the machine tool should take into consideration of all the possible regions during the machining.

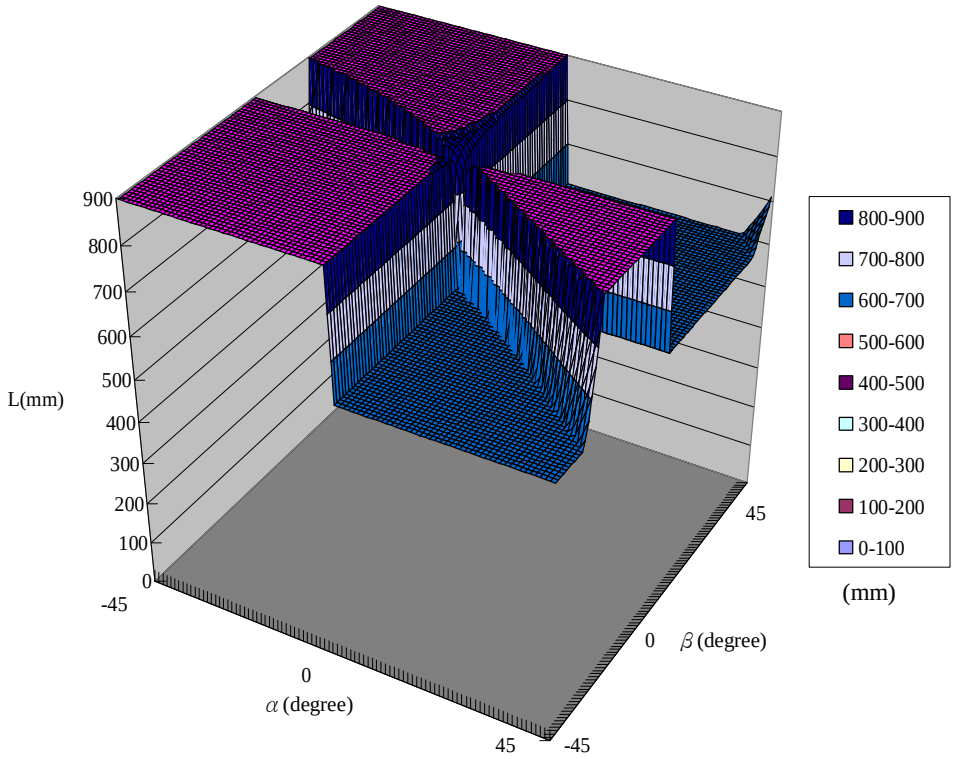

Figure 3-17**a** The optimum results for the parameter L. (computing parameters are the same with Figure 3-16a)

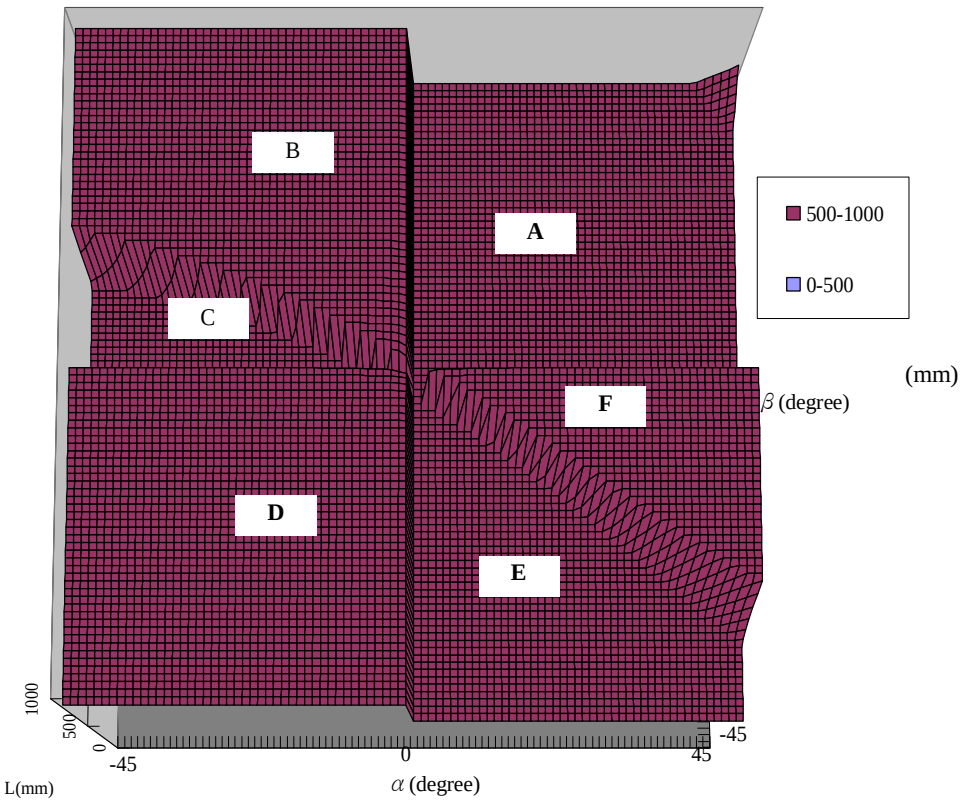

Figure 3-17 **(b)** The top view of the optimum results for the parameter L.

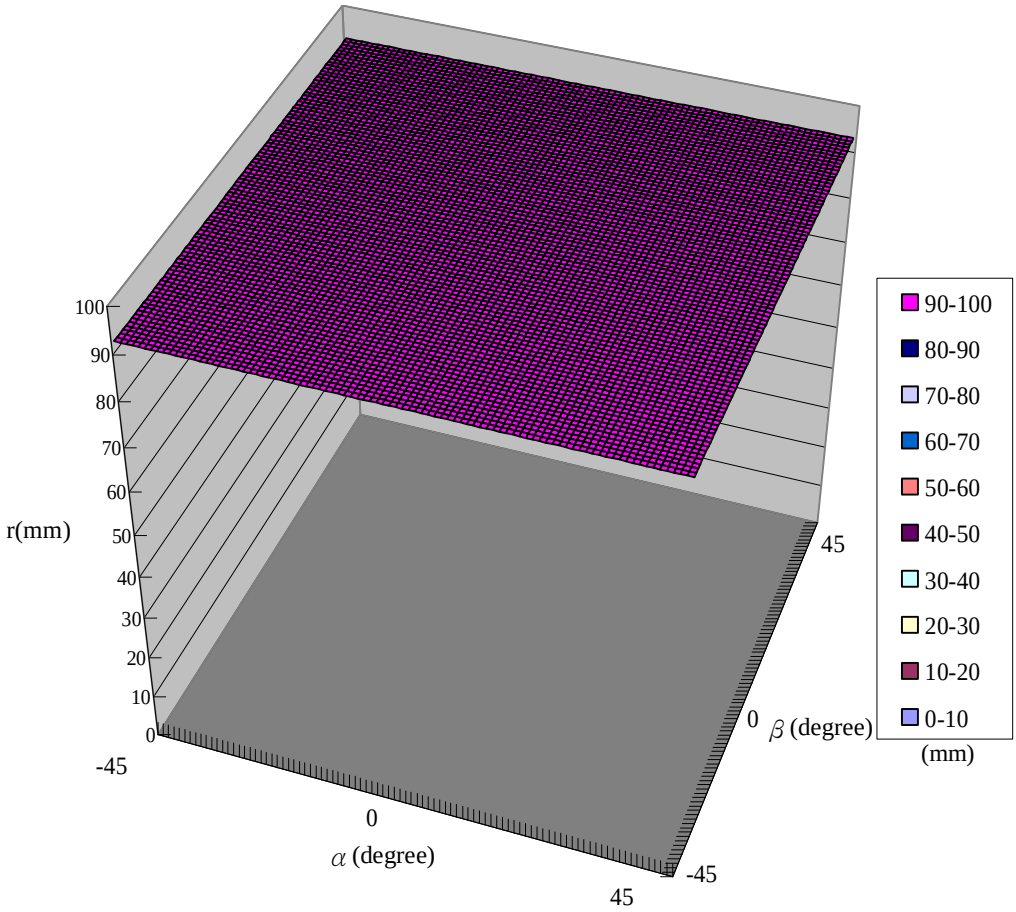

Figure 3-18 The optimum results for the parameter r. (computing parameters are the same with Figure 3-16a)

Figure 3-18 shows the optimization results of the ratio r/R. The optimal value of the ratio r/R approaches to the lower bound 0.31 within the domain $-45^{o} \le \alpha \le +45^{o}$, and $-45^{o} \le \beta \le +45^{o}$. This is the combination of (r = 93 mm, R = 300 mm). The results show that the smaller the tool frame radius, the better the design will be. This means that the larger (α, β) workspace can be created by using a smaller radius of the tool frame with the consideration of the constraints of mechanical components. The effects of the constraints of mechanical joints are to be further discussed in the following sections.

B. Dimensional optimization with joint constraints

In the previous calculation, the constraint of the pin joint is 90^0 and the constraint of the ball joint is 85^0. A hydrastatic ball joint is possible to reach the 85^0 rotation angle. However, it is difficult to manufacture and expensive. Therefore, the ball joint is decomposed into three pin joints in this research. It is possible and practical from the engineering viewpoint. Also, it is easy to be made and cost down. The optimization results will be verified again with the consideration of joint constraints. A set of parameters is selected for analysis as an illustration:

1. The radius R of the upper base frame is 300 mm.
2. Parameters α and β rotate between $\pm 45^0$.
3. The rotating-angle limitation of the pin joint is from 0^0 to 80^0.
4. The rotating-angle limitation of ball joint is from 0^0 to 30^0.
5. The height of the cutter Z is fixed at 2000 mm.
6. The ratio of (r/R) is limited by $0.31 \le (r / R) \le 0.8$.
7. In considering the reasonable dimensions of the machine tool, the ratio of (L/R) is set to be limited by $1.55 \le (L / R) \le 4.0$.

From Figure 3-19a, it is found that the rotating angle of the tool frame is limited by the joint constraints. The boundary of the circular block in Figure 3-19a is the extreme position of the machine tool motion. The results outside the circular block are the motion (of (α, β)) can not be reached under the consideration of the joints constraints. Some cross-sections of optimum results for different β are shown in Figure 3-19b. It is clearly seen that the (surface) slope of DS is divided into two regions. Compared with Figure 3-16, the concave results of the DS curve in Figure 3-19 can be deduced due to the effects of the joints constraints.

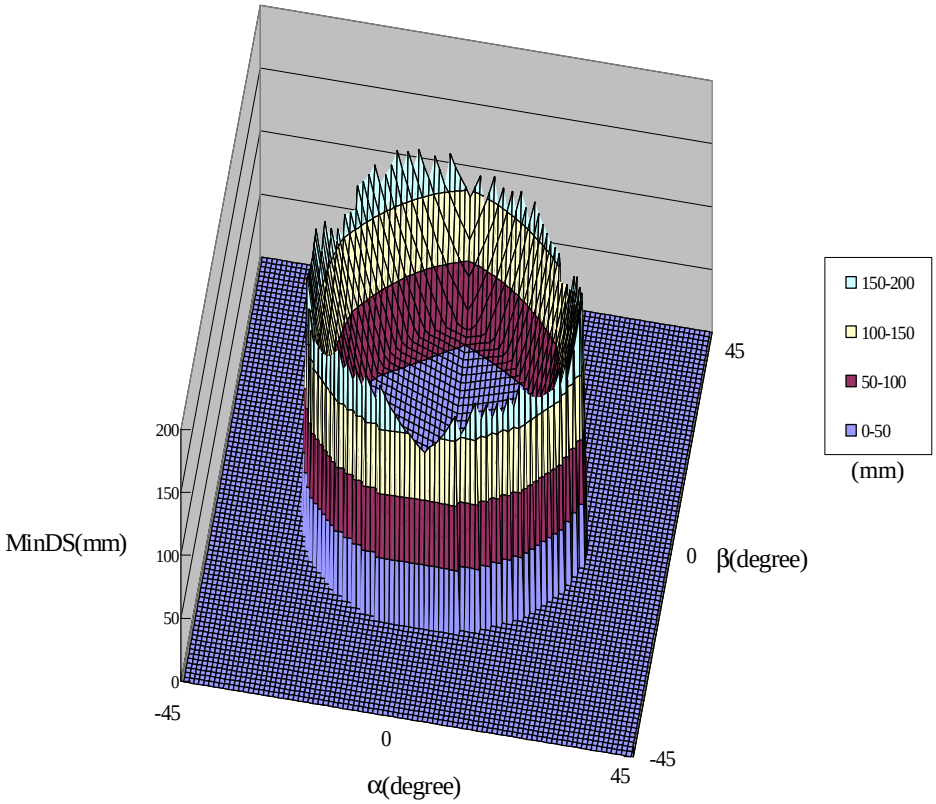

Figure 3-19a The optimum results for the parameter MinDS. (R = 300mm; r = 93~240mm; L = 465~1200mm; pin joint constraint = 0~80°; ball joint constraint = 0~30°)

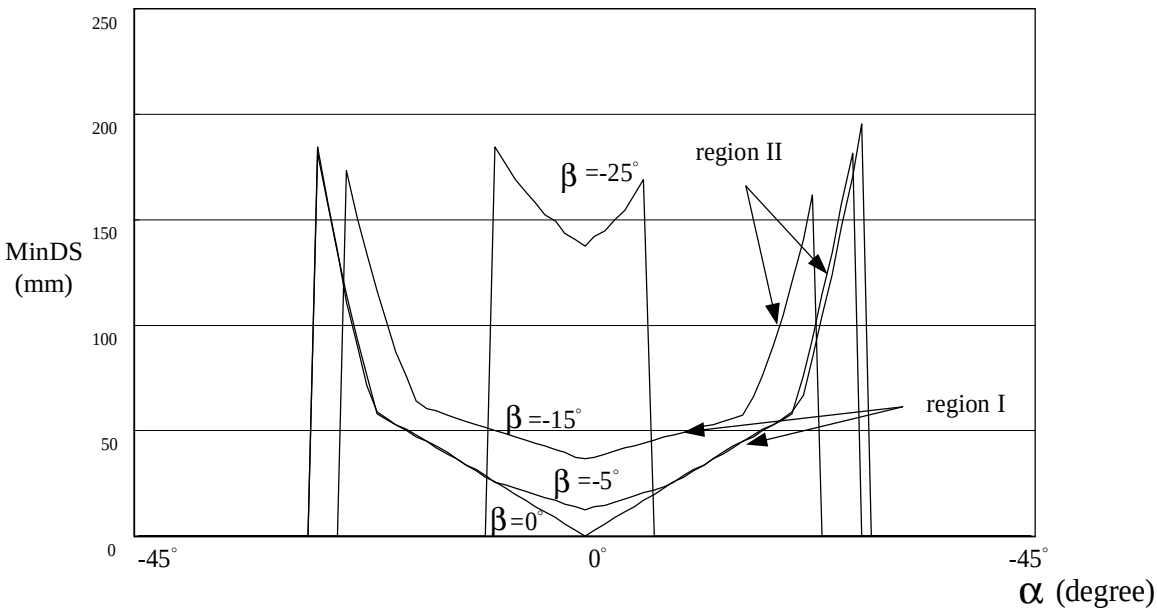

Figure 3-19b The MinDS optimum results of Figure 3-19a on the sections β= 0°, β= -5°, β= -15°, β= -25°.

Figure 3-20a shows the optimization results of the parameter r. The results in the region with smaller rotating angles (central part of the circular block) are similar to the results calculated without the joint constraints (see Figure 3-18). The optimal values of the parameter r are rapidly increased near the extreme position (outside circle edge) where is limited by the joint constraints. It can be seen from the relationship of the different cross section in Figure 3-20b. This is because larger tool frame (larger r) lead to smaller joint rotating angle with the same feed stroke variation, then it can satisfy the joint constraints easily. This can explain the results of the value of r raise up. In excess of the extreme position, however, any value of r in the calculation domain can not satisfy the joint constraints. The above results implies that the tool frame radius is as smaller as possible for a better design. After comparing the results with different constraints, it can be concluded that the increasing workspace is generated because of the larger (loosen) joint constraints.

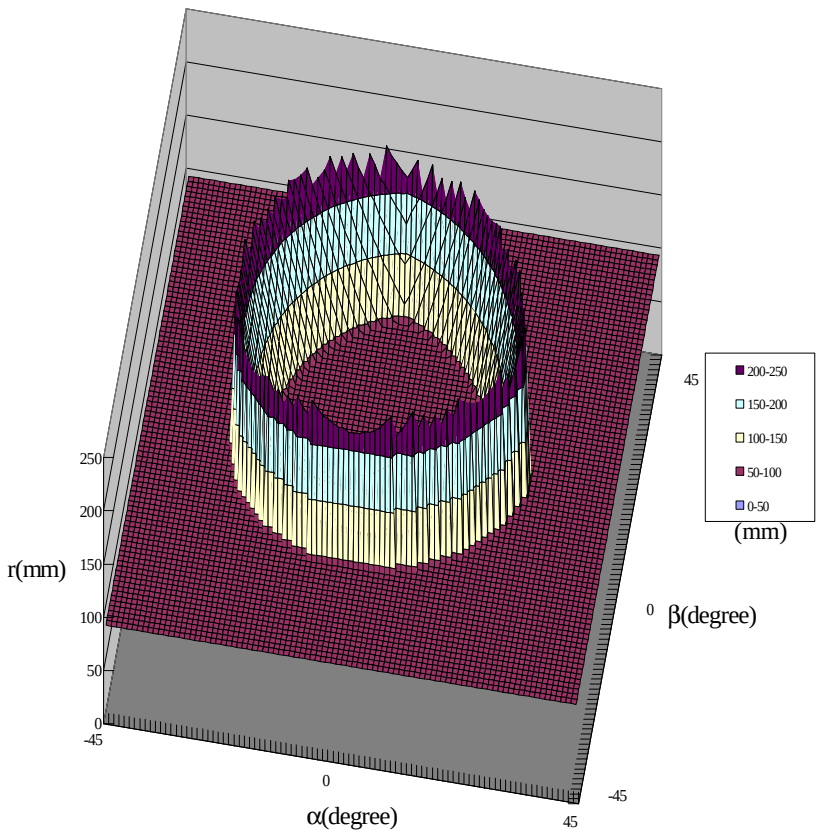

Figure 3-20a The optimum results for the parameter r. (computing parameters are the same with Figure 3-19a)

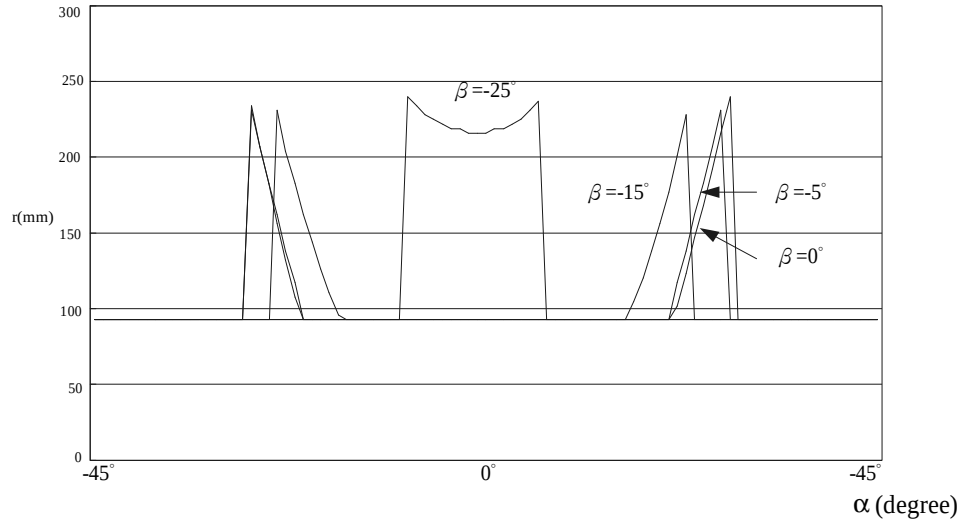

Figure 3-20b The optimum results on some sections (β= 0°, β= -5°, β= -15°, β= -25°) for the parameter r.

Figure 3-21 presents the optimum results of the parameter L. There are three regions approaching the (L) lower bound in the central part. The other parameters all approaching the upper bound. The reason may be caused by the longer linkage length with the same position parameters will lead to smaller rotating angle of the ball joint in geometry.

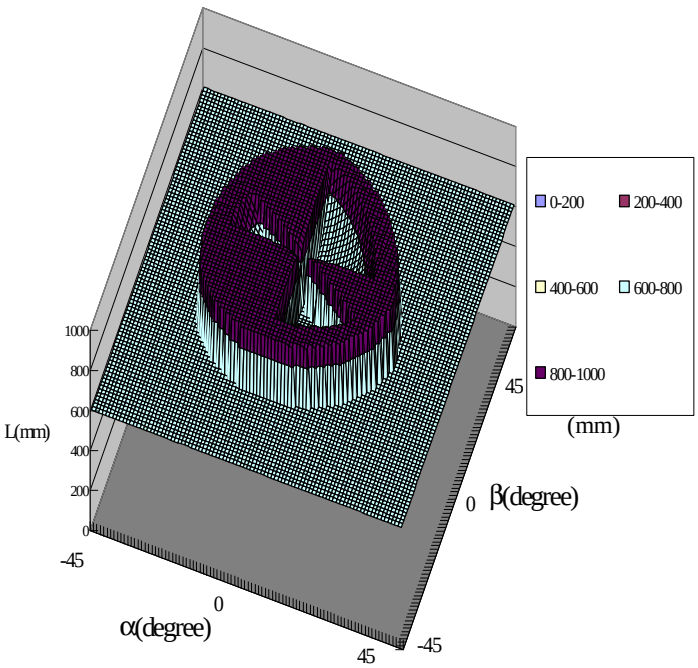

Figure 3-21 The optimum results for the parameter L. (computing parameters are the same with Figure 3-19 a)

Two sets of machine dimension parameters are selected for workspace analysis. The linkage length is given as 900 mm or 610 mm. The radius of the tool frame is 93 mm. The other parameters are set as those in the previous optimization. In Figure 3-22, the narrower workspace is constructed by (r/R, L/R) = (0.31, 2.03) and the wider workspace is constructed by (r/R, L/R) = (0.31, 3). Figure 3-22 shows the comparison result that one solid model is shifted to superpose on another solid model along the z-axis. For example, the two solid models are located at 573~1073 mm for ((r/R, L/R) = (0.31, 2.03)) and 876~1376 mm for ((r/R, L/R) = (0.31, 3)). The two solid models are then superposed together. The results of (L/R=2.03) and (L/R=3.0) are separately indicated in white and green color in Figure 3-22. The purpose of this work is to clearly compare the workspace with different design parameters. The results in Figure 3-22 are sufficient to explain the advantages of using the optimization.

It is surprising that the length distribution of the workspace along the z-axis is nearly the same with different kinematics parameters. The new algorithm for evaluation the optimization of workspace is then defined as the maximum area of the cross section α and β plane in the workspace. To further understand the effects of the parameters (r/R, L/R) on the length of workspace along the Z-axis, another parameters (r/R, L/R)=(0.67, 3.33), (r/R, L/R)=(0.67, 2.33) are selected for analysis. Two workspaces are given in Figure 3-23. It is again that the length of the workspaces along z-axis direction is almost the same, but the area of the cross section of the workspace is different. Two areas of the cross sections are approximately 14738 (deg^2) for (r/R, L/R) = (0.67, 2.33) mm and 18162 (deg^2) for (r/R, L/R) = (0.67, 3.33) mm, individually. The maximum area of the cross section of the workspace is the dominant cost function for the design parameter optimization. For the parameters given in Figure 3-19, the systematic analysis and comparison are performed with varied (r/R, L/R) ratio. It is found that the optimum results exist at (r/R, L/R) = (0.31, 3).

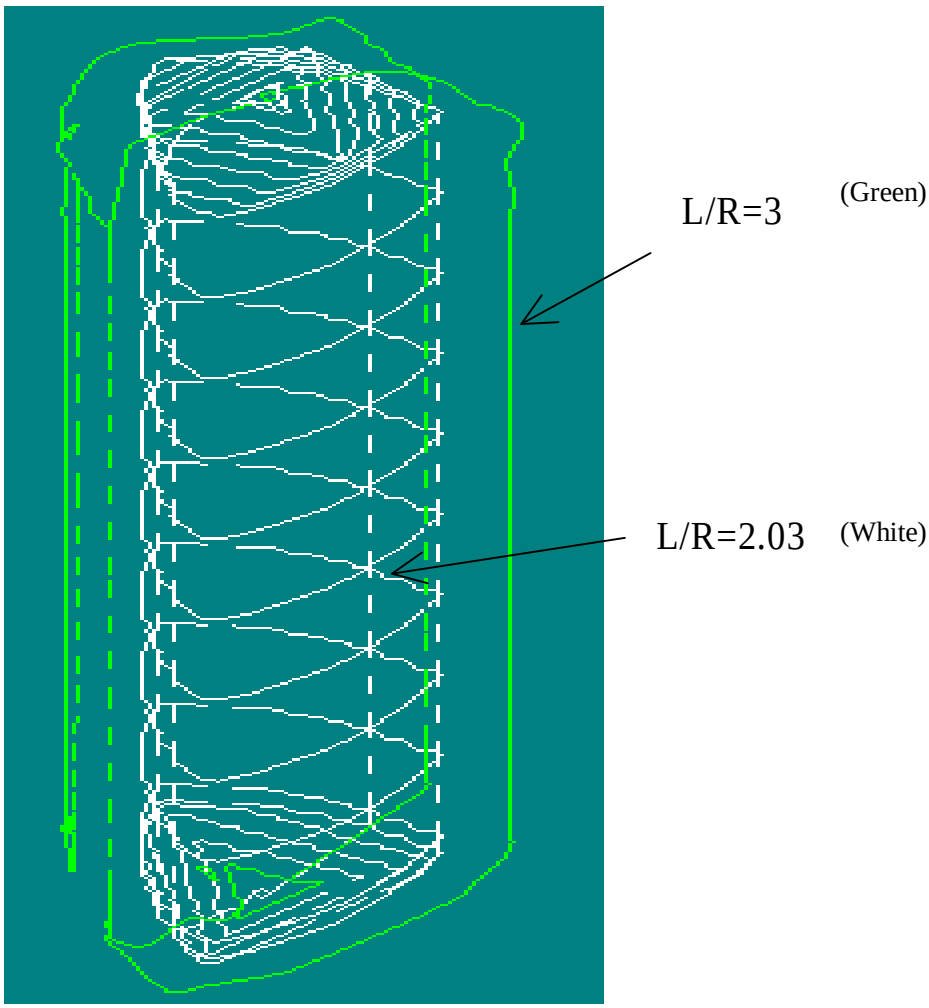

Figure 3-22 The angular workspace comparison of 3D wireframe model of L/R = 2.03 and L/R = 3.

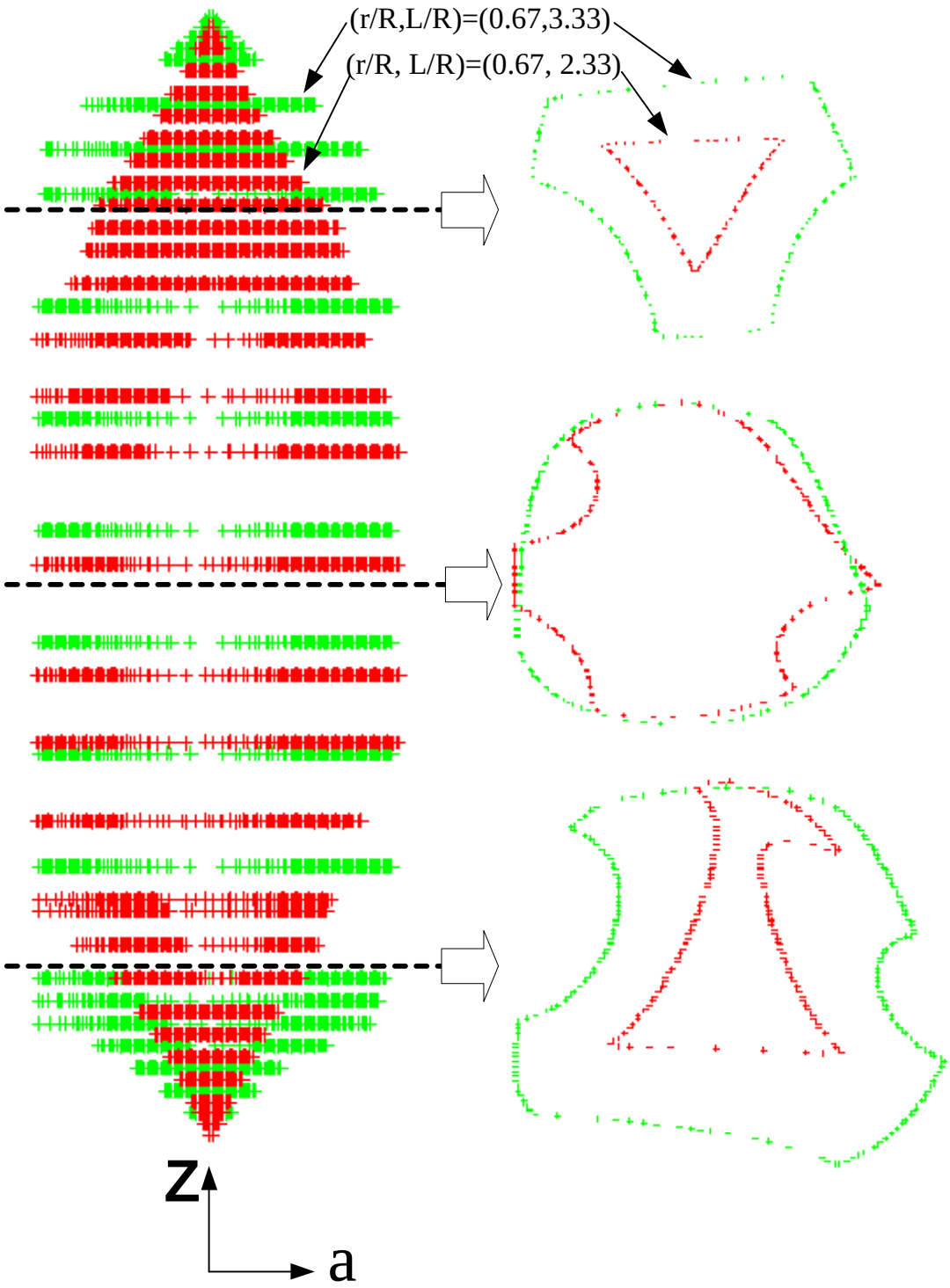

Figure 3-23 Two overlapped workspaces with parameters (r/R, L/R) = (0.67, 2.33) and (r/R, L/R) = (0.67, 3.33). (R = 300mm; feed stroke of ball screw = 0~500mm; pin joint constrain = 0~80°; ball joint constrain = 0~30°)

3.5 Conclusions

In this chapter, the method of Denavit-Hartenberg notation is adopted to define the geometric relation among the structure in the TRR-XY machine tool and then to derive the inverse kinematics solution.

An equivalent component method is addressed in this research to simplify the singularity analysis for a three DOF mechanism. An interesting result is concluded from the analysis of this chapter that the shorter link length with larger tool frame diameter has a relative smaller workspace and relative better independent degree of constraint.

A principle for the optimization of the design parameters of the parallel link machine tool is proposed in this chapter. A TRR-XY hybrid type parallel link machine tool is analyzed and discussed. From the analysis, one conclusion can be obtained that the larger area of the α and β plane is derived from the longer length of the linkage. The optimum design for the parallel link machine tool should consider the joint constraints. The joint constraints are found in the analysis to have large effects on the workspace. The cost function of the optimization should include the length of the workspace along the z-axis direction and the maximum area of the cross section on the α and β plane, simultaneously. In general, the optimal workspace can be obtained by using the smaller ratio of (radius of tool frame/radius of base frame) and the larger ratio of (length of linkage/radius of base frame). This conclusion seems very useful for the engineer to design a new PLM. From a viewpoint of practical development, the mechanical and control stiffness is an important factor to determine the size of machine. This topic is very essential and valuable for the applications of this machine tool into real machining. It worths a further investigation.

References

[1] Grübler,M., 1917, Getriebelehre, Springer-Verlag, Berlin.

[2] D. Stewart, A Platform with Six Degrees of Freedom, in Proceedings of the Institute of Mechanical Engineering, Vol. 180, No. 5, P.P. 371-386, 1965.

[3] W. Liu, C. D. Crane, and J. Duffy, Closed Form Forward Displacement Analysis of the 4-5 In-Parallel Platforms, ASME Journal of Mechanical Design Vol. 116, P.P. 47-55, 1994.

[4] B. Dasgupta and T. S. Mruthyunjaya, A Canonical Formulation of the Direct Position Kinematics Problem for a General 6-6 Stewart Platform, Mechanism and Machine Theory. Vol. 29, No. 6, P.P. 819-927, 1994.

[5] M. Raghavan, The Stewart Platform of General Geometry Has 40 Configurations, ASME Journal of Mechanical Design. Vol. 115 P.P. 277-282, 1993.

[6] C. W. Wampler, Forward Displacement Analysis of General Six-In-Parallel SPS (Stewart) Platform Manipulators Using Soma Coordinates, Mechanism and Machine Theory. Vol. 31, No. 3, P.P. 331-337, 1996.

[7] M. Griffis and J. Duffy, A Forward Displacement Analysis of a Class of Stewart Platforms, Journal of Robotic Systems.Vol. 6 P.P. 703-720, 1989.

[8] P. Nanua, K. J. Waldron and V. Murthy, Direct kinematics solution of a Stewart platform, IEEE Journal of Robotics and Au0tomation. Vol. 6, No. 4 P.P. 438-443, 1990.

[9] C. Innocenti and V. Parenti-Castelli, Direct position analysis of the Stewart platform mechanism, Mechanism and Machine Theory. Vol. 25, No. 6, P.P. 611-621, 1990.

[10] D. M. Ku, Direct displacement analysis of a Stewart platform mechanism, Mechanism and Machine Theory, Vol. 34, P.P. 453-465, 1999.

[11] K. H. Hunt and E. J. F. Primrose, Assembly Configurations of Some In-Parallel-Actuated Manipulators, Mechanism and Machine Theory. Vol. 28, No.1 P.P. 31-42, 1993.

[12] Z. J. Geng and L. S. Haynes, A "3-2-1" Kinematics Configuration of a Stewart Platform and Its Application to Six Degree of Freedom Pose Measurements, Robotics and Computer-Integrated Manufacturing. Vol. 11, No. 1 P.P. 23-34, 1994.

[13] M. Husian and K. J. Waldron, Direct Position Kinematics of the 3-1-1-1 Stewart Platform, ASME Journal of Mechanical Design. Vol. 166, P.P.1102-1107, 1994.

[14] H. Bruyninckx, Forward Kinematics for Hunt-Primrose Parallel Manipulators, Mechanism and Machine Theory. Vol. 34 P.P. 657-664, 1999.

[15] K. M. Lee and D. K. Shah, Kinematics Analysis of a Three Degree of Freedom In-Parallel Actuated Manipulator, IEEE Journal of Robotics and Automation. Vol. 4, No. 3 P.P. 354-360, 1988.

[16] K. J. Waldron, M. Raghavan and B. Roth, Kinematics of a Hybrid Series-Parallel Manipulation System, Journal of Dynamic Systems, Measurement and Control. Vol. 111, No. 2, P.P. 211-221, 1989.

[17] M. Husain and K. J. Waldron, Position Kinematics of a Three-Limbed Mixed Mechanism, ASME Journal of Mechanical Design. Vol. 116 , P.P. 924-929, 1994.

[18] Z. Huang, W. S. Tao and Y. F. Fang, Study on the Kinematics Characteristics of 3 DOF In-Parallel Actuated Platform Mechanism, Mechanism and Machine Theory. Vol. 31, No. 8, P.P. 999-1007, 1996.

[19] J. A. Carretero, R. P. Podhorodeski, M. A. Nahon, and C. M. Gosselin, Kinematics Analysis and Optimization of a New Three Degree-of-Freedom Spatial Parallel Manipulator, ASME Journal Mechanical Design. Vol. 122, No. 1, P.P. 17-24, 2000.

[20] Hartenberg, R., and Denavit, J., *Kinematics Synthesis of Linkages*. McGraw-Hill, New York., 1964

[21] K.H. Hint, "Special Configurations of Robot Arms via Screw Theory, Part 2: Available End-Effector Displacements, "Robotics, Vol. 5,pp.17~22, 1987a.

[22] E.F. Fichter, "A Stewart Platform-Based Manipulator: General Theory and

Practical Construction", The International Journal of Robotics Research, Vol. 5, No. 2, pp. 157-182, 1986.

[23] L.W. Tsai, "Robot Analysis The Mechanics of Serial and Parallel Manipulators", A Wiley-Interscience Publication, John Wiley & Sons, inc. 1999

[24] C. Gosselin, J. Angels, "Singularity Analysis of Closed-Loop Kinematics Chains". IEEE Transactions on Robotics and Automation, Vol. 6, No. 3, pp. 281-290, 1990.

[25] M.Z. Huang, S. H. Ling, Y. Sheng, "A Study of Velocity Kinematics for Hybrid Manipulators with Parallel-Series Configuration," Proceedings, 1993 IEEE International Conference on Robotics and Automations, pp. 456-461, 1993.

[26] K.-M. Lee, Shah, D. K., "Kinematics Analysis of a Three-Degrees-of-Freedom In-Parallel Actuated Manipulator", IEEE Journal of Robotics and Automation, Vol.4 No.3, pp. 354-360, 1988.

[27] Shi, X., Fenton, R. G.,1994, "A Complete and General Solution to the Forward Kinematics Problem of Platform-Type Robotic Manipulators", Proceedings of the 1994 IEEE, International Conference on Robotics and Automation, Los Alamitos, CA, USA, pp.3055-3062.

[28] L. M. Tosatti, , Bianchi, G., Fassi, I., Boer, C. R., Jovane, F., "An Integrated Methodology for the Design of Parallel Kinematics Machines(PKM)", Annals of the CIRP, Vol.46, pp.341-345, 1997.

[29] J. Wang,, "Workspace Evaluation and Kinematics Calibration of Stewart Platform", Ph.D. Dissertation Florida Atlantic University, 1992.

[30] Q. Y. Wang, H. Zou, M. Y. Zhao, Q. M. Li, H. W. Zheng, "Design and Kinematics of a Parallel Manipulator for Manufacturing", Annals of the CIRP, Vol.46, pp.297-300, 1997.

Chapter 4 Inverse dynamic analysis for driving force variation

4.1 Introduction

In general, the geometry of the machine tool (tool platform size relative to base size) has significant affects on the required actuator driving force for driving a PLM. Therefore, a dynamic analysis and modeling of the PLM to take full advantage of the geometry and size, in order to minimize the actuator driving force and increase the machining efficiency, is very interesting and is focused on this research. For high-speed and high-payload machining processes, this subject becomes even more important.

In developing dynamic equations for parallel mechanisms, the Newton-Euler and Euler-Lagrange formulations are the two common adopted approaches. Utilization of the Newton-Euler approach to parallel mechanisms normally leads to a large number of equations [1-3]. Do and Yang [2] claimed that if a proper sequence is taken, the number of equations of motion for the Stewart platform can be reduced to six for solving the inverse dynamic problem. The Euler-Lagrange approach has been applied to obtain the dynamic equations for parallel mechanisms [4-9]. Because of the numerous constraints imposed by closed loops of a parallel manipulator, additional coordinates along with a set of Lagrangian multipliers are often introduced. It is worthy noted that in general the development of dynamic equations for parallel mechanisms are more straightforward in task-space than in joint space because the inverse kinematics problems are easier to solve. However, it might not be applicable to the 3-PRS mechanism. The dynamic equations that utilize coordinates in task-space are very complicated [10].

To design platforms with good dynamic performance and to fully understanding the dynamic behavior of the machine tool, simply using numerical solutions is not enough and an analytical dynamic equation of motion is required.

Machining efficiency is the ratio of the input actuator driving force to the payload or external cutting force. Therefore, the analysis of the driving force variation is very important for understanding the machining performance of the developed machine tool system.

4.2 Inverse dynamic model

4.2.1 Assumptions

Due to the complexity of the mechanical structure, the mathematical models of the dynamic cutting behavior are too complicated to be completely solved with all the coefficients considered. The following assumptions are used in this research to simplify the analysis intricacy:

a. The friction force is neglected.

b. All the components and links are rigid.

c. The thermal expansion of component is not considered.

The above assumptions may be unreasonable from the practical dynamics point of view. However, the purpose of this chapter is focussed on the analysis of driving force variation using inverse dynamic concept. The required driving forces are obviously much larger than the friction forces. Also, the inertia forces are much larger than the friction forces. Therefore, the neglect of the friction force in the analysis is reasonable here. The component deformation and thermal expansion are not important for the driving force analysis. But, they are very important for the analysis of machining accuracy issues.

4.2.2 Position analysis using D-H notation

4.2.2.1 Cutting location based on part surface coordinate

The coordinate transformation matrix from the upper base $(XYZ)_0$ coordinate to

working coordinate $(XYZ)_W$ and to part surface local coordinate $(XYZ)_L$ and to cutting location coordinate $(XYZ)_t$ can be given as follows (see Figure 4-1a):

$$\underline{\underline{A}}_t^0 = \underline{\underline{A}}_W^0 \underline{\underline{A}}_L^W \underline{\underline{A}}_t^L \tag{4-1}$$

The coordinate of a part surface related to working coordinate $(XYZ)_W$ that can be obtained from a CAD model. The relationship for $(XYZ)_W$ referring to $(XYZ)_0$ can be given as:

$$\underline{\underline{A}}_W^0 = \underline{\underline{Trans}}(\underline{P_{O_0O_W}}) = \begin{bmatrix} \mathbf{I3} \\ 1 \end{bmatrix} \cdot \begin{bmatrix} \mathbf{I3} & \underline{P_{O_0O_W}} \end{bmatrix}, \quad \mathbf{I3} = \begin{bmatrix} 1 & 0 & 0 \\ 0 & 1 & 0 \\ 0 & 0 & 1 \end{bmatrix} \tag{4-2}$$

Here, $\underline{P_{O_0O_W}} = \mathrm{OWx}\underline{\mathrm{i}}_0 + \mathrm{OWy}\underline{\mathrm{j}}_0 + \mathrm{OWz}\underline{\mathrm{k}}_0$ is the distance between the origin of $(XYZ)_W$ and the origin of $(XYZ)_0$. For a part surface to be cut, a cutter location source file (CLSF) is normally generated by commercial CAD/CAM software. The information of cutter location data [x y z i j k] is usually included in the CLSF, based on the part surface local coordinate system $(XYZ)_L$. Here, the x, y, z, represent the position of CP (cutting point). The i, j, k, represent the direction of normal vector of the part surface, referring to the frame $(XYZ)_W$, in other words, i, j, k represent the orientation of $\underline{\mathrm{k}}_L$. From Figure 4-1a, the transformation matrix between $(XYZ)_L$ and $(XYZ)_W$ can be given as:

$$\underline{\underline{A}}_L^W = \begin{bmatrix} \mathbf{I3} \\ 1 \end{bmatrix} \cdot \begin{bmatrix} \underline{i_L} & \underline{j_L} & \underline{k_L} & \underline{P_{WL}} \end{bmatrix} \tag{4-3}$$

In the above equation, $\underline{j_L}$ is the unit vector of the feed direction at the cutting point, and $\underline{k_L}$ is the unit vector of the normal direction of the part surface. $\underline{k_L}$ = $i\,\underline{i_W} + j\,\underline{j_W} + k\,\underline{k_W}$. $\underline{P_{WL}} = x\,\underline{i_W} + y\,\underline{j_W} + z\,\underline{k_W}$ represents the distance between the origin of $(XYZ)_L$ to the origin of $(XYZ)_W$.

a.

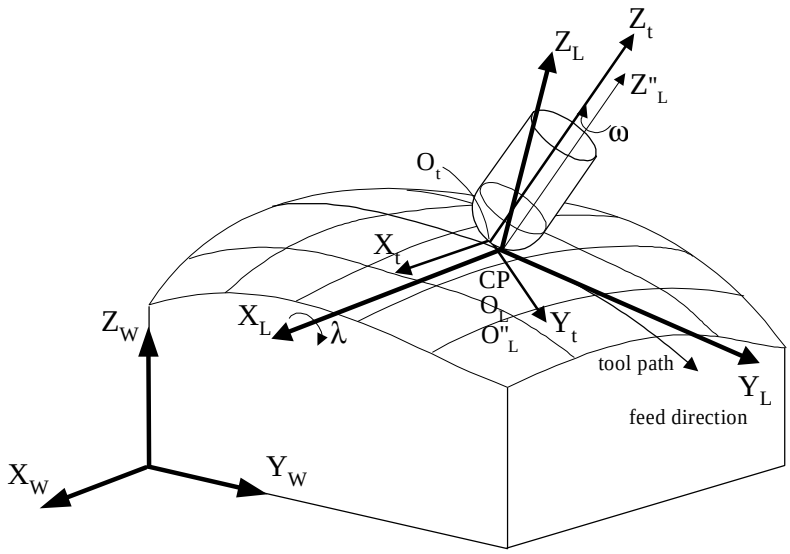

b.

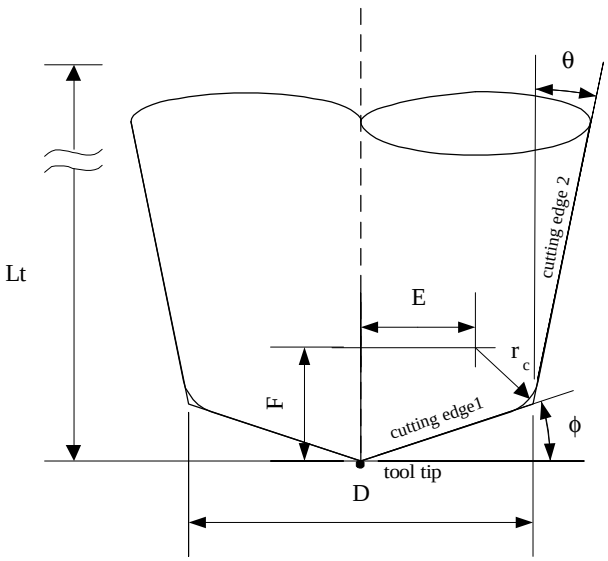

Parameters	Physical definition
D	Tool radius
r_c	Radius of cutting edge
E	Horizontal distance
F	Vertical distance
ϕ	Horizontal angle of cutting edge 2
θ	Vertical angle of cutting edge 1
Lt	Tool length

c.

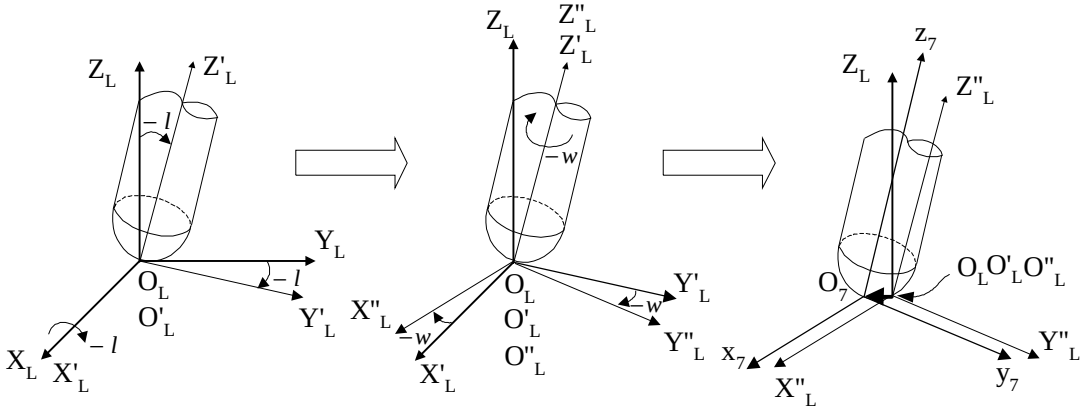

d.

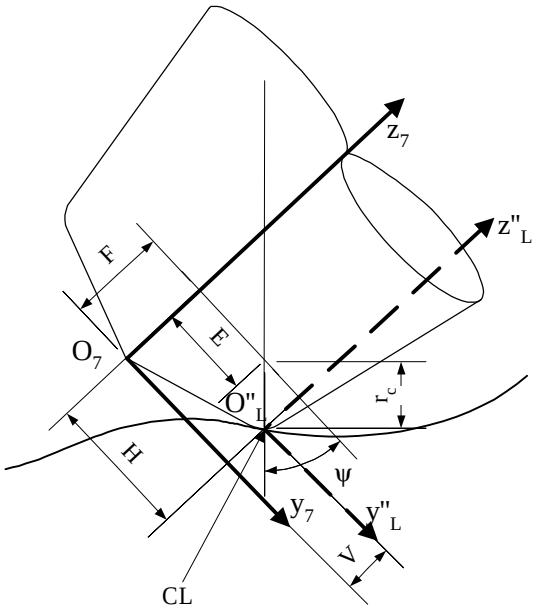

$$A^{L"}{}_7 = \begin{bmatrix} 1 & 0 & 0 & 0 \\ 0 & 1 & 0 & -H \\ 0 & 0 & 1 & -V \\ 0 & 0 & 0 & 1 \end{bmatrix}$$

$$H = E + r_C \cos\psi$$

$$V = F - r_C \sin\psi$$

$(XYZ)_t$: tool coordinate;

$(XYZ)_L$: local coordinate of part surface

$(XYZ)"_L$: coordinate system after the yaw angle and tilt angle transformation

CP: cutting point. Y_L: feed direction. Z_t: tool axis.

O_L is the coordinate system after the yaw angle ω, and tilt angle λ transformation

Ψ: angle of cutting point

Figure 4-1 (a) Non-normal direction cutting

(b) Tool parameters definition of DIN66215 (1987) standard

(c) Angle transformation of a non-normal direction cutting

(d) Coordinate system translation using parametric tool definition

To increase the usability, a parametric tool definition (DIN66215, 1987) is introduced in this research [11]. The parametric tool definition is given in Figure 4-1b. There are seven parameters included in this tool definition. The physical meaning of these seven parameters is also displayed in Figure 4-1b. Figure 4-1a shows the geometric relationship of non-normal cutting. Figure 4-1c shows the angle transformation of non-normal direction cutting. Figure 4-1d shows the coordinate translation using parametric tool definition. In Figure 4-1a, $(XYZ)_t$ is cutting location coordinate and $(XYZ)_L$ is local coordinate of part surface. $(XYZ)''_L$ is the coordinate system after the yaw angle and tilt angle transformation, and CP is the cutting point. Y_L is the feed direction and Z_t is the cutter axis. In Figure 4-1c, O_L is the coordinate system after the yaw angle (ω), and tilt angle (λ) transformation. In Figure 4-1d, the transformation matrix for non-normal cutting between coordinate $(XYZ)_t$ and $(XYZ)_L$, can be given as follows:

$$\underline{\underline{A}}_t^L = \text{Rot}(X_L, \lambda)\ \text{Rot}(Z'_L, \omega)\ \text{Trans}(0, -H, -V) \tag{4-4}$$

In the above equation,

$$H = E + r_C \cos\psi$$
$$V = F - r_C \sin\psi \tag{4-5}$$

4.2.2.2 Cutter location based on upper base coordinate

The frame $(XYZ)_7$ must be described with respect to the frame $(XYZ)_0$. Using the definition of Z-Y-Z Euler angles [11], the frame $(XYZ)_7$ can be described as follows: (1). The frame $(XYZ)_7$ is firstly assumed to be coincident with the frame $(XYZ)_0$. (2). Rotate $(XYZ)_7$ about $\hat{\underline{Z}}_7$ by an angle α, then rotate about $\hat{\underline{Y}}_7$ by an angle β and

rotate about $\hat{\underline{Z}}_7$ by an angle γ. (3). Let $\underline{P}_{07} = Px_7\,\underline{i}_0 + Py_7\,\underline{j}_0 + Pz_7\,\underline{k}_0$ represent the distance between the origin of $(XYZ)_7$ and the origin of $(XYZ)_0$. In this representation, each rotation is performed about an axis of the moving coordinate $(\hat{X}\hat{Y}\hat{Z})_7$, rather than the fixed reference, $(XYZ)_7$. Such a set of three rotations is called Euler angles. Note that each rotation takes place about an axis whose location depends upon the preceding rotation result. Because the three rotations occur about the axes $\hat{\underline{Z}}_7$, $\hat{\underline{Y}}_7$ and $\hat{\underline{Z}}_7$, we will call this representation Z-Y-Z Euler angles. We have:

$$\underline{\underline{T}}_7^0 = \underline{\underline{T}}\text{rans}\,(Px_7, Py_7, Pz_7)\,\underline{\underline{R}}\text{ot}\,(\hat{\underline{k}}_7, \alpha)\,\underline{\underline{R}}\text{ot}\,(\hat{\underline{j}}_7, \beta)\,\underline{\underline{R}}\text{ot}\,(\hat{\underline{k}}_7, \gamma) \tag{4-6}$$

When the surface of a part has been cut, the cutter coordinate $(XYZ)_7$ will coincide with the cutting location coordinate $(XYZ)_t$. From Eq.(4-2)~(4-4) and Eq.(4-6), we then have:

$$\underline{\underline{T}}_7^0 = \underline{\underline{A}}_W^0\,\underline{\underline{A}}_L^W\,\underline{\underline{A}}_t^L \tag{4-7}$$

Comparing the components of both sides of the above equation, the Px_7, Py_7, Pz_7, α, β, γ can be solved. The Px_7, Py_7, Pz_7, α, β, γ are the parameters that define the location and orientation of the cutter referred to the $(XYZ)_0$ coordinate. This means that the generated cutter location data, [x y z i j k], from a commercial CAD/CAM software, can be used to solve the geometric relationship between coordinate system $(XYZ)_7$ and $(XYZ)_0$.

4.2.3 Derivation of joint states $\underline{q}$, $\dot{\underline{q}}$, $\ddot{\underline{q}}$

In the C chain, a vector $\underline{P}$ is used to represent the position of origin of coordinate $(XYZ)_{C6}$. The "C chain" is a kinematic chain of the machine tool defined in Figure 4-2. The direction of $\underline{k}_{C6}$ is coincident with $\underline{k}_7$. Here, $\underline{k}_{C6}$ is the z-axis unit vector of coordinate $(XYZ)_{C6}$ and $\underline{k}_7$ is the z-axis unit vector of coordinate $(XYZ)_7$. This also means that $\underline{k}_{C6}$ is the direction of the cutter axis.

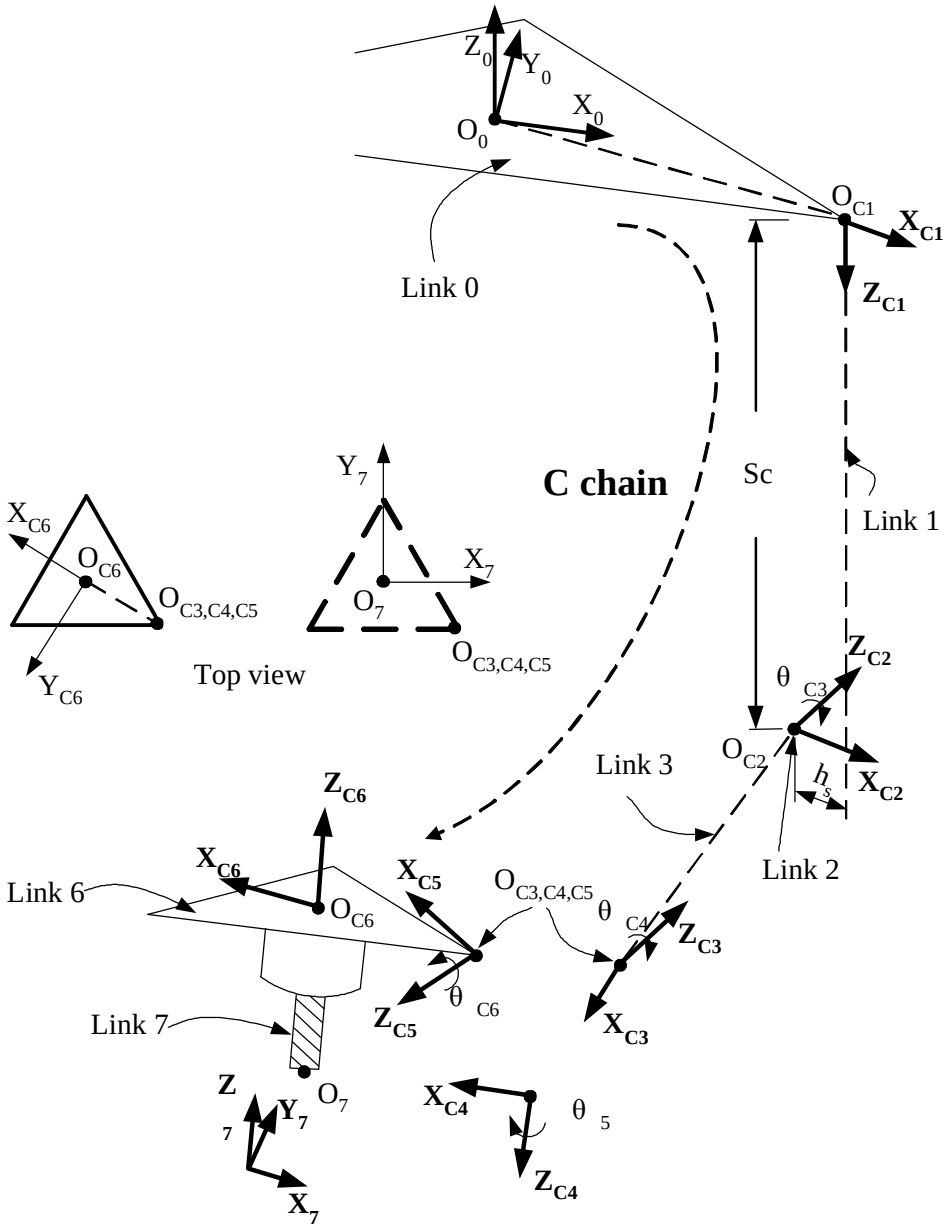

Figure 4-2 Coordinate system definition for D-H notation method

$$\underline{P} = [Px_6 \quad Py_6 \quad Pz_6]^T \tag{4-8}$$

Where,

$$[Px_6 \quad Py_6 \quad Pz_6 \quad 0]^T = \underline{\underline{T}}_7^0 (\underline{\underline{A}}_7^6)^{-1} [0 \quad 0 \quad 0 \quad 1]^T . \tag{4-9}$$

Here, $\underline{\underline{A}}_7^6$ is defined as the definition given in Table 3-1 and Eq.4-1. The angular position of a joint can be solved using inverse kinematic theory. The inverse kinematic solution is well developed and will not be discussed here. We define joint space $\underline{q}_i$ (i = A, B, C) as:

$$\underline{q}_i = [\theta_{i1} \quad S_i \quad \theta_{i3} \quad \theta_{i4} \quad \theta_{i5} \quad \theta_{i6}]^T \tag{4-10}$$

In the above equation, S_i is the motion distance of the pin joint. In the case of a revolute joint, θ_i is the rotation angle. Using the Manipulator Jacobian theorem [9] and the results in Eq.(4-8) and Eq.(4-10), we have:

$$\dot{\underline{P}} = \underline{\underline{J}} \cdot \dot{\underline{q}} \quad , \text{or} \quad \dot{\underline{q}} = \underline{\underline{J}}^{-1} \dot{\underline{P}} \tag{4-11}$$

For C chain, in the above equation, $\dot{\underline{q}}$ is the (angular) velocity of the components. We have:

$$\dot{\underline{P}} = \begin{bmatrix} \underline{V}_e \\ \underline{\omega}_e \end{bmatrix} = \begin{bmatrix} \delta Px_6 \\ \delta Py_6 \\ \delta Pz_6 \\ \delta \Phi x_6 \\ \delta \Phi y_6 \\ \delta \Phi z_6 \end{bmatrix}, \quad \underline{\underline{J}} = \begin{bmatrix} \frac{\partial Px_6}{\partial \theta_1} & \frac{\partial Px_6}{\partial \theta_2} & \frac{\partial Px_6}{\partial \theta_3} & \frac{\partial Px_6}{\partial \theta_4} & \frac{\partial Px_6}{\partial \theta_5} & \frac{\partial Px_6}{\partial \theta_6} \\ \frac{\partial Py_6}{\partial \theta_1} & \frac{\partial Py_6}{\partial \theta_2} & \frac{\partial Py_6}{\partial \theta_3} & \frac{\partial Py_6}{\partial \theta_4} & \frac{\partial Py_6}{\partial \theta_5} & \frac{\partial Py_6}{\partial \theta_6} \\ \frac{\partial Pz_6}{\partial \theta_1} & \frac{\partial Pz_6}{\partial \theta_2} & \frac{\partial Pz_6}{\partial \theta_3} & \frac{\partial Pz_6}{\partial \theta_4} & \frac{\partial Pz_6}{\partial \theta_5} & \frac{\partial Pz_6}{\partial \theta_6} \\ \frac{\partial \Phi x_6}{\partial \theta_1} & \frac{\partial \Phi x_6}{\partial \theta_2} & \frac{\partial \Phi x_6}{\partial \theta_3} & \frac{\partial \Phi x_6}{\partial \theta_4} & \frac{\partial \Phi x_6}{\partial \theta_5} & \frac{\partial \Phi x_6}{\partial \theta_6} \\ \frac{\partial \Phi y_6}{\partial \theta_1} & \frac{\partial \Phi y_6}{\partial \theta_2} & \frac{\partial \Phi y_6}{\partial \theta_3} & \frac{\partial \Phi y_6}{\partial \theta_4} & \frac{\partial \Phi y_6}{\partial \theta_5} & \frac{\partial \Phi y_6}{\partial \theta_6} \\ \frac{\partial \Phi z_6}{\partial \theta_1} & \frac{\partial \Phi z_6}{\partial \theta_2} & \frac{\partial \Phi z_6}{\partial \theta_3} & \frac{\partial \Phi z_6}{\partial \theta_4} & \frac{\partial \Phi z_6}{\partial \theta_5} & \frac{\partial \Phi z_6}{\partial \theta_6} \end{bmatrix},$$

$$\underline{q} = \begin{bmatrix} 0 \\ V_c \\ w_{c3} \\ w_{c4} \\ w_{c5} \\ w_{c6} \end{bmatrix}$$

(4-12)

The derivative of Eq.(4-11) with respect to time can be obtained as:

$$\ddot{\underline{P}} = \dot{\underline{\underline{J}}}\dot{\underline{q}} + \underline{\underline{J}}\ddot{\underline{q}} \quad \text{, or} \quad \ddot{\underline{q}} = \underline{\underline{J}}^{-1}\ddot{\underline{P}} - \underline{\underline{J}}^{-1}\dot{\underline{\underline{J}}}\dot{\underline{q}} \tag{4-13}$$

In the above equation, $\ddot{\underline{q}}$ is the (angular) acceleration. We have,

$$\ddot{\underline{q}} = \begin{bmatrix} 0 \\ a_c \\ a_{c3} \\ a_{c4} \\ a_{c5} \\ a_{c6} \end{bmatrix} \qquad \ddot{\underline{P}} = \begin{bmatrix} \dot{\underline{V}}_e \\ \dot{\underline{\omega}}_e \end{bmatrix} \qquad \dot{\underline{\underline{J}}} = \frac{\partial \underline{\underline{J}}}{\partial t} \tag{4-14}$$

From the above discussions, it is obvious that the locations, velocities and accelerations

of the joints ($\underline{q}$, $\dot{\underline{q}}$, $\ddot{\underline{q}}$) can be calculated from the CAD data [x y x i j k] of a part surface, that can be generated by a commercial CAD/CAM software.

4.2.4 External forces exerted on tool platform

The force exerted on the cutter at the cutting point is set as $\underline{F}_{CP} = Fx_{CP}\,\underline{i}_0 + Fy_{CP}\,\underline{j}_0 + Fz_{CP}\,\underline{k}_0$ in this research. In the Jacobian matrix derivation, the tool platform is considered as the end effector and the endpoint is the centroid of the tool platform. Therefore, $\underline{F}_{CP}$ must be transferred into a form with external force $\underline{F}_{ext}$. Here, $\underline{F}_{ext}$ is the external force and external moment applied on the origin of $(XYZ)_6$.

$$\underline{F}_{ext} = \begin{bmatrix} \underline{f}_{ext} & \underline{m}_{ext} \end{bmatrix}^T = \begin{bmatrix} F_{xext} & F_{yext} & F_{zext} & M_{xext} & M_{yext} & M_{zext} \end{bmatrix}^T \tag{4-15}$$

In the above equation, $\underline{f}_{ext} = \underline{F}_{CP}$, $\underline{m}_{ext} = \underline{r}_{6,L} \times \underline{F}_{CP}$ and, $\underline{r}_{6,L}$ is the distance between $(XYZ)_L$ and $(XYZ)_6$ referred to $(XYZ)_0$. We have, $\underline{r}_{6,L} = (Px_L - Px_6)\,\underline{i}_0 + (Py_L - Py_6)\,\underline{j}_0 + (Pz_L - Pz_6)\,\underline{k}_0$.

4.2.5 Lagrange equations for the PLM

Here, the force applied on tool platform from ball joints, $\underline{F}_{ball}$, and the torque required $\underline{\tau}$ will be derived by using the well-known Lagrange equations [9,12]. We have:

$$\sum_{j=1}^{n} H_{ij}\ddot{q}_j + \sum_{j=1}^{n}\sum_{k=1}^{n} h_{ijk}\dot{q}_j\dot{q}_k + G_i = Q_i \qquad i=1,2,\ldots\ldots,n \tag{4-16}$$

In the above equation,

$\underline{\underline{H}}(\underline{q})$: is a 6×6 configuration-dependent positive-definite symmetric matrix for inertia torques and interaction torques.

$h_{ijk}\dot{q}_j\dot{q}_k$: the Coriolis forces and centrifugal forces

$\underline{G}(\underline{q})$: gravity torques

$\underline{Q}$: all non-conservative generalized forces.

$\dot{\underline{q}}$, $\ddot{\underline{q}}$: are defined by Eqs.12~14.

n : the number of links.

The calculations of $\underline{\underline{H}}(\underline{q})$, $\sum_{j=1}^{n}\sum_{k=1}^{n}h_{ijk}\dot{q}_j\dot{q}_k$, $\underline{G}$, $\underline{Q}$ are shown in follows.

The $\underline{\underline{H}}(\underline{q})$ in Eq.(4-16) can be computed as follows:

$$\underline{\underline{H}}(\underline{q}) = \sum_{i=1}^{6}\left[m_i(\underline{\underline{J}}_L^{(i)})^T\underline{\underline{J}}_L^{(i)} + (\underline{\underline{J}}_A^{(i)})^T\underline{\underline{I}}_i\underline{\underline{J}}_A^{(i)}\right] \qquad \text{(a1)}$$

In the above equation,

$$\underline{J}_{Lj}^{(i)} = \begin{cases} \underline{b}_{j-1} & \text{, for prismatic joints} \\ \underline{b}_{j-1}\times\underline{r}_{j-1,ci} & \text{, for revolute joints} \end{cases},$$

$$\underline{J}_{Aj}^{(i)} = \begin{cases} 0 & \text{, joint j = prismatic} \\ \underline{b}_{j-1} & \text{, joint j = revolute} \end{cases}, \qquad j = 1, 2,\ldots\ldots, i \qquad \text{(a2)}$$

where $\underline{r}_{j-1,ci}$ is the position vector of the centroid of link i referred to the origin of coordinate $(XYZ)_{j-1}$, and $\underline{b}_{j-1}$ is the 3×1 unit vector along joint axis j-1.

The $\sum_{j=1}^{n}\sum_{k=1}^{n} h_{ijk}\dot{q}_j\dot{q}_k$ i, j, k = 1, 2, ……,6 can be calculated as follows:

$$h_{ijk} = \frac{\partial H_{ij}}{\partial q_k} - \frac{1}{2}\frac{\partial H_{jk}}{\partial q_i}$$

When i = 1~6, the Eq.a3 can be displayed as follows:

$$\begin{aligned}
h_{1jk} &= \frac{\partial H_{1j}}{\partial q_k} - \frac{1}{2}\frac{\partial H_{jk}}{\partial q_1} \\
h_{2jk} &= \frac{\partial H_{2j}}{\partial q_k} - \frac{1}{2}\frac{\partial H_{jk}}{\partial q_2} \\
h_{3jk} &= \frac{\partial H_{3j}}{\partial q_k} - \frac{1}{2}\frac{\partial H_{jk}}{\partial q_3} \\
h_{4jk} &= \frac{\partial H_{4j}}{\partial q_k} - \frac{1}{2}\frac{\partial H_{jk}}{\partial q_4} \\
h_{5jk} &= \frac{\partial H_{5j}}{\partial q_k} - \frac{1}{2}\frac{\partial H_{jk}}{\partial q_5} \\
h_{6jk} &= \frac{\partial H_{6j}}{\partial q_k} - \frac{1}{2}\frac{\partial H_{jk}}{\partial q_6}
\end{aligned} \qquad \text{(a4)}$$

Where, H_{ij} is the i-th row and j-th column component of $\underline{\underline{H}}(\underline{q})$.

The $\underline{G} = [G_1 \quad G_2 \quad G_3 \quad G_4 \quad G_5 \quad G_6]^T$ can be calculated from the following relationship.

$$G_i = -\sum_{j=1}^{6} m_j \cdot \underline{g}^T J_{Li}^{(j)} \qquad i=1,2,\ldots\ldots,6 \qquad \text{(a5)}$$

Where, $\underline{g} = [0 \quad 0 \quad -g]^T$ is the gravitational acceleration. When i > j, $J_{Li}^{(j)} = 0$.

The $\underline{Q}$ in Eq.(4-16) can be calculated from the following relationship [9]:

$$\underline{\tau} + \underline{\underline{J}}^{T} \cdot \underline{F}_{ext} = \underline{Q} \qquad \text{(a6)}$$

where, $\underline{\tau} = [\tau_1 \quad \tau_2 \quad \tau_3 \quad \tau_4 \quad \tau_5 \quad \tau_6]^T$ are joint torque (force). $\underline{F}_{ext}$ is defined in Eq. (4-15)

The C chain is selected as an example to explain the theory and the definitions that given in the appendix A. We have:

$$\underline{Ct} = [t_{C1} \quad PowC \quad 0 \quad 0 \quad 0 \quad 0]^T$$

$$\underline{CF}_{ext} = [CF_{xext} \quad CF_{yext} \quad CF_{zext} \quad CM_{xext} \quad CM_{yext} \quad CM_{zext}]^T \qquad \text{(4-17)}$$

Where, $\underline{Ct}$ represents the $\underline{\tau}$ on the C chain. τ_{C1} (along axis Z_0) is the moment applied to the upper base by C chain. The PowC is the required actuator driving force for C chain. As we don't consider the joint friction on joints 3, 4, 5 and 6, so $\tau_3 = \tau_4 = \tau_5 = \tau_6 = 0$. The $\underline{CF}_{ext}$ is the force on the C chain, which is composed of the external force $\underline{F}_{ext}$ and the forces from ball joints A and B (see Figure 4-3). The $\underline{F}_{ext}$ is calculated referred to $(XYZ)_0$.

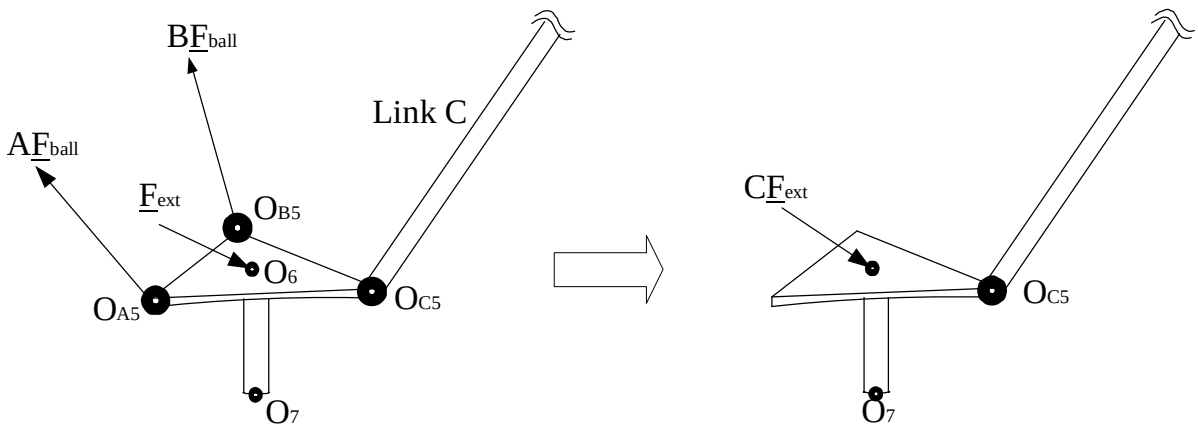

Figure 4-3 Free body diagram of the tool frame

4.2.5.1 The final form of the Lagrange equation

Applying equations (a1) through a6 into Lagrangian equation, we have

$$\underline{\underline{H}}(q)\begin{bmatrix}0\\ a_c\\ \alpha_{c3}\\ \alpha_{c4}\\ \alpha_{c5}\\ \alpha_{c6}\end{bmatrix}+\begin{bmatrix}\sum_{j=1}^{n}\sum_{k=1}^{n}h_{1jk}\dot{q}_j\dot{q}_k\\ \sum_{j=1}^{n}\sum_{k=1}^{n}h_{2jk}\dot{q}_j\dot{q}_k\\ \sum_{j=1}^{n}\sum_{k=1}^{n}h_{3jk}\dot{q}_j\dot{q}_k\\ \sum_{j=1}^{n}\sum_{k=1}^{n}h_{4jk}\dot{q}_j\dot{q}_k\\ \sum_{j=1}^{n}\sum_{k=1}^{n}h_{5jk}\dot{q}_j\dot{q}_k\\ \sum_{j=1}^{n}\sum_{k=1}^{n}h_{6jk}\dot{q}_j\dot{q}_k\end{bmatrix}+\begin{bmatrix}G_1\\ G_2\\ G_3\\ G_4\\ G_5\\ G_6\end{bmatrix}=\begin{bmatrix}\tau_{C1}\\ PowC\\ 0\\ 0\\ 0\\ 0\end{bmatrix}+\underline{\underline{J}}^{T}\begin{bmatrix}CF_{xext}\\ CF_{yext}\\ CF_{zext}\\ CM_{xext}\\ CM_{yext}\\ CM_{zext}\end{bmatrix} \tag{4-18}$$

$$\text{Let}\quad \left(\underline{\underline{J}}^{T}\right)^{-1}\cdot\left(\underline{\underline{H}}(q)\begin{bmatrix}0\\ a_c\\ \alpha_{c3}\\ \alpha_{c4}\\ \alpha_{c5}\\ \alpha_{c6}\end{bmatrix}+\begin{bmatrix}\sum_{j=1}^{n}\sum_{k=1}^{n}h_{1jk}\dot{q}_j\dot{q}_k\\ \sum_{j=1}^{n}\sum_{k=1}^{n}h_{2jk}\dot{q}_j\dot{q}_k\\ \sum_{j=1}^{n}\sum_{k=1}^{n}h_{3jk}\dot{q}_j\dot{q}_k\\ \sum_{j=1}^{n}\sum_{k=1}^{n}h_{4jk}\dot{q}_j\dot{q}_k\\ \sum_{j=1}^{n}\sum_{k=1}^{n}h_{5jk}\dot{q}_j\dot{q}_k\\ \sum_{j=1}^{n}\sum_{k=1}^{n}h_{6jk}\dot{q}_j\dot{q}_k\end{bmatrix}+\begin{bmatrix}G_1\\ G_2\\ G_3\\ G_4\\ G_5\\ G_6\end{bmatrix}\right)=[\text{constC1}]_{6\times1} \tag{4-19}$$

and,

$$\left(\underline{\underline{J}}^{T}\right)^{-1}\cdot\begin{bmatrix}\tau_{C1}\\ PowC\\ 0\\ 0\\ 0\\ 0\end{bmatrix}=\left(\underline{\underline{J}}^{T}\right)^{-1}(:,1)\cdot\tau_{C1}+\left(\underline{\underline{J}}^{T}\right)^{-1}(:,2)\cdot PowC$$

$$=[\text{constC2}]_{6\times1}\cdot\tau_{C1}+[\text{constC3}]_{6\times1}\cdot PowC \tag{4-20}$$

Where, $\left(\underline{\underline{J}}^{T}\right)^{-1}(:,1)$ and $\left(\underline{\underline{J}}^{T}\right)^{-1}(:,2)$ are the 1st and 2nd column vectors of $\left(\underline{\underline{J}}^{T}\right)^{-1}$. The $[\text{constC1}]_{6\times1}$, $[\text{constC2}]_{6\times1}$ and $[\text{constC3}]_{6\times1}$ are the known constants that were obtained from Eqs. (4-19)~(4-20). Substituting Eqs.(4-19)~(4-20) into Eq.(4-18), we have:

$$\underline{CF}_{ext} = [constC1] + [constC2]_{6\times1} \cdot t_{C1} + [constC3]_{6\times1} \cdot PowC \tag{4-21}$$

The Lagrange equations of A chain and B chain can be derived in the similar method. Therefore, from $\sum \underline{F} = 0$ and $\sum \underline{M} = 0$, we have:

$$\begin{cases} AF_{xext} + BF_{xext} + CF_{xext} + F_{xext} = 0 \\ AF_{yext} + BF_{yext} + CF_{yext} + F_{yext} = 0 \\ AF_{zext} + BF_{zext} + CF_{zext} + F_{zext} = 0 \\ AM_{xext} + BM_{xext} + CM_{xext} + M_{xext} = 0 \\ AM_{yext} + BM_{yext} + CM_{yext} + M_{yext} = 0 \\ AM_{zext} + BM_{zext} + CM_{zext} + M_{zext} = 0 \end{cases} \tag{4-22}$$

From Eq.(4-22), τ_{A1}, PowA, τ_{B1}, PowB, τ_{C1} and PowC can be obtained. If we replace these calculated results into Eq.(4-21), the $\underline{AF}_{ext}$ and $\underline{BF}_{ext}$, then $\underline{CF}_{ext}$ can be solved. In the C chain, the forces applied to the tool platform by the ball joints are denoted by:

$$\underline{CF}_{ball} = \begin{bmatrix} CF_{xball} & CF_{yball} & CF_{zball} \end{bmatrix}^{T} = -\underline{CF}_{ext} - m_6 \cdot \underline{g} + m_6 \cdot \underline{\ddot{V}}_{e} \tag{4-23}$$

In the same way, the linear force of $\underline{AF}_{ball}$ and $\underline{BF}_{ball}$, acting on the tool platform in A chain and B chain of ball joint, can be obtained. Then, we can solve the required actuator driving force for the A, B and C actuators. The reaction forces on all of the components can also be solved.

4.3. Tool paths planning for simulation

The tool axis orientation is always varied in 3D surface machining using the PLM, with a non-orthogonal structure. To fully understand the dynamic behavior of this machine, a path planing is then necessary. The tool paths, accompanied with the velocity and acceleration variation, are designed here to investigate the force variation on the ball joints and the actuator driving force variation. The external force applied on the tip of cutter is set as $\underline{F}_{ext}$ =0. The mass of the link is: m2 = 5, m3 = 80, m4 = 1, m5 = 1, m6 + m7 = 50 (mi : mass of link i, Kg), gravity acceleration g = 9.81 m/sec^2. Mass moment inertia: Ixx1 = 0, Iyy1 = 0, Izz1 = 0, Ixx2 = 0, Iyy2 = 0, Izz2 = 0, Ixx3 = 5000, Iyy3 = 3e6, Izz3 = 3e6, Ixx4 = 0, Iyy4 = 0, Izz4 = 0, Ixx5 = 0, Iyy5 = 0, Izz5 = 0, Ixx6 = 2.5e5, Iyy6 = 2.5e5, Izz6 = 3e5 (Ixxi: mass of moment inertia referred to x-axis, Kg-mm^2). One set of the design parameter r/R = 0.8, t/R = 1.08, L/R = 2.4 is selected as the benchmark of the discussion. The tool axis orientation is shown in Figure 4-4a. In Figure 4-4a, O'_0 and O_7 are coincident and varied with different tool locations. The orientation definition of $(XYZ)'_0$ is coincident with $(XYZ)_0$. The tool axis $\underline{t}$ can be described as:

$$\underline{t} = t \cdot \sin(\phi)\cos(\varphi)\underline{i}'_0 + t \cdot \sin(\phi)\sin(\varphi)\underline{j}'_0 + t \cdot \cos(\phi)\underline{k}'_0 \qquad (4\text{-}24)$$

In the above equation, ϕ is the angle between cutter and Z'-axis. The φ is the angle

between the tool axis X'-Y' projection and X'-axis. The tool paths planing is separately explained as follows:

Path 1: The initial cutter location is $\phi = 30^{\circ}$, $\varphi = 90^{\circ}$ and z = -22. The ϕ and φ are kept constant in the simulation (cutter orientation is fixed). The cutter orientation, variation and motion planing are shown in Figure 4-4b, Figure 4-4c. The total simulation time is 0~3 seconds. The time interval for computing is d time = 0.2 seconds. In 0~1seconds, the tool platform is accelerated by a = 10 m/sec^2 (along positive Z_0 direction). In 1~2 seconds, the tool platform maintains a constant velocity. In 2~3 seconds, the tool platform decelerates by a = -10 m/sec^2.

Path 2: The cutter orientation variation and motion planing are shown in Figure 4-4b, 4-4c. The initial location is $\phi = -60^{\circ}$, $\varphi = 0^{\circ}$, z = -1. The total simulation time is 0~3 seconds. The time interval for computing is d time = 0.2 seconds. In this simulation, the location z and φ of the cutting point (CP) are kept at constant and the tool platform is rotated about the Y'_0 axis with $\phi = -60^{\circ} \sim +60^{\circ}$, $\dot{\phi} = 40^{\circ}/\sec$, $\ddot{\phi} = 0^{\circ}/\sec^2$.

Path 3: The cutter orientation variation and motion planing are shown in Figure 4-4b, 4-4c. The initial location is $\phi = 30^{\circ}$, $\varphi = 0^{\circ}$, z = -1. The total simulation time is 0~3 seconds. The time interval for computing is d time = 1/24 seconds. In this simulation period (0~3 seconds) , the location z and ϕ of the cutting point are kept at constant and the tool platform is rotated about the Z'_0 axis with $\varphi = 0^{\circ} \sim 360^{\circ}$, $\dot{\varphi} = 120^{\circ}/\sec$, $\ddot{\varphi} = 0^{\circ}/\sec^2$.

Path 4: The cutter orientation variation and motion planing are shown in Figure

4-4b, 4-4c. The initial location is $\phi = 30^{\circ}$, $\varphi = 0^{\circ}$, z = -1. The total simulation time is 0~3 seconds. The time interval for computing is d time = 0.2 seconds. In this simulation, the location z and ϕ of the cutting point are kept at constant and the tool platform is rotated about the Z'_0 axis with $\varphi = 0^{\circ} \sim 75^{\circ}$. In 0~1 seconds, the acceleration of φ is $\ddot{\varphi} = 30^{\circ}/\sec^2$. In 1~3 seconds, the motion is $\dot{\varphi} = 30^{\circ}/\sec$, $\ddot{\varphi} = 0^{\circ}/\sec^2$.

Path 5: The cutter orientation variation and motion planing are the same with Path 4 except that the initial location is $\phi = 60^{\circ}$, $\varphi = 0^{\circ}$, z = -1. The total simulation time is 0~3 seconds. The time interval for computing is d time = 0.2 seconds. In this simulation, the location z and ϕ of the cutting point are kept at constant and the tool platform is rotated. About the Z'_0 axis with $\varphi = 0^{\circ} \sim 75^{\circ}$. In 0~1 seconds, the acceleration of φ is $\ddot{\varphi} = 30^{\circ}/\sec^2$. In 1~3 seconds, the motion is $\dot{\varphi} = 30^{\circ}/\sec$, $\ddot{\varphi} = 0^{\circ}/\sec^2$.

a.

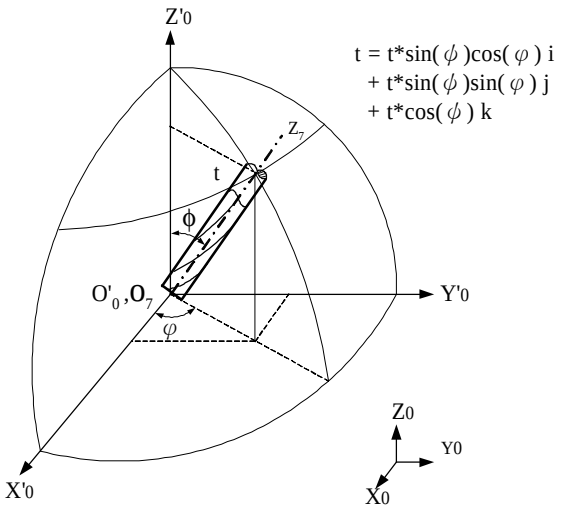

b.

c.

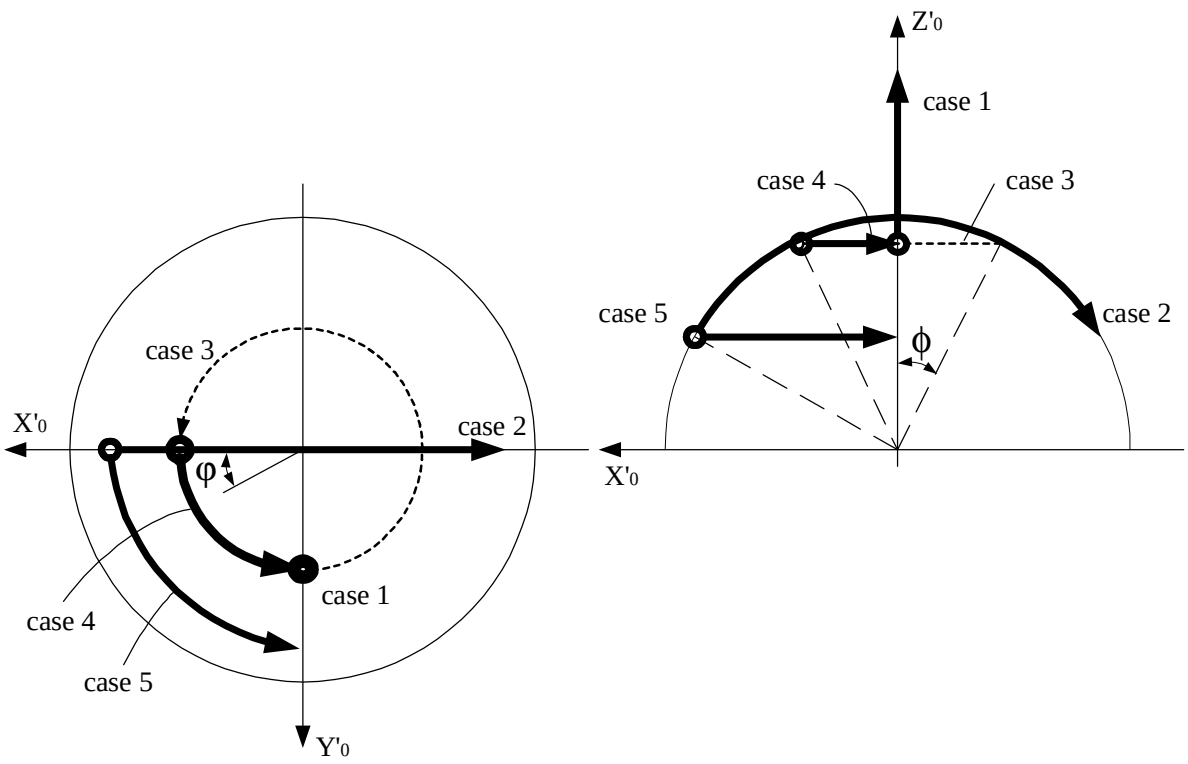

Figure 4-4 Tool path (cutter inclination angle) planing for the simulation. Figure 4-4b is the top view of Figure 4-4a. Figure 4-4c is the front view of Figure 4-4a.

4.4. Results and discussions

From the coordinate definition in Figure 4-2, the positive direction of the slider A, B, or C is along the Z-axis of coordinate $(XYZ)_{A1}$, $(XYZ)_{B1}$, or $(XYZ)_{C1}$. Therefore, a positive applied force means an downward applied force and a negative actuator driving force means an upward driving force.

For path 1, the variation of the actuator driving force is shown in Figure 4-5. For path 1, the C chain has the following results : joints angles $\theta_3 = 90.91^0$, $\theta_4 = -9.541^0$, $\theta_5 = -25.905^0$, $\theta_6 = -82.369^0$; joints angular velocity $\omega_3 = \omega_4 = \omega_5 = \omega_6 = 0^0$; joints angular acceleration $\alpha_3 = \alpha_4 = \alpha_5 = \alpha_6 = 0^0$. This means that the driving axes A, B, C generate an upward force to drive the tool platform upwards or downward in the simulation period. However, the geometric relationship of the machine is unvaried. Therefore, the calculated driving forces are kept at constant during the motion period. It is worth mentioning that the initial cutter orientation $\phi = \varphi = 0^\circ$ will cause the determinant of the Jacobian matrix to be zero. The Matlab simulation program will give the following message: Matrix is close to singular or badly scaled. Results may be inaccurate. From the D-H coordinate definition shown in Figure 4-4, the three links of the parallel link mechanism are symmetric at $\phi = \varphi = 0^\circ$. This may reduce a constraint DOF and the solution can not be found. This situation has also occasionally occurred in the manipulator research [9,12]. This situation can be avoided with the cutter having a slight offset from $\phi = \varphi = 0^\circ$. This can be achieved without difficulty in the practical machining applications.

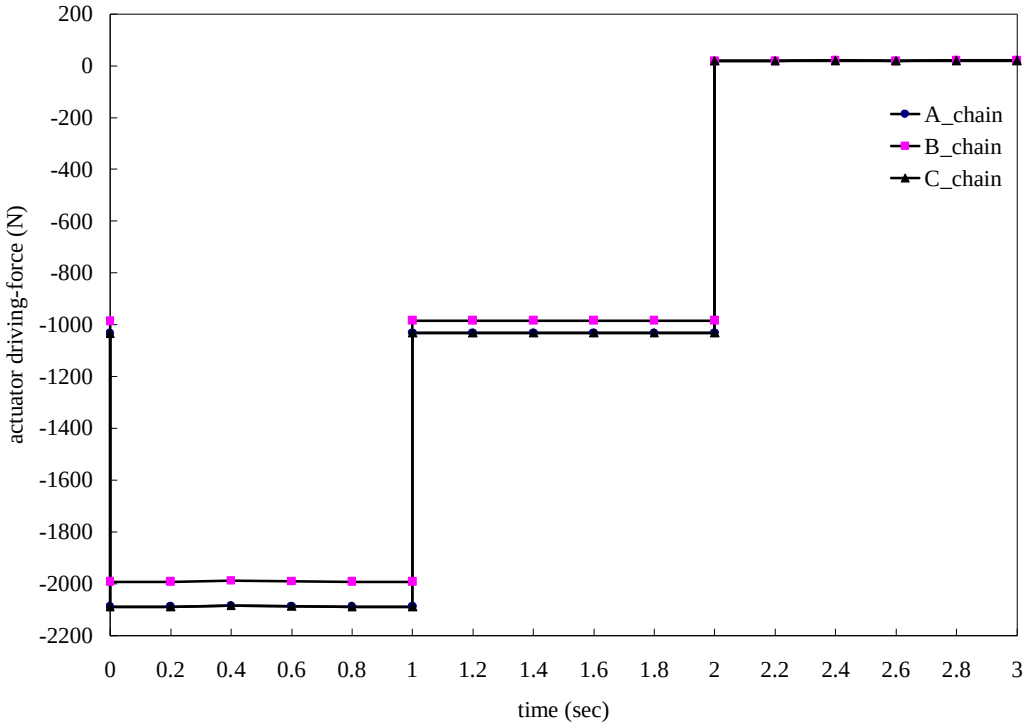

Figure 4-5 Actuator force variation of the A, B, and C chains for path 1 $\phi=30^0$, $\varphi=90^0$: 0~1 sec, a = 10 mm/ sec^2 ; 1~2sec, a = 0 mm/ sec^2 ; 2~3sec, a = -10 mm/ sec^2 .

For path 2, the simulated tool path is the tool platform rotated about the Y'_0 axis between $\phi = \pm 60^{\circ}$ with $\varphi = 0^{\circ}$ and z = -1. The calculated results are shown in Figure 4-6. Figure 4-6 shows the actuator driving forces on A, B, and C chains for path 2. In Figure 4-6, the actuator driving forces are found to be increased very rapidly with $|\phi| > 40^{\circ}$. This means that the working space with smaller ϕ is better for PLM machining applications.

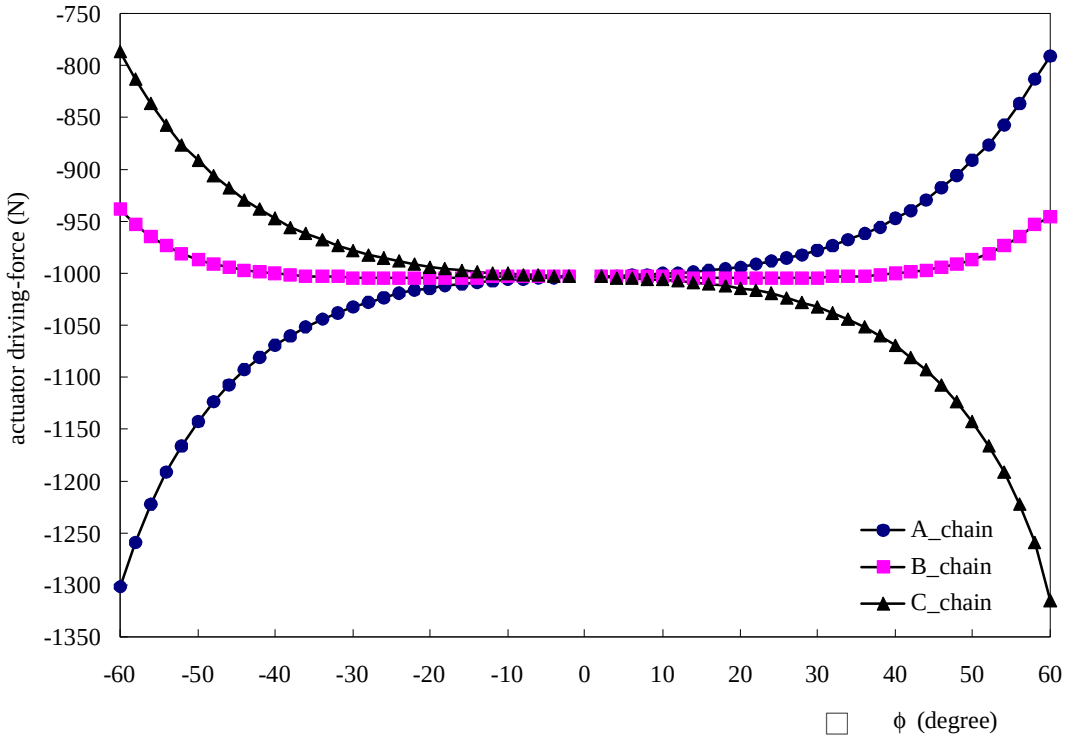

Figure 4-6 Actuator driving forces variation on A, B, and C chains for path 2: ϕ= -60^0~ +60^0, $\varphi = 0^\circ$, $\dot{\phi} = 40^\circ/\sec$, $\ddot{\phi} = 0^\circ/\sec^2$.

For path 3, the tool platform is rotated counterclockwise about the Z'_0–axis from $\varphi = 0^\circ$ to $\varphi = 360^\circ$. Figure 4-7 shows the actuator driving force on A, B, and C chains for path 3. In the driving force analysis results of Figure 4-7, the jerks are found at six locations : $\varphi = 30^\circ$, $\varphi = 90^\circ$, $\varphi = 150^\circ$, $\varphi = 210^\circ$, $\varphi = 270^\circ$, $\varphi = 330^\circ$. The reason for this can be explained by the coordinate definition of Figure 4-4. For C chain, $\theta_{C5} = 0^\circ$ and Z_{C3} and $-Z_{C5}$ are coincident when $\varphi = 150^\circ$ and $\varphi = 330^\circ$. From the previous discussion, θ_{C4} and θ_{C6} must satisfy one of the following two conditions: $\theta_{C3} + \theta_{C4} - \theta_{C6} + \varphi = 180^0$ (with $\varphi = 0^\circ \sim 180^\circ$) and $\theta_{C3} + \theta_{C4} - \theta_{C6} - \varphi = 180^0$ (with $\varphi = 180^\circ \sim 360^\circ$). The θ_{C3} is computed from the inverse kinematic method and θ_{C4}, θ_{C6} are unstable at this location. This reduces a constraint DOF and makes a singularity

result. These singular results can be summarized and displayed as three surfaces. They are shown in Figure 4-8. By carefully examining the driving force results in Figure 4-7, a very interesting result is found: the actuator driving force is larger with the higher z position. For example, the actuator driving force of B joint is larger than the actuator driving force of A joint or C joint when the z position of B joint is higher than the z position of A joint or C joint.

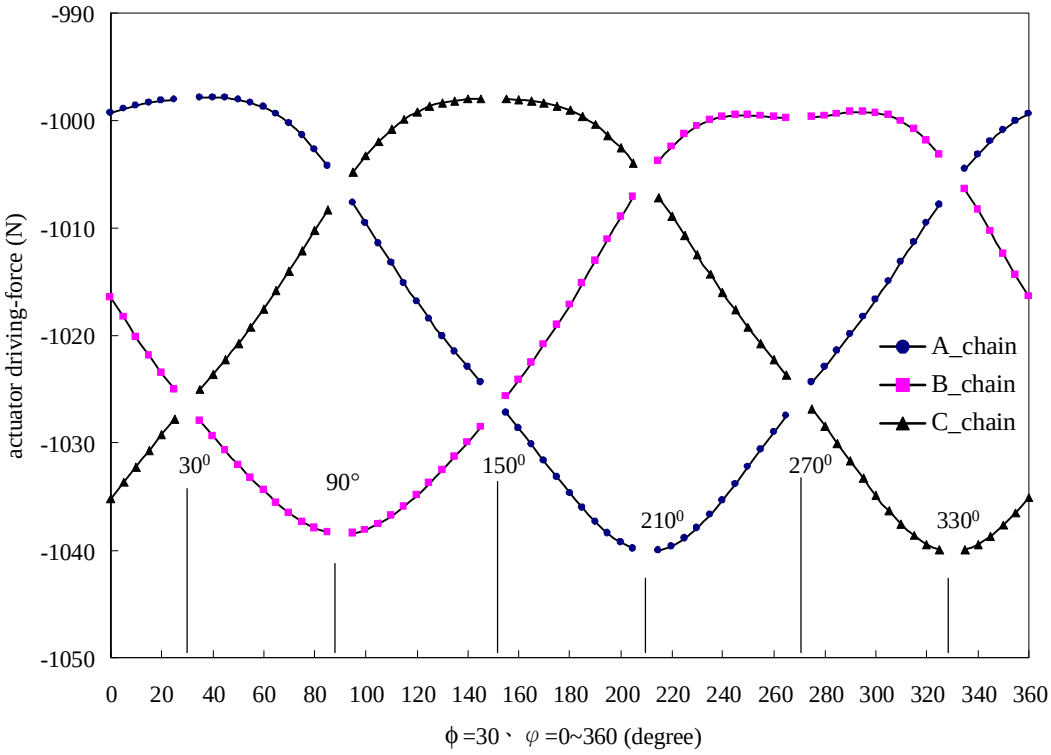

Figure 4-7 Actuator driving force variation on A, B, and C chains for path 3: $\phi = 30^{\circ}, \varphi = 0^{\circ} \sim 360^{\circ}$, $\dot{\phi} = 120^{\circ}/\sec$, $\ddot{\phi} = 0^{\circ}/\sec^2$.

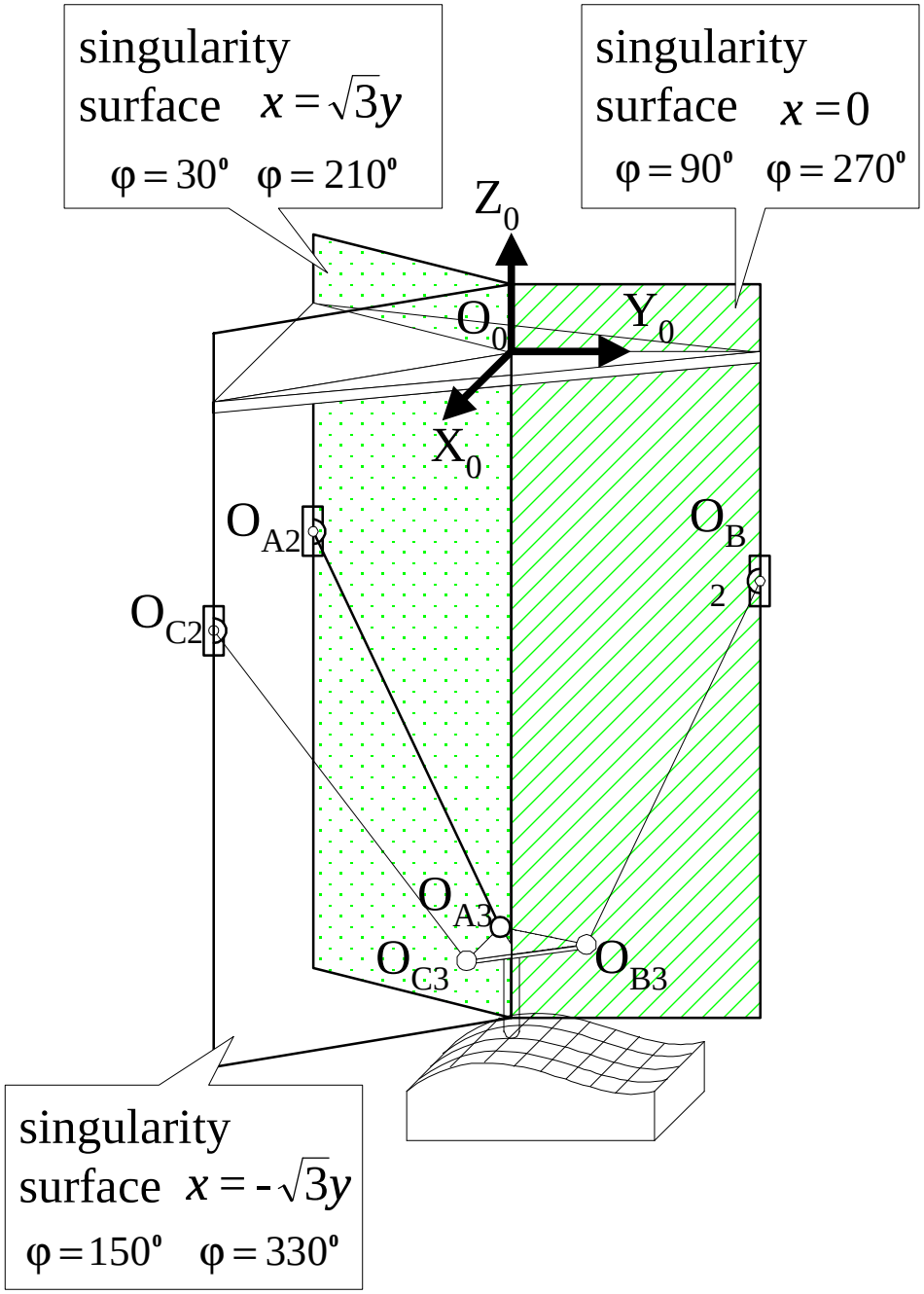

Figure 4-8 Singularity surfaces

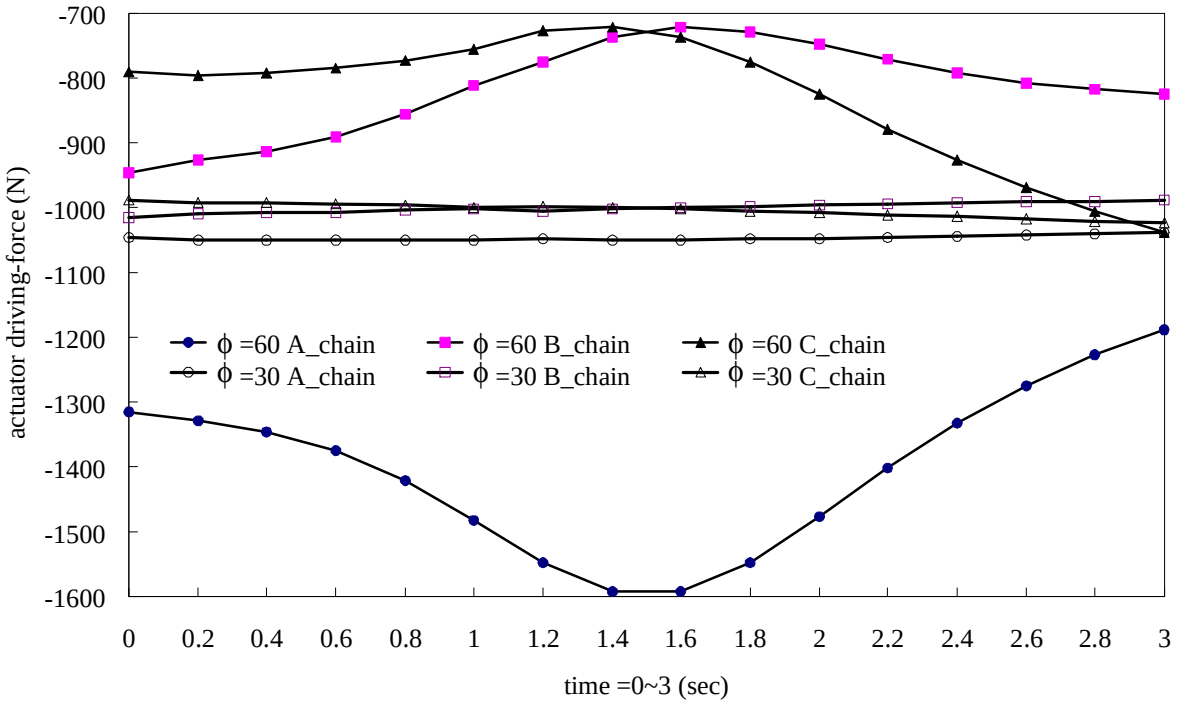

Figure 4-9 Actuator driving force variation on A, B, and C chains for path 4 $\phi=60^0$, $\varphi=0\sim75^0$, path 5 $\phi=30^0$, $\varphi=0\sim75^0$: 0~1sec, $\ddot{\varphi}=30^o/\sec^2$; 1~3 sec $\dot{\phi}=30^o/\sec$, $\ddot{\phi}=0^o/\sec^2$.

For path 4 and path 5, Figure 4-9 shows the actuator driving force on A, B, and C chains for path 4, path 5.

By comparing the actuator driving forces obtained in Figure 4-9, the required A chain actuator driving force for $\phi = 30^0$, $\varphi=60^o$ (-1600N) is singnificantly larger than the required driving force for $\phi = 30^0$, $\varphi=30^o$ (-1050N). This again implies that the required actuator driving forces during the machining processes are mainly affected by the inclination angle (ϕ) of the tool platform. The effects of the angular acceleration of the tool platform are relatively small. This result is also very useful for the design process of PLM.

4.5. Conclusions

An investigation for the dynamic analysis and modeling of a TRR-XY PLM to fully understand the required actuator driving force is shown in this research. The actuator driving force variation on A, B, C chains for five different cutting paths are obtained using D-H notation method, parametric tool concept, and Lagrange-equation theory. The effects of the dimensions, geometry, inertial parameters of a PLM are investigated. For the TRR-XY PLM, it is found that the required actuator driving forces during the machining processes are mainly affected by the inclination angle (ϕ) of the tool platform. The effects of the angular acceleration of the tool platform are relatively small. The actuator driving forces are found to be increased very rapidly with $|\phi|>40°$. This means that the working space within smaller ϕ is generally better for PLM machining applications. This derived model can also be applied to the other PLM constructions. This will enable the designer to understand some important characteristics of dynamic behavior of a PLM. For high-speed and high-payload machining processes, this subject becomes even more important.

Appendix

A.1 Calculation of $\underline{\underline{H}}(\underline{q})$

The $\underline{\underline{H}}(\underline{q})$ in Eq. 17 can be computed as follows:

$$\underline{\underline{H}}(\underline{q}) = \sum_{i=1}^{6}\left[m_i (\underline{\underline{J}}_{L}^{(i)})^T \underline{\underline{J}}_{L}^{(i)} + (\underline{\underline{J}}_{A}^{(i)})^T \underline{\underline{I}}_i \underline{\underline{J}}_{A}^{(i)}\right] \tag{a1}$$

In the above equation,

$$\underline{J}_{Lj}^{(i)} = \begin{cases} \underline{b}_{j-1} & \text{, for prismatic joints} \\ \underline{b}_{j-1} \times \underline{r}_{j-1,ci} & \text{, for revolute joints} \end{cases},$$

$$\underline{J}_{Aj}^{(i)} = \begin{cases} 0 & \text{, joint j = prismatic} \\ \underline{b}_{j-1} & \text{, joint j = revolute} \end{cases}, \quad j=1, 2,\ldots\ldots, i \tag{a2}$$

where $\underline{r}_{j-1,ci}$ is the position vector of the centroid of link i referred to the origin of coordinate $(XYZ)_{j-1}$, and $\underline{b}_{j-1}$ is the 3×1 unit vector along joint axis j-1.

A.2 Calculation of $\sum_{j=1}^{n}\sum_{k=1}^{n} h_{ijk}\dot{q}_j\dot{q}_k$

The $\sum_{j=1}^{n}\sum_{k=1}^{n} h_{ijk}\dot{q}_j\dot{q}_k$ i,j,k=1,2,……,6 can be calculated as follows:

$$h_{ijk} = \frac{\partial H_{ij}}{\partial q_k} - \frac{1}{2}\frac{\partial H_{jk}}{\partial q_i} \tag{a3}$$

When i=1~6, the Eq. a3 can be displayed as follows:

$$h_{1jk} = \frac{\partial H_{1j}}{\partial q_k} - \frac{1}{2}\frac{\partial H_{jk}}{\partial q_1}$$

$$h_{2jk} = \frac{\partial H_{2j}}{\partial q_k} - \frac{1}{2}\frac{\partial H_{jk}}{\partial q_2}$$
$$h_{3jk} = \frac{\partial H_{3j}}{\partial q_k} - \frac{1}{2}\frac{\partial H_{jk}}{\partial q_3}$$
$$h_{4jk} = \frac{\partial H_{4j}}{\partial q_k} - \frac{1}{2}\frac{\partial H_{jk}}{\partial q_4}$$
$$h_{5jk} = \frac{\partial H_{5j}}{\partial q_k} - \frac{1}{2}\frac{\partial H_{jk}}{\partial q_5}$$
$$h_{6jk} = \frac{\partial H_{6j}}{\partial q_k} - \frac{1}{2}\frac{\partial H_{jk}}{\partial q_6} \qquad \text{(a4)}$$

Where, H_{ij} is the i-th row and j-th column component of $\underline{\underline{H}}(\underline{q})$.

A.3 Calculation of $\underline{G}$

The $\underline{G} = [G_1 \quad G_2 \quad G_3 \quad G_4 \quad G_5 \quad G_6]^T$ can be calculated from the following relationship.

$$G_i = -\sum_{j=1}^{6} m_j \cdot \underline{g}^T J_{Li}^{(j)} \qquad i=1,2,\ldots\ldots,6 \qquad \text{(a5)}$$

Where, $\underline{g} = [0 \quad 0 \quad -g]^T$ is the gravitational acceleration. When i > j, $J_{Li}^{(j)}=0$.

A.4 Calculation of $\underline{Q}$

The $\underline{Q}$ in Eq. 17 can be calculated from the following relationship [13]:

$$\underline{\tau} + \underline{\underline{J}}^T \cdot \underline{F}_{ext} = \underline{Q} \qquad \text{(a6)}$$

where, $\underline{\tau} = [\tau_1 \quad \tau_2 \quad \tau_3 \quad \tau_4 \quad \tau_5 \quad \tau_6]^T$ are joint torque (force). $\underline{F}_{ext}$ is define in Eq.16

References

[1] B. Dasgupta and P. Choudhury, 1999, " A general strategy based on the Newton-Euler approach for the dynamic formulation of parallel manipulators", Mechanism and Machine Theory, Vol. 34 pp. 801-824.

[2] W. Q. D. Do and D. C. H. Yang, 1988, " Inverse dynamic analysis and simulation of a platform type of robot," Journal of Robotic Systems, Vol. 5, No. 3, pp. 209-227.

[3] P. Guglielmetti, and R. Longchamp, 1994, " A closed form inverse dynamics model of the Delta parallel Robot", Proc. International Federation of Automatic Control Conference on Robot Control, (1994) 39-44.

[4] K. M. Lee and D. K. Shah, 1988, "Dynamic analysis of a three-degrees-of-freedom in-parallel actuated manipulators," IEEE Journal of Robotics and Automation, Vol. 4, no.3 .

[5] J. D. Lee and Z. Geng, 1993, "A dynamic model of a flexible Stewart platform," Computers & Structures, Vol. 48, no. 3 pp. 367-374.

[6] G. Lebret, K. Liu, and F. L. Lewis, 1993, "Dynamic analysis and control of a Stewart platform manipulator," Journal of Robotic Systems, Vol. 10, no. 5, (1993) 629-655.

[7] H. Pang, and M. Shahingpoor, 1994, "Inverse dynamics of a parallel manipulator," Journal of Robotic Systems, Vol. 11, no. 8, pp. 693-702.

[8] K. Miller and R. Clavel, 1992, "The Lagrange-Based model of Delta-4 Robot dynamics," Robotersysteme, Vol. 8, pp. 49-54.

[9] L. W. Tsai, 1999, Robot Analysis-The Mechanics of Serial and Parallel Manipulators, John Wiley & Sons.

[10] S. L. Chen, T. H. Chang, and I. G. Chang, 2000, "Dynamic analysis and modeling of hybrid TRR-XY parallel kinematics machine", Proceedings of the 17th National Conference on Mechanical Engineering, pp. 683-690.

[11] DIN, 1987, "Din 66215:CLDATA", NC-Mascginen, Berlin, Köln, Beuth Verlage,

pp. 49-100.

[12] J. J. Craig, 1989, “Introduction to Robotics Mechanics and Control”, Addison-Wesley Publishing Company.

Chapter 5 Error Analysis

Because of parallel link machine tool having five non-orthogonal simultaneously driven axes, it is much complexity to analyze the error sources. Generally, the error sources having effects on accuracy of machine tool can be classified into static errors and dynamic errors [1-7]. The static errors are resulted from geometric errors (manufacturing error assembly error, structure deformation error) and thermal deformation errors (thermal extensibility of guide and spindle, changeable environmental temperature, structure thermal deformation, etc.). The value of errors is relevant to machining position. This kind of error is called position dependent error. The dynamic error is referred to the difference between the practical tool path and the given tool path. Due to the fact that the XY-table is commonly used in the industry and the technology is well developed, this chapter focuses on the error model analysis of the three DOF parallel-link mechanisms. There are several errors usually encountered in the machining and assembly of this machine tool. The base frame errors, the pin joint errors, ball joints assembly errors, and tool frame assembly errors of this machine tool are considered in this chapter. There are several tens error data will be included into the errors mentioned above and make the theoretical analysis for completely understanding the effects of each error very difficult. From the practical viewpoint, there are only eleven manufacturing errors selected in this research. There are some other factors may also influence the machine accuracy [8-10]. Most of the eleven errors are component-machining errors and assembly errors and the data of the errors can be measured by using a common measuring method. The component machining errors and assembly errors are considered as manufacturing errors in this chapter.

The commercial controller is adopted in the developed prototype PLM for this research. For commercial controller, only several error parameters can be adjusted including ball joint position errors, pin joint position errors, link length errors, and tool length error. The error verification in this research will be developed based on the adjustable parameters of commercial controller. A simulation is performed to evaluate the performance of the developed error model.

5.1 Theoretical error model analysis

5.1.1 Error definitions

Two translation errors and three orientation errors are considered as the assembly errors of the machine tool. The assembly errors of the B-axis are selected as an example to explain the errors and shown in Figure 5-1.

For the assembly errors of the B-axis, the translation errors are δ_{FxB}, δ_{FyB}; and the orientation errors are α_B, β_B, and γ_B. The assembly errors can be described by a homogeneous transformation matrix (HTM) in the D-H notation method. For example, the HTM for the B-chain is displayed as $[Frame]_B$, which is

$$[Frame]_B = \begin{pmatrix} 1 & g_B & b_B & d_{FxB} \\ g_B & 1 & a_B & d_{FyB} \\ b_B & a_B & 1 & 0 \\ 0 & 0 & 0 & 1 \end{pmatrix} \quad (5\text{-}1)$$

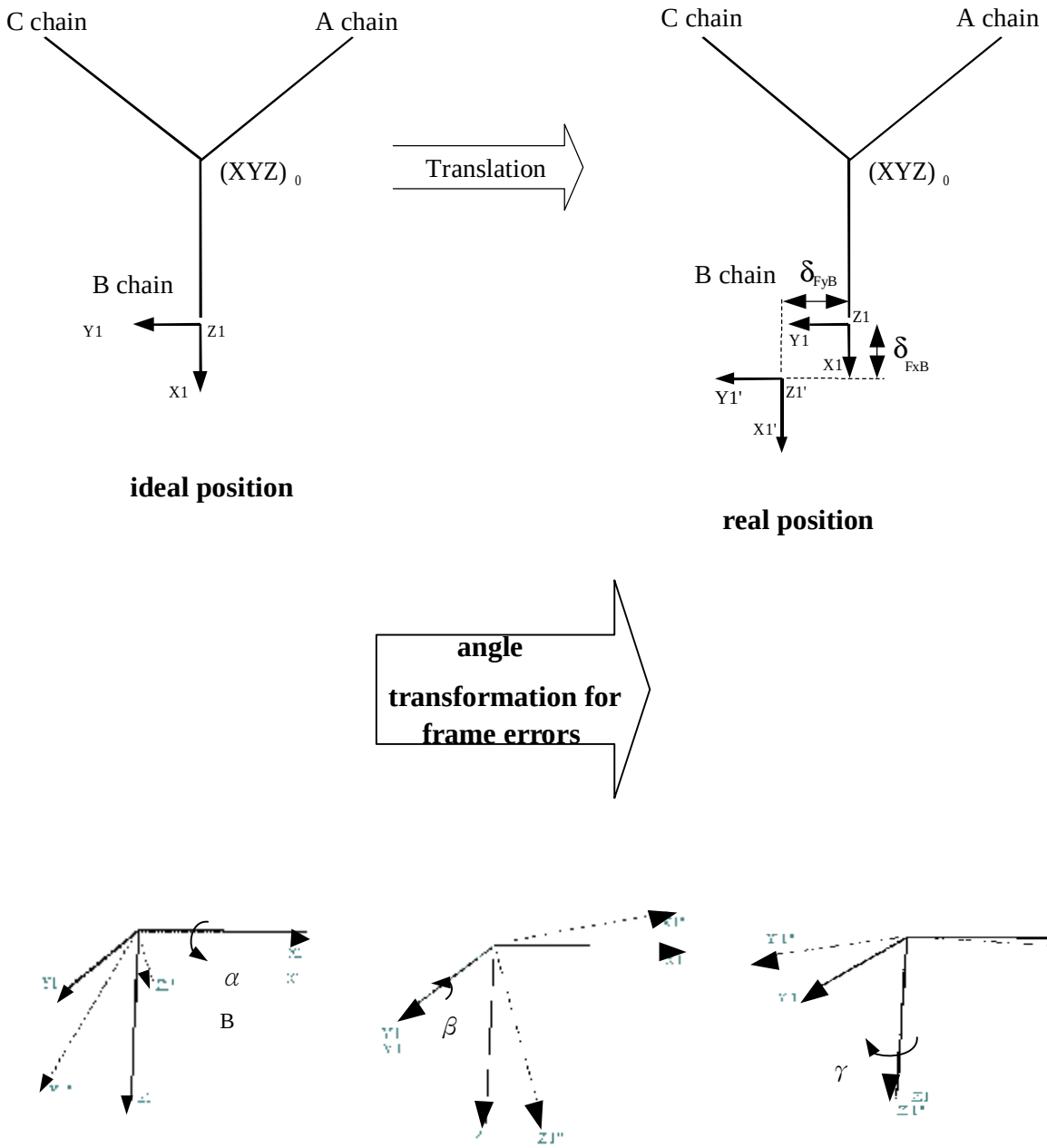

Figure 5-1 Definition of coordinate transformation for frame errors

Two orientation errors are considered as the assembly errors of the pin joints. The assembly errors of the pin joint on the B-axis are selected as an example to explain the errors considered in this research and shown in Figure 5-2.

For the assembly errors of the pin joint on the B chain, the orientation errors are ϕ_B, and λ_B. The assembly errors of pin joint can be described by a HTM $[Pin]_B$, which is

$$[Pin]_B = \begin{pmatrix} 1 & 0 & \lambda_B & 0 \\ 0 & 1 & -\phi_B & 0 \\ -\lambda_B & \phi_B & 1 & 0 \\ 0 & 0 & 0 & 1 \end{pmatrix} \quad (5\text{-}2)$$

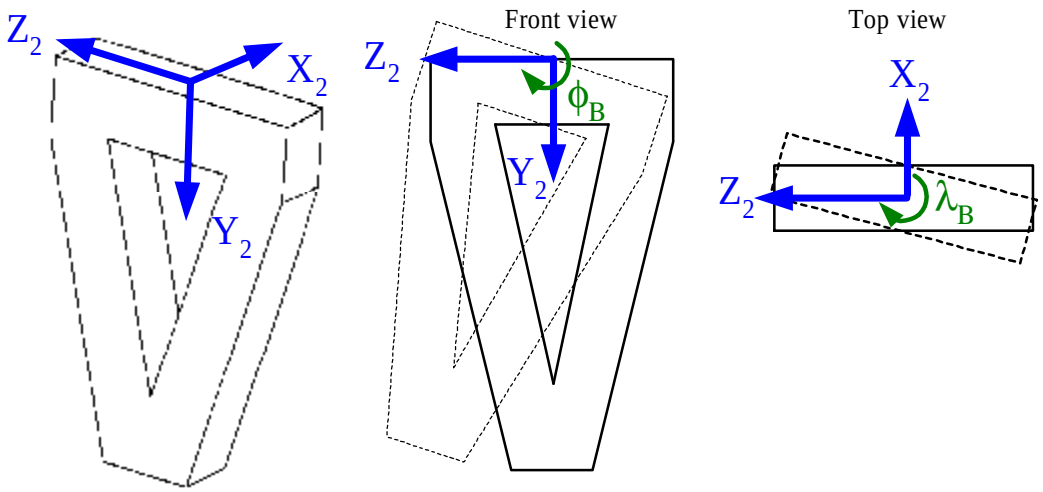

Fig. 5-2 Geometric definition for pin joint manufacturing errors

For the ball joints, they are considered to have an offset manufacturing error related to the ideal local coordinate system. The offset manufacturing error is defined by two parameters (Figure 5-3).

A homogeneous transformation matrix [Ball] is used to include these two parameters. For example, the HTM for the B-chain is displayed as $[Ball]_B$, which is

$$[Ball]_B = \begin{pmatrix} 1 & 0 & 0 & \delta_{JxB} \\ 0 & 1 & 0 & 0 \\ 0 & 0 & 1 & \delta_{JzB} \\ 0 & 0 & 0 & 1 \end{pmatrix} \qquad (5\text{-}3)$$

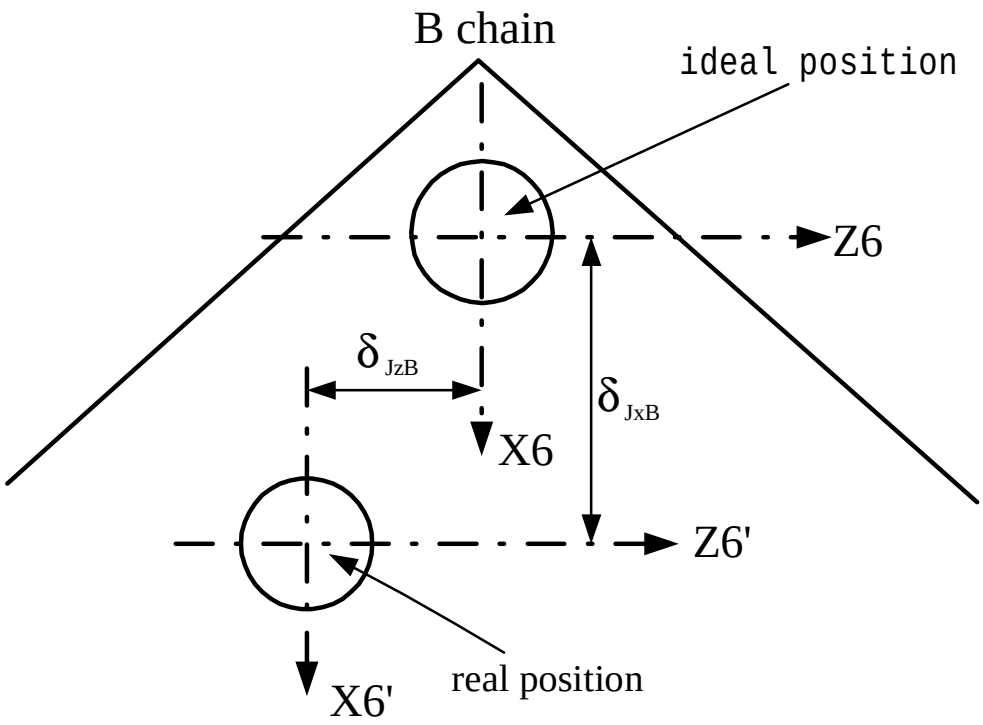

Figure 5-3 Geometric definition for ball joint manufacturing errors

For the spindle shaft, it is considered to have an offset manufacturing error related to the ideal local coordinate system. The offset manufacturing error is defined by two parameters (Figure 5-4).

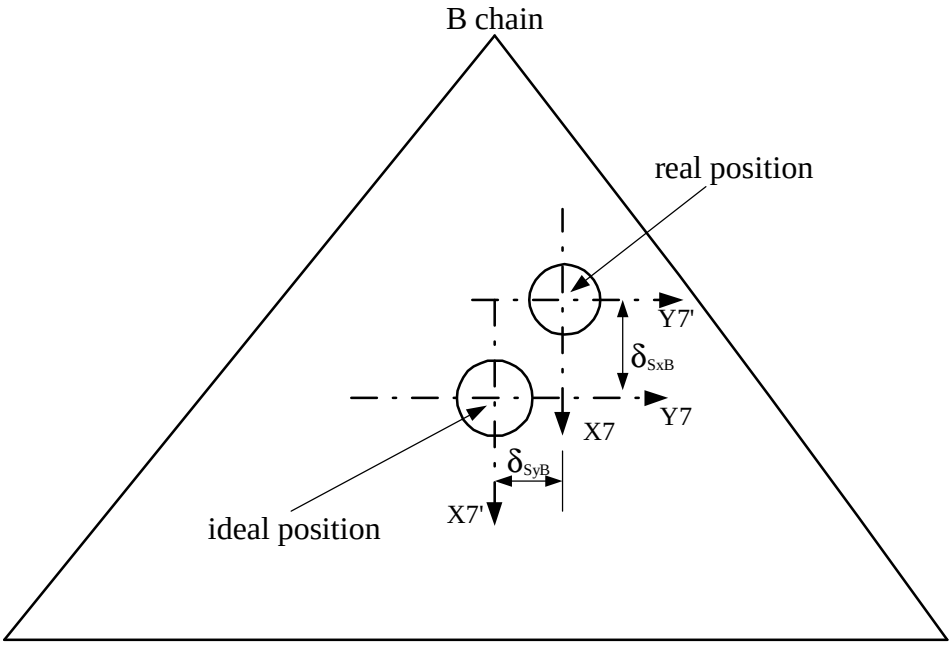

Figure 5-4 Geometric definition for spindle location manufacturing errors

A homogeneous transformation matrix [Spindle] is used to include these two parameters. For example, the HTM for the B chain is displayed as $[Spindle]_B$, which is

$$[Spindle]_B = \begin{pmatrix} 1 & 0 & 0 & \delta_{SxB} \\ 0 & 1 & 0 & \delta_{SyB} \\ 0 & 0 & 1 & 0 \\ 0 & 0 & 0 & 1 \end{pmatrix} \quad (5\text{-}4)$$

The coordinate systems defined for the D-H coordinate transformation are shown in Figure 5-5.

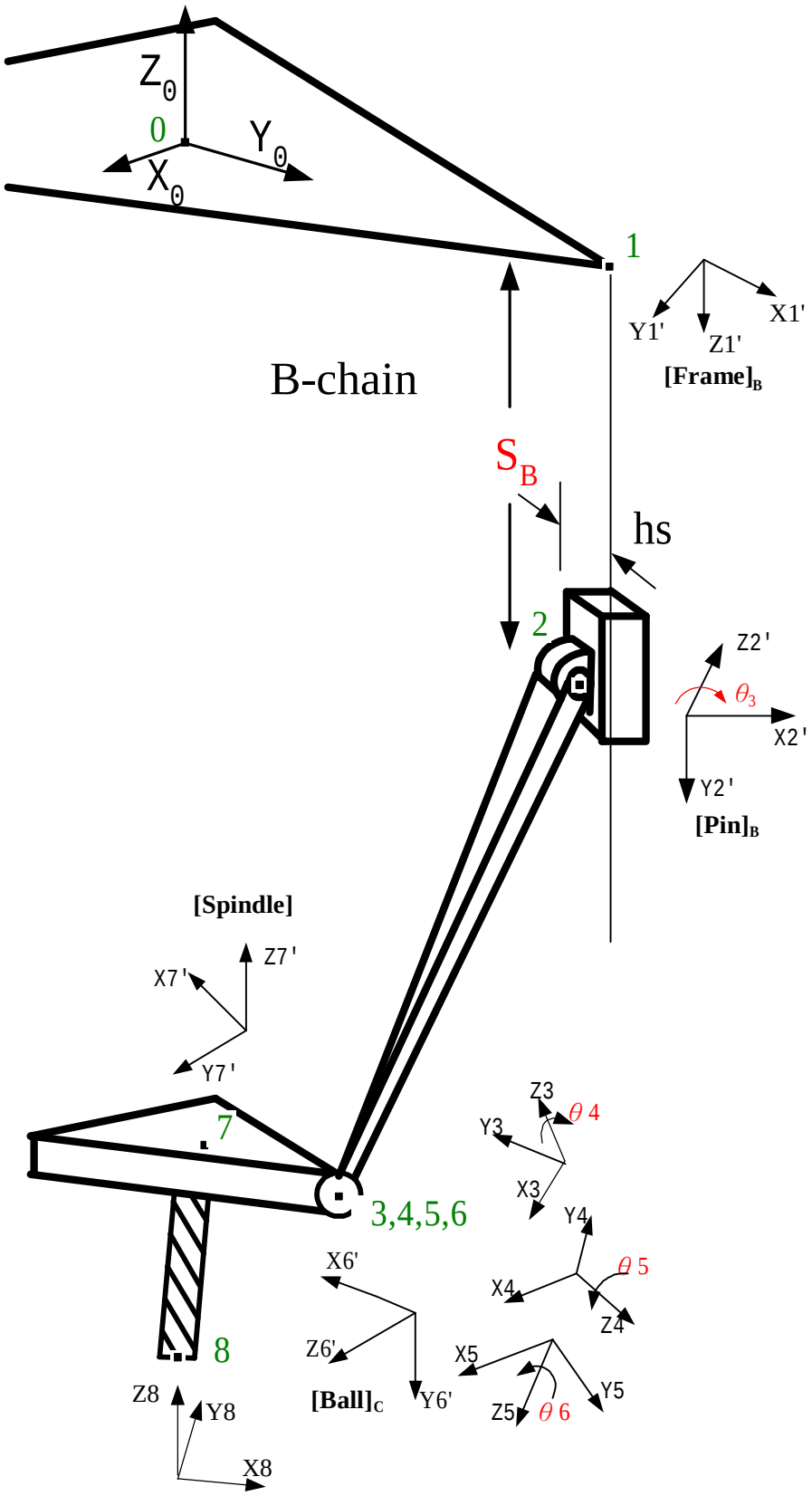

Figure 5-5 The coordinate systems defined for the D-H coordinate transformation

5.1.2 Error model analysis

Considering the error definitions that given in the above section, the HTM between the coordinate system $(XYZ)_8$ (cutter tip) and the coordinate system $(XYZ)_0$ (upper base frame) can be written as follows: For B chain

$$({}^0A_8)_B={}^0A_1[\text{Frame}]_B{}^1A_2[\text{Pin}]_B{}^2A_3{}^3A_4{}^4A_5{}^5A_6[\text{Ball}]_B{}^6A_7[\text{Spindle}]_B{}^7A_8 \quad (5\text{-}5)$$

In the above equation,

$${}^0A_1 = \begin{pmatrix} 0 & 0 & -1 & 0 \\ 1 & 0 & 0 & R \\ 0 & -1 & 0 & 0 \\ 0 & 0 & 0 & 1 \end{pmatrix} \quad (5\text{-}6a)$$

$${}^1A_2 = \begin{pmatrix} 1 & 0 & 0 & -hs \\ 0 & 0 & -1 & 0 \\ 0 & 1 & 0 & S_B \\ 0 & 0 & 0 & 1 \end{pmatrix} \quad (5\text{-}6b)$$

$${}^2A_3 = \begin{pmatrix} \cos(\theta_{3B}) & -\sin(\theta_{3B}) & 0 & L\cdot\cos(\theta_{3B}) \\ \sin(\theta_{3B}) & \cos(\theta_{3B}) & 0 & L\cdot\sin(\theta_{3B}) \\ 0 & 0 & 1 & 0 \\ 0 & 0 & 0 & 1 \end{pmatrix} \quad (5\text{-}6c)$$

$${}^3A_4 = \begin{pmatrix} \cos(\theta_{4B}) & 0 & \sin(\theta_{4B}) & 0 \\ \sin(\theta_{4B}) & 0 & -\cos(\theta_{4B}) & 0 \\ 0 & 1 & 0 & 0 \\ 0 & 0 & 0 & 1 \end{pmatrix} \quad (5\text{-}6d)$$

$$ {}^{4}A_{5} = \begin{pmatrix} \cos(\theta_{5B}) & 0 & \sin(\theta_{5B}) & 0 \\ \sin(\theta_{5B}) & 0 & -\cos(\theta_{5B}) & 0 \\ 0 & 1 & 0 & 0 \\ 0 & 0 & 0 & 1 \end{pmatrix} \quad (5\text{-}6e) $$

$$ {}^{5}A_{6} = \begin{pmatrix} \cos(\theta_{6B}) & -\sin(\theta_{6B}) & 0 & 0 \\ \sin(\theta_{6B}) & \cos(\theta_{6B}) & 0 & 0 \\ 0 & 0 & 1 & 0 \\ 0 & 0 & 0 & 1 \end{pmatrix} \quad (5\text{-}6f) $$

$$ {}^{6}A_{7} = \begin{pmatrix} 1 & 0 & 0 & r \\ 0 & 0 & -1 & 0 \\ 0 & 1 & 0 & 0 \\ 0 & 0 & 0 & 1 \end{pmatrix} \quad (5\text{-}6g) $$

$$ {}^{7}A_{8} = \begin{pmatrix} 0 & -1 & 0 & 0 \\ 1 & 0 & 0 & 0 \\ 0 & 0 & 1 & -t \\ 0 & 0 & 0 & 1 \end{pmatrix} \quad (5\text{-}6h) $$

Rearrange Eq.5-5 , we have

$$ ({}^{0}A_{8})_{B} = {}^{0}A_{1}[\text{Frame}]_{B}\,{}^{1}A_{P}\,{}^{2}A_{3}\,{}^{3}A_{4}\,{}^{4}A_{5}\,{}^{5}A_{8} \quad (5\text{-}7) $$

In the above equation,

$$ {}^{1}A_{P} = {}^{1}A_{2}[\text{Pin}]_{B} \quad (5\text{-}8) $$

In Eq.5-7, ${}^{5}A_{8}$ is defined as:

$$ {}^{5}A_{8}={}^{5}A_{6}[\text{Ball}]_{B}{}^{6}A_{7}[\text{Spindle}]_{B}{}^{7}A_{8} \tag{5-9} $$

Rearrange Eq.5-7, a HTM T is used to represent the multiplication of $[\text{Frame}]_{B}^{-1}({}^{0}A_{1})^{-1}({}^{0}A_{8})_{B}$. The components of HTM [T] is defined as follows:

$$ T=\begin{bmatrix} N1 & T1 & B1 & D1 \\ N2 & T2 & B2 & D2 \\ N3 & T3 & B3 & D3 \\ 0 & 0 & 0 & 1 \end{bmatrix} \tag{5-10} $$

Replace Eqs.5-8~5-10 into Eq.5-7, we have

$$ T={}^{1}A_{P}{}^{2}A_{3}{}^{3}A_{4}{}^{4}A_{5}{}^{5}A_{8} \tag{5-11} $$

Rearrange Eq.5-11,

$$ ({}^{1}A_{P})^{-1}T({}^{5}A_{8})^{-1}={}^{2}A_{3}{}^{3}A_{4}{}^{4}A_{5} \tag{5-12} $$

The translation components of the both sides of the Eq.5-12 are extracted and compared, the control position S_B of B chain can then be obtained. The translation component of the left-hand side of Eq.5-12 is given as follows:

$$ [I3\ 0]({}^{1}A_{P})^{-1}T({}^{5}A_{8})^{-1}[\ 0\ 0\ 0\ 1\ ]^{T} $$

$$ = \begin{pmatrix} F_B + \lambda_B \cdot G_B + hs \\ -\phi_B \cdot G_B + H_B - S_B \\ \lambda_B \cdot F_B - G_B - \phi_B \cdot H_B + \phi_B \cdot S_B + \lambda_B \cdot hs \end{pmatrix} \tag{5-13} $$

In the above equation, F_B, G_B, and H_B are defined as:

$$\begin{pmatrix} F_B \\ G_B \\ H_B \\ 1 \end{pmatrix} = \begin{pmatrix} N1 & T1 & B1 & D1 \\ N2 & T2 & B2 & D2 \\ N3 & T3 & B3 & D3 \\ 0 & 0 & 0 & 1 \end{pmatrix} \begin{pmatrix} 0 & 0 & 1 & -\delta_{SyB} - \delta_{JzB} \\ -\cos(\theta_{6B}) & -\sin(\theta_{6B}) & 0 & \delta_{JxB} + \delta_{SxB} + r \\ \sin(\theta_{6B}) & -\cos(\theta_{6B}) & 0 & t \\ 0 & 0 & 0 & 1 \end{pmatrix} \begin{pmatrix} 0 \\ 0 \\ 0 \\ 1 \end{pmatrix} \tag{5-14}$$

The translation component of the right-hand side of Eq.5-14 is given as follows:

$$[\ I3\ 0\ ]^2A_3{}^3A_4{}^4A_5[\ 0\ 0\ 0\ 1\ ]^T = \begin{pmatrix} L \cdot \cos(\theta_{3B}) \\ L \cdot \sin(\theta_{3B}) \\ 0 \end{pmatrix} \tag{5-15}$$

By using the relationship that the results of Eq.5-13 is equal to the results of Eq.5-15, the inverse kinematic solution of the machine tool can be obtained as follows:

$$\begin{pmatrix} F_B + \lambda_B \cdot G_B + hs \\ -\phi_B \cdot G_B + H_B - S_B \\ \lambda_B \cdot F_B - G_B - \phi_B \cdot H_B + \phi_B \cdot S_B + \lambda_B \cdot hs \end{pmatrix} = \begin{pmatrix} L \cdot \cos(\theta_{3B}) \\ L \cdot \sin(\theta_{3B}) \\ 0 \end{pmatrix} \tag{5-16}$$

$$S_B = (-\phi_B \cdot G_B + H_B) - \sqrt{[L^2 - (F_B + \lambda_B \cdot G_B + hs)^2]} \tag{5-17}$$

The solving procedures for the A chain and C chain are very similar with that for B-chain. The detail solving procedures for A chain and C chain are neglected. However, the results are summarized as follows:

$$S_A = (-\phi_A \cdot G_A + H_A) - \sqrt{[L^2 - (F_A + \lambda_A \cdot G_A + hs)^2]} \tag{5-18}$$

$$S_C = (-\phi_C \cdot G_C + H_C) - \sqrt{[L^2 - (F_C + \lambda_C \cdot G_C + hs)^2]} \qquad (5\text{-}19)$$

5.1.3 a, b, g derivation with the errors considered

One of the coordinate system relationship between $(XYZ)_8$ and $(XYZ)_0$ is given in Eq.5-5. The coordinate system relationship $({}^0A_8)_B$ between $(XYZ)_8$ and $(XYZ)_0$ can also be directly represented by one translation HTM and three rotational HTM [3]. The translation displacements are Px, Py, Pz and the rotation angles are α, β, γ. The $({}^0A_8)_B$ can be written as follows:

$$({}^0A_8)_B = \text{Trans}(Px,Py,Pz)\ R_{ZYX}(\gamma, \beta, \alpha) \qquad (5\text{-}20)$$

In the real machining process, a neutral cutter location file (CL-file) for the part surface is usually generated by a commercial software [11-12]. The basic format for a CL-file is (X Y Z $\vec{i}$ $\vec{j}$ $\vec{k}$). The (X Y Z) is the coordinate data of the cutting point and the ($\vec{i}$ $\vec{j}$ $\vec{k}$) is the unit vector of the tool axis. To simplify the theory derivation, the orientation of tool axis is considered to be coincide with the normal direction of the part surface at the cutting point. We have,

$$(\vec{i}\ \vec{j}\ \vec{k})^T = R_{ZYX}(\gamma, \beta, \alpha)\ [\,0\ 0\ 1\,]^T \qquad (5\text{-}21)$$

From Eq.5-21, ($\vec{i}$ $\vec{j}$ $\vec{k}$) can be obtained as:

$$(\vec{i}\ \vec{j}\ \vec{k})^T = \begin{bmatrix} \sin(\beta) \\ -\sin(\alpha)\cdot\cos(\beta) \\ \cos(\alpha)\cdot\cos(\beta) \end{bmatrix} \qquad (5\text{-}22)$$

From Eq.5-22, the rotation angle α and β can be separately given as follows:

$$\sin\alpha = (-\vec{j}) / \cos\beta \qquad (5\text{-}23)$$

$$\cos\alpha = \vec{k} / \cos\beta \qquad (5\text{-}24)$$

In the above equation,

$$\beta = \sin^{-1}(i) \qquad (5\text{-}25)$$

$$\alpha = \tan^{-1}(\sin\alpha / \cos\alpha) \qquad (5\text{-}26)$$

In the ideal condition (no manufacturing errors in the machine tool), the rotation angle γ of this developed system can be obtained by using the geometry constraints from pin joints. The pin joints constrain the three ball joints moved only on three planes separately. The geometric relationships of the three planes are:

$$\begin{aligned} X &= 0 \text{ ---------- B chain constraint plane} \\ Y &= \frac{X}{\sqrt{3}} \text{ ---------- A chain constraint plane} \\ Y &= -\frac{X}{\sqrt{3}} \text{ ---------- C chain constraint plane} \end{aligned} \qquad (5\text{-}27)$$

Using the geometric relationship in Eq.5-27, the rotation angle γ can be obtained as:

$$\gamma = \tan^{-1}\left(\frac{-\sin(\alpha)\cdot\sin(\beta)}{\cos(\alpha)+\cos(\beta)}\right) \qquad (5\text{-}28)$$

With the consideration of the manufacturing errors, it is very obvious that the γ relationship given in Eq.5-28 will not be retained. In the derivation of the new γ relationship with the manufacturing errors defined in previous section considered, the three constraint planes that generated by the pin joints are still be used. The geometric relationship (Eq.5-27) of the three planes is changed with the errors included. The derivation of the equations for the three constraint planes is required for further obtained the γ relationship.

Assume $P_0(x_0,y_0,z_0)$ and P(x, y, z) are two (non-zero) points located on the constraint plane. The normal unit vector of the constraint plane is written as:

$$N = Ai + Bj + Ck \qquad (5\text{-}29)$$

From the geometric relationship, we have equation of the constraint plane:

$$A(x-x_0) + B(y-y_0) + C(z-z_0) = 0 \qquad (5\text{-}30)$$

In each A chain, B chain or C chain, the center point of pin joint (origin point of $(X_2,Y_2,Z_2)_e$) and center point of ball joint are separately located on the constraint plane. Assume the pin joint axis is always perpendicular to the constraint plane. Therefore, the unit vector of pin joint axis is selected as the normal vector of the constraint plane. The two points given in Eq.5-30 together with the normal vector (pin joint axis) can be used to solve the equation of the constraint plane. The solving procedures of the B

chain constraint plane are given in the following as an example. The constraint plane unit normal vector of the B chain can be written as:

$$N_B = {}^0A_1[Frame]_B{}^1A_2[Pin]_B[\ 0\ 0\ 1\ 0\ ]^T \quad (5\text{-}31)$$

The origin point of pin joint (coordinate 2) with the errors considered can be written as:

$$P_B=(X_2,Y_2,Z_2)_e = {}^0A_1[Frame]_B{}^1A_2[Pin]_B[\ 0\ 0\ 0\ 1\ ]^T \quad (5\text{-}32)$$

The coordinate data of the ball joint center point can be written as:

$$B_1=({}^0A_8)_B[\ 0;r;\ t;1\ ]^T \quad (5\text{-}33)$$

Replace Eqs.5-31~5-33 into Eq.5-30 and rearrange the equation, the constraint plane equation can be rewritten as:

$$B1\ Px+B2\ Py+BS\ \sin(\gamma)+BC\ \cos(\gamma)=BP \quad (5\text{-}34)$$

In the above equation, B1, B2, BS, BC, and BP are given in appendix. The constraint plane equation of A chain and C chain can be solved using the same procedures discussed in the above. The constraint plane equation for the A chain can be obtained as:

$$A1\ Px+A2\ Py+AS\ \sin(\gamma)+AC\ \cos(\gamma)=AP \quad (5\text{-}35)$$

In the above equation, A1, A2, AS, AC, and AP are given in appendix. For C chain, the constraint plane equation can be written as:

$$C1\ Px+C2\ Py+CS\ \sin(\gamma)+CC\ \cos(\gamma)=CP \tag{5-36}$$

In the above equation, C1, C2, CS, CC, and CP are given in appendix.

N_C is the constraint plane unit normal vector of C chain. Both sin(γ) and cos(γ) are appeared in the constraint plane equation Eq.5-34, Eq.5-35 and Eq.5-36. The relationship of sin(γ) and cos(γ) is required for solving the constraint plane equation.

$$\sin(\gamma)^2+\cos(\gamma)^2=1 \tag{5-37}$$

Solving Eq.5-34, Eq.5-35 Eq.5-36 and Eq.5-37 simultaneously, the relationship between γ and α, β can be obtained as follows:

$$\frac{\sin(\gamma)}{\cos(\gamma)}=\frac{\begin{pmatrix} B1 & B2 & BP & BC \\ A1 & A2 & AP & AC \\ C1 & C2 & CP & CC \\ 0 & 0 & 1 & \cos(\gamma) \end{pmatrix}}{\begin{pmatrix} B1 & B2 & BS & BP \\ A1 & A2 & AS & AP \\ C1 & C2 & CS & CP \\ 0 & 0 & \sin(\gamma) & 1 \end{pmatrix}} \tag{5-38}$$

It is clear that the angle γ is a dependent variable and α, β are independent variable. The above Eq.5-38 can be used to solve the result of rotation angle γ. However, the control position of the three motion chain (S_A, S_B, S_C) are appeared in the coefficients of Eq.a.5, Eq.b.5, and Eq.c.5. This makes the solution procedure of Eq.5-38 become very complicate. The angle γ can be expressed as:

$$\gamma = f(\text{(error parameter)}, S_A, S_B, S_C) \tag{5-39}$$

A finite difference concept is adopted to solve the above equation for the rotation angle γ and S_A, S_B, S_C. In the normal situation, the manufacturing errors appeared in machine tools are small. The S_A, S_B, S_C difference between ideal machine tool and the real machine tool (with errors considered) should be not very large. Therefore, the S_A, S_B, S_C data for ideal machine tool are adopted as the initial guess values for the finite difference solution scheme to solve the S_A, S_B, S_C for the machine tool with the errors considered. The displacement for the center point of tool frame (parallel link mechanism) in the X, Y direction is separately called Px and Py. It is worth mentioning that the Px and Py are not independent variables. Solving the Eq.5-34, Eq.5-35, Eq.5-36 and Eq.5-37 simultaneously, the Px and Py can also be obtained as:

$$Px = \frac{\begin{pmatrix} BP & B2 & BS & BC \\ AP & A2 & AS & AC \\ CP & C2 & CS & CC \\ 1 & 0 & \sin(\gamma) & \cos(\gamma) \end{pmatrix}}{\begin{pmatrix} B1 & B2 & BS & BC \\ A1 & A2 & AS & AC \\ C1 & C2 & CS & CC \\ 0 & 0 & \sin(\gamma) & \cos(\gamma) \end{pmatrix}} \tag{5-40}$$

$$PY = \frac{\begin{pmatrix} B1 & BP & BS & BC \\ A1 & AP & AS & AC \\ C1 & CP & CS & CC \\ 0 & 1 & \sin(\gamma) & \cos(\gamma) \end{pmatrix}}{\begin{pmatrix} B1 & B2 & BS & BC \\ A1 & A2 & AS & AC \\ C1 & C2 & CS & CC \\ 0 & 0 & \sin(\gamma) & \cos(\gamma) \end{pmatrix}} \tag{5-41}$$

5.2. Effects of manufacturing errors on the machining accuracy

After solving the inverse kinematics solution in the above sections, a very interesting issue is that "How is the effects of the manufacturing errors on the positioning accuracy of the machine tool ". There are four different types of manufacturing errors included in this research: frame errors, pin joint errors, ball joint errors and tool frame (location of spindle shaft) errors. To find the errors that affect the position accuracy very much will be helpful for the engineer to keep his attention to improve the accuracy of these key components. This is obvious helpful for improving the position accuracy of the machine tool. Finding the errors from some components that affect the accuracy little is also beneficial for cost down. These components can be designed with lower precision requirement.

The tool paths for analyzing the effects of manufacturing errors are designed for the upper parallel link mechanism. Figure 5-6 shows the definition of the tool paths for tool frame. The $\vec{i}$, $\vec{j}$ and $\vec{k}$ in Figure 5-6 separately represent display the unit vectors of the tool axis. The $\vec{i}$ and $\vec{j}$ components are varied with various φ with $\vec{k}$ component fixed. A circular tool path will be generated with a fixed $\vec{k}$ value (Figure 5-6). The inclination angle of the tool axis is represented as ϕ. The effects of the manufacturing errors on the position accuracy of the parallel link machine tool are separately discussed in the following.

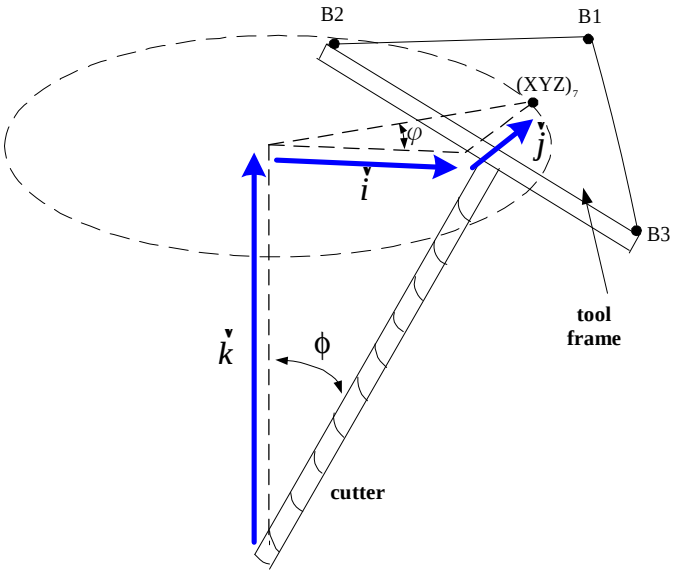

Figure 5-6 Tool paths planning for the error model analysis.

A. Separately analyze and compare the effects of the errors from A chain, B chain, and C chain. If the effects of different chains are similar, the analysis and discussion will be focussed on only one chain.

B. Analyze the effects from the eleven errors (in each motion chain). Find which one is the most significant one that affecting the position accuracy.

C. Investigate the effects of errors with different tool path ($\vec{k}$ is varied). In this research, $\vec{k}$ component is set as: $\vec{k}$=0.2 (ϕ=78.4^0), $\vec{k}$=0.5 (ϕ=60^0), $\vec{k}$=0.8 (ϕ=37^0).

D. Investigate the effects of errors with different machine tool size. In this research, the dimensionless parameters r/R and L/R are selected to represent the dimension of the machine tool. The machine tool size is set as: 1. r/R=0.4 2. r/R=0.6 3. r/R=0.8 4. L/R=5 5. L/R=2.4 6. L/R=1. L is the link length, R is the radius of the upper base frame and r is the tool frame radius.

Part A: Figure 5-7, Figure 5-8 and Figure 5-9 separately show the variation dS_A, dS_B and dS_C with only B chain, A chain, C chain eleven manufacturing errors considered. The dS_A, dS_B, and dS_C separately represent the driving axes displacement variation with and without manufacturing errors consideration. The definitions of dS_A, dS_B and dS_C are:

$dS_A = S_{A\ error}$ (Eq. 5-18) $- S_{A\ without\ error}$ (Eq. 3-22);

$dS_B = S_{B\ error}$ (Eq. 5-17) $- S_{B\ without\ error}$ (Eq. 3-18);

$dS_C = S_{C\ error}$ (Eq. 5-19) $- S_{C\ without\ error}$ (Eq. 3-26).

In Figure 5-7, the eleven B chain manufacturing errors are (1) $[\text{Frame error}]_B$: α_B, β_B, $\gamma_B = 1^0$, $\delta_{FxB} = \delta_{FyB}$ =1mm. (2) $[\text{Pin error}]_B$: $\phi_B = 1^0$, $\lambda_B = 1^0$. (3) $[\text{Ball error}]_B$: δ_{JxB}=1mm, δ_{JzB}=1mm. (4)$[\text{Spindle error}]_B$: δ_{SxB} =1mm, δ_{SyB} =1mm. In Figure 5-8, the eleven A chain manufacturing errors are (1) $[\text{Frame error}]_A$: α_A, β_A, $\gamma_A = 1^0$, $\delta_{FxA} = \delta_{FyA}$ =1mm. (2) $[\text{Pin error}]_A$: $\phi_A = 1^0$, $\lambda_A = 1^0$. (3) $[\text{Ball error}]_A$: δ_{JxA}=1mm, δ_{JzA}=1mm. (4)$[\text{Spindle error}]_A$: δ_{SxA} =1mm, δ_{SyA} =1mm. In Figure 5-9, the eleven A chain manufacturing errors are (1) $[\text{Frame error}]_C$: α_C, β_C, $\gamma_C = 1^0$, $\delta_{FxC} = \delta_{FyC}$ =1mm. (2) $[\text{Pin error}]_C$: $\phi_C = 1^0$, $\lambda_C = 1^0$. (3) $[\text{Ball error}]_C$: δ_{JxC}=1mm, δ_{JzC}=1mm. (4) $[\text{Spindle error}]_C$: δ_{SxC} =1mm, δ_{SyC} =1mm.

From the analysis results in Figure5-7, Figure 5-8, and Figure 5-9, it is found that the eleven manufacturing errors generated from different kinematic chain have nearly the same effects on the position accuracy of the hybrid parallel link machine tool. This result seems reasonable because the three moving axes are evenly arranged on a circle to form an equilateral triangle. The circle is located on the XY-plane of the $(XYZ)_0$ coordinate system. From the geometric relationship, it is obvious that the arrangement has a symmetric structure. Therefore, only the effects from the eleven

manufacturing errors that appeared on the B chain will be discussed in the following sections. The symmetric situation can also be understood by shifting forward 120^o of the results in Figure 5-8 and shifting forward 240^o of the results in Figure 5-9. The shifting angle 120^o is the angle between the B chain and A chain and 240^o is the angle between the B chain and C chain. It is found that the results of Figure 5-8 and Figure 5-9 are the same with the results of Figure 5-7 after the shifting.

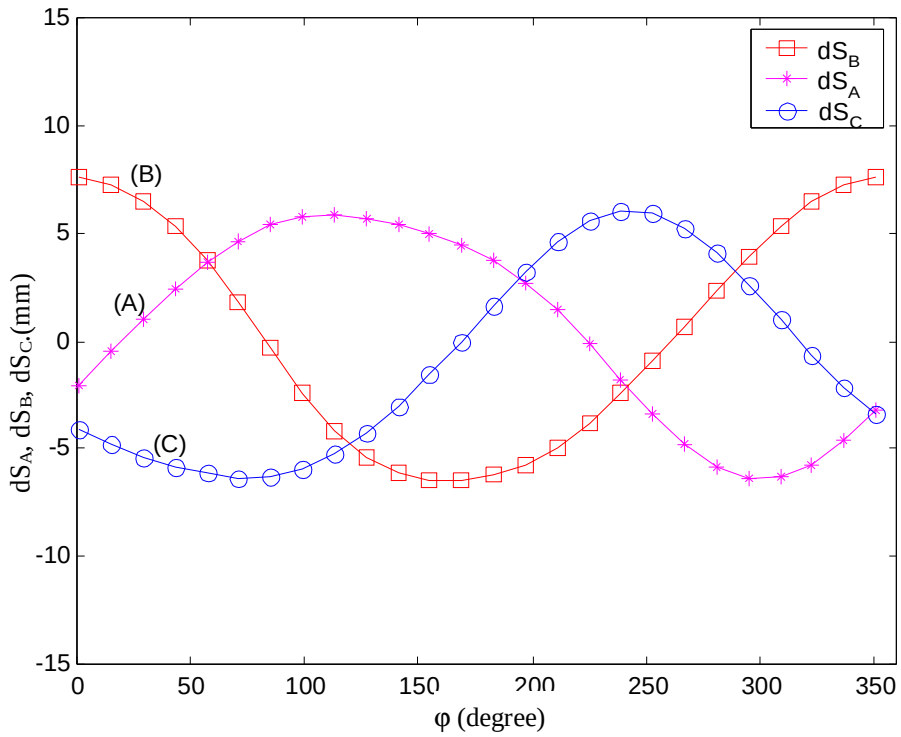

Figure 5-7 The effects of the B chain manufacturing errors on the variation of dS_A, dS_B, dS_C control position ($\dot{k}$ =0.8).

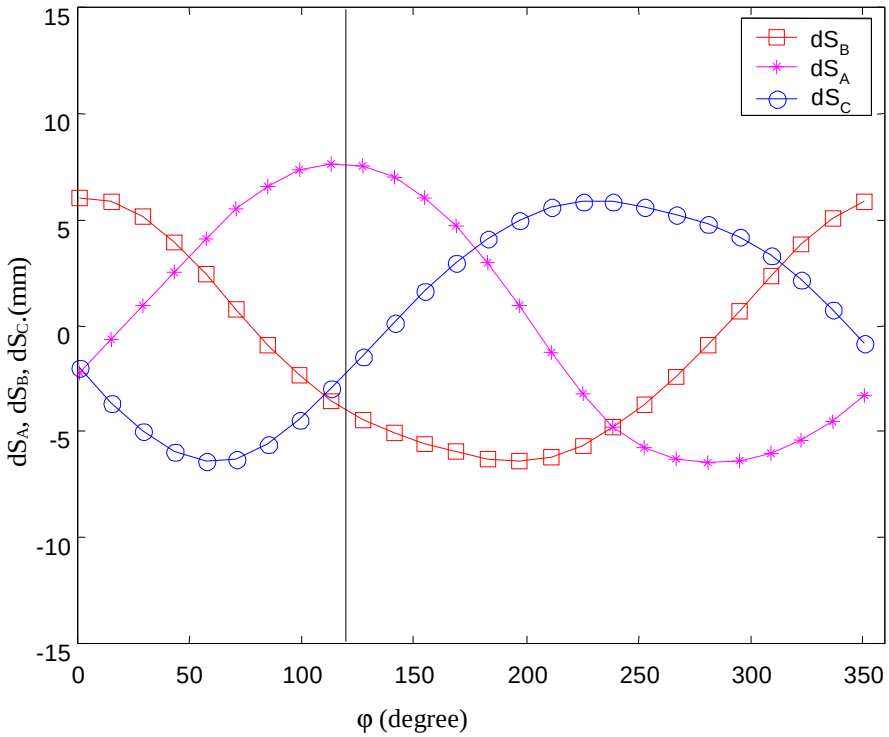

Figure 5-8 The effects of the A chain manufacturing errors on the variation of dS_A, dS_B, dS_C control position ($\dot{k}$ =0.8).

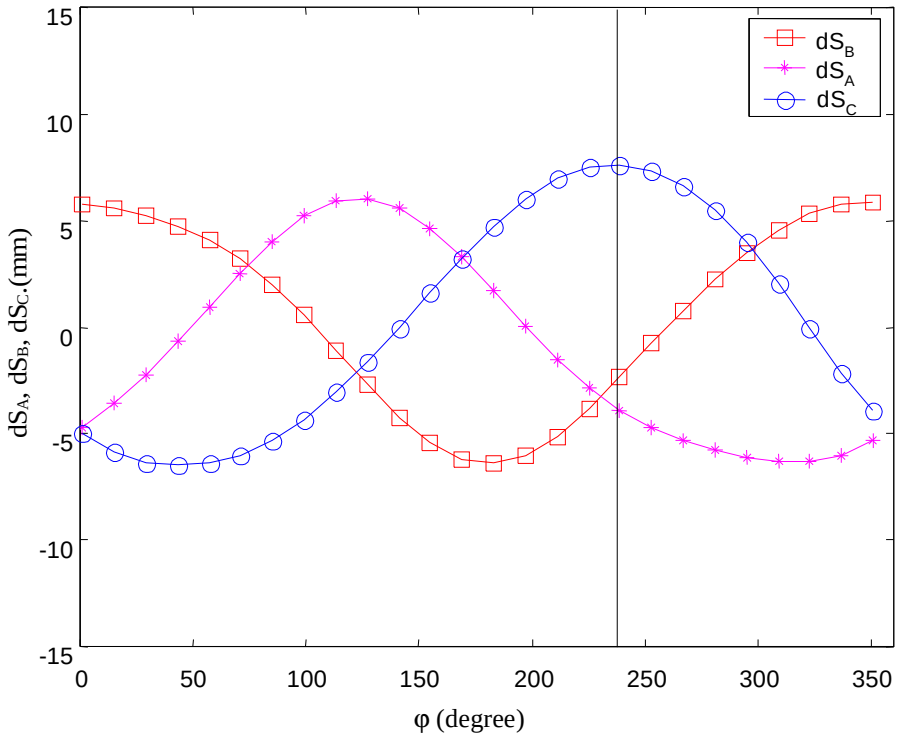

Figure 5-9 The effects of the C chain manufacturing errors on the variation of dS_A, dS_B, dS_C control position ($\dot{k}$ =0.8).

Part B: Figure 5-10 shows the effects of the B chain eleven manufacturing errors on the dS_A, dS_B and dS_C with k=0.8. The effects of $\alpha_B=1^0$, $\beta_B=1^0$, $\phi_B=1^0$ are shown in Figure 5-10a. The effects of $\gamma_B=1^0$, $\lambda_B=1^0$, δ_{FxB}=1mm are shown in Figure 5-10b. The effects of δ_{FyB}=1mm, δ_{JxB}=1mm, δ_{JzB}=1mm, δ_{SxB}=1mm, δ_{SyB}=1mm are shown in Figure 5-10c. From the results in Figure 5-10, it is clearly seen that the dS_A, dS_B, dS_C are varied not only with the error types but also with the tool position φ. The variation of the magnitude of dS_A, dS_B, dS_C are twingle together with the φ varied. Comparing the analysis results about the effects of errors on the control position variation dS_A, dS_B and dS_C in Figure 5-10a~5-10c, however, it is found that the $\alpha_B=1^0$ is the most significant one and the $\phi_B=1^0$ is the second one. The effects of $\gamma_B=1^0$, $\lambda_B=1^0$, δ_{FxB}=1mm and δ_{FyB}=1mm, δ_{JxB}=1mm, δ_{JzB}=1mm, δ_{SxB}=1mm, δ_{SyB}=1mm are relative small. The $\alpha_B=1^0$ is one of the frame error and $\phi_B=1^0$ is one of the pin joint error. This result implies that precise assembly processes are more important than the other components manufacturing processes. Pin joints are also considered as the key components of the hybrid parallel link machine tool.

a.

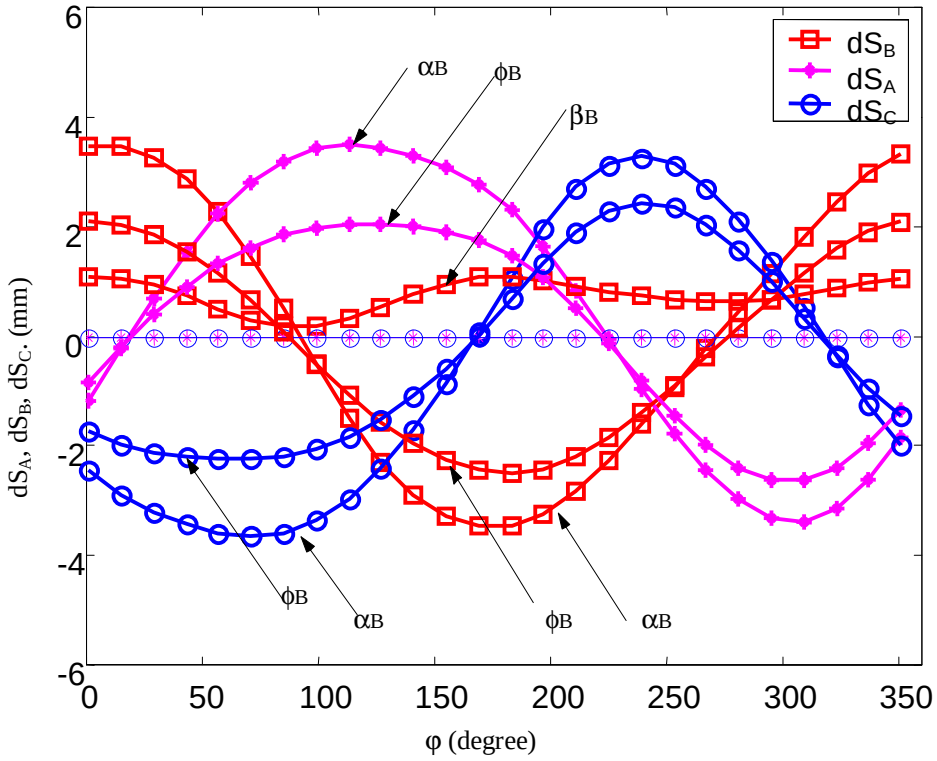

b.

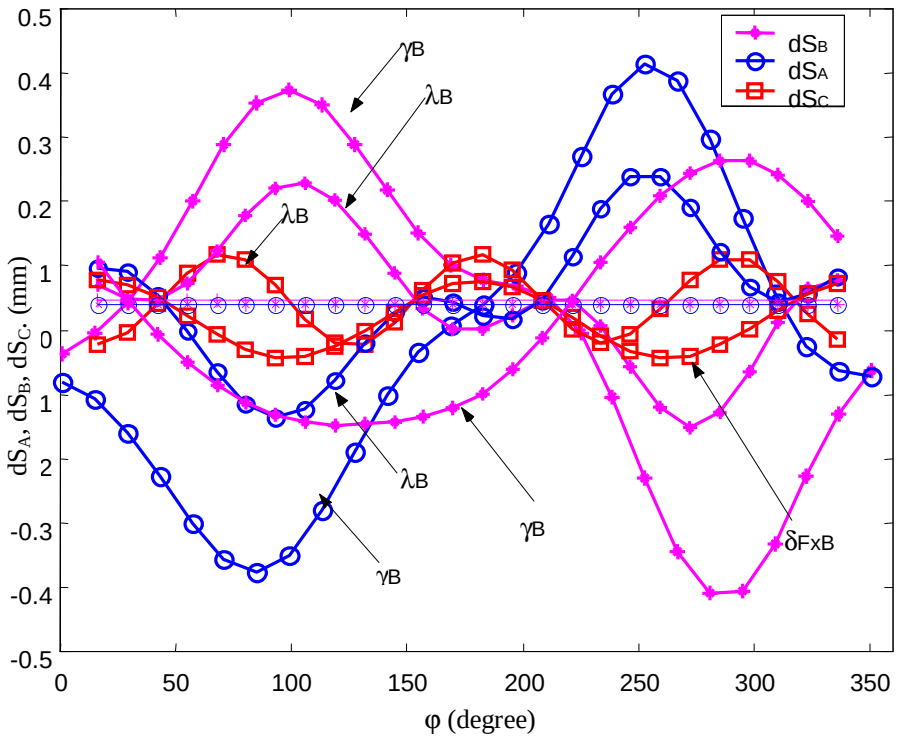

c.

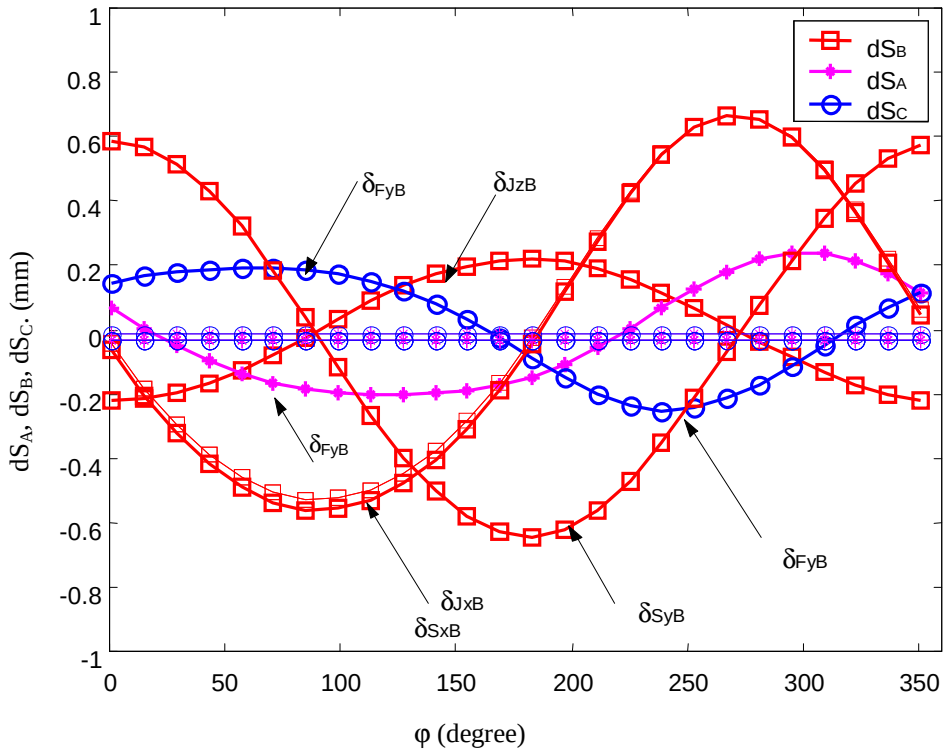

Figure 5-10 Comparison on the effects of different type B chain errors on the control position variation of dS_A, dS_B, dS_C (k=0.8). (a) $\alpha_B=1^0$, $\beta_B=1^0$, $\phi_B=1^0$ (b) $\gamma_B=1^0$, $\lambda_B=1^0$, δ_{FxB}=1mm (c) δ_{FyB}=1mm, δ_{JxB}=1mm, δ_{JzB}=1mm, δ_{SxB}=1mm, δ_{SyB}=1mm

Part C: The tool paths planing for the analysis were already discussed in the previous section. The smaller $\vec{k}$ value means that the inclination angle of tool axis is larger (Figure 5-6). In Figure 5-11, the smaller $\vec{k}$ value is found to have larger dS_A, dS_B and dS_C variation. In the other wards, the larger effects of the manufacturing errors are found with the larger tool axis inclination angle. Although only the errors in the B chain are considered, the result tendency is appeared in all the A, B, and C chain. From a practical machining viewpoint, this result in Figure 5-11 implies that small tool axis inclination angle is better and is suggested for the machine design.

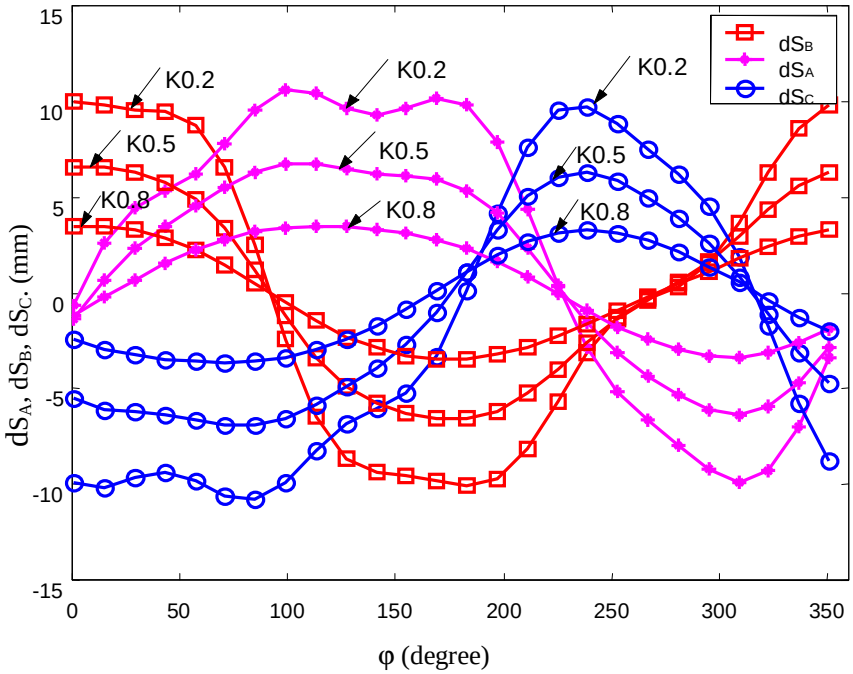

Figure 5-11 Comparison on the effects of various $\vec{k}$ components on the control position variation of dS_A, dS_B, dS_C with B chain errors considered. (1) k=0.2, α_B=1° (2) k=0.5, α_B =1° (3) k=0.8, α_B =1°

Part D: The effect of the dimension variation of the machine tool is another interesting topic for applying the developed machine tool into the real machining processes. In this research, two dimensionless variables (r/R and L/R) are adopted to represent the dimension variation of the machine tool. Figure 5-12 shows the effects of r/R on the variation of dS_A, dS_B and dS_C with (1) r/R=0.8, $\alpha_B = 1^0$ (2) r/R=0.6, $\alpha_B = 1^0$ (3) r/R=0.4, $\alpha_B = 1^0$. There is no variation of dS_B found with r/R varied from r/R=0.8, r/R=0.6, and r/R=0.4 in the whole range of angle. In the A chain and C chain, the absolute value of dS_A and dS_C are significantly increased with the r/R ratio decreased from 0.8, 0.6, to 0.4 in the range $0^o \leqq \varphi \leqq 240^o$. On the contrary, the absolute value of dS_A and dS_C are decreased with the r/R ratio decreased from 0.8, 0.6, to 0.4 in the $240^o \leqq \varphi \leqq 360^o$. It is worth mentioning that no any manufacturing errors from A chain and C chain are included in this analysis. Figure 5-13 shows the effects of L/R on the variation of dS_A, dS_B and dS_C with (1) L/R =5, $\alpha_B = 1^o$ (2) L/R =2.4, $\alpha_B = 1^0$ (3) L/R =1.0, $\alpha_B = 1^0$. There is only very little variation of dS_B found with L/R varied from L/R=5, L/R=2.4, and L/R=1.0 in the whole range of angle ϕ. In the A chain and C chain, the dS_A and dS_C are slightly decreased with the L/R ratio increased from 1.0, 2.4, to 5.

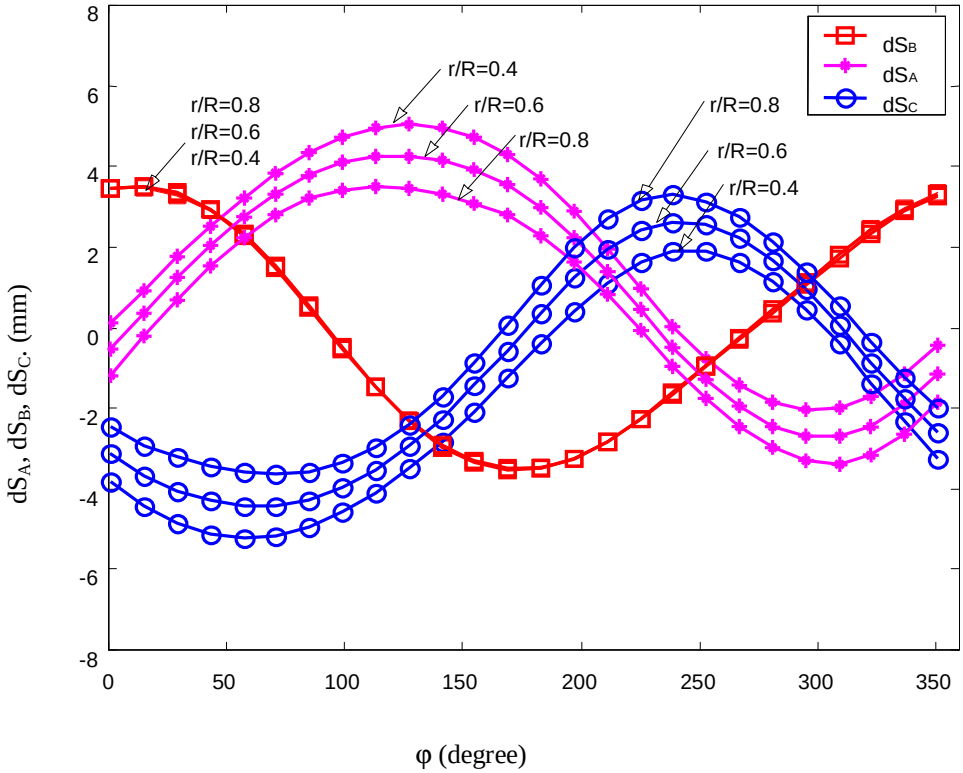

Figure 5-12 Comparison on the effects of various r/R ratio on the control position variation of dS_A, dS_B, dS_C with B chain errors considered. (1) r/R=0.8, $\alpha_B = 1^0$ (2) r/R=0.6, $\alpha_B = 1^0$ (3) r/R=0.4, $\alpha_B = 1^0$

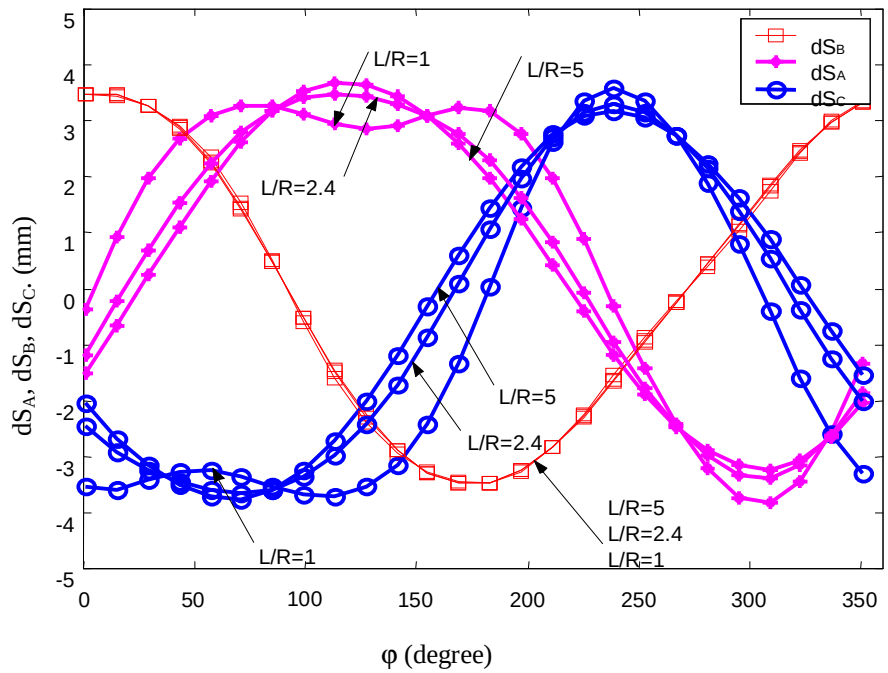

Figure 5-13 Comparison on the effects of various L/R ratio on the control position variation of dS_A, dS_B, dS_C with B chain errors considered. (1) L/R =5, $\alpha_B = 1^0$ (2) L/R =2.4, $\alpha_B = 1^0$ (3) L/R =1.0, $\alpha_B = 1^0$

5.3 Theoretical error model analysis for commercial controller

It is of great difficulty to verify the error model in practice. In this section, analytical model of error sensitivity is developed based on the parameters that offered by the commercial controller. The reason is that the commercial control is used in the hybrid machine tool developed for this research. By considering all the adjustable error parameters in commercial controller, the error model derivation and simulation are carried out again to verify the error model theories.

5.3.1 Definition of error parameters

Type, symbol and meaning of error sources for the commercial controller are summarized in Table 5-1.

Table 5-1 Type, symbol and meaning of error source

Type		Symbol	remark
Ball joint error	i =A、B、C	ΔX_{iB}、ΔY_{iB} ΔZ_{iB}	Assuming that offset exists between real rotational axis of ball joint and its ideal assembly position.
Pin joint error	i =A、B、C	ΔX_{iP}、ΔY_{iP}	Assuming that offset lies in real rotational axis of pin joint and its ideal assembly position.
Link length error	i =A、B、C	ΔL_i	Length error of links resulted from manufacturing processes.
Tool length error		ΔL_T	Tool length error generated by manufacturing processes.

5.3.2 Error model of direct kinematics

The homogeneous transformation matrix between endpoints $O_{bA}', O_{bB}', O_{bC}'$ of three ball joints on tool platform relative to spatial coordinates system $(XYZ)_{0'}$ is established and the relationship of coordinates transformation can be written as follows:

a. Coordinates of ball joint of A chain,

$$O_{bA}'=({}^{0'}A_0)_A\,({}^0A_1)_A\,({}^1A_2)_A\,[\mathrm{Pin}]_A\,({}^2A_3)_A\,[\mathrm{Ball\ \ joint}]_A\begin{bmatrix}0\\0\\0\\1\end{bmatrix}=\begin{bmatrix}X_{bA}'\\Y_{bA}'\\Z_{bA}'\\1\end{bmatrix} \tag{5-42}$$

in Eq.(5-42)

$$[\mathrm{Pin}]_A=\begin{bmatrix}1&0&0&\Delta X_{AP}\\0&1&0&\Delta Y_{AP}\\0&0&1&0\\0&0&0&1\end{bmatrix} \tag{5-43}$$

$$[\mathrm{Ball\_joint}]_A=\begin{bmatrix}1&0&0&\Delta X_{AB}\\0&1&0&\Delta Y_{AB}\\0&0&1&\Delta Z_{AB}\\0&0&0&1\end{bmatrix} \tag{5-44}$$

b. Coordinates of ball joint of B chain,

$$O_{bB}'=({}^{0'}A_0)_B({}^0A_1)_B({}^1A_2)_B[Pin]_B({}^2A_3)_B[Ball\_joint]_B\begin{bmatrix}0\\0\\0\\1\end{bmatrix}=\begin{bmatrix}X_{bB}'\\Y_{bB}'\\Z_{bB}'\\1\end{bmatrix} \tag{5-45}$$

in Eq. (5-45)

$$[\mathrm{Pin}]_B=\begin{bmatrix}1&0&0&\Delta X_{BP}\\0&1&0&\Delta Y_{BP}\\0&0&1&0\\0&0&0&1\end{bmatrix} \tag{5-46}$$

$$[\text{Ball\_joint}]_B = \begin{bmatrix} 1 & 0 & 0 & \Delta X_{BB} \\ 0 & 1 & 0 & \Delta Y_{BB} \\ 0 & 0 & 1 & \Delta Z_{BB} \\ 0 & 0 & 0 & 1 \end{bmatrix} \tag{5-47}$$

c. Coordinates of ball joint of C chain

$$O_{bC}' = ({}^{0'}A_0)_C ({}^0A_1)_C ({}^1A_2)_C [Pin]_C ({}^2A_3)_C [Ball\_joint]_C \begin{bmatrix} 0 \\ 0 \\ 0 \\ 1 \end{bmatrix} = \begin{bmatrix} X_{bC}' \\ Y_{bC}' \\ Z_{bC}' \\ 1 \end{bmatrix} \tag{5-48}$$

in Eq. (5-48)

$$[\text{Pin}]_C = \begin{bmatrix} 1 & 0 & 0 & \Delta X_{CP} \\ 0 & 1 & 0 & \Delta Y_{CP} \\ 0 & 0 & 1 & 0 \\ 0 & 0 & 0 & 1 \end{bmatrix} \tag{5-49}$$

$$[\text{Ball\_joint}]_C = \begin{bmatrix} 1 & 0 & 0 & \Delta X_{CB} \\ 0 & 1 & 0 & \Delta Y_{CB} \\ 0 & 0 & 1 & \Delta Z_{CB} \\ 0 & 0 & 0 & 1 \end{bmatrix} \tag{5-50}$$

Due to tool platform being equilateral triangle structure, using Eqs.(5-42), (5-45) and (5-48), three geometric equations including error parameters can be obtained. We have,

$$\begin{aligned} &(X_{bB}'-X_{bA}')^2 + (Y_{bB}'-Y_{bA}')^2 + (Z_{bB}'-Z_{bA}')^2 = C^2 \\ &(X_{bA}'-X_{bC}')^2 + (Y_{bA}'-Y_{bC}')^2 + (Z_{bA}'-Z_{bC}')^2 = C^2 \\ &(X_{bB}'-X_{bC}')^2 + (Y_{bB}'-Y_{bC}')^2 + (Z_{bB}'-Z_{bC}')^2 = C^2 \end{aligned} \tag{5-51a}$$

Rewrite the above equation by using the geometric relations in Eq. (5-42) ~Eq. (5-50), we have

$$(\frac{\sqrt{3}}{2}\cdot L\cdot\cos(q_{A3})-\frac{\sqrt{3}}{2}\cdot hs+\frac{\sqrt{3}}{2}\cdot R)^2+(L\cdot\cos(q_{B3})-\frac{3}{2}\cdot hs+\frac{3}{2}\cdot R+\frac{L}{2}\cdot\cos(q_{A3}))^2+(-L\cdot\sin(q_{B3})-S_B+L\cdot\sin(q_{A3})+S_A)^2=C^2$$

$$(\frac{-\sqrt{3}}{2}\cdot L\cdot\cos(q_{A3})+\sqrt{3}\cdot hs-\sqrt{3}\cdot R-\frac{\sqrt{3}}{2}\cdot L\cdot\cos(q_{C3}))^2+(\frac{-L}{2}\cdot\cos(q_{A3})+\frac{L}{2}\cdot\cos(q_{C3}))^2+(-L\cdot\sin(q_{A3})-S_A+L\cdot\sin(q_{C3})+S_C)^2=C^2$$

$$(\frac{-\sqrt{3}}{2}\cdot L\cdot\cos(q_{C3})+\frac{\sqrt{3}}{2}\cdot hs-\frac{\sqrt{3}}{2}\cdot R)^2+(L\cdot\cos(q_{B3})-\frac{3}{2}\cdot hs+\frac{3}{2}\cdot R+\frac{L}{2}\cdot\cos(q_{C3}))^2+(-L\cdot\sin(q_{B3})-S_B+L\cdot\sin(q_{C3})+S_C)^2=C^2$$

(5-51b)

By carefully examining Eq.(5-51a, b), a high non-liner relationship is existed in Eq. (5-51b). The θ_{A3}, θ_{B3}, and θ_{C3} can not be solved analytically. A numerical method is obviously needed to solve the θ_{A3}, θ_{B3}, and θ_{C3}. The newton-Raphson method is employed in this research to solve these three variables θ_{A3}, θ_{B3}, and θ_{C3}.

To solve the normal vector of tool platform, assuming that local coordinates system of tool platform is { p' } as shown in Figure 5-14. Letting rotational matrix between { p' } and spatial coordinates system be ${}^{0'}(R_{xyz})_{P'}$

$${}^{0'}(R_{xyz})_{P'}=\begin{bmatrix} I_x' & J_x' & K_x' \\ I_y' & J_y' & K_y' \\ I_z' & J_z' & K_z' \end{bmatrix}=\begin{bmatrix} I' & J' & K' \end{bmatrix} \quad (5\text{-}52)$$

Where I', J', K' are the unit vectors of coordinate system { p' } along X, Y, Z-direction. For $X_{p'}$-axis being parallel to line $\overline{O_{bA}'O_{bC}'}$ and $Y_{p'}$-axis normal to line $\overline{O_{bA}'O_{bC}'}$, so I'、J'、K' can be represented as

$$I'=\frac{\overline{O_{bA}'O_{bC}'}}{\left\|\overline{O_{bA}'O_{bC}'}\right\|}=(\frac{O_{bC}'-O_{bA}'}{C}) \quad (5\text{-}53a)$$

$$J'=\frac{\sqrt{3}}{3C}(2\cdot O_{bB}'-(O_{bC}'-O_{bA}')) \quad (5\text{-}53b)$$

$$K'=I'\times J' \quad (5\text{-}53c)$$

Where $\begin{bmatrix} K_x' \\ K_y' \\ K_z' \end{bmatrix}$ is K' orientational component between local coordinates system of tool platform { p' } and coordinates system {0} of upper platform. K` is the normal vector of tool platform plane, also the direction of cutting tool.

$$\begin{bmatrix} i' \\ j' \\ k' \end{bmatrix} = \begin{bmatrix} K_x' \\ K_y' \\ K_z' \end{bmatrix} \tag{5-54}$$

So the geometric center position of tool platform can be solved from the following equation

$$O_C' = \begin{bmatrix} \frac{(X_{bA}'+X_{bB}'+X_{bC}')}{3} \\ \frac{(Y_{bA}'+Y_{bB}'+Y_{bC}')}{3} \\ \frac{(Z_{bA}'+Z_{bB}'+Z_{bC}')}{3} \end{bmatrix} = \begin{bmatrix} O_{CX}' \\ O_{CY}' \\ O_{CZ}' \end{bmatrix} \tag{5-55}$$

Thus, we can work out the center position of tool endpoint with error considered from D-H Transformation.

$$O_E' = O_C' - \begin{bmatrix} i' \\ j' \\ k' \end{bmatrix} \cdot (L_T + \Delta L_T) = \begin{bmatrix} O_{EX}' \\ O_{EY}' \\ O_{EZ}' \end{bmatrix} \tag{5-56a}$$

It is obvious that the center position of tool endpoint with no error considered is,

$$O_E = O_C - \begin{bmatrix} i \\ j \\ k \end{bmatrix} \cdot (L_T) = \begin{bmatrix} O_{Ex} \\ O_{Ey} \\ O_{Ez} \end{bmatrix} \tag{5-56b}$$

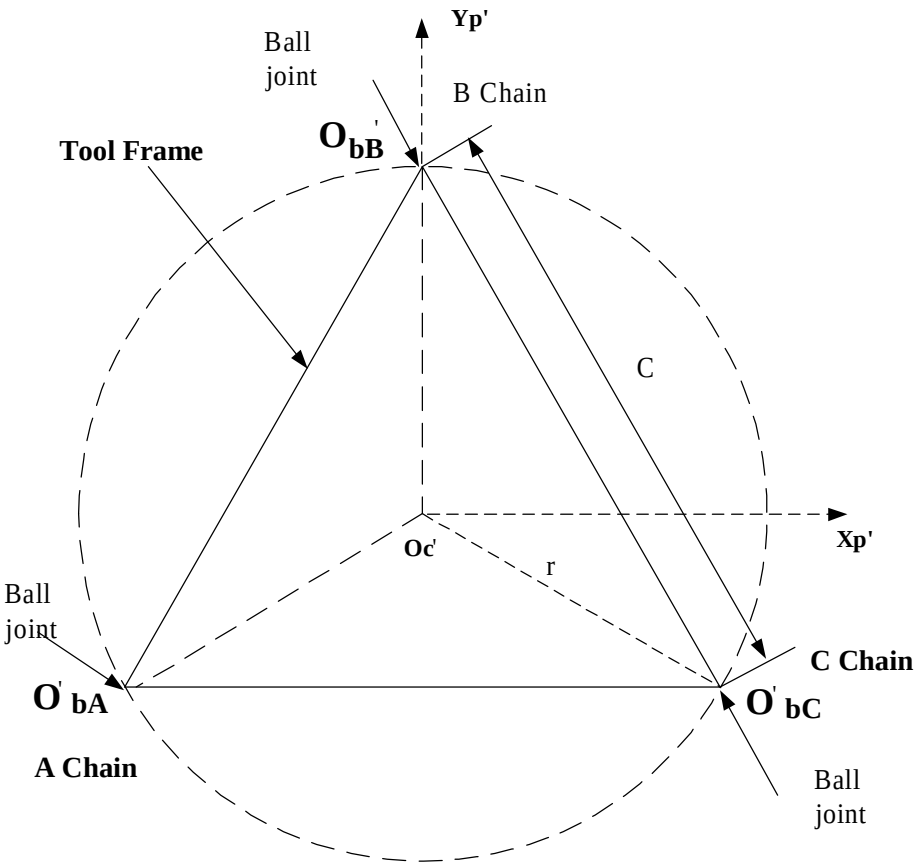

Figure 5-14 Local coordinates system { p' } of tool platform

5.3.3. Sensitivity analysis of error parameters

By performing simulation step by step, we can find out which error parameters have larger effects on position accuracy of machine tool. Simulation in this section is based on the equations of error model of direct kinematic solution derived above and the simulated curve is compared with the ideal designed curve. Dimension setting of the ideal designed curve is a semi-sphere whose radius is 150mm, and the angle of cutting area is $0\sim24^0$ relative to z-axis (see Figure 5-15a). The dimensions of the developed hybrid PLM are summarized in Table 5-3. The sensitivity analysis of the error model is calculated based on the dimensions given in Table 5-3. The flowchart of the calculation and analysis is shown in Figure 5-15b. Sensitivity of error parameters for A chain according to previous error model are shown in Figure 5-16 to 5-22. The same results are found for B chain and C chain. The results for these three chains are symmetrical.

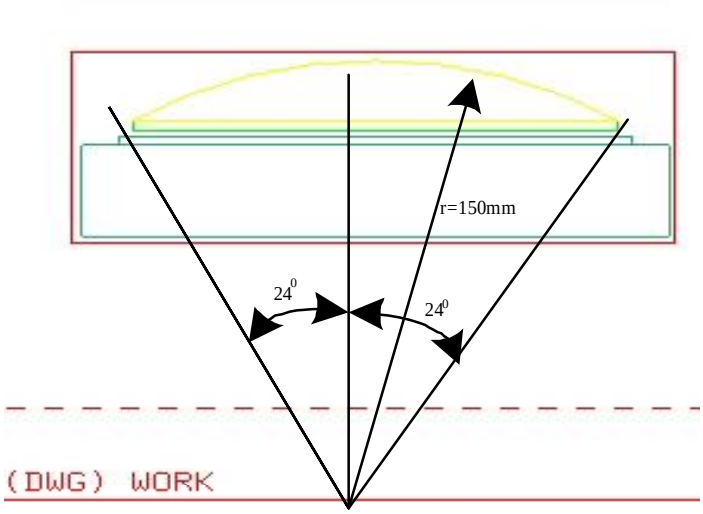

Figure 5-15a CAD model of semi-sphere for simulation

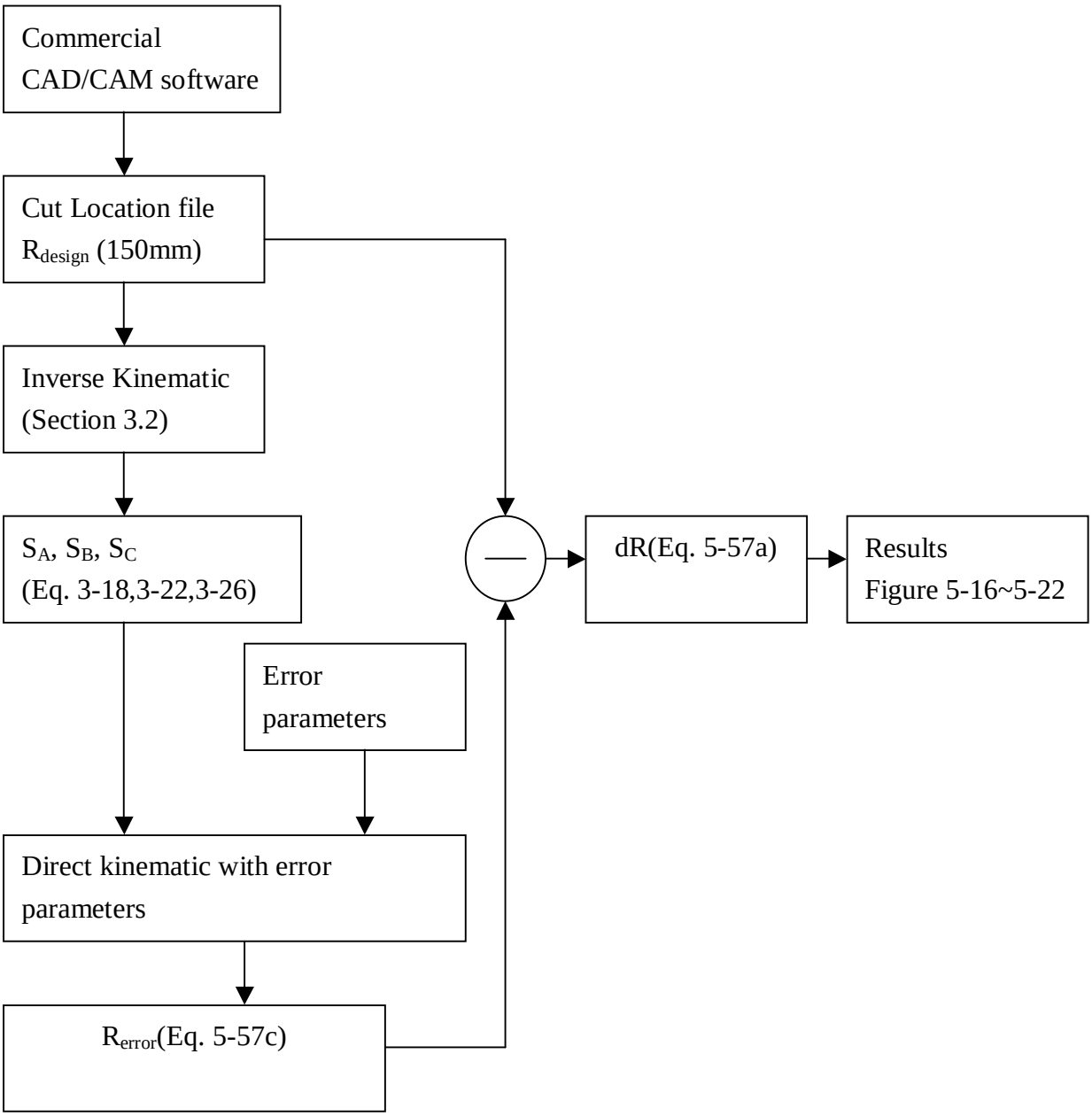

Figure 5-15b Flowchart of the calculation for sensitivity analysis

Table 5-2 Error parameters of the hybrid machine tool based commercial controller

error parameters	ΔX_{AP}	0.015mm	ΔX_{BP}	0.015mm	ΔX_{CP}	0.015mm
	ΔY_{AP}	0.015mm	ΔY_{BP}	0.015mm	ΔY_{CP}	0.015mm
	ΔX_{AB}	0.015mm	ΔX_{BB}	0.015mm	ΔX_{CB}	0.015mm
	ΔY_{AB}	0.03mm	ΔY_{BB}	0.015mm	ΔY_{CB}	0.015mm
	ΔL_A	0.05mm	L_B	0.05mm	L_C	0.05mm
	ΔL_T	0.01mm				

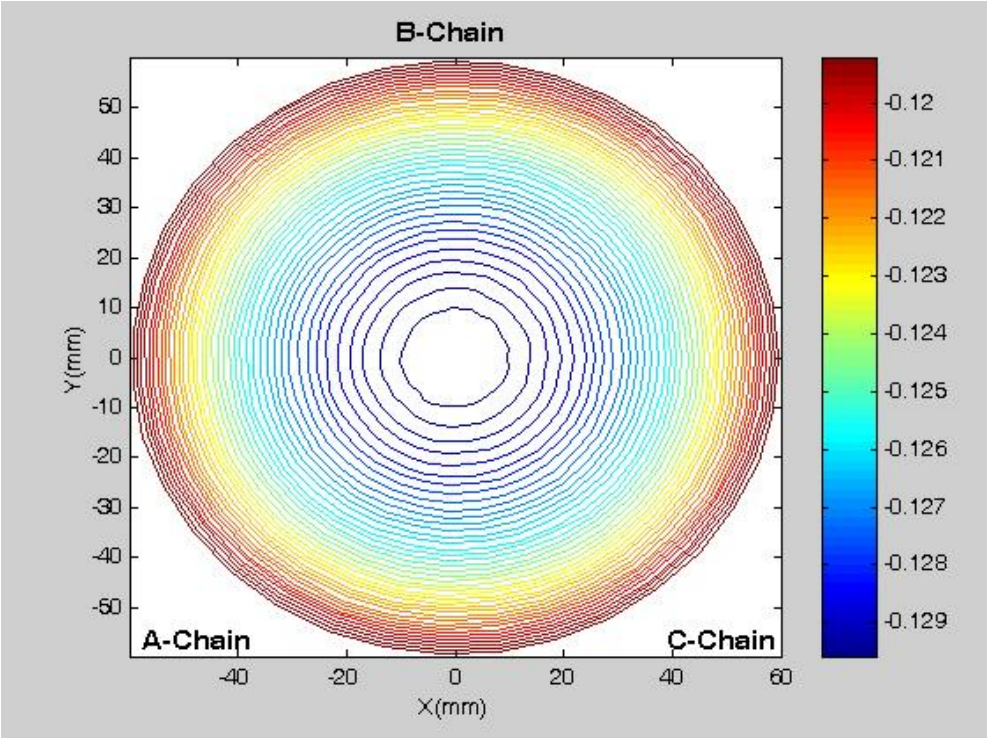

Figure 5-16 Sensitivity analysis with all error parameters included (error parameters are shown in Table 5-2)

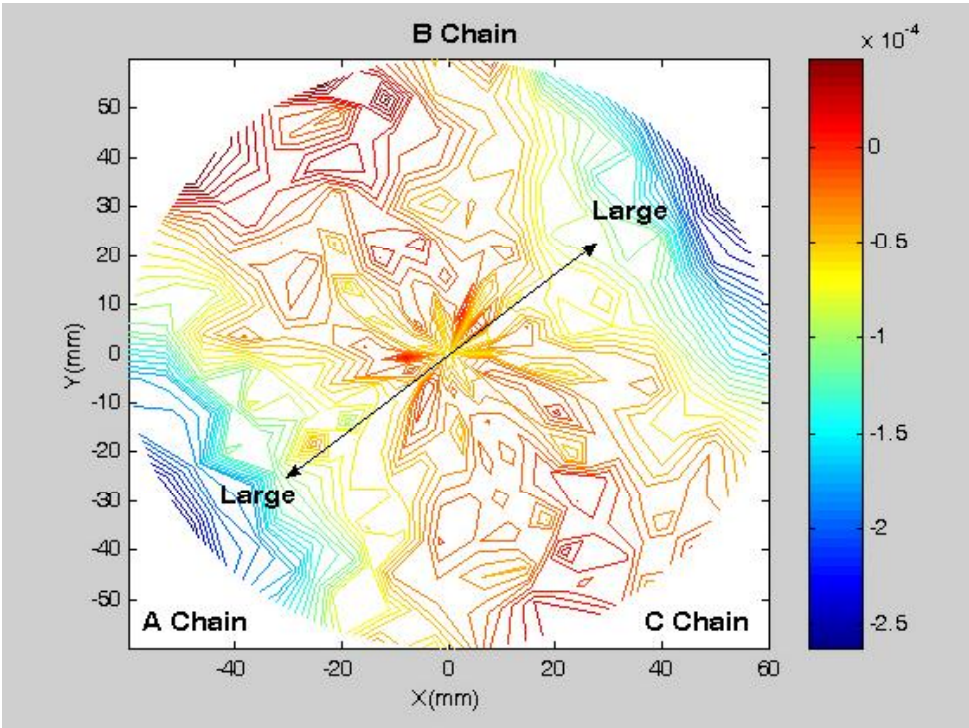

Figure 5-17 Sensitivity analysis of error parameter $\Delta X_{AP} = 0.015\,\text{mm}$ and the other errors are zero

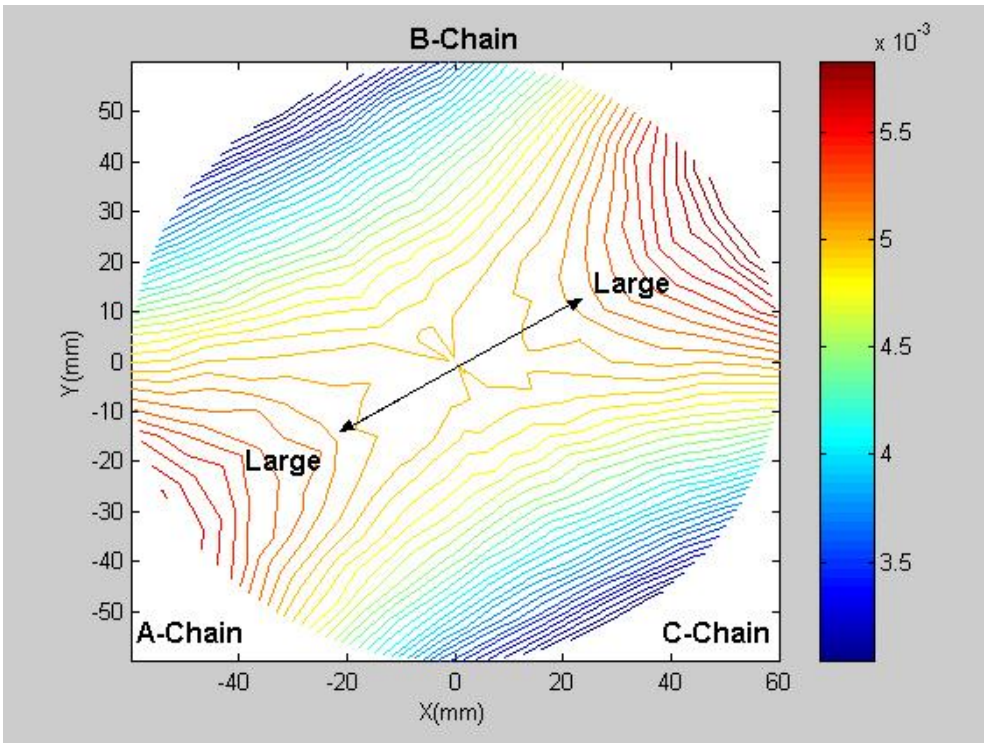

Figure 5-18 Sensitivity analysis of error parameter $\Delta Y_{AP} = 0.015$ mm and the other errors are zero

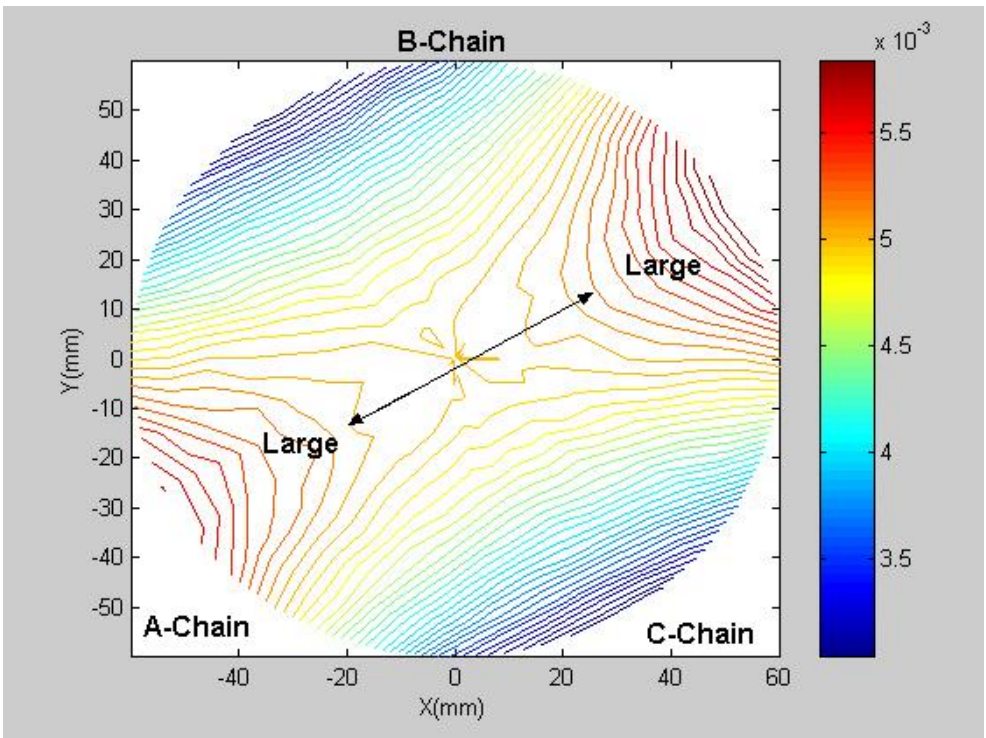

Figure 5-19 Sensitivity analysis of error parameter $\Delta X_{AB} = 0.015$ mm and the other errors are zero

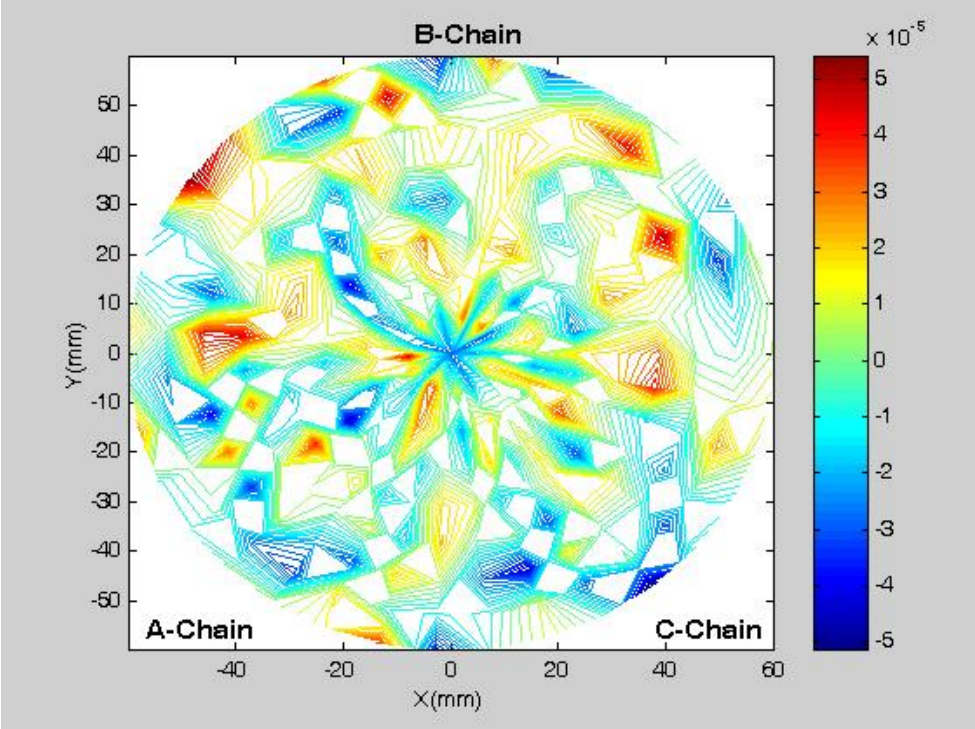

Figure 5-20 Sensitivity analysis of error parameter $\Delta Y_{AB} = 0.03$ mm and the other errors are zero

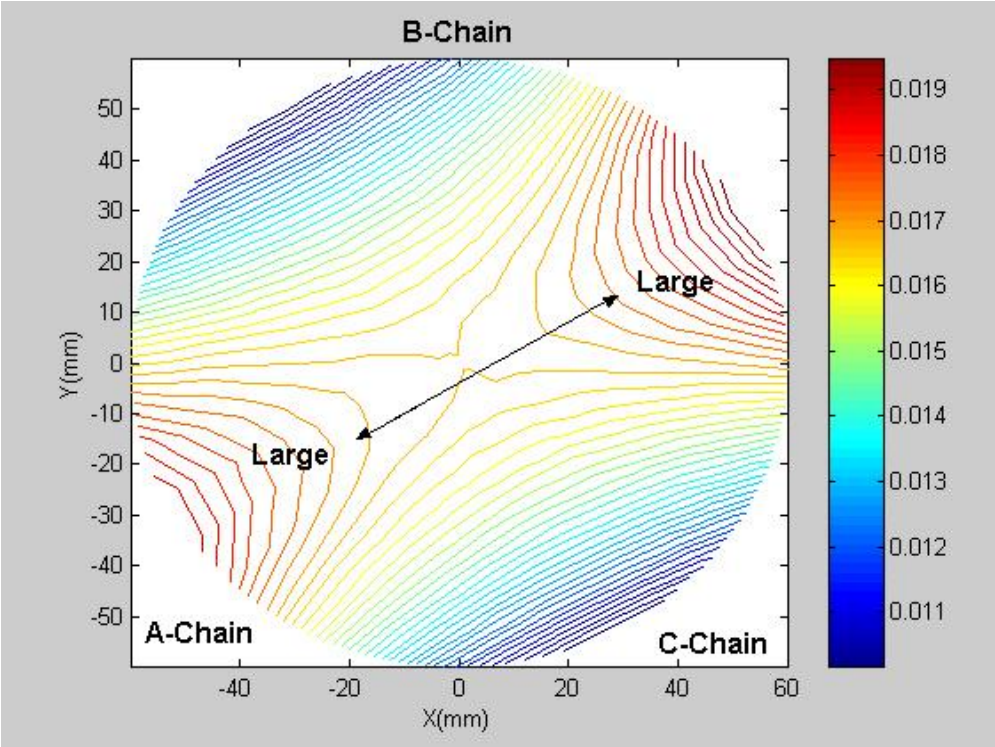

Figure 5-21 Sensitivity analysis of error parameter $\Delta L_A = 0.05$ mm and the other errors are zero

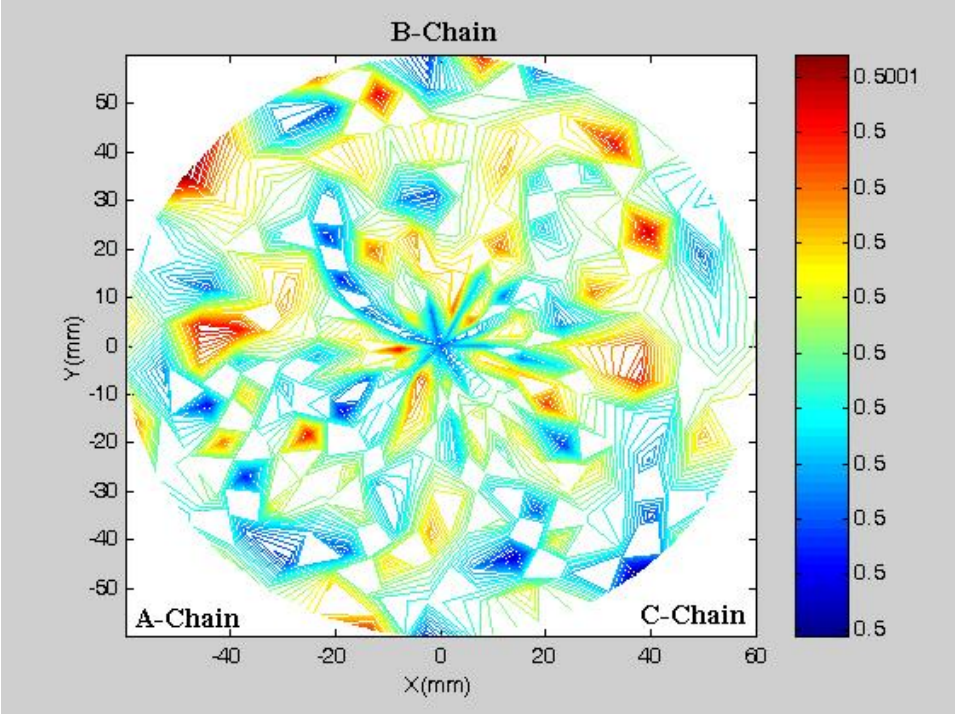

Figure 5-22 Sensitivity analysis of error parameter ΔL_T = 0.01mm and the other errors are zero

The tool paths are given on a semi-sphere and at the cutting position, the angle between tangent of semi-sphere and Z-axis is 5,15, and 25 degree respectively.
The machining error obtained in this analysis is defined to be the radius variation along the normal vector on the point. We have

$$dR = R_{design} - R_{error} = dxi + dyj + dzk \quad (5\text{-}57a)$$

In the above equation, R_{design} is defined as,

$$R_{design} = \sqrt{O_{Ex}^{\ 2} + O_{Ey}^{\ 2} + O_{Ez}^{\ 2}} \quad (5\text{-}57b)$$

Also, R_{error} is defined as,

$$R_{error} = \sqrt{O'_{Ex}^{\ 2} + O'_{Ey}^{\ 2} + O'_{Ez}^{\ 2}} \quad (5\text{-}57c)$$

The flowchart of the calculation and analysis is shown in Figure 5-15b. In Figure

5-15b, the R_{design} is 150mm. The coordinate of R_{design} can be obtained from commercial CAD/CAM software. The inverse kinematics is used to obtain S_A, S_B, and S_C. Both of the obtained S_A, S_B, S_C and the error parameters are input to direct kinematics for calculating the R_{error}. The dR results shown in Figure 5-16~Figure 5-22 can be obtained from Eq. 5-57a.

Table 5-3 Original dimension of machine tool Unit：mm

	A Chain	B Chain	C Chain
Pin joint position	X=298.5871 Y=172.3894	X=0 Y=-345.1346	X=-298.2304 Y=172.1834
Link length	L=1107	L=1107	L=1107
Ball joint position	X=173.4712 Y=100.1409	X=-0.078 Y=-200.0109	X=-172.9441 Y=100.9582

Figure 5-16 shows the machining error results with all manufacturing error parameters considered. The parallel A axis, B axis and C axis are symmetric from geometry viewpoint. The error parameter setting is also symmetric. Therefore, Figure 5-16, displays the symmetric and even character. The largest error region occurs at the center of parallel mechanism. The smallest error is occurs at the boundary area of the machining surface. The variation of machining error is not large, only about 0.015mm.

From Figure 5-17 we can know that the error range is 0.00005~-0.00025 mm with ΔX_{AP} = 0.015mm and the other errors are zero. For ΔY_{AP} = 0.015mm (shown in Figure 5-18), it is found that the error range is 0.006~0.003 mm. In Figure 5-19 (ΔX_{AB} = 0.015mm), the error range of is 0.006~0.003 mm. Figure 5-20 shows that when ΔY_{AB} = 0.03mm, the error range is 0.00005~-0.00005 mm. We can know from Figure 5-21 that the error range is 0.019~0.011 mm when ΔL_A = 0.05mm. It is shown in Figure 5-22 (ΔL_T = 0.01mm) that the error range is 0.5001~0.5 mm. It is worth mentioning that the tool length L_T used in this analysis is 196 mm.

From the results of Figure 5-17 to Figure 5-22, we can further found that when the manufacturing errors comes from the A chain, the generated machining errors are

significantly varied along the plane passing the A chain and mechanism center O′c. The generated machining errors also symmetrically varied with the A chain plane (passing O′c). The maximum machining errors are separately located at the far are nearest region opposite to the A driving axis on the A chain plane. However, the minimum machining errors are located at far region of the A chain plane. Due to the symmetric structure of the parallel mechanism used in this research, the analytical results of manufacturing error sensitivity for B chain and C chain are similar to that of A chain.

The machining errors with error parameters $\Delta X_{AP} = 0.015$mm, $\Delta Y_{AB} = 0.03$mm are separately shown in Figure 5-17 and Figure 5-20. The machining errors generated by these two error parameters are relatively small. For example, the machining error is only about 10^{-3}mm with ΔY_{AB} up to 3mm. Therefore, the effects from these two parameters can be neglected in the practical machining applications.

Figure 5-22 shows the machining error generated by manufacturing error of tool length. It is obvious that the machining error evenly offsets 0.1mm along z-axis with the change of tool length 0.5mm.

5.4 Conclusions

The effects of the manufacturing errors on position accuracy for the hybrid parallel link machine tool to take the advantage of geometry to minimize the errors and increase the accuracy are investigated in this chapter. There are eleven manufacturing errors considered in each kinematics chain. The α_B, β_B, ϕ_B are the most significant errors in the B chain that have large effects on the position accuracy of the machine tool. As the machine tool has a symmetric structure, the α_A, β_A, ϕ_A in A chain and α_C, β_C, ϕ_C in C chain are also significantly affect the position accuracy of the machine tool. Therefore, the engineer is suggested to pay more attention on the tolerance and manufacturing errors of frame structure in the design process. The smaller tool axis inclination angle has better position accuracy with the same manufacturing errors.

Engineer is suggested to use small tool inclination angle in the real machining processes. The effects of the r/R ratio on the position accuracy variation are found more significant than that for the L/R ratio.

In this section, according to error parameters setting of commercial controller, we derived the error model of direct kinematics solution and established error analytical model with the manufacturing errors and assembly errors of machine tool considered. Based on the error model of direct kinematics, the error sensitivity analysis is carried out. From the analytical results, the position error along Y-axis of pin joint, position error along X-axis of ball joint and the length error of links are found to have significant effects on the machining errors of the developed hybrid machine tool. In the real situation, the manufacturing errors of the hybrid machine tool are very difficult to be obtained. To verify the correctness of the developed error model, a special experiment arrangement is necessary. The error measurement tests are discussed in Section 6.4. Here, the error parameters are given into Commercial controller and machining errors are measured by using Double Ball bar.

Appendix

Part A:

$B1 = N_B(1,1)$ (a.1)

$B2 = N_B(2,1)$ (a.2)

$BS = N_B(1,1)(-\cos(\beta)r) + N_B(2,1)(-r\sin(\beta)\sin(\alpha)) + N_B(3,1)(r\cos(\alpha)\sin(\beta))$ (a.3)

$BC = N_B(2,1)(r\cos(\alpha)) + N_B(3,1)(r\sin(\alpha))$ (a.4)

$UP = P_B(1,1)N_B(1,1) + P_B(2,1)N_B(2,1) + P_B(3,1)N_B(3,1)$

$-Nu(1,1)(\sin(\beta)t) - Nu(2,1)(-\cos(\beta)\sin(\alpha)t) - Nu(3,1)(\cos(\alpha)\cos(\beta)t + Pz)$ (a.5)

Part B:

$A1 = N_A(1,1)$ (b.1)

$A2 = N_A(2,1)$ (b.2)

$$AS = N_A(1,1)\left(\frac{1}{2}\cos(b)r\right) + N_A(2,1)\left(\frac{-1}{2}\sqrt{3}r\cos(a) + \frac{1}{2}r\sin(b)\sin(a)\right) + N_A(3,1)\left(\frac{-1}{2}\sqrt{3}r\sin(a) - \frac{1}{2}r\cos(a)\sin(b)\right) \quad \text{(b.3)}$$

$$AC = N_A(1,1)\left(\frac{-1}{2}\cos(b)\sqrt{3}r\right) + N_A(2,1)\left(\frac{-1}{2}\sqrt{3}r\sin(a)\sin(b) - \frac{1}{2}r\cos(a)\right) + N_A(3,1)\left(\frac{1}{2}\sqrt{3}r\cos(a)\sin(b) - \frac{1}{2}r\sin(a)\right) \quad \text{(b.4)}$$

AP= $P_A(1,1)N_A(1,1)+ P_A(2,1)N_A(2,1)+ P_A(3,1)N_A(3,1)$

$$-N_A(1,1)\sin(b)t - N_A(2,1)(-\cos(b)\sin(a)t) - N_A(3,1)(\cos(a)\cos(b)t + Pz)$$

(b.5)

Part C:

C1 =$N_C(1,1)$ (c.1)

V2 =$N_C(2,1)$ (c.2)

$$CS = N_C(1,1)(\frac{1}{2}\cos(b)r) + N_C(2,1)(\frac{1}{2}\sqrt{3}r\cos(a) + \frac{1}{2}r\sin(b)\sin(a)) +$$

$$N_C(3,1)(\frac{1}{2}\sqrt{3}r\sin(a) - \frac{1}{2}r\cos(a)\sin(b))$$ (c.3)

$$CC = N_C(1,1)(\frac{1}{2}\cos(b)\sqrt{3}r) + N_C(2,1)(\frac{1}{2}\sqrt{3}r\sin(a)\sin(b) - \frac{1}{2}r\cos(a)) +$$

$$N_C(3,1)(\frac{-1}{2}\sqrt{3}r\cos(a)\sin(b) - \frac{1}{2}r\sin(a))$$ (c.4)

CP=

$P_C(1,1)N_C(1,1)+ P_C(2,1)N_C(2,1)+ P_C(3,1)N_C(3,1)$

$$-N_C(1,1)\sin(b)t - N_C(2,1)(-\cos(b)\sin(a)t) - N_C(3,1)(\cos(a)\cos(b)t + Pz)$$ (c.5)

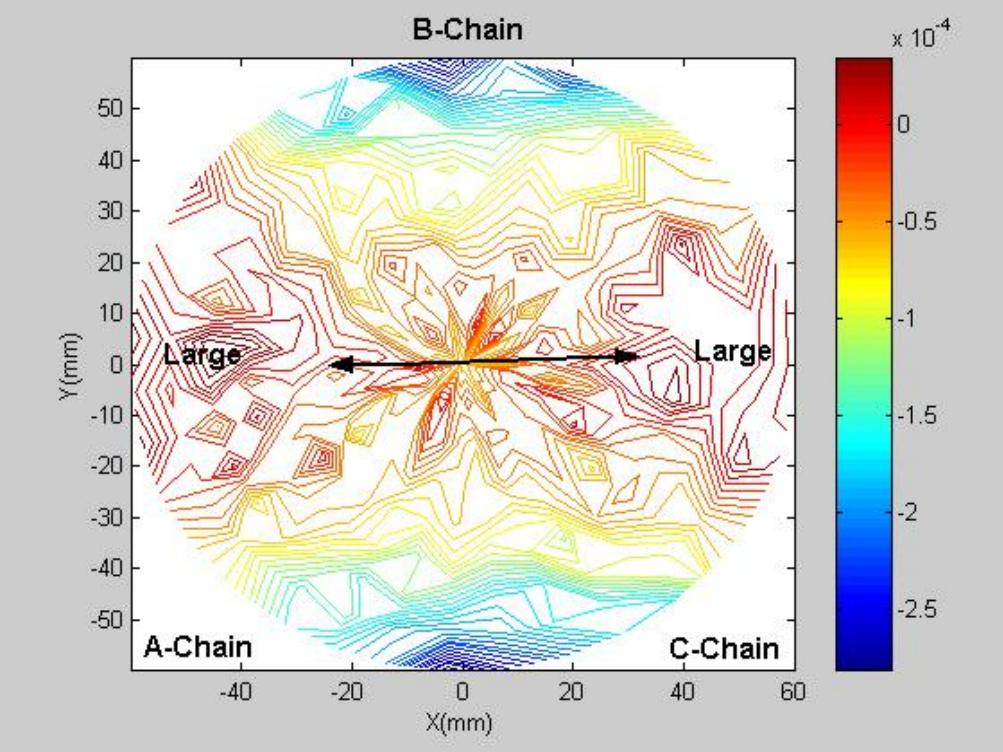

Figure A1 Sensitivity analysis of error parameter $\triangle X_{BP}$=0.015 mm and the other errors are zero

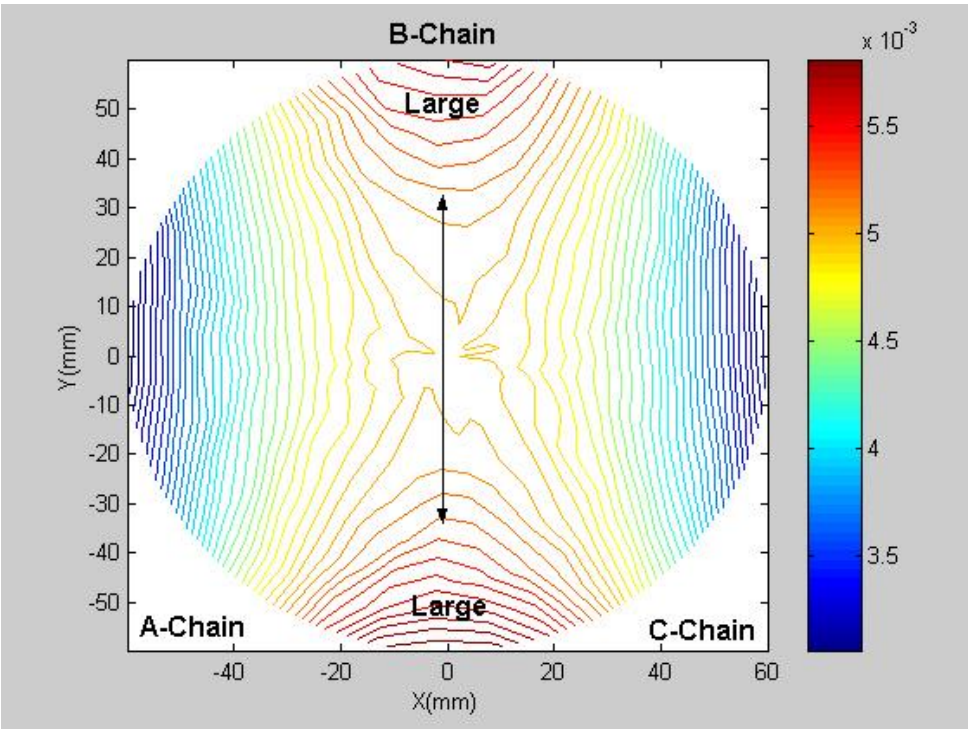

Figure A2 Sensitivity analysis of error parameter $\triangle Y_{BP}$=0.015mm and the other errors are zero

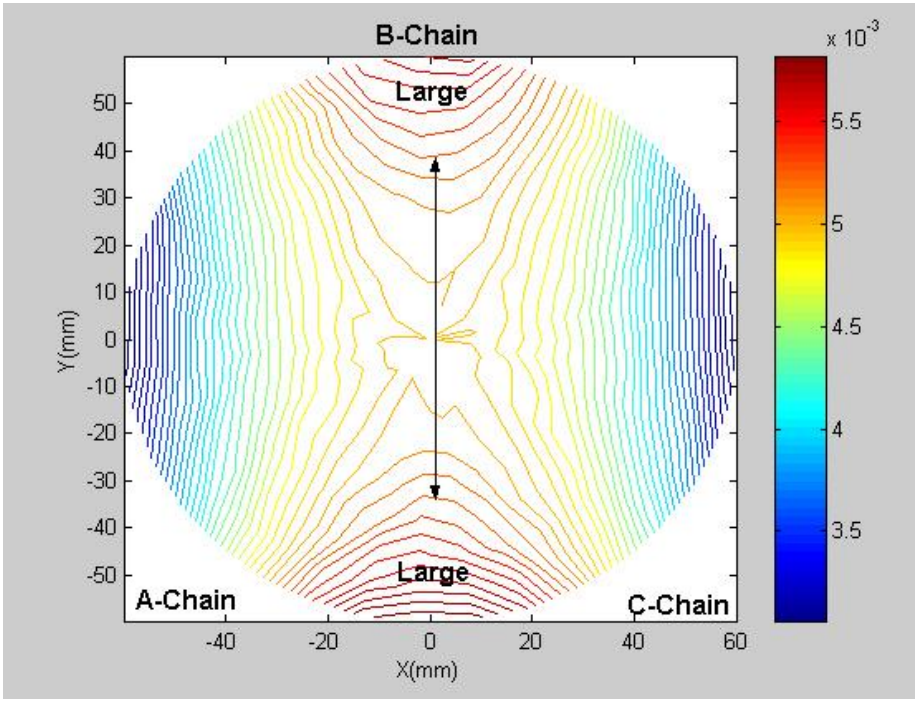

Figure A3 Sensitivity analysis of error parameter $\triangle X_{BB}$=0.015mm and the other errors are zero

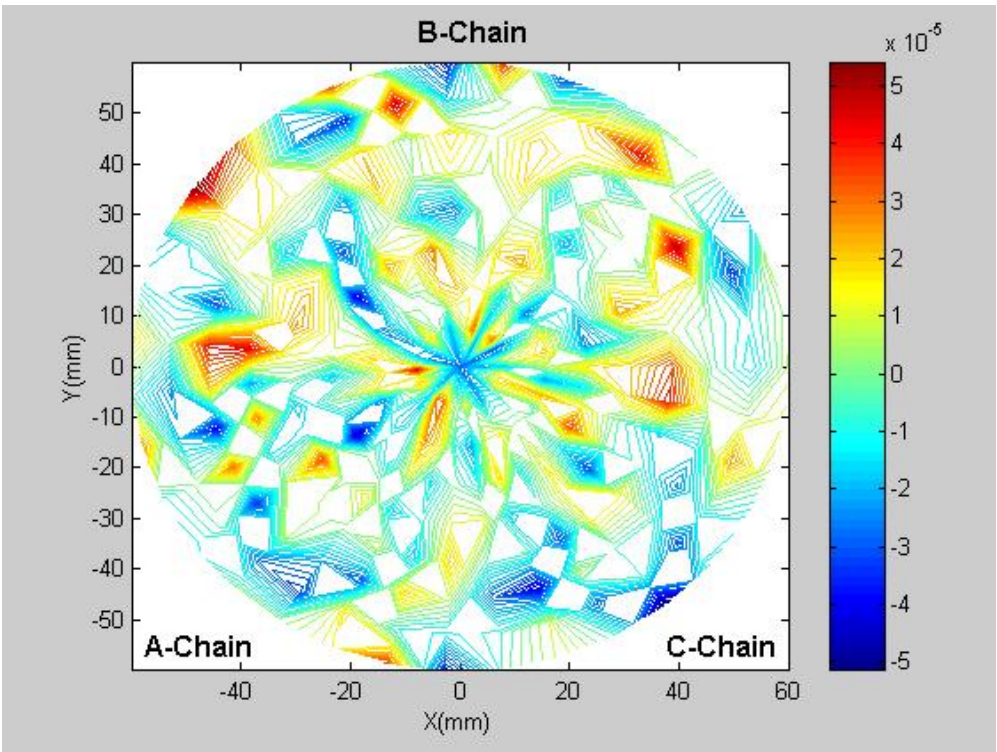

Figure A4 Sensitivity analysis of error parameter $\triangle Y_{BB}$=0.015mm and the other errors are zero

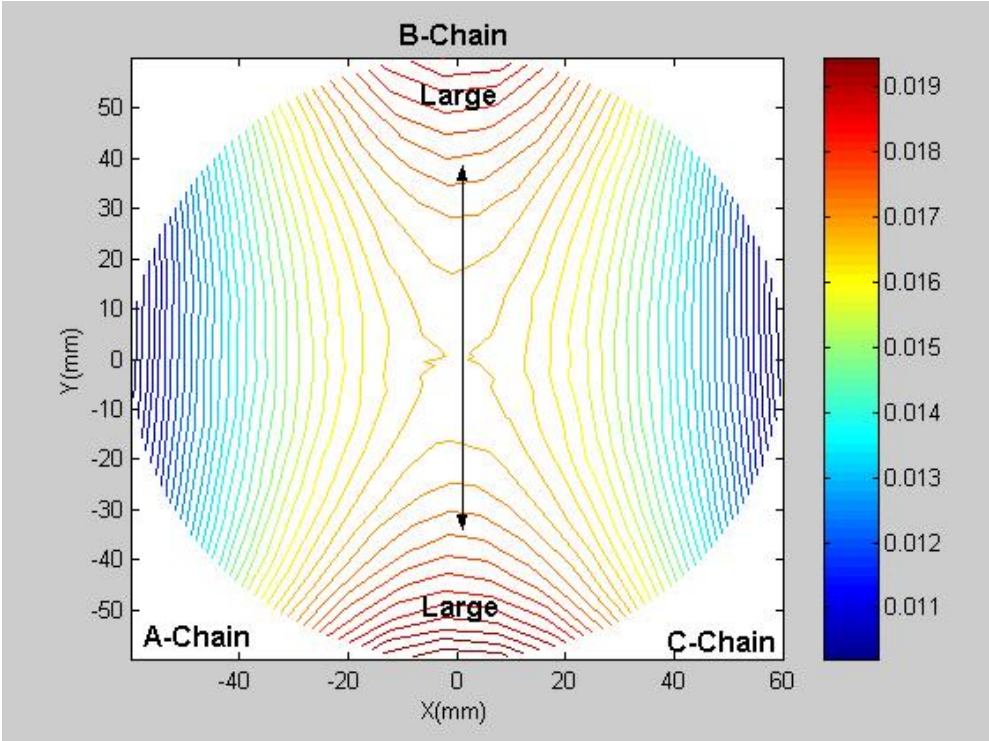

Figure A5 Sensitivity analysis of error parameter $\triangle L_B$=0.05mm and the other errors are zero

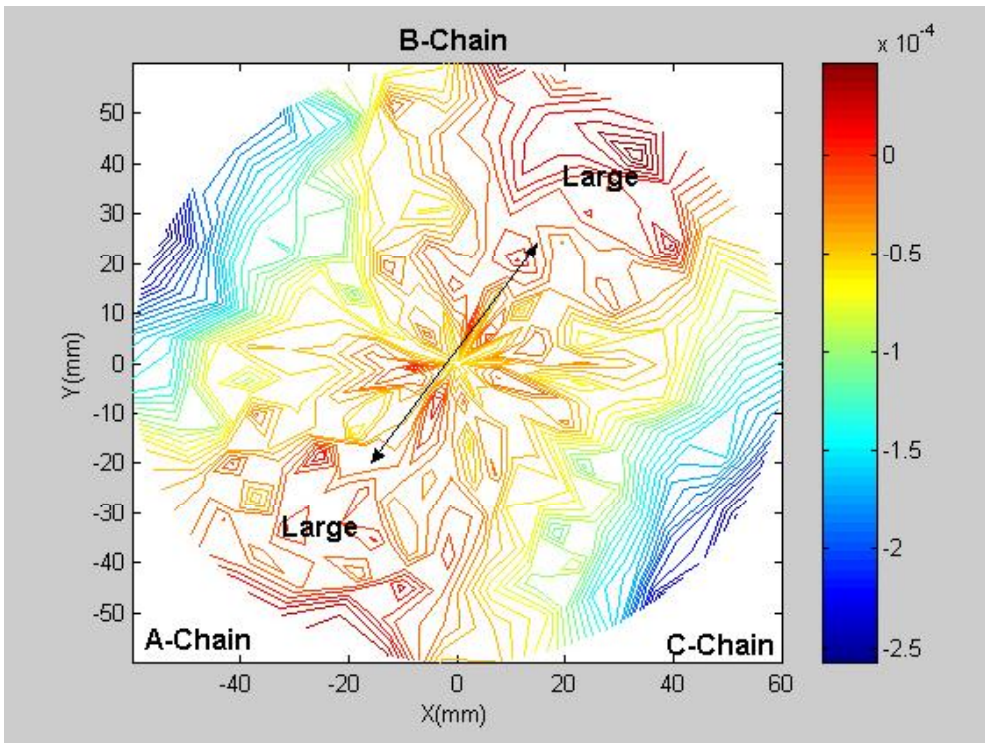

Figure A6 Sensitivity analysis of error parameter $\triangle X_{CP}$=0.015mm and the other errors are zero

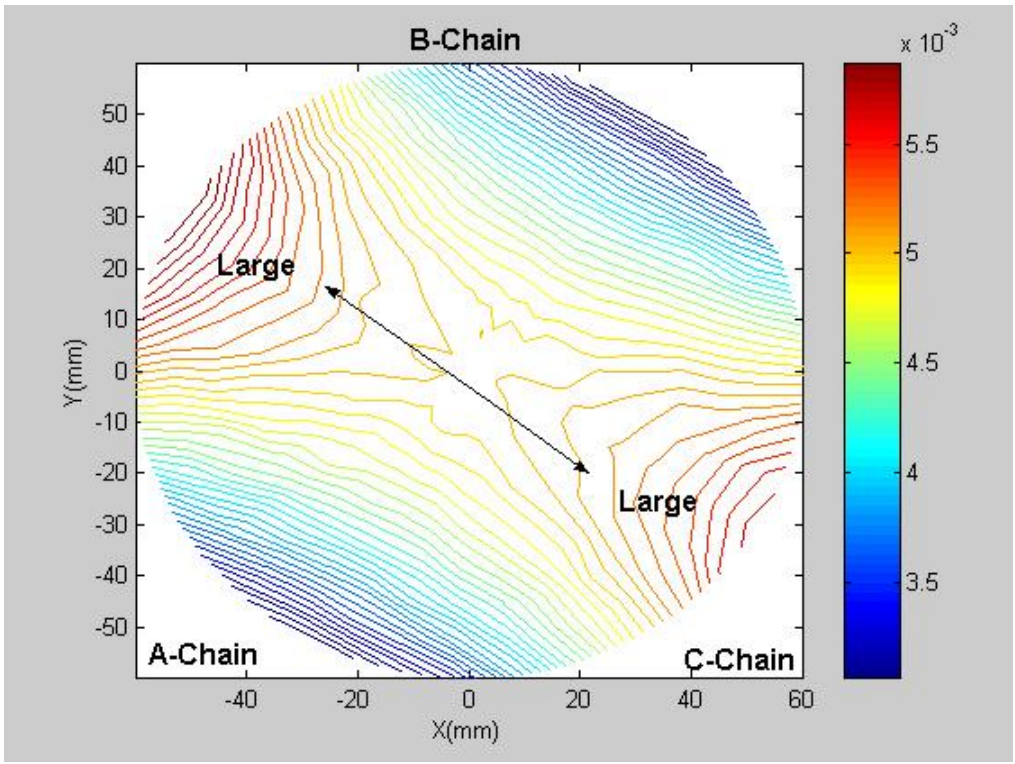

Figure A7 Sensitivity analysis of error parameter $\triangle Y_{CP}$=0.015mm and the other errors are zero

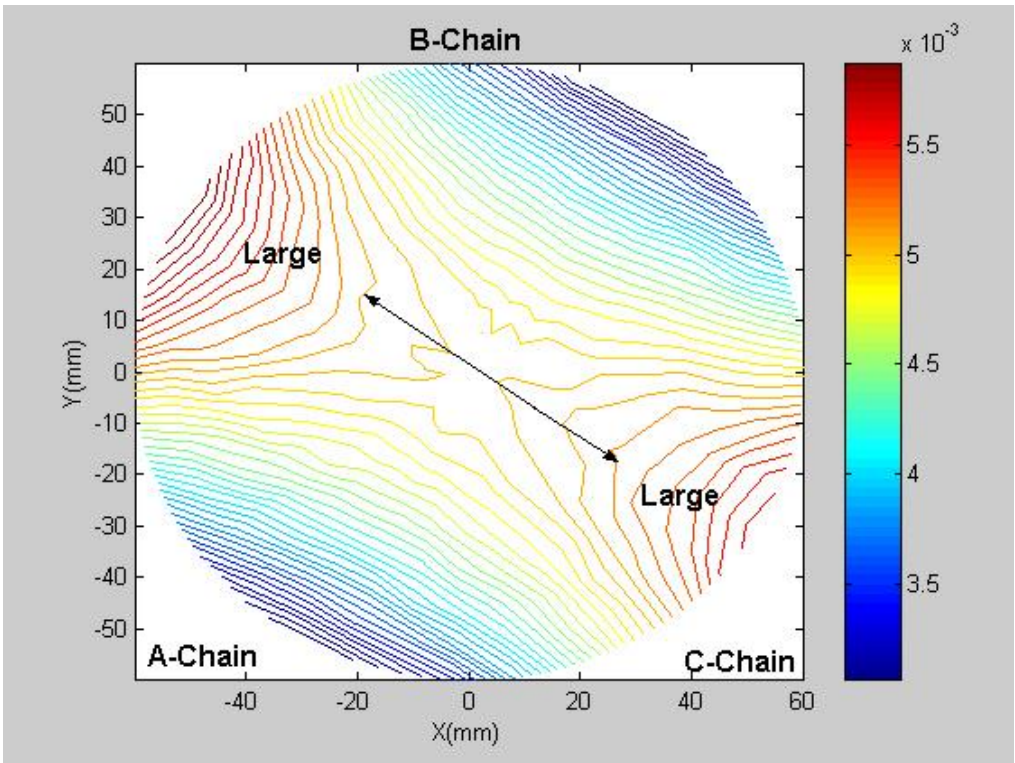

Figure A8 Sensitivity analysis of error parameter $\triangle X_{CB}$=0.015mm and the other errors are zero

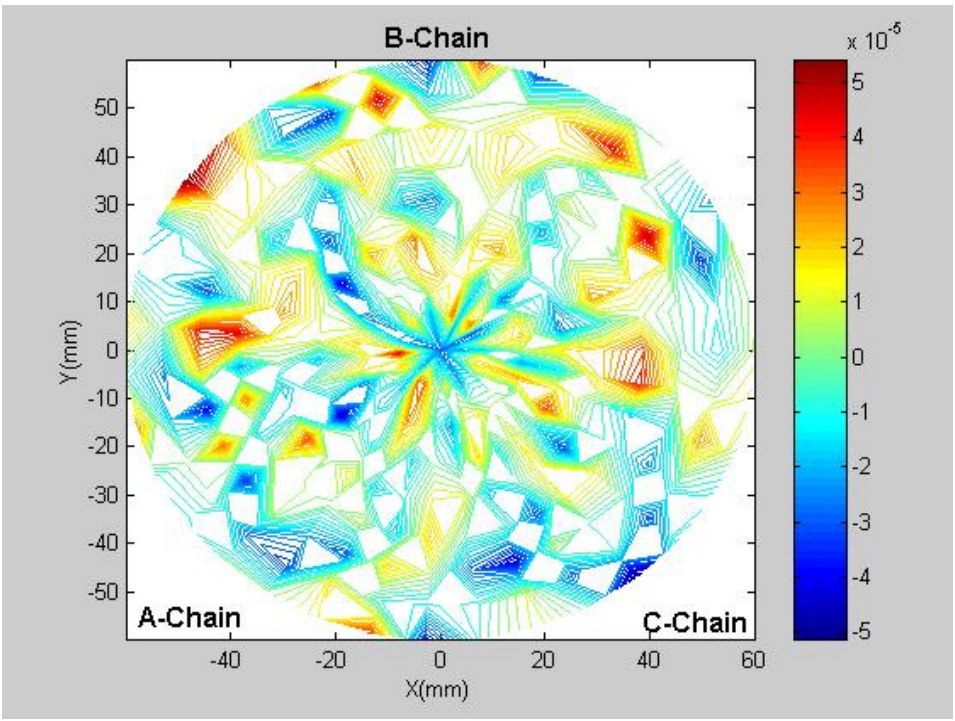

Figure A9 Sensitivity analysis of error parameter △Ycb=0.015mm and the other errors are zero

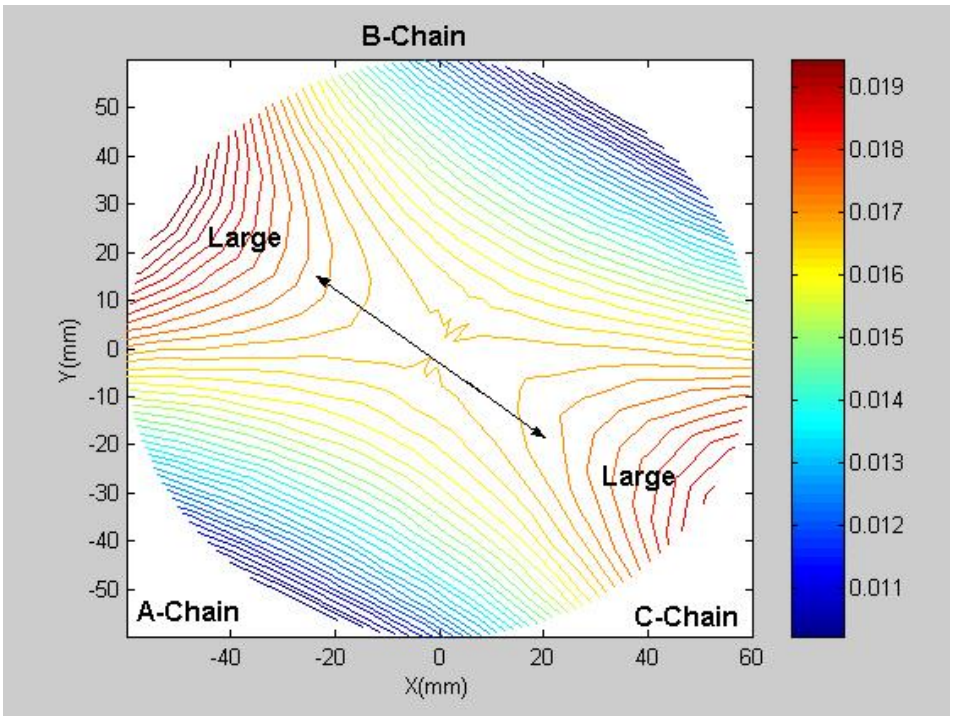

Figure A10 Sensitivity analysis of error parameter $\triangle L_C$=0.05mm and the other errors are zero

References

1. O. Masory, and J. Wang, H. Zhuang, "On the Accuracy of a Stewart Platform-Part II Kinematics Calibration and Compensation," *Proceedings of the 1993 IEEE, International Conference on Robotics and Automation*, pp. 725-731, 1993.

2. J. Wang, and O. Masory, "On the Accuracy of a Stewart Platform-Part I The Effect of Manufacturing Tolerances ," *Proceedings of the 1993 IEEE, International Conference on Robotics and Automation*, pp. 114-120, 1993.

3. H. Zhuang,"Method for kinematics calibration of stewart platform," Journal of robotic system, pp.391-405, 1993.

4. H. Zhuang,"Kinematics Calibration of a Stewart Platform Using Pose Measurement Obtained by a Single Theodolite," IEEE, 1995.

5. H. Zhuang,"Self-calibration of parallel mechanisms with a case study on Stewart platforms," IEEE, 1997.

6. 鄭中緯,"並聯機構平台機構參數自我校正之研究," 國立中正大學機械工程研究所碩士論文，嘉義，1999.

7. 謝清祿,"序列式和史都華平台式多軸工具機之誤差補償研究," 中原大學機械工程研究所碩士論文，中壢，2000.

8. Wiens, G. J., & Walker, C. W., Hexapod machine tool error analysis with inclusion of system dynamics. MED, Vol. 8, Proceedings of the ASME, 1998.

9. Weck, M., & Dammer, M., Design, calculation and control of machine tools based on parallel kinematics. MED, Vol. 8, Proceedings of the ASME, 1998.

10. Soons, J. A., On the geometric and thermal errors of a hexapod machine tool. In C. R. Boer, L. Molinari-tosatti, & K. S. Smith (eds.), Parallel Kinematics Machines, pp.151~169, 1999. London: Springer.

11. Zeid, I., *CAD/CAM theory and practice*,1991, New York: McGraw-Hill Inc.

12. Unigraphics solutions, "*UG CAD/CAM user manual*", 1999, Maryland Heights: EDS Co..

Chapter 6 Evaluation of cutting performance

Based on the aforementioned theory derivation, a prototype machine tool is designed and assembled to perform experiments for verifying the correctness of the theory derived above.

6.1 Features of TRR-XY machine tool

The prototype parallel link machine tool to be tested in this research is shown in Figure 6-1 and Figure 6-2, which is composed of a three DOF mechanism spindle platform and a two DOF conventional serial type XY table. The tool platform has two rotational DOF (direction) and one vertical translation DOF, and XY table provides two DOFs for horizontal movement (perpendicular). Spindle is mounted on tool platform, which is connected to three rigid linkages through three ball joints or 3 DOF universal joints. The other end of the each linkage is connected to the corresponding slide by three rotation joints. Slides are mounted on three groups of guides and driven by ball-screw to move up and down along Z direction. The vertical column, to which guides are attached, intersects the kinematics plane formed by R-joints and universal joints at the center, and the angle between each other is 120 degree. In addition with XY table's two direction motions, the hybrid parallel link machine tool has five DOF, and Table 6-1 shows the specifications of the prototype hybrid machine tool.

Table 6-1 Specifications of TRR-XY machine tool

Item	Unit	Specification
X/Y/Z travel distance	mm	650x850x650
A/B rotation angle	degree	±45
X/Y/Z rapid travel rate	m/min	32
Pallet size	mm	500x500
Controller	---	Siemens Sinumerik 840D
Spindle speed	rpm	12000
Spindle drive motor	kw	8
Taper	---	BT-40
Workpiece max. weight	kg	500

The SIEMENS 840D controller is adopted to control the machine tool. Five feed motors are all Siemens IFK6083 servo-motors. It rated speed is 3000 rpm, rated torque is 10.5Nm and transient max. torque is 50Nm. In the design of spindle, the motor built-in type high-speed spindle is adopted with the max. speed 12000 rpm and max. power 8 kW. In the design of designing tool holder, BT-40 is chosen. The TRR-XY hybrid parallel link machine tool is tested in the standard workshop of ITRI. The area occupied by the machine tool is about 3.5m×2.5m and the height is 3.6m. The room temperature is kept at 25℃ by air-conditioner during machining. The working voltage is 380V and working pressure of air resource is about 0.5~0.6MPa.

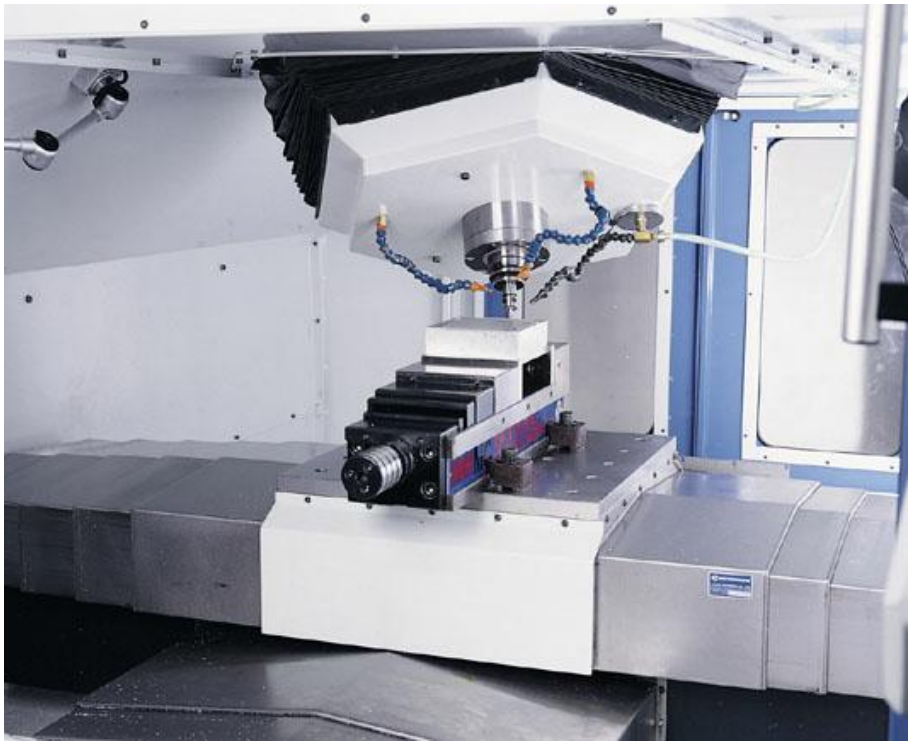

Figure 6-1 Local veiw of TRR-XY hybrid parallel link machine tool

Figure 6-2 TRR-XY hybrid parallel link machine tool

6.1.1 Coordinate measuring machine (CMM) measurement

Apart from testing of machine tool in the standard workshop, relevant testing parts also need to be tested through CMM. In this research, all relevant parts are tested through CMM in CMM laboratory of IRTI as shown in Figure 6-3. Temperature is kept about 22℃ in CMM room. Before practical testing, all parts are placed in CMM laboratory over 4 hours statically to decrease testing errors resulted from temperature. The specification of CMM is introduced as below.

Figure 6-3 CMM measurement of the testing parts

- Manufacturer: ZEISS (Germany)
- Type：PRISMO 10 (HTG high temperature gradient)
- Max workpiece loading：2000 kg
- Three-axis distance：(X, Y, Z) = (1200, 1800, 1000) mm
- Testing precision：U1 ≤ 2.4+L/300 μm，U3 ≤ 2.9+L/300 μm (L：measuring length，unit：mm)
- Testing software：UMESS、HOLOS(3D curved surface)

6.2 Two machining experiments

To verify the correctness of the derived kinematics model and to verify the performance design of TRR-XY parallel link machine tool, two machining experiments are planned. The machining planning is described respectively in the following sections.

6.2.1 Tire mold machining experiment

The first planned machining experiment is the curved surface of the tire mold. The designed CAD model for complicate tire mold machining test is shown in Figure 6-4. The size of specimen is about 240×220×60mm. Designing this mold surface for testing is aiming to verify the fact that this developed machine tool has good performance for five-axis machining. With large quantity of complicate surface machining experiments, the derived inverse kinematics, tool length compensation and tool path for machining are verified to be correct.

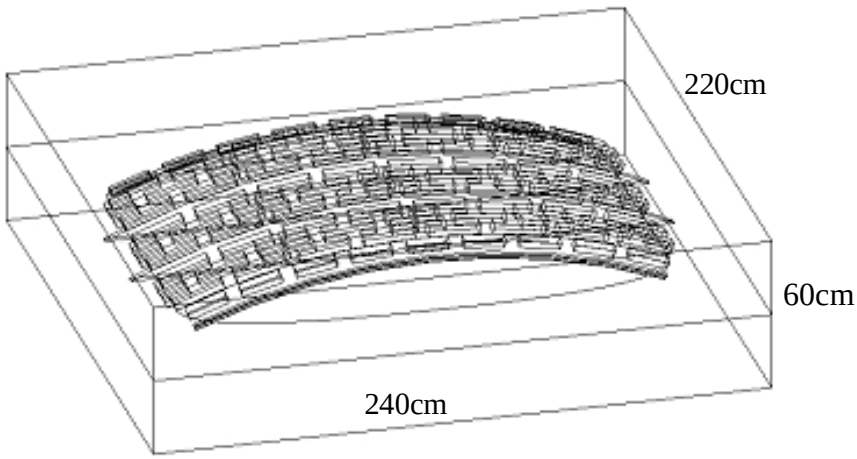

Figure 6-4 CAD model of tire mold

A 3-axis milling machine is used for the rough machining. For the machining experiments, a 6mm end mill is used for rough cutting with 1mm depth per each cut. For the finish machining, a 3mm end mill is used and the tool axis is designed to be normal with the machining surface. Both of the male and female surfaces of the tire mold are machined. The wood is selected as the blank material for machining. Therefore, no cutting fluid or oil fog is needed during the machining experiments.

6.2.2 Spherical surface machining experiment

In order to know more about the machining accuracy of this machine tool, a simple geometric model, which is easy to be measured, is designed for machining experiments. Machining accuracy can be obtained according to the data results measured by using CMM.

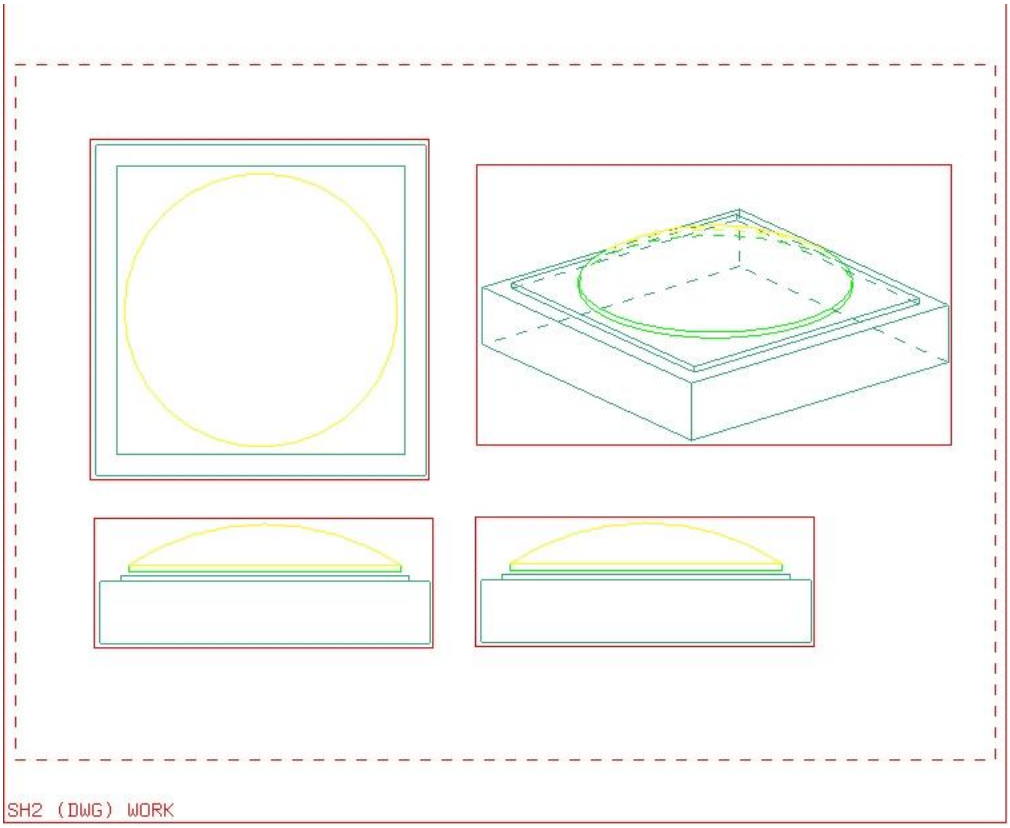

Figure 6-5 CAD model of spherical surface for machining experiments

As shown in Figure 6-5, the size of blank material is about 150×150×65mm. A 3-axis milling machine with 6mm end mill is used to perform the rough cut. The depth per rough-cut is 0.5mm. For the finish machining, the 5 DOF hybrid TRR-XY parallel link machine tool with 3mm end mill is used. The tool axis is designed to be normal with the machining surface. The tool path is continuously milled from the outside circular path toward the center of spherical surface. The A6061 aluminum is selected as the blank material for this experiment. Lubrication oil is used to avoid chip adhering on the tool face. For avoiding interference during machining processes, the tool axis angle, relative to z-axis, is also calculated and checked.

6.3 Experimental results and discussions

6.3.1 Results from tire mold machining experiments

A tire mold machining experiment is shown in Figure 6-6. According to the examination of the relative position between tool tip and machining CAD model, we can know the compensation of tool length and the tool path are right. The direction of tool axis is varied continuously during machining different curved surface of tire. While tool axis tilts, XY table is also moved to compensate the offsets resulted from spindle tilting. The theory of X-Y table compensating the offsets resulted from spindle tilting is derived in Chapter 3.

Figure 6-6 Machining of tire mold

The machining program, including the calculation of tool tip position and tool axis vector, is planned by using a commercial CAM software. According to the inverse kinematics solution derived in Chapter 3, the machining program is transformed into feed instructions of each feed axis to drive machine tool. So, there are a few meanings existing in tire mold machining process: (1) correctness of derivation of inverse kinematics solution is verified; (2) the compensating value and feed relationship studied in Chapter 3 are confirmed; (3) the performance of entire system design of the hybrid machine tool is verified. This developed hybrid machine tool

can really realized five-axis machining which has the same machining performance as a general five-axis machine tool.

6.3.2 Result from spherical surface machining experiment

The machining result of the spherical machining experiment is shown in Figure 6-7. To know the machining accuracy of the developed machine tool, the machined part is sent to CMM for measuring. During measuring process the information of surface CAD model is input into CMM. The CMM measures the part using the CAD model that the same with that for the machining experiments. The measured results of spherical surface using CMM are shown in Figure 6-8. The difference between CAD model and measured results are shown by thick or light color. The maximum difference between all measured radius results and CAD model is about –0.6mm, and that the maximum difference between thick and light color is about 0.3mm. The thicker the color is the smaller the size. This implies that a – 0.6+0.3 = -0.3mm Z-axis direction machining error is existed in the whole machining area. The Z-axis machining error –0.3mm can be compensated very easily. It is worth mentioning that the machine error increased with the tilt angle increased. This also can be found from the machining result in Figure 6-8.

From the machining result in Figure 6-7, an interesting fact was found. There are four lines are clearly seen on the machined spherical surface. One line is parallel to X-axis, one line is parallel to Y-axis and the others are parallel to the directions of A chain, B chain, or C chain planes respectively. This result probably was caused by the backlash of ball-screw.

Figure 6-7 Machining result of the spherical surface machining experiment

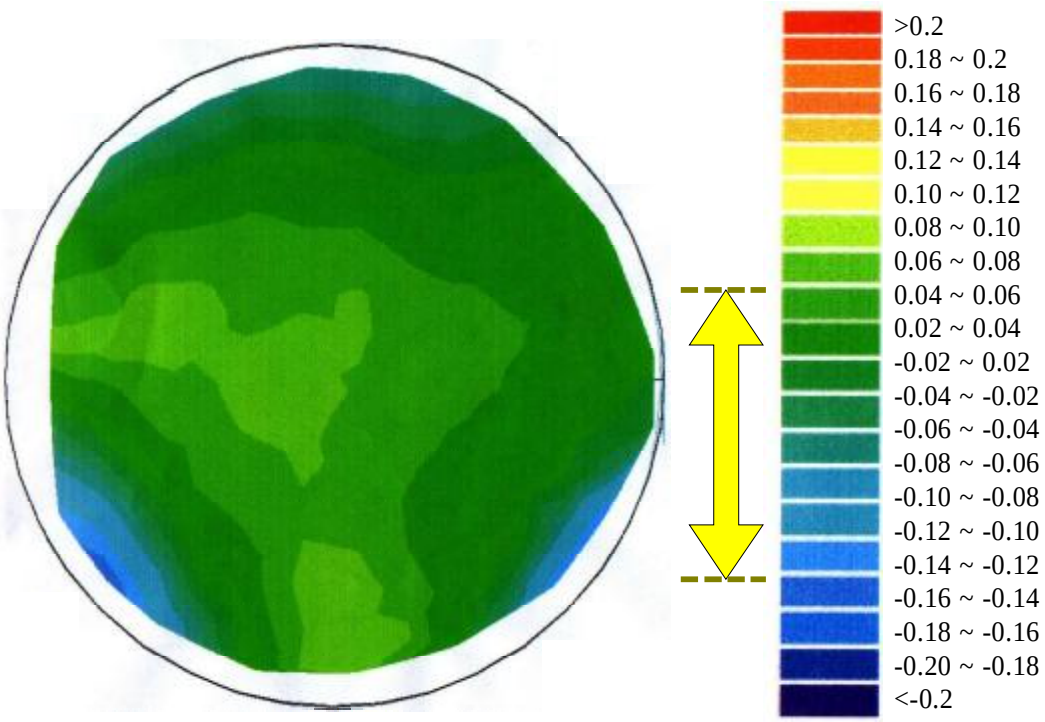

Figure 6-8 CMM measuring results of spherical surface

The backlash effects on the machining accuracy were studied very extensively for traditional machine tools. However, very few researches have been done on parallel link mechanisms. In this research, the signum function of the moving velocity is used to establish some fundamental understandings of the backlash effects. To investigate the backlash effects using the forward kinematics model, the input command is modified as:

$$S_i' = S_i + d_b \cdot sign(\dot{S}_i) \tag{6-1}$$

Where S'_i is the modified displacement of the ball screws, δ_b is the value of backlash, sing is the signum function, and S_i is the feed rates of the ball screws. Replacing S_i by S'_i into the direct kinematics, a new trajectory caused by backlash effect can be determined. The S_i for the spherical surface machining is determined by the inverse kinematics model. The real input S_i including the backlash is obtained from Eq.6-1.

Figure 6-9 shows the projection trajectory on the X-Y plane of the spherical surface's trajectory with the backlash considered. The backlash effects on the TRR mechanism are mainly on the vertical direction. In Figure 6-9, three protrusions are found in the Z-direction caused by the backlash. It is because the motions of the sliders in TRR mechanism are in the Z-direction, and the X-Y table needs to move simultaneously with the TRR mechanism in the machining process. The tip of the cutter is set to be normal to the spherical surface. The backlash existing in both the X-Y table and the TRR mechanism causes the protrusions on the spherical surface at the locations of degrees 0^0, 60^0, 90^0, 120^0, 180^0, 240^0, 270^0, 300^0. They are shown in Figure 6-9. For clear illustration, the value of δ_b is assumed to be 0.1mm in Figure 6-9. Compare the simulation result in Figure 6-9 and the machining result in Figure 6-7, the effects of backlash are verified from the quantitative viewpoint.

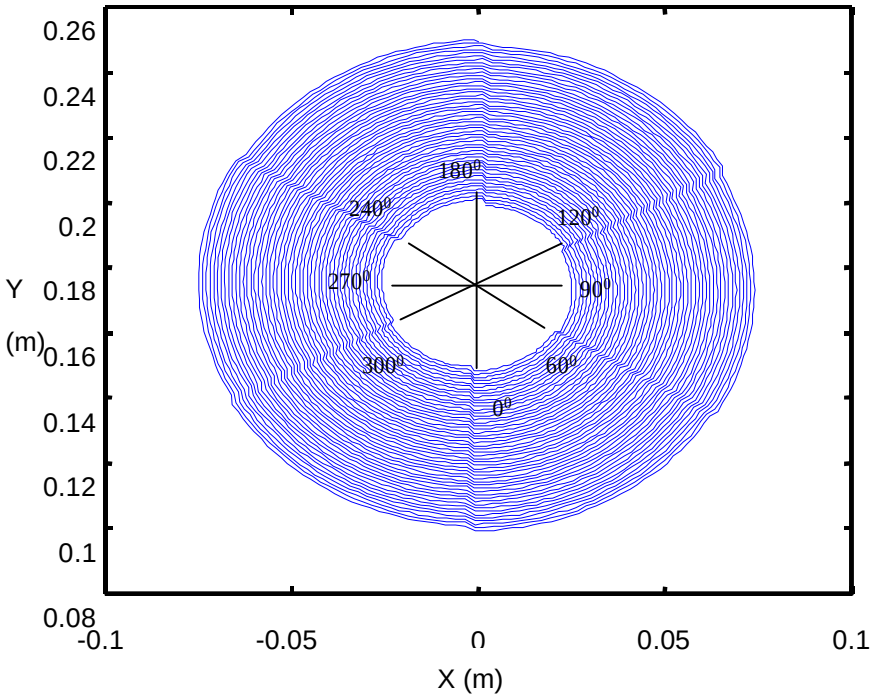

Figure 6-9 Projection trajectory on the X-Y plane of the spherical surface's trajectory with backlash considered

6.4 Error measurement tests

In order to verify the correctness of the derivation of kinematics model, dynamic model and error model some measurement tests are online performed with DBB method. Some important specifications of the DBB used in this research are summarized and explained in Appendix. The DBB arrangement for measuring the motion accuracy and its repeatability is shown in Figure 6-10. Several circular tool paths with five axes moving simultaneously are simulated by the DBB system for measuring the errors and verifying the error model. The length of ball bar of the DBB system used in this research is 150 mm. The dimensions of this machine tool are shown in Table 5-3. Assume that there are three error groups in each kinematics chain. Table 6-2 shows the error data that will be used in the experiments. Both of the pin joint and ball joint have the errors along the X and Y direction. Actually, the circular tool paths are located on a sphere with radius 150mm. The tool axis is planned to be normal with the spherical surface during the measurement test. In Figure 6-11, three circular tool paths with tool axis inclination angle to be 5^0, 15^0, and

20^0 are tested. The feed rates for cutting those three paths are 3478, 3066, 3478 mm/min respectively. There are some important results can be obtained from the DBB measurement results. They are summarized in the following sections. The start data point and end data point of the DBB measuring results are nearly the same. This means that the repeatability of the hybrid machine tool is high and the kinematics model derived in this research is correct.

The safe range of the DBB measuring system used in this research is (149.2 mm $\leq$ r $\leq$ 150.8mm). In the DBB measuring tests with error parameters given in Table 6-2, it is found that the DBB doesn't be bent or damaged. In order to understand the effects of each error parameter, the error parameters in Table 6-2 are set to be much larger than the practical situation. Ten times of the scale are manufacturing errors. A comparison between the theoretical results and error measurement results is also given in this section. The flowchart in Figure 6-10b explains the detail of the comparison. The same circular tool path from commercial CAD/CAM software is used for comparison. The theoretical results are obtained in Table 6-2~Table 6-5. The error measurement results are obtained by performing the DBB measurement tests on the parallel link prototype machine tool with error parameters considered. The differences between the theoretical results and the measured results are further decomposed into X and Y components. The comparison results are summarized in Figure 6-14, 6-15, 6-17, 6-18, 6-20,6-21, and 6-23, 6-24.

It is worth mentioning that the Siemens controller is adopted in these error measurement tests. Therefore, the definitions of the error parameters in Table 6-2 are shown in Table 5-1. This again shows the correctness of the error model or kinematics model derived in this study.

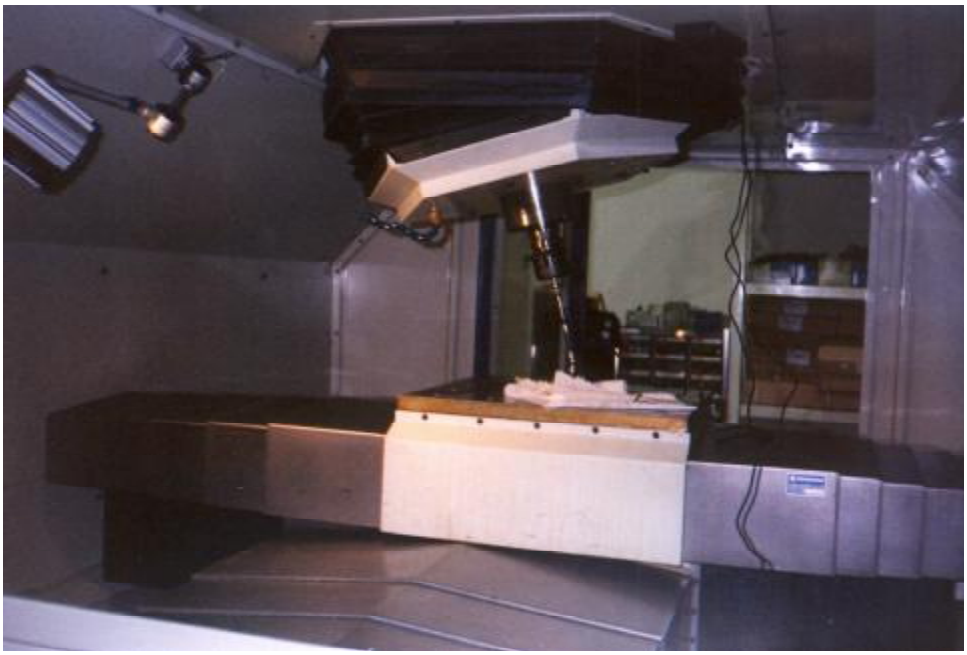

Figure 6-10a Double ball bar measuring system

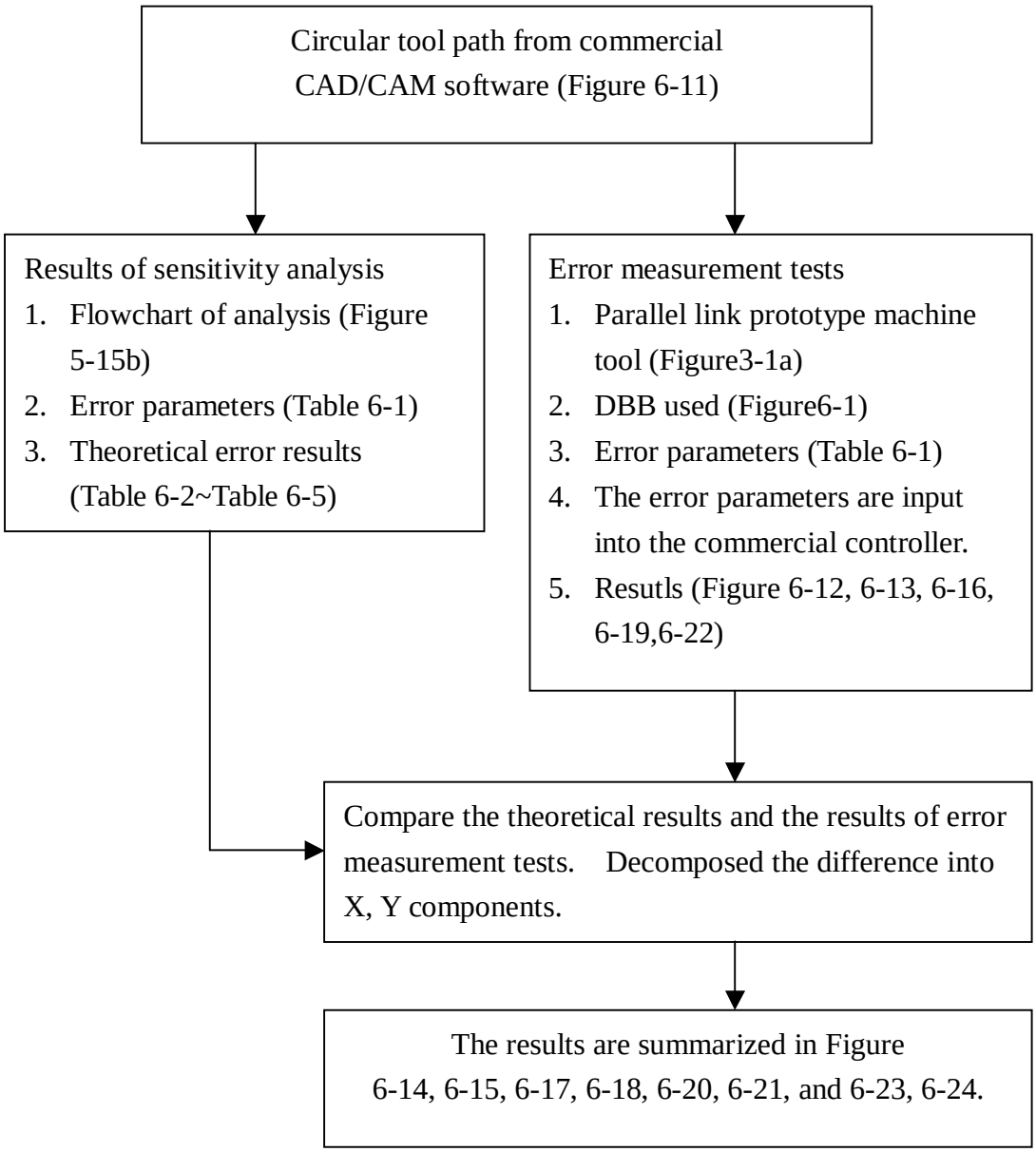

Figure 6-10b The flowchart shows the detail of comparison between theoretical results and experimental results.

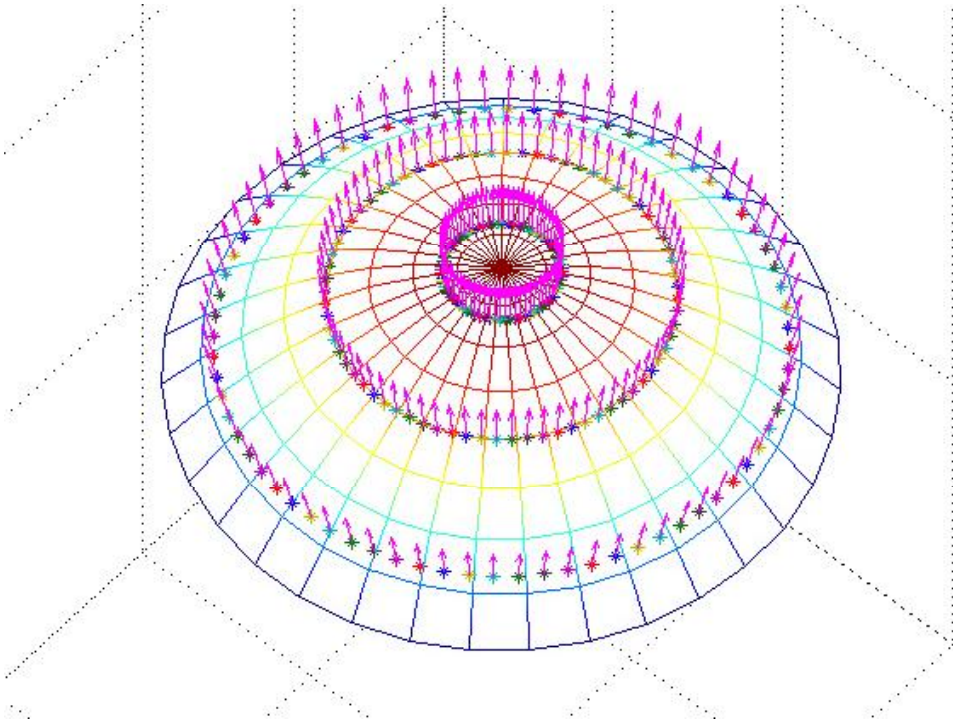

Figure 6-11 Three circular tool paths with tool axis inclination angle to be 5^0, 15^0, and 25^0. The arrow shows the tool axis normal to the spherical surface. The sphere radius is 75mm.

Generally, if there are manufacturing errors in a kinematic chain, the errors may increase or decrease the machining errors along the normal plane of axis direction. It is worth mentioning that no error parameter is input to the controller in the test of Figure 6-12. This means that the manufacturing errors in the test of Figure 6-12 are originally existed in the machine tool. An interesting result is also found that the machining errors are increased with the tool axis inclination angle increased. When the tool axis inclination is varied from 5^0, 15^0, to 25^0, the out of roundness of the machining data is varied from 21.8μm, 56.4μm, to 140.4μm.

By carefully examining the measured results in Figure 6-12, it was found that the machining errors on the A chain and C chain are relatively larger than that for B chain. The reasons for this larger machining error may be caused by the backlash of the ball screws. The ball screws are used in the A chain, B chain, C chain, and X-Y table. Due to the larger variation in A chain and C chain, the repeatability of A chain and C chain will be poor. Therefore, only B chain will be selected for the comparison

between theoretical results and experimental results.

Table 6-2 Assumed error parameters for error measurement tests

	A Chain	B Chain	C Chain
Pin joint error	△X=+3.5,-3.5 △Y=+2,-2	△X=+3.5,-3.5 △Y=+2,-2	△X=+3.5,-3.5 △Y=+2,-2
Link length error	△L=+1,-1	△L=+1,-1	△L=+1,-1
Ball joint error	△X=+2,-2 △Y=+2,-2	△X=+2,-2 △Y=+2,-2	△X=+2,-2 △Y=+2,-2

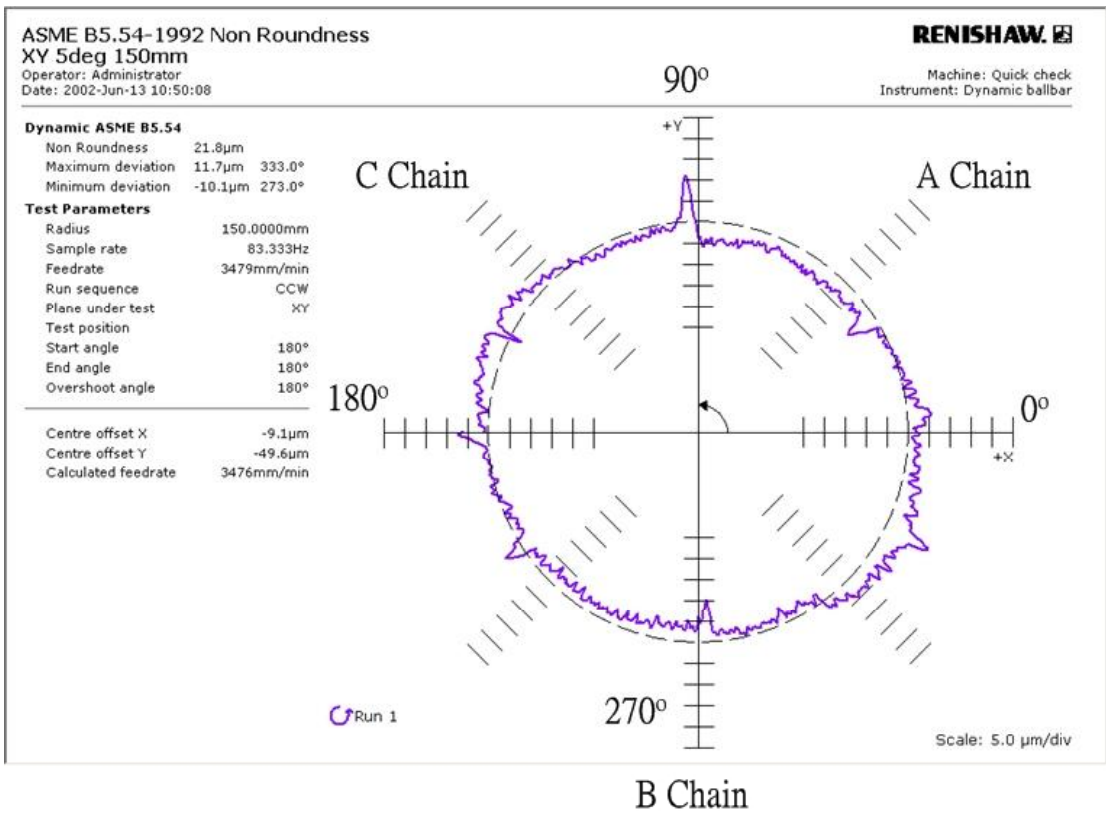

B Chain

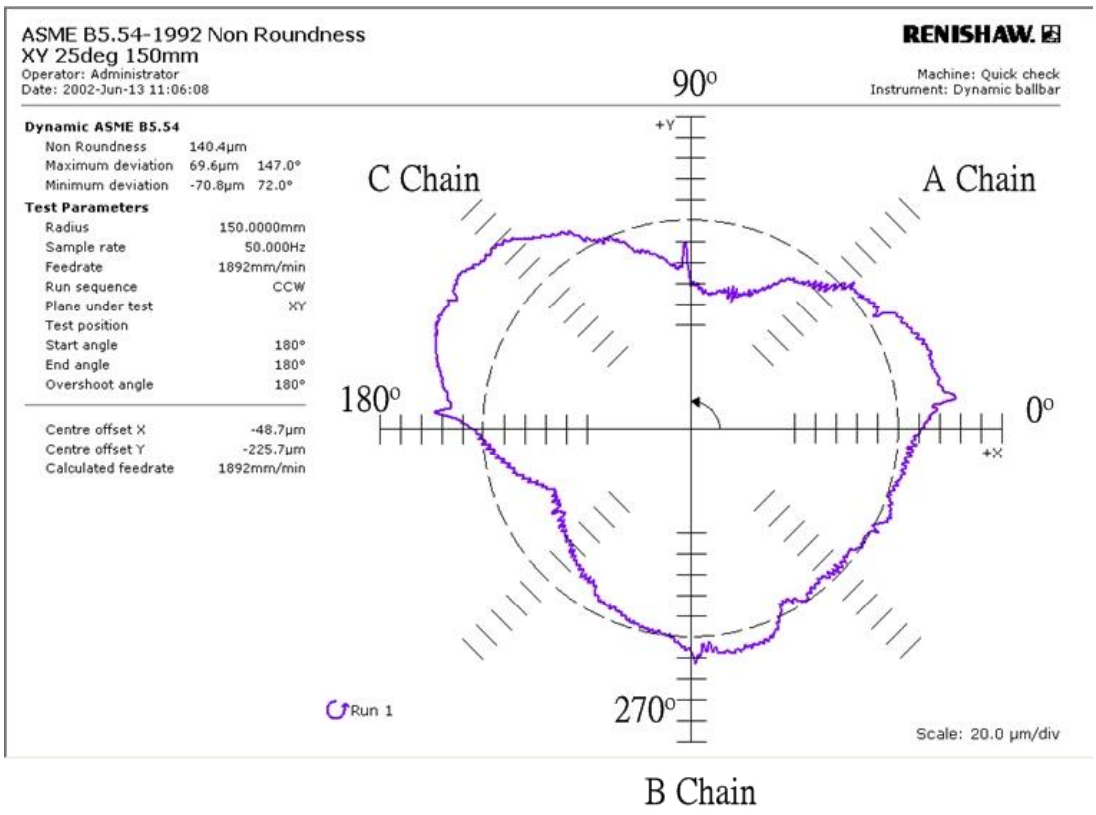

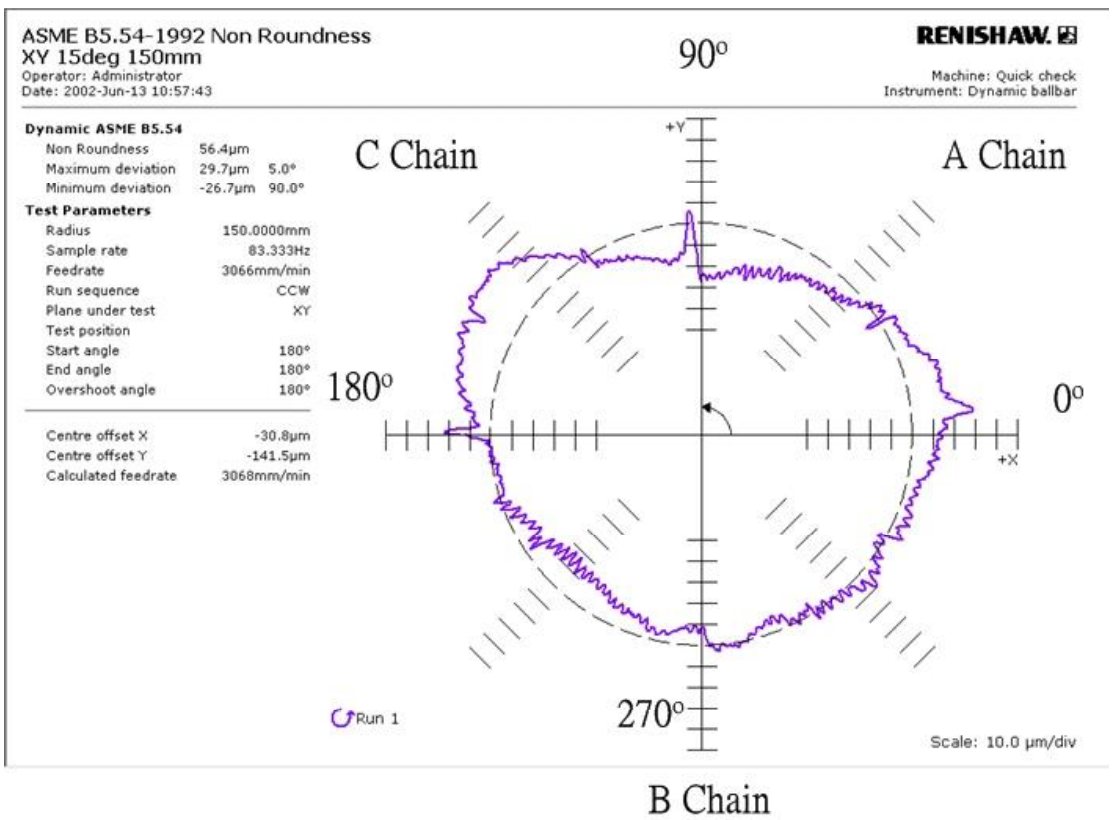

Figure 6-12 DBB measuring results with tool axis inclination angle varied from 5^0,15^0, and 25^0. Only the error parameters originally existed in the machine tool are considered in this case.

Figure 6-13 show the DBB measuring results with tool inclination angle 25^0 and link length error. L_b=+1 mm. Table 6-3 shows the error data results from the theoretical calculation with tool inclination angle 25^0 and link length error L_b=+1 mm. It is worth mentioning that only the X component and Y component of the error data results are listed in Table 6-3, Table 6-4, Table 6-5, and Table 6-6. It is convenient and reasonable for the comparison between the DBB measuring data and theoretical data. There are only four locations in Figure 6-13 and Table 6-3 selected for the comparison. Figure 6-14 show the X component of error results on four locations of the tool path 0^0, 90^0, 180^0, 270^0. Figure 6-15 shows the Y component of error results on four locations of the tool path 0^0, 90^0, 180^0, 270^0. The comparison results in Figure 6-14 and Figure 6-15 show that the theoretical error results are nearly the some with the measured results. There are still some difference existed between measured results and theoretical results. This is believed to be caused by the backlash of the ball screws or ball joints.

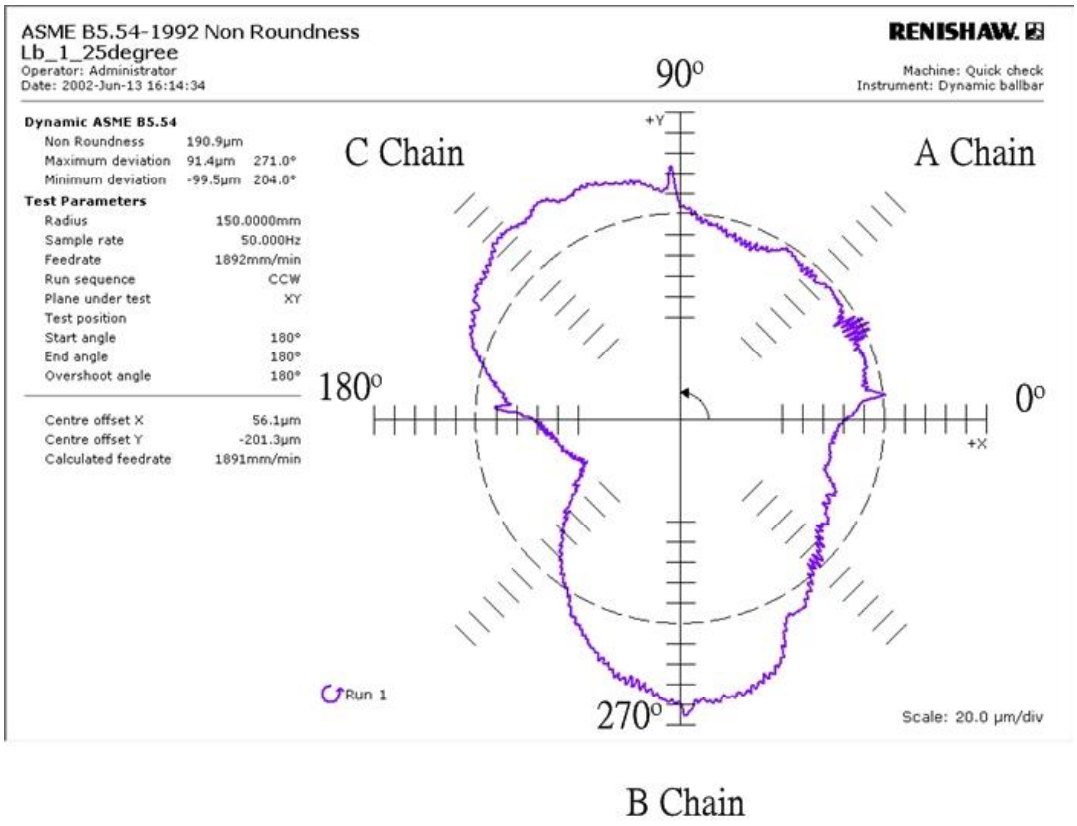

Figure 6-13 DBB measuring results with tool axis angle $\phi = 25^0$. The manufacturing errors is $\triangle L_B$=+1mm

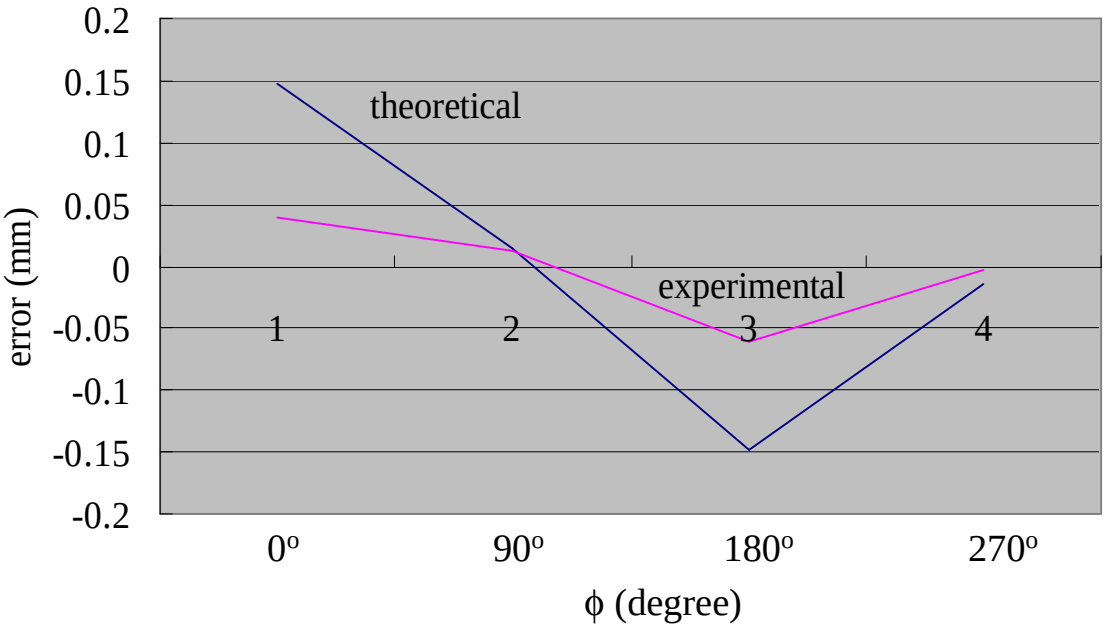

Figure 6-14 X component of error results with L_B=+1 mm

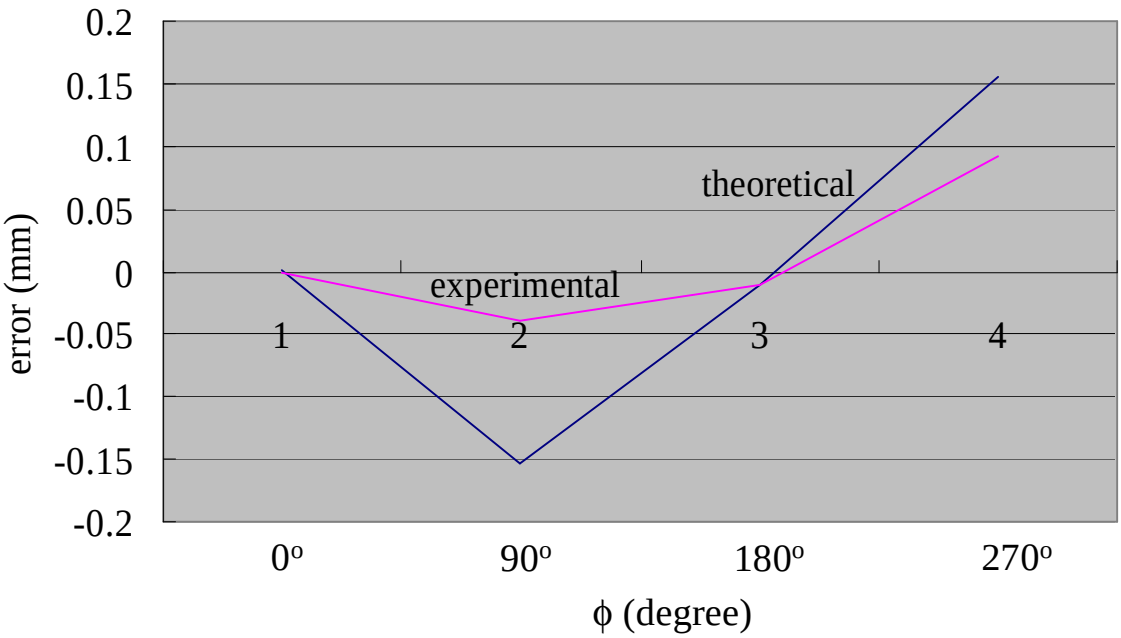

Figure 6-15 Y component of error results with L_B =+1 mm

Table 6-3 Theoretical error results with tool axis angle $\phi = 25^0$. The manufacturing errors is $\triangle L_B$=+1mm

ϕ	0^o ~89^o			90^o ~189^o			189^o~269^o			270^o~359^o		
axis		dX	dY		dX	dY		dX	dY		dX	dY
Theoretical error (mm)	0^o	0.1478	0.0010	90^o	0.0000	-0.1539	180^o	-0.1478	0.0010	270^o	0.0000	0.1570
		0.1476	-0.0112		-0.0141	-0.1533		-0.1471	0.0132		0.0143	0.1563
		0.1465	-0.0235		-0.0280	-0.1513		-0.1455	0.0253		0.0285	0.1541
		0.1445	-0.0357		-0.0416	-0.1480		-0.1431	0.0373		0.0423	0.1504
		0.1414	-0.0479		-0.0548	-0.1435		-0.1397	0.0492		0.0555	0.1454
		0.1374	-0.0599		-0.0675	-0.1377		-0.1355	0.0608		0.0681	0.1391
		0.1322	-0.0717		-0.0795	-0.1309		-0.1304	0.0723		0.0798	0.1318
		0.1260	-0.0831		-0.0907	-0.1230		-0.1244	0.0834		0.0907	0.1235
		0.1187	-0.0941		-0.1010	-0.1141		-0.1174	0.0943		0.1006	0.1144
		0.1104	-0.1044		-0.1104	-0.1044		-0.1095	0.1046		0.1095	0.1046
		0.1010	-0.1141		-0.1187	-0.0941		-0.1006	0.1144		0.1174	0.0943
		0.0907	-0.1230		-0.1260	-0.0831		-0.0907	0.1235		0.1244	0.0834
		0.0795	-0.1309		-0.1322	-0.0717		-0.0798	0.1318		0.1304	0.0723
		0.0675	-0.1377		-0.1374	-0.0599		-0.0681	0.1391		0.1355	0.0608
		0.0548	-0.1435	179^o	-0.1414	-0.0479		-0.0555	0.1454		0.1397	0.0492
	89^o	0.0416	-0.1480		-0.1445	-0.0357	269^o	-0.0423	0.1504	359^o	0.1431	0.0373
		0.0280	-0.1513		-0.1465	0.0235		-0.0285	0.1541		0.1455	0.0253
		0.0141	-0.1533		-0.1476	-0.0112		-0.0143	0.1563		0.1471	0.0132

Figure 6-16 show the DBB measuring results with tool inclination angle 25^0 and link length error. L_B=-1 mm. Table 6-4 shows the error data results from the theoretical calculation with tool inclination angle 25^0 and link length error L_B=-1 mm. There are only four locations in Figure 6-16 and Table 6-4 selected for the comparison. Figure 6-17 show the X component of error results on four locations of the tool path 0^0, 90^0, 180^0, 270^0. Figure 6-18 shows the Y component of error results on four locations of the tool path 0^0, 90^0, 180^0, 270^0. The comparison results in Figure 6-17 and Figure 6-18 show that the theoretical error results are nearly the same with the measured results.

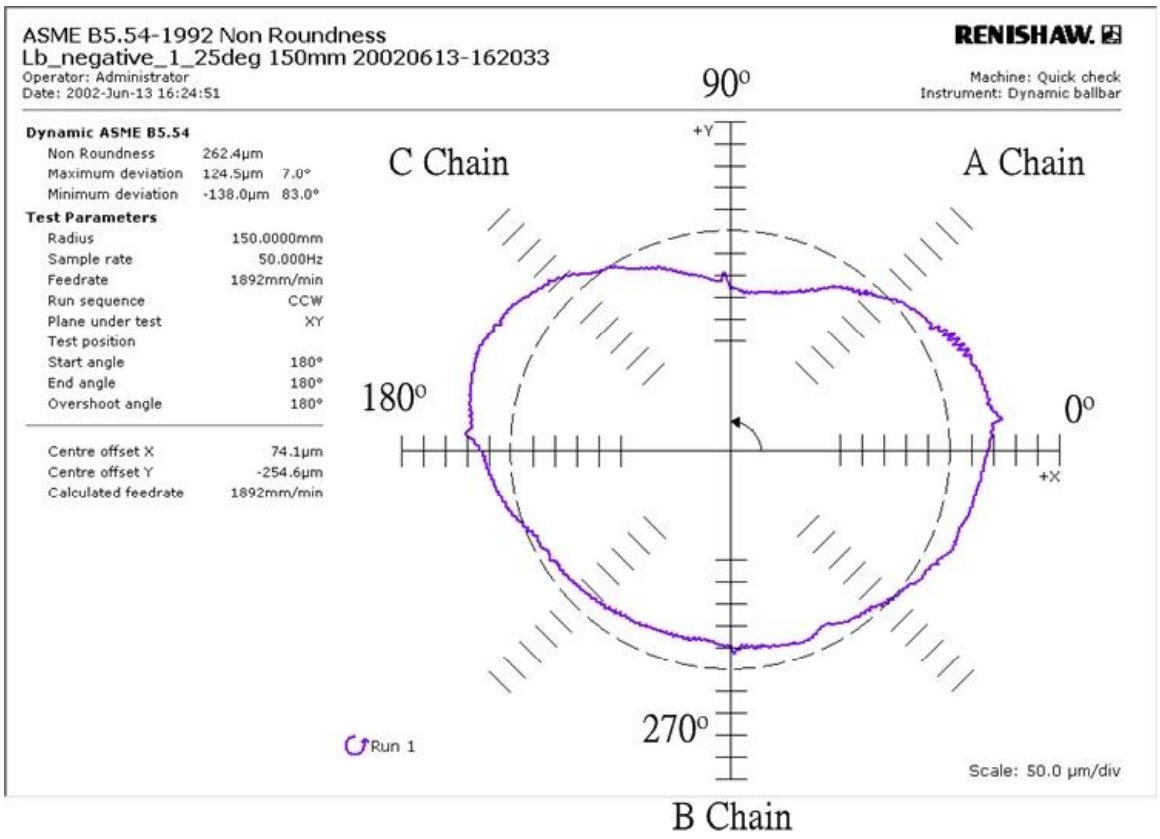

Figure 6-16 DBB measuring results with tool axis angle $\phi = 25^0$. The manufacturing errors is $\triangle L_B$=-1mm

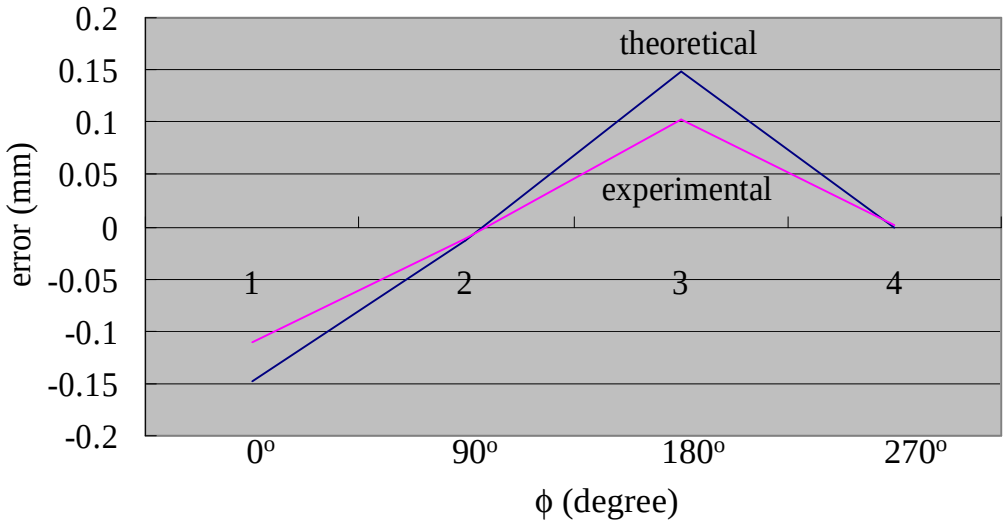

Figure 6-17 X component of error results with L_B=-1 mm

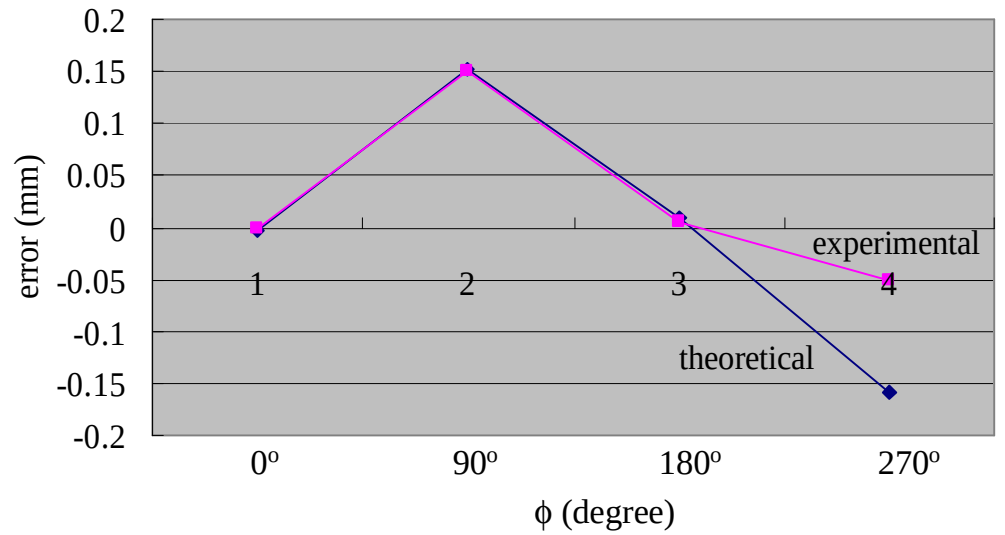

Figure 6-18 Y component of error results with L_B=-1 mm

Table 6-4 Theoretical error results with tool axis angle $\phi = 25^0$. The manufacturing errors is $\triangle L_B$=-1mm

ϕ	0^o ~89^o			90^o ~189^o			189^o~269^o			270^o~359^o		
axis		dX	dY		dX	dY		dX	dY		dX	dY
Theoretical error (mm)	0^o	-0.1478	0.0010	90^o	0.0000	-0.1539	180^o	0.1478	0.0010	270^o	0.0000	0.1570
		-0.1476	-0.0112		0.0140	-0.1533		0.1471	0.0132		-0.0144	0.1563
		-0.1465	-0.0235		0.0279	-0.1513		0.1455	0.0253		-0.0286	0.1541
		-0.1444	-0.0357		0.0415	-0.1480		0.1431	0.0373		-0.0424	0.1504
		-0.1413	-0.0479		0.0547	-0.1435		0.1398	0.0492		-0.0557	0.1454
		-0.1372	-0.0599		0.0674	-0.1377		0.1356	0.0608		-0.0682	0.1391
		-0.1320	-0.0717		0.0793	-0.1309		0.1306	0.0723		-0.0800	0.1318
		-0.1258	-0.0831		0.0905	-0.1230		0.1246	0.0834		-0.0908	0.1235
		-0.1185	-0.0941		0.1008	-0.1141		0.1176	0.0943		-0.1008	0.1144
		-0.1102	-0.1044		0.1102	-0.1044		0.1097	0.1046		-0.1097	0.1046
		-0.1008	-0.1141		0.1185	-0.0941		0.1008	0.1144		-0.1176	0.0943
		-0.0905	-0.1230		0.1258	-0.0831		0.0908	0.1235		-0.1246	0.0834
		-0.0793	-0.1309		0.1320	-0.0717		0.0800	0.1318		-0.1306	0.0723
		-0.0674	-0.1377		0.1372	-0.0599		0.0682	0.1391		-0.1356	0.0608
		-0.0547	-0.1435		0.1413	-0.0479		0.0557	0.1454		-0.1398	0.0492
		-0.0415	-0.1480		0.1444	-0.0357		0.0424	0.1504		-0.1431	0.0373
	89^o	-0.0279	-0.1513	179^o	0.1465	0.0235	269^o	0.0286	0.1541	359^o	-0.1455	0.0253
		-0.0140	-0.1533		0.1476	-0.0112		0.0144	0.1563		-0.1471	0.0132

Figure 6-19 show the DBB measuring results with tool inclination angle 25^0 and link length error. $\triangle X_{BB}$=+2 mm. Table 6-5 shows the error data results from the theoretical calculation with tool inclination angle 25^0 and link length error $\triangle X_{BB}$=+2 mm. There are only four locations in Figure 6-19 and Table 6-5 selected for the comparison. Figure 6-20 show the X component of error results on four locations of the tool path 0^0, 90^0, 180^0, 270^0. Figure 6-21 shows the Y component of error results on four locations of the tool path 0^0, 90^0, 180^0, 270^0. The comparison results in Figure 6-20 and Figure 6-21 show that the theoretical error results are nearly the some with the measured results.

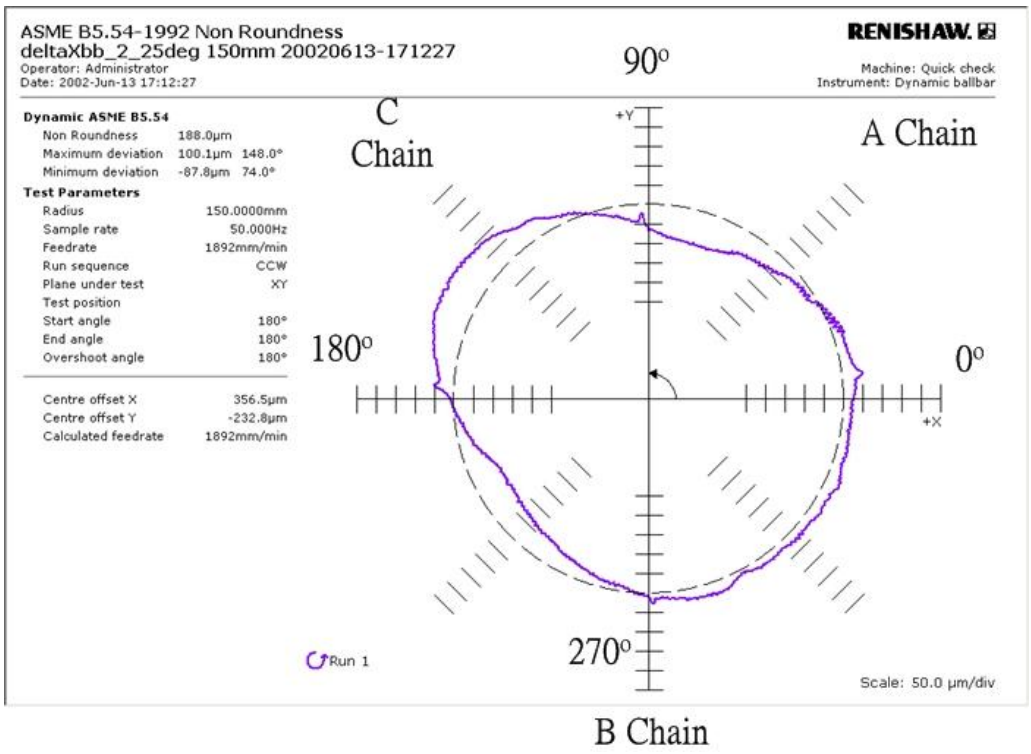

Figure 6-19 DBB measuring results with tool axis angle $\phi = 25^0$. The manufacturing errors is $\triangle X_{BB}$=+2mm

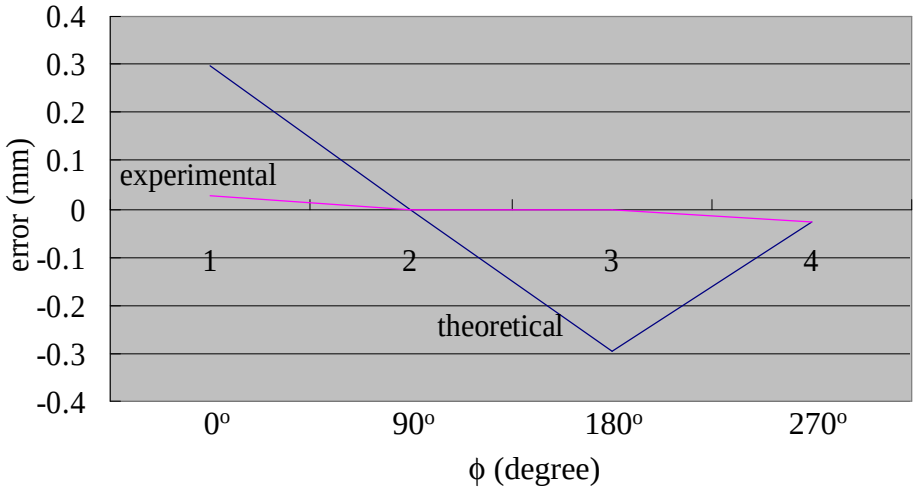

Figure 6-20 X component of error results with X_{BB}=+2 mm

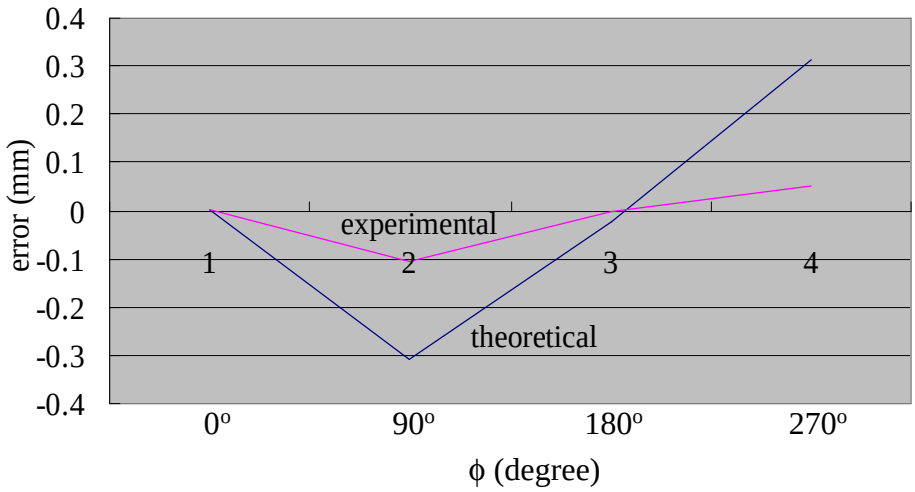

Figure 6-21 Y component of error results with X_{BB}=+2 mm

Table 6-5 Theoretical error results with tool axis angle $\phi = 25^0$. The manufacturing errors is $\triangle X_{BB}$=+2mm

ϕ	0^o ~89^o			90^o ~189^o			189^o~269^o			270^o~359^o		
axis		dX	dY		dX	dY		dX	dY		dX	dY
Theoretical error (mm)	0^o	0.2957	0.0010	90^o	0.0000	-0.3093	180^o	-0.2957	0.0010	270^o	0.0000	0.3125
		0.2954	-0.0235		-0.0281	-0.3080		-0.2942	0.0253		0.0286	0.3110
		0.2932	-0.0481		-0.0560	-0.3040		-0.2910	0.0496		0.0570	0.3066
		0.2891	-0.0726		-0.0833	-0.2974		-0.2861	0.0735		0.0845	0.2992
		0.2830	-0.0969		-0.1097	-0.2883		-0.2794	0.0972		0.1109	0.2892
		0.2749	-0.1210		-0.1351	-0.2768		-0.2709	0.1205		0.1360	0.2768
		0.2646	-0.1446		-0.1591	-0.2630		-0.2607	0.1434		0.1594	0.2622
		0.2522	-0.1674		-0.1815	-0.2472		-0.2487	0.1656		0.1811	0.2456
		0.2376	-0.1894		-0.2022	-0.2295		-0.2347	0.1872		0.2010	0.2274
		0.2209	-0.2101		-0.2209	-0.2101		-0.2188	0.2079		0.2188	0.2079
		0.2022	-0.2295		-0.2376	-0.1894		-0.2010	0.2274		0.2347	0.1872
		0.1815	-0.2472		-0.2522	-0.1674		-0.1811	0.2456		0.2487	0.1656
		0.1591	-0.2630		-0.2646	-0.1446		-0.1594	0.2622		0.2607	0.1434
		0.1351	-0.2768		-0.2749	-0.1210		-0.1360	0.2768		0.2709	0.1205
		0.1097	-0.2883		-0.2830	-0.0969		-0.1109	0.2892		0.2794	0.0972
		0.0833	-0.2974		-0.2891	-0.0726		-0.0845	0.2992		0.2861	0.0735
	89^o	0.0560	-0.3040	179^o	-0.2932	-0.0481	269^o	-0.0570	0.3066	359^o	0.2910	0.0496
		0.0281	-0.3080		-0.2954	-0.0235		-0.0286	0.3110		0.2942	0.0253

Figure 6-22 show the DBB measuring results with tool inclination angle 25^0 and link length error. $\triangle X_{BP}$=+2 mm. Table 6-6 shows the error data results from the theoretical calculation with tool inclination angle 25^0 and link length error $\triangle X_{BP}$=+2 mm. There are only four locations in Figure 6-22 and Table 6-6 selected for the comparison. Figure 6-23 show the X component of error results on four locations of the tool path 0^0, 90^0, 180^0, 270^0. Figure 6-24 shows the Y component of error results on four locations of the tool path 0^0, 90^0, 180^0, 270^0. The comparison results in Figure 6-23 and Figure 6-24 show that the theoretical error results are nearly the some with the measured results.

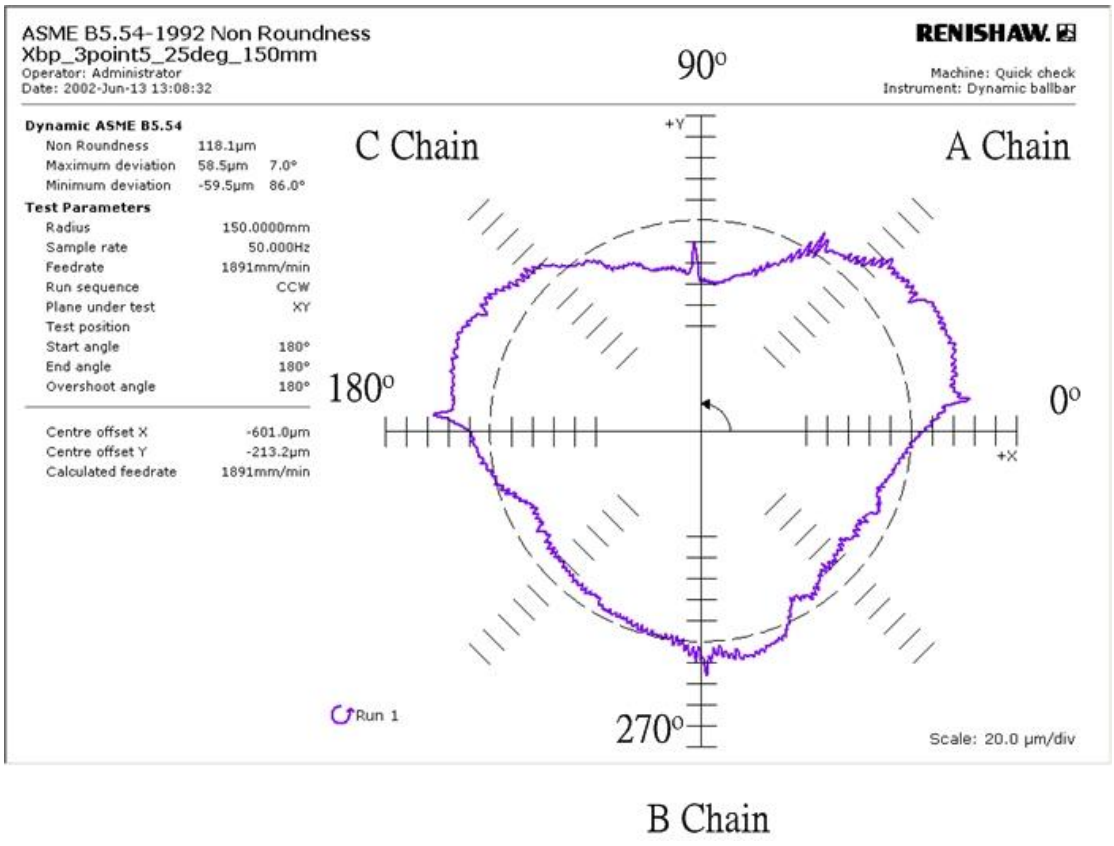

Figure 6-22 DBB measuring results with tool axis angle $\phi = 25^0$. The manufacturing errors is $\triangle X_{BP}$=+2mm

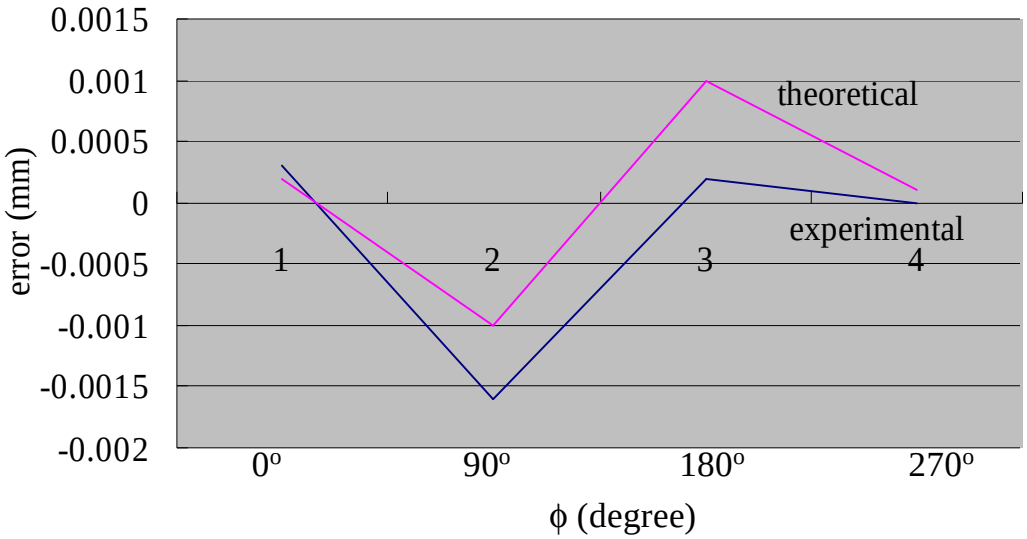

Figure 6-23 X component of error results with X_{BP}=+2 mm

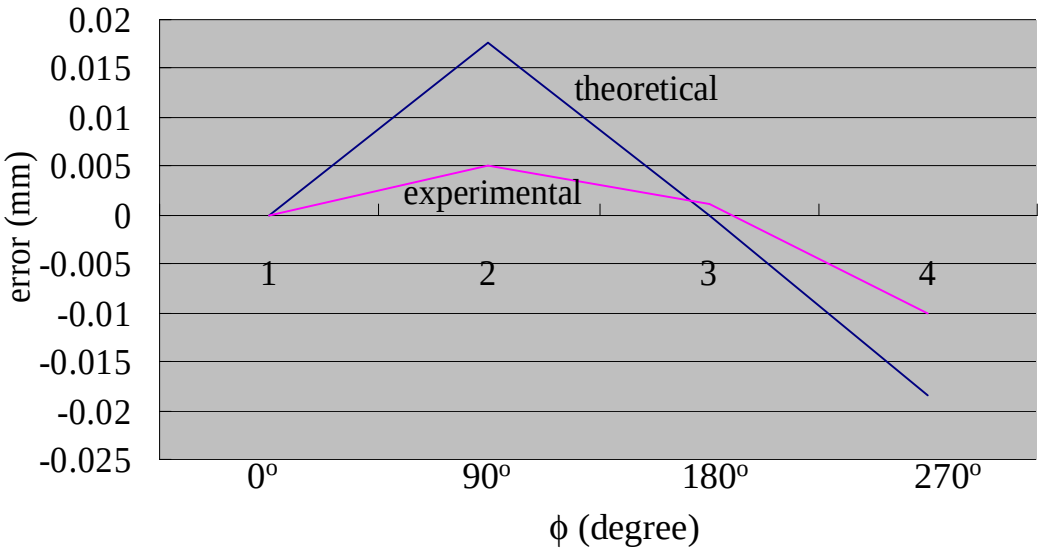

Figure 6-24 Y component of error results with X_{BP}=+2 mm

Table 6-6 Theoretical error results with tool axis angle $\phi = 25^0$. The manufacturing errors is $\triangle X_{BP}$=+2mm

ϕ	0^o ~89^o			90^o ~189^o			189^o~269^o			270^o~359^o		
axis		dX	dY		dX	dY		dX	dY		dX	dY
Theoretical error (mm)	0^o	0.0003	0.0000	90^o	0.0000	0.0178	180^o	-0.0003	0.0000	270^o	0.0000	-0.0184
		0.0002	0.0000		0.0016	0.0176		-0.0001	0.0000		-0.0017	-0.0182
		-0.0002	0.0000		0.0031	0.0170		0.0002	0.0000		-0.0032	-0.0175
		-0.0009	0.0002		0.0045	0.0160		0.0009	-0.0002		-0.0046	-0.0164
		-0.0017	0.0006		0.0056	0.0146		0.0017	-0.0006		-0.0057	-0.0150
		-0.0026	0.0011		0.0064	0.0130		0.0026	-0.0012		-0.0065	-0.0134
		-0.0037	0.0020		0.0069	0.0113		0.0036	-0.0020		-0.0069	-0.0115
		-0.0047	0.0030		0.0070	0.0095		0.0046	-0.0031		-0.0070	-0.0096
		-0.0056	0.0044		0.0068	0.0076		0.0055	-0.0045		-0.0068	-0.0078
		-0.0063	0.0059		0.0063	0.0059		0.0063	-0.0060		-0.0063	-0.0060
		-0.0068	0.0076		0.0056	0.0044		0.0068	-0.0078		-0.0055	-0.0045
		-0.0070	0.0095		0.0047	0.0030		0.0068	-0.0096		-0.0046	-0.0031
		-0.0069	0.0113		0.0037	0.0020		0.0069	-0.0115		-0.0036	-0.0020
		-0.0064	0.0130		0.0026	0.0011		0.0065	-0.0134		-0.0026	-0.0012
		-0.0056	0.0146		0.0017	0.0006		0.0057	-0.0150		-0.0017	-0.0006
		-0.0045	0.0160		0.0009	0.0002		0.0046	-0.0164		-0.0009	-0.0002
	89^o	-0.0031	0.0170	179^o	0.0002	0.0000	269^o	0.0032	-0.0175	359^o	-0.0002	-0.0000
		-0.0016	0.0176		-0.0002	0.0000		0.0017	-0.0182		0.0001	-0.0000

6.5 Conclusions

Through machining experiments and measuring of two parts: tire mold and spherical surface, the following destinations are reached:

(1) The correctness of the inverse kinematics is again verified.

(2) The tool position and tool axis are proved to be right.

(3) There are four evident lines on surface of finished part, which result from the backlash of ball-screw according to error model. It is shown that experimental results are completely in accordance with the theoretical results.

The error parameters adjustable in the commercial controller are considered as the main error parameters in this chapter. The effects of the selected error parameters are investigated by several DBB error measurement tests. A comparative study shows that the DBB measured results are nearly the same with the simulation results of chapter 5 when all the error parameters are set to be zero. The CMM measurement of the machined workpiece shows that the average machining error is about 0.3 mm. The sources of the manufacturing errors are discussed and deduced in this chapter. The three linear driving axes are not equilaterally arranged on a circle with angle 120^{o} is believed to be one of the important manufacturing error. The unparallel of the three linear driving axes is another important manufacturing error that significantly affects the machining accuracy. The experimental results show that the theories developed in this research are correct. Using the DBB measurement results for analyzing and finding the manufacturing errors and to improve the machining accuracy is a very essential and important topic. Much more efforts are worth and necessary in the further work.

Appendix

The RENISHAW QC10 ballbar

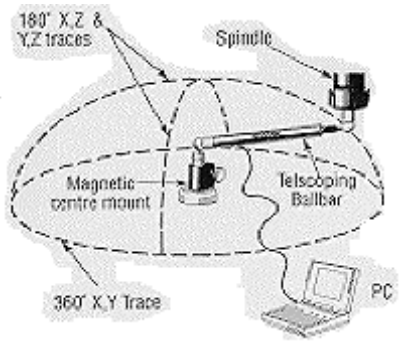

Figure A-1 Schematic diagram of QC10 ballbar

The Renishaw QC10 machine tool checking gauge(DBB) is simple in concept and elegant in design. The QC10 ballbar consists of an high accuracy displacement sensor housed inside a telescopic bar. The sensor contains two coils and a moving core and works on similar electromagnetic principles to those used in LVDT technology (Linear Variable Differential Transformer). As the ballbar length changes, the core moves inside the coils, and causes their inductance to change. This change in inductance is detected by laser calibrated measurement circuitry which converts the change in inductance into a position readout with a resolution of 0.1 microns and an accuracy of 0.5 microns at 20^{o}C.

The sensor is coupled directly to a precision ball on one end, and to a magnetic cup on the other. Another high precision ball is held in a magnetic base which is set on the machine's bed. This ball connects to the cup in the end of the ballbar body and is retained against a kinematic mount by a strong magnet. The kinematic mounting allows the measuring bar to rotate in any attitude. The ball on the end of the sensor is attached to another magnetic cup held in the machine spindle.

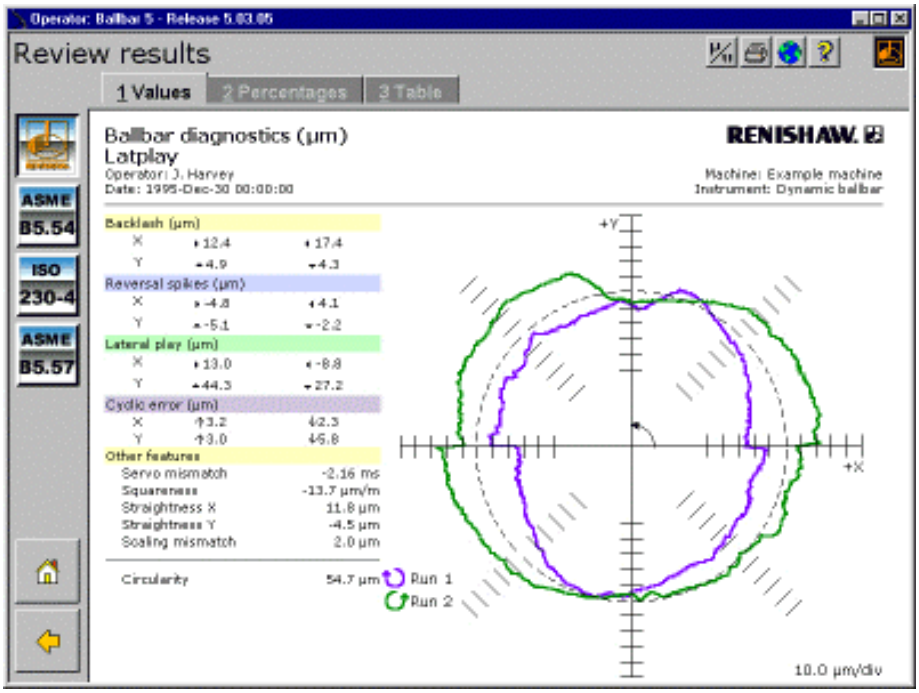

Figure A-2 Example of ballbar diagnostics screen

In this way, the ballbar is held magnetically between the machine table and the machine spindle. The machine spindle is driven round the centre point, by programming the machine to follow a circular path, with a radius equal to the length of the ballbar. As the machine moves, the sensor measures any variation in the path radius. From this, the PC based Renishaw software can derive volumetric accuracy, squareness values, repeatability, backlash, contouring ability, linearity XYZ, and servo performance. Driving the spindle through one flat circle, for example in the XY plane, will give X and Y lengths, XY squareness, backlash and servo performance. The whole process takes just a couple minutes.

The conditioning electronics is contained in a small box of electronics, which is battery powered. Two cables are used, one connected to the sensor, the other to the COM port of the computer. Data is sent to the computer using RS232 protocol. The electronics interface has a magnet on the back so that the box can be simply clamped to the machine.

The system is capable of a maximum sample rate of 250 values per second with maximum data points of 3600 per run. This allows dynamic checking of the machine tool as it is driven at different feedrates. From the same data, the QC10 calculates the contour error, allowing the operator to see the machine error at various feedrates. For example, if a contour was being machined on a particular machine tool, it would be possible to see which speed would give the best accuracy.

The QC10 can also pick up change of direction in the backlash of the drive systems, which happens when two axes change direction as they go through the 90^{o} quadrants of the test circle.

The QC10 is specified for operation from 0^{o}C to 40^{o}C, and the test is simple and quick to perform. An optional Zerodur Calibrator can also be used to provide radius verification to an accuracy of 1 micron, and compensation routines are included to normalize the readings back to 20^{o}C. Renishaw´s calibration software for the QC10 runs on any IBM compatible PC, simply requiring a RS232 serial (COM) port. Designed to be used by shop-floor operators, the menu driven software requires no programming knowledge. Standard lengths of the measuring bar with carbon fiber extensions can go up to 600 mm radius (1200mm diameter).

The QC10 is not only a checking gauge but is also part of standards for machine tool calibration and pass-off. Ballbar testing is included in a number of standards for machine tool accuracies i.e. ISO 230, ASME B5.54 and BS3800.

Reference : http://www.renishaw.com/userfiles/htm/CAL-WHI-0007.html

Chapter 7 Conclusions

7.1 Summary

A TRR-XY hybrid five DOF parallel link machine tool is developed in this research, which is a multi-axis machine tool and is composed of a parallel link mechanism and a serial link mechanism. This machine tool can improve the shortage of Stewart platform based machine tool and has some merits as follows: (1) improve ratio of workspace relative to machine volume; (2) enlarge workspace and improve singularity; (3) simplify the complexity of control system; (4) modular design and manufacturing are possible. Then, it can be cost down.

On this TRR-XY machine tool, the research topics include singularity analysis of workspace, design optimization of angular workspace, minimization of the driving forces, the effects of the manufacturing errors and the assembling errors on the machining accuracy. A prototype machine tool is developed to perform the experiments for verifying the correctness of the theory. The effects of the design dimensions R, r, L on the singularity, angular workspace, and machining accuracy are summarized in Table 7.1

Topic	Criterion	r/R	L/R
Singularity	The larger save workspace	Insensitive	Larger
Angular workspace	Maximum angular workspace	Smaller	Larger
Machining accuracy	High machining accuracy	Sensitive	Insensitive

Table 7.1 The effects of design dimensions(R, r, L) on the singularity, angular workspace, and machining accuracy.

The effect of the L/R ratio on the singularity is very significant. The smaller the L/R ratio has the smaller safe workspace. The workspace volume is not significantly varied with different r/R ratio. To consider the effects of L/R and r/R together, it is found that the shorter link length (L) with larger tool frame diameter (r)

has a relative smaller workspace. To obtain a maximum angular workspace of the machine tool by changing dimension parameters is one of the main purposes of this research. In general, the optimal workspace can be obtained by smaller r/R ratio and larger L/R ratio.

For a practical situation, the rotation angles of pin joint and ball joint are limited. The optimization result will be affected by the limitation of the rotation angles of pin joint and ball joint. Generally speaking, the conclusions of angular workspace optimization and singularity analysis are agreed in this research. For the machining accuracy issue, the effects of the r/R ratio on the machining accuracy are found more significant than that for the L/R ratio. The effects are varied with different cutting positions.

The dynamic analysis and modeling for the TRR-XY PLM are derived based on D-H notation method. The parametric tool concept and Lagrange-equation theory are also included in the derivation. The main results show that the required actuator driving forces are mainly affected by the inclination angle (ϕ) of the tool platform. The effects of the angular acceleration of the tool platform are relatively small. The actuator driving forces are increased very rapidly with $|\phi|>40°$. This means that the working space within smaller ϕ is suitable for TRR-XY PLM machining applications.

Two error models are developed in this research: manufacturing error model and controller parameter error model. Due to the symmetry structure of TRR-XY machine tool, analytical machining errors results are also symmetry with A, B, and C chains. The research results show that precision components and precise assembly processes are very important in the developing of a PLM.

The controller parameter error model is developed based on the error definition of a commercial controller. The sensitivity of manufacturing errors is investigated and discussed in this research. From the analytical results, we know that pin joint Y direction position error, ball joint X direction position error and link length error have larger effects on the machining accuracy.

It can be observed from the real cutting experiments that machining accuracy is changed in different cutting zones due to different assembly precision of the three

kinematic chains. Four protrusive lines are obviously appeared on the spherical cutting surface. They may be caused by backlash of ball screws.

The CMM is used to measure the spherical machining surface results. The maximum difference between measured results and CAD model is about 0.3mm. It is worth mentioning that the machining error increased with the tilt angle increased. The manufacturing errors of the machine tool were also carefully measured. The radius error of the circle, that the three driving axes are located on, is about 0.5-0.6mm. The locations of the driving axes of A, B, C chains are also found to be slightly not in parallel. The radius error and not in parallel of the three driving axes are considered to be the causes for the poor machining accuracy. These deduction results are agreed with the analysis results of manufacturing error model.

To verify the correctness of the error model, some online measuring tests are performed by DBB measuring system. Three tool paths on a spherical surface are planed for testing. The machining accuracy and its repeatability are measured based on the manufacturing errors that originally existed in the hybrid machine tool. Some error parameters also input to the manufacturing error model for a theoretical investigation. Comparing the sensitivity analysis results with the theoretical results, it is not difficult for us to find that the experimental results agree with those of simulated results without the consideration of the moving axes in reverse motion. However, the theoretical results are slightly different with the experimental results under the situation of moving axes in reverse motion. It is deduced that the different results may be caused by the backlash of moving axes in reverse motion. The correctness of the error model presented in this research is then testified.

7.2 Discussion

A novel TRR-XY hybrid parallel link mechanism is developed and applied into the design of a new machine tool for the machining applications. High productivity, high accuracy, high reliability, and cost down are the most important issues that must be considered in the design stage. The larger volume may make the machine tool

cost up and also poor machining accuracy. Specially, the thermal expansion is usually very difficult to be eliminated with a large machine dimension. Therefore, lower down the workspace/machine volume ratio is a very essential issue for developing a new machine tool. The system stiffness of a parallel link machine tool is also very important for developing a new machine tool. The design requirements from the system stiffness viewpoint may be contradicted to the design requirements from linkage dimension (R, r, L, θ_{max}) optimization results. However, thermal expansion problems are more complicate and very difficult to be solved compared with the system stiffness problems. The larger dimensions are obviously increasing the difficulty of the thermal expansion problems. Therefore, the workspace/machine volume ratio will be investigated first in this research before developing a new parallel link machine tool. The effects of the parameters L, R, and r on the workspace/machine volume ratio are investigated in this research. From the conclusions in the above section, it is found that a larger workspace can be obtained with smaller r and larger L. The limitation of rotation angle of ball joint significantly affects the domain and range of workspace. Therefore, it must be considered first on optimizing the machine tool dimension (R, r, L, θ_{max}). The machining efficiency or the power consumption is the second important topic. A high speed machining with low power consumption is the aim of this research. The inverse dynamic analysis shows the force variation with different cutting conditions. The analysis results are very useful for the designer to choice a suitable servomotor. The analysis results also show that the spindle inclination angle ϕ significantly affects the driving force variation. A ϕ limitation is existed for each machine tool. Machining outside the ϕ limitation, the required driving force is rapidly increased. Therefore, the developed TRR-XY hybrid machine tool is suitable for $0°<\varphi<360°$ high speed five-axis machining within the limited ϕ angle. The manufacturing errors and assembling errors of a machine tool will affect not only the machining accuracy but also the cost. The effects of the manufacturing errors and the assembling errors on the machining accuracy are the third topic investigated in this research. It is found that the 1 mm translation errors, such as δ_{Sxi}, δ_{Syi}, δ_{Jxi}, δ_{Jzi}, δ_{Fxi}, δ_{Fyi}, may have

the ds stroke error about -0.6 ~ +0.6mm. However, the 1° orientation errors, such as α_i, ϕ_i, β_i, may have the ds stroke error about -4 ~ +4mm. Therefore, accurately arrange and assemble the three linear sliding axes is very important. The three linear axes should be equilaterally located on a circle with radius R. It is obvious that the parallel of the three linear axes is also important. The backlash of the slider is also found to have significant effects on the machining results. The research results of this thesis show many useful theories and important data that are very helpful for the designer to develop this new machine tool.

7.3 Future work

Using the TRR-XY hybrid parallel link mechanism into a machine tool is addressed in this research. A five-axis PLM machining center made by Cincinnati Company (USA) and DS Technology Company (Germany) was demonstrated in IMTS'2002. This PLM machine center uses the same structure as TRR-XY machine tool built in this research. Both of them are composed of a TRR three-axis parallel link mechanism and a two-axis X Y serial link mechanism. This implied that the developed hybrid parallel link machine tool has already reached an applicable stage. To fully understand the fundamental theories and essential characters of this machine tool is important. Several important topics are still required to be worked out for fully understanding the performance of this machine tool. For example, optimization system stiffness, theory of error compensation, and etc…

Tilt angle of tool axis has great effect on cutting performance. Actuator driving force is increased greatly and rapidly once the tilt angle exceeds a critical value. For the TRR-XY machine tool developed in this research, the critical tilt angle is about 40 degree. Theoretically, the actuator driving force can be decreased by enlarging the machine tool size and by increasing the link length. The interaction and relationships for ϕ, machine tool size, and driving force does need in-depth study.

Spatial precision measuring is an important topic and required to be studied in multi-axis machine tool. The DBB measuring system employed in this research is

an indirect measuring method. The accuracy can only be verified with direct physical measurement. The accuracy is very difficult to be testified by experiments because the position of tool tip cannot be measured directly. The same problem also exists with manufacturing error measurement. In the measuring experiments, the dimensions of each part are measured and used to investigate the assembled accuracy. The effects of the measured errors on the machining accuracy may be averaged, counteracted, or decreased in the practical applications for the developed machine tool. At present, it cannot be concluded whether this phenomenon is a general case, existed for all the PLM, or only a special case for this developed TRR-XY hybrid machine tool. So, this topic is worth an in-depth discussion. The manufacturing errors that measured by DBB measuring system are the errors from the whole machine tool. Due to mutual effect of the error factors, it is not easy to fine the error sources according to the measured data from DBB method. Creating a figured database of error tracking and sensitivity analysis is helpful for engineers or users to take as reference. How to improve and compensate the manufacturing errors is definitely the important work in next stage.